PROBABILITY BASED MODELS FOR THE POWER DRAW AND ENERGY SPECTRA OF A TUMBLING MILL

by

BBOSA, Lawrence Sidney

Thesis presented for the degree of
DOCTOR OF PHILOSOPHY
In the Department of
Chemical Engineering
March 2013

CENTRE FOR MINERALS RESEARCH
UNIVERSITY OF CAPE TOWN

ABSTRACT

Positron Emission Particle Tracking (PEPT) and the Discrete Element Method (DEM) are used to develop probability based models for the power draw and collision energy spectra of a tumbling mill. Experiments are conducted using dry spherical glass bead charge in a laboratory scale tumbling mill, which is mounted with a torque transducer and tachometer to measure mill power. Particle tracking information from PEPT is used to reconstruct the motion of glass beads and infer the overall charge behaviour, while DEM is employed to simulate particle motion and interaction, with collision mechanics calculated using the Hertz-Mindlin contact model. For both sets of data, the product of torque and average angular velocities in discrete cells are accumulated to obtain mill power. This method is found to be within statistical agreement with measured power for all tests. The information from both techniques is then used to develop a model for the power draw as a function of particle size, mill speed and volumetric filling. Predictions of the model match well with measured and calculated values. Based on frequency distributions of collision energies from DEM, a model for the energy spectra of each particle size per steady state mill revolution is developed. This model is found to predict collision frequencies within close agreement with DEM simulation data and follows trends consistent with existing work on tumbling mill modelling.

PLAGIARISM DECLARATION

I am aware that plagiarism, the reproduction of the work of another author is wrong.

2. I have used the scientific convention for citation and referencing. Each significant contribution to, and quotation in this thesis from the work(s) of other people has been attributed, and has been cited and referenced.

3. This thesis is my own work.

4. I have not allowed, and will not allow anyone to copy my work with the intention of passing it off as his or her own work.

Signature: Signed by candidate Signature Removed

Date: 14th March 2013

TABLE OF CONTENTS

ACKNOWLEDGEMENTS

Gratitude must be expressed toward a number of people for their contribution to this thesis:

Prof. Aubrey Mainza for his thorough feedback and advice while overseeing this work.

Dr Indresan Govender for his encouragement and support during the course of this study.

Prof. David Parker and Dr. Thomas Leadbeater for their assistance with carrying out the PEPT experiments.

Dr. Matt Sinnott for his assistance with the finer points of Discrete Element Modelling.

Anglo American Platinum for enabling this research work to be conducted.

To the CMR team for acting as sanity checkers by facilitating and engaging in robust discussions on this project.

To my parents for being the greatest cheerleaders and support imaginable.

And lastly to my adorable wife, for your incredible patience and belief throughout the course of this study. (*and for Emmy*).

LIST OF ABBREVIATIONS AND NOMENCLATURE

The following is an alphabetical list of abbreviations as used in this thesis:

DEM- The Discrete Element Method

PEPT- Positron Emission Particle Tracking

CoC – Centre of Circulation

E_{90} – Energy below which 90% of collisions occur in tumbling mill

N_{100} – Energy at which collision frequencies decay to 100 collisions

E_0 – Collision energy below which inconsequential damage occurs to particles.

Nomenclature used for Equations (in order of appearance)

y- Dependent variable

x- Independent variable

M_c- Total charge mass

J - Fractional mill volumetric filling

V_m- Mill volume

ε - Charge porosity

ρ - Charge density

a_0, a_1, $a_2 \ldots a_n$, b_0, b_1, b_2, b_3, b_n - Fitted function parameters

P_{MEAS}- Measured mill power draw from torque sensor

K_c – Torque sensor calibration factor

V – Voltage recorded by torque sensor

ω - Angular mill speed

P_i – Number of particles in each size class

V_i – Particle volume

b_1, b_2- Fitted function parameters

c_1,c_2- Fitted function parameters

P_{PEPT} – Power draw calculated using cumulative torque per bin method from PEPT data

M_i – Charge mass present in each grid location i

g- Acceleration due to gravity

x_i – Distance from mill centre to bin i

ω_t - Charge angular velocity in bin i

P_{BIN}- Power draw calculated using cumulative torque per bin method with DEM data

P_{GEOM}- Power draw calculated from DEM data using force balance approach against mill geometry

N_{GEOM}- Number of nodes in mesh used in DEM simulation

F_g- Force at each node extracted from DEM

V_g- Velocity at each node extracted from DEM

R_1, R_2 – Radii of two contacting particles

R_m - Inner radius of the mill geometry.

ζ - Damping coefficient of two colliding particles

$Pr(C_Y)$- Probability that a collision will occur either between two particles or a particle and the mill geometry over a given time step

$Pr(C_N)$- Probability that for a given particle no collision occurs over a given time step

$Pr(C_{pp})$- Probability that two selected particles will collide over a given time step

$Pr(C_{pm})$- Probability that a particle will collide with the mill over a given time step

$Pr(E_1<E<E_2|C_y)$- Probability that a collision will take place between two particles with the dissipated energy between E_1 and E_2 over a given time step

K_1, $K_2 \ldots K_n$ - Fitted function parameters

E- Energy dissipated during collision between two particles

N- Frequency of collisions that occur between a discrete energy band

A - Fitting parameter for first initial value term in double exponential decay collision frequency model

B - Fitting parameter for lower value decay rate in double exponential decay collision frequency model

C - Fitting parameter for second initial value term in double exponential decay collision frequency model

D - Fitting parameter for higher value decay rate in double exponential decay collision frequency model

p- Particle size (m) in collision frequency model

c- Mass fraction of total charge present in particular size class

ω_m- Fraction of mill critical speed

LIST OF TABLES

CHAPTER 2

CHAPTER 3

CHAPTER 4

CHAPTER 5

CHAPTER 6

CHAPTER 7

CHAPTER 8

LIST OF FIGURES

CHAPTER 2

CHAPTER 3

CHAPTER 4

CHAPTER 5

CHAPTER 6

CHAPTER 7

CHAPTER 8

CHAPTER 1

INTRODUCTION

1.1 Background and Hypotheses

In comminution circuits, the power draw of tumbling mills is an important design and operating variable. The net power draw of a tumbling mill refers to the energy expended per unit time in causing motion of the contents, or charge (Austin et al., 1987). This quantity is determined as a product of the torque exerted by the charge on the external shell and the specified mill rotational speed (Arbiter and Harris, 1982). The energy imparted to the charge is subsequently dissipated in the form of particle interactions which may lead to breakage (Mishra and Rajamani, 1992).

Many models have been proposed to predict the power draw of tumbling mills (See Section 2.1). Early models relied on simplified assumptions of charge motion as the factors which influenced internal mill dynamics could not be analytically determined (Taggart, 1945). In the last several decades, advancement in measurement and computational tools has enabled more detailed study of the mechanisms that govern charge motion behaviour. This has provided the opportunity to develop mechanistic models which describe the power draw in terms of the variables that influence charge motion (Govender and Powell, 2006).

The Discrete Element Method (DEM) is one such means of analysing the internal dynamics of tumbling mill motion (Agrawala et al., 1997. Cleary, 1998. van Nierop et al., 2001). With this computational technique, the motion of individual bodies is calculated using Newton's laws while the body interactions are simulated using a set of equations referred to as the contact model (Cundall and Strack, 1979). The contact model calculates the forces and energy losses associated with inter-particle interactions as well as interactions with the mill geometry. A number of contact models with distinctly different implementations have been employed to conduct tumbling mill simulations (Cleary et al., 2003. Mishra and Rajamani, 1992. Zhang and Vu-Quoc, 2007). The selected contact model, along with its specified material parameters, dictates whether the numerical simulation reflects an accurate representation of charge motion and interaction.

Validation of the particle motion and interaction information from DEM simulations of tumbling mills is necessary to verify that the system represents an accurate representation of the internal environment. This presents a challenge due to the impracticalities associated with direct measurement of motion, contact forces and collision energy losses in such an aggressive and stochastic system.

From the force and collision energy data extracted from DEM simulations, the net power draw can be determined (Mishra and Rajamani, 1992. Cleary, 1998). The measured power draw from tumbling mill experiments designed to replicate the computational system can be compared to the predictions from DEM as a means of assessing whether the energy environment is simulated accurately (Misra and Cheung, 1999). While the calculated power draw prediction may be in agreement with measurement, this does not necessarily mean that the motion of particles is correctly represented (Martins et. al, 2012).

Several techniques have been used to analyse actual charge motion in tumbling mills and used for comparison with predictions from DEM simulations. These have mainly involved studying particle motion in simplified systems via means such as high speed filming, piezo-electric sensor measurement and X-Ray photography (Cleary et al., 2003. Dong and Moys, 2001. Mishra, 2003. Govender et al, 2001a). Positron Emission Particle Tracking (PEPT) is also a technique that has been utilized to analyse charge motion in rotating drums (Parker et al., 1997). The premise of the method involves obtaining the position of a radioactive particle at discrete time intervals in the field of view of Positron Emission Tomography (PET) equipment (Parker and Fan, 2008).

Using PEPT, the trajectory of a single particle in a stochastic system such as a tumbling mill can be obtained (Govender et al., 2011). The bulk properties of the charge body can then be represented by averaging the motion of the single particle tracked at steady state, provided that sufficient time elapses such that the data is statistically representative (Conway-Baker et al., 2002). The unique value of this aspect is that data from PEPT can be used to calculate the average kinematic properties of every size within a charge distribution. This information can be used to compare the motion behaviour of each size class within the distribution (Bbosa et al., 2011). In a similar way to DEM simulation data, calculated power draw from PEPT data can be validated by comparison with the net power draw from measurement. The

average kinematic properties of charge motion in a tumbling mill from PEPT experiments can then be compared against similar properties from DEM simulations of identical systems (Yang et al., 2003). This offers a unique quantitative method of verifying the results of DEM simulations which considers the charge motion characteristics in addition to validating the energy environment against power draw measurement.

A major advantage of using DEM is the ability to simulate the interactions between discrete bodies, and consequently obtain the collision history of every particle in the system. From this data the frequency distribution of dissipated collision energy losses, or 'energy spectra' of the charge can be determined (Rajamani et al., 2000). This information has led to significant improvements in the understanding of tumbling mill energy utilization, such as highlighting that the distribution is dominated by relatively low level collision energies (Powell and McBride, 2004).

Energy spectra plots from DEM simulations are distributions which are influenced by the charge motion characteristics which arise from the mill operating variables. The effects of operating variables such as particle size and mill speed on the energy spectra have been studied in prior research (Khanal and Morrison, 2009. Yang et al., 2008). Trends observed from these distributions suggest that the energy spectra can be modelled as a function of the mill operating variables that influence it (Powell et al, 2008).

This study aimed to integrate computational data with experiment in order to analyse the power draw and subsequent energy dissipation of charge particles in tumbling mills. To accomplish this, single particle tracking experiments using PEPT were performed using dry glass beads in a laboratory scale tumbling mill. These tests were used to examine the charge motion behaviour and calculate time averaged kinematic properties of each size. DEM simulations replicating the experimental conditions were carried out using the Hertz-Mindlin contact model. The average kinematic properties of the charge particles extracted over a single steady state mill revolution were then compared against PEPT data. In addition, measured power draw and calculated power from PEPT experiments were used to validate that the energy environment calculated by the DEM simulation correctly depicted the actual motion. Functions that describe the charge motion characteristics of each size were subsequently used to develop a model for the mill power draw. Further, the collision energy

spectra data from DEM was used to construct a model for the dissipated energy loss per particle size over a mill revolution. The hypotheses for this study were as follows:

Hypotheses

- Kinematic data from PEPT and DEM can be used to examine and quantify the influence of particle size, mill speed and volumetric filling on charge motion, and consequently the power draw. This is because the two constituents required to determine power draw, the charge packing and particle velocity can be calculated from these techniques.

- For a drum filled with a given charge distribution and volumetric filling rotating at a given speed, the probability that particles will collide resulting in a particular energy loss can be predicted from DEM simulation data. This is because the collision information logged from DEM simulations can be used to calculate the relative occurrences of collisions at different energy levels during a single rotation.

1.2 Objectives and Scope

This thesis analysed the outcomes of PEPT experiments and DEM simulations in order to address the following objectives:

1. To calculate time averaged charge kinematic properties of each size class in a tumbling mill from PEPT experiments, including location probability, velocity, porosity and power draw.

2. To extract information from DEM simulations and calculate identical charge kinematic properties that could be compared against PEPT data.

3. To utilize charge motion information from PEPT and DEM to develop a mathematical model for the power draw of each particle size in a charge distribution

4. To use extracted collision energy data from DEM to develop a model for the frequency distribution of energy losses for each size.

As described in the background, this project aimed to utilize experimental and computational techniques to develop models for the power draw and collision energy distribution of each particle size over a steady state mill revolution.

For each PEPT experiment, a single particle was tracked in a 300mm diameter laboratory scale tumbling mill. Spherical glass beads in a distribution from 2-8mm were used as charge. Individual tracking experiments were carried out for each size and used to reconstitute the behaviour of the overall charge.

EDEM, a software package developed by DEM Solutions (DEM Solutions, 2006), was used for the numerical modelling work. Simplified CAD design drawings were imported to the software for use in all simulations.

The contact model utilized in this study was the Hertz-Mindlin (no slip) model, with viscous damping enabled. This was the default contact model in the computational software and recommended by the designers as it implemented a force displacement model which varied

according to Hertzian theories of elastic contact (DEM Solutions, 2006). It has also been demonstrated to correctly represent particle interaction in tumbling mills (Kulya, 2008. Khanal and Morrison, 2009).

A laboratory scale tumbling mill was used for the tests and simulations in this study. As the mill was operated in batch mode, particle motion in the feed trunnion and grate discharge was not considered. This was because prior research indicated that charge motion in these regions mainly affects material transport, with negligible effect on power draw and energy dissipation (Mishra and Rajamani, 2003).

Since glass beads were used as charge, the complexities introduced by the variation in charge density were not considered in this work. In addition, the interaction forces generated by the motion of the beads were too low to cause breakage. This allowed the study to focus on the analysis of a homogenous charge independent of breakage.

A single lifter geometry was used for the experiments and simulations in this thesis. While it is known that the lifter geometry affects charge motion, and in turn power draw (Datta et al., 1999), the focus of this study was primarily to analyse the influence of particle size on the power draw and energy dissipation of the mill. The influence of lifter height and lifter angle on the charge motion has been investigated by other authors (Djordjevic, 2003. Brodner, 2013).

The single particle tracking experiments and DEM simulations were conducted under dry conditions, neglecting the effects of charge viscosity. Viscosity has been demonstrated to be a significant factor influencing power draw in tumbling mills (Fuerstenau, 1990. Moys, 1990). However, the experimental work in this thesis was a simplified system which analysed the motion of dry granular media. This was a simplification based on prior work by other authors for which the behaviour of dry granular charge was investigated independent of charge viscosity (Parker et al., 1997. Mellmann, 2001, Yang et al., 2008. Govender et al., 2012). This allowed the computational modelling to be carried out using DEM independently, without the use of multiphase modelling techniques such as Computational Fluid Dynamics (Anderson, 1995) or Smoothed Particle Hydrodynamics (Gingold and Monaghan, 1977).

1.3 Plan of development

CHAPTER 1: This Chapter provides a background to the thesis, and provides the hypotheses, objectives and scope of the study.

CHAPTER 2: This Chapter is a review of literature from prior research that is relevant to the work in this thesis.

CHAPTER 3: The experimental methodology used in conducting PEPT experiments and DEM simulations is laid out in this Chapter.

CHAPTER 4: Results from the analysis of data from PEPT experiments are given in this Chapter.

CHAPTER 5: This Chapter provides a summary of results from DEM simulations and a comparison against PEPT results. The collision energy spectra is discussed thereafter.

CHAPTER 6: The approach taken to model the charge and the average angular velocity distributions of each size are detailed in this Chapter. The methodology followed to develop the power draw model of each size is then described.

CHAPTER 7: The formulation of the energy spectra model and its subsequent testing against simulation data is provided in this Chapter.

CHAPTER 8: A discussion of the model and its limitations is given in this Chapter, along with an examination of its predictive capabilities using results from a pilot plant tumbling mill simulated with DEM.

CHAPTER 9: Conclusions based on the work from this thesis are provided, and recommendations are made for future work in this area.

CHAPTER 2

LITERATURE REVIEW

Overview

This chapter discusses research from prior work that is pertinent to this thesis. A summary of the approaches that have been taken toward predicting power draw in tumbling mills is given, followed by a discussion of research outcomes from utilizing the Discrete Element Method (DEM) and Positron Emission Particle Tracking (PEPT). The chapter concludes by highlighting key aspects from research that form the basis for this study.

2.1 History of tumbling mill Power Draw models

Comminution is well known to be the largest consumer of energy in mineral processing circuits (Napier-Munn et al., 1999). As tumbling mills are the most commonly installed device in such circuits, their power draw, or the energy per unit time required to operate them is regarded as a key design and operating variable (Morell, 1992). The effective utilization of this applied energy in causing size reduction of the charge is similarly of important consideration (Mishra, 2003).

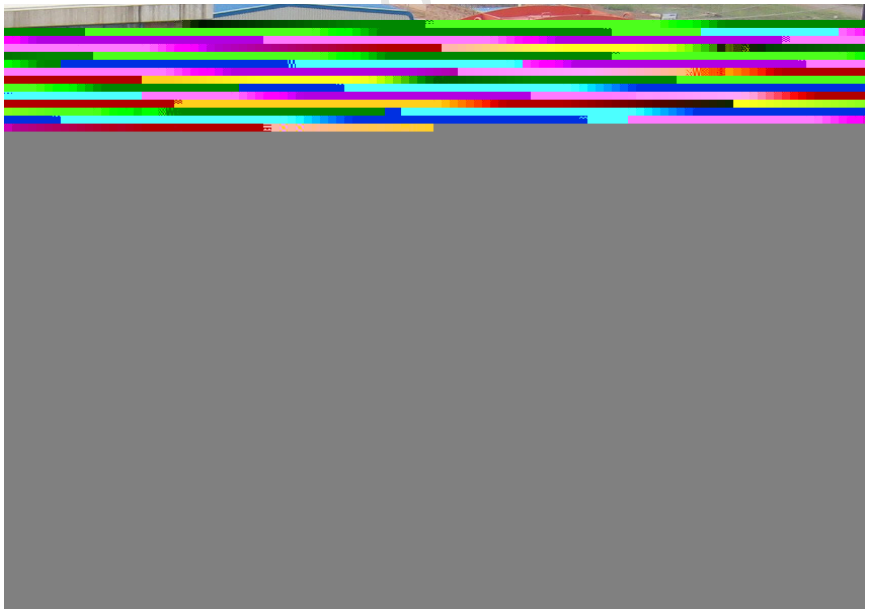

Figure 2.1: Tumbling mill in a comminution circuit

Tumbling mills are known to be highly energy intensive and inherently inefficient (Fuerstenau and Abouzeid, 2002). Industrial scale tumbling mills, an example of which is depicted in Figure 2.1, are typically driven by a gear and pinion assembly mounted on the external shell

(Wills and Napier-Munn, 2006). The power required to rotate the shell at a specified speed is a direct consequence of the torque caused by the motion of charge, independent of a consideration of breakage (Mishra et al., 1990). The use of this energy in achieving size reduction is then a result of the particular mode of breakage that is dominant under the operating conditions (Napier-Munn et al., 1999).

There have been many approaches taken to mathematically describe charge motion behaviour with a view to predicting power draw in tumbling mills. A discussion of the progression made with these methods is given in the sections that follow.

Summary of charge motion characteristics

The power drawn by a rotating mill has a direct correlation with the type of charge motion produced by the regime in which it operates (Wills and Napier-Munn, 2006). The charge motion, and consequently power draw has been demonstrated to be influenced by mill operating variables such as lifter height and speed, as well as charge parameters such as size and volumetric filling (Powell and Nurick, 1996c).

The work of Mellmann (Mellmann, 2001) aptly summarizes the different types of charge motion that occur with increasing speed in a rotating mill. As shown in Figure 2.2, charge motion is largely divided into three basic types, which can be further divided into seven subtypes. Differences in appearance and an indication of the resistance to flow that characterizes each regime are highlighted.

Basic form	Slipping motion		Cascading ("tumbling") motion			Cataracting motion	
Subtype	Sliding	Surging	Slumping	Rolling	Cascading	Cataracting	Centrifuging
Schematic							
Physical process	Slipping		Mixing			Crushing	Centrifuging
Froude number Fr [-]	$0 < Fr < 10^{-4}$		$10^{-5} < Fr < 10^{-3}$	$10^{-4} < Fr < 10^{-2}$	$10^{-3} < Fr < 10^{-1}$	$0.1 < Fr < 1$	$Fr \geq 1$
Filling degree f [-]	$f < 0.1$	$f > 0.1$	$f < 0.1$	$f > 0.1$		$f > 0.2$	
Wall friction coeff. μ_w [-]	$\mu_w < \mu_{w,c}$	$\mu_w \geq \mu_{w,c}$	$\mu_w > \mu_{w,c}$			$\mu_w > \mu_{w,c}$	
Application	no use		Rotary kilns and reactors; rotary dryers and coolers; mixing drums			Ball mills	no use

Figure 2.2: Transverse motion of solids in rotating cylinders (taken from Mellmann, 2001)

In comminution, the type of motion that is desired in tumbling mills is a combination of the cascading and cataracting regimes. As indicated in the diagram, this motion encourages the most mixing and grinding of material which are key objectives in such mills.

From the work by Mellmann (Mellmann, 2001), the motion of charge in the different regimes is summarized as follows. At lower speeds, such as rolling, while mixing may occur, the charge does not generate much motion, which severely reduces the amount of size reduction that is generated via impact. At higher speeds, at which centrifuging occurs, the charge mainly clings to the periphery of the mill which leads to little in the way of grinding and mixing and is of no use. Additionally, at speeds close to the centrifuging value, the trajectory of falling material begins to impact against the mill shell rather than the charge which is damaging to the internal surface. Due to the undesirable consequences of running a tumbling mill in these regimes, it is of great importance to ensure that the operating conditions create the desired collision environment.

Several descriptors of charge motion have been introduced to characterize the degree of mixing and impact in tumbling mills. These features are evident when charge motion is captured using techniques such as videographic filming (Venegopal and Rajamani, 2001), PEPT (Govender et al., 2004) and DEM (Powell and McBride, 2004). The work by Powell and McBride (Powell and McBride, 2004), illustrated in Figure 2.3, provides a summary of the main features that are customarily used to describe motion in tumbling mills. In this diagram, the particle trajectory in the cascading and cataracting regime was visualized in a two-dimensional plane along the transverse mill face and used to define several descriptors for the bulk motion.

The head was defined as the highest vertical position attained by the charge. The departure shoulder was defined as the uppermost point at which the charge departed from the mill shell. Powell and McBride defined two distinct toe regions in their work. The bulk toe was located at the point at which the cascading charge collided against the mill shell and the impact toe was the point at which the cataracting charge collided with the shell. A flow region known as the equilibrium surface was also defined, a region of zero velocity which separated the ascending charge from the descending charge. Along this surface, the point about which the charge in the mill rotated was termed the centre of circulation. The free surface was the curve that separated the bulk rising and cascading charge from the cataracting material in free flight.

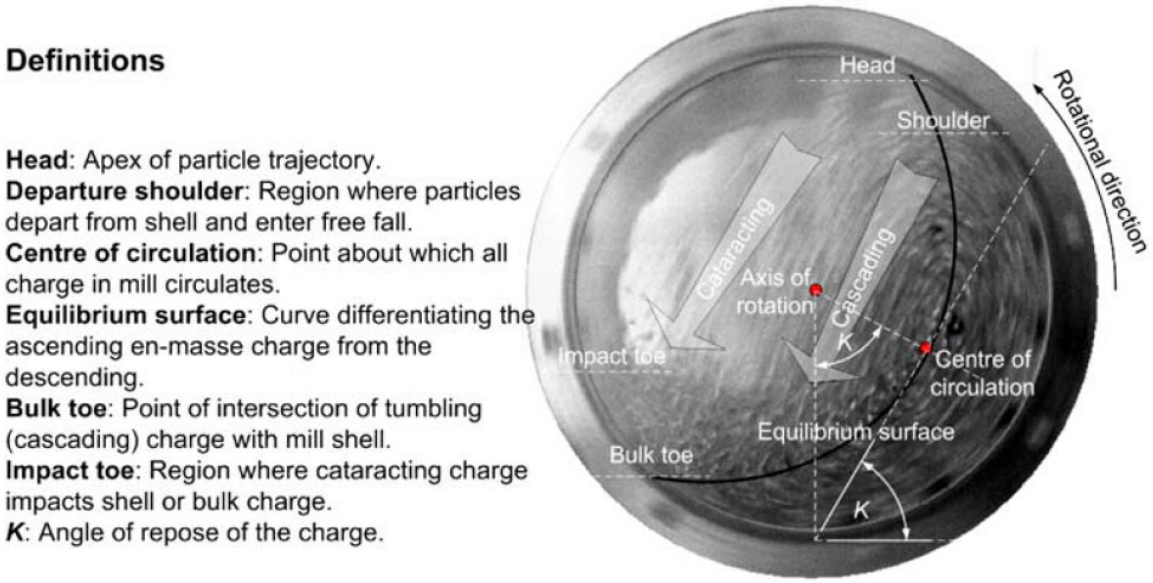

Figure 2.3: Charge motion features as described by Powell and McBride (Powell and McBride, 2004)

Power Draw models

The work of Davis in 1919 (Davis, 1919) was among the first attempts made to determine mill power in terms of charge motion. Davis applied a simplified description of motion by assuming that particles moved along fixed concentric paths with the mill shell of radius *r* under the influence of gravity and centrifugal force. Upon reaching a critical point, the charge then departed from the bulk zone and returned to the base of the mill under free fall. The point of departure from the rising bulk charge along each concentric radial line was given geometrically by a so called 'Davis circle' as shown in Figure 2.4.

After calculating an expression for the point of impact of each departing path, Davis used an energy balance to derive the kinetic energy as a function of radial position. This function could be integrated over all the motion paths to give an expression for Power Draw (in horsepower) as given in Equation 2.1

$$P = W r_1^{\frac{3}{2}} \left[\frac{4.467 \cdot (1 - K^3)}{1000 \cdot (1 + K^2)^{\frac{1}{8}}} - \frac{3.7 \cdot (1 - K^5)}{1000 \cdot (1 + K^2)^{\frac{3}{8}}} + \frac{8.8 \cdot (1 - K^7)}{10000 \cdot (1 + K^2)^{\frac{5}{8}}} \right] \qquad \textbf{Equation 2.1}$$

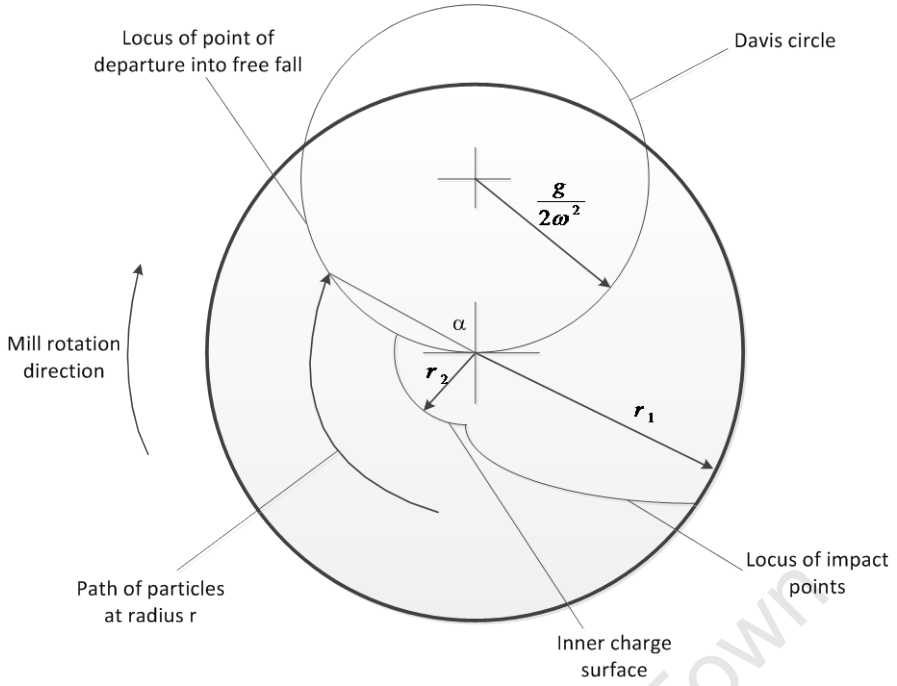

Figure 2.4: Schematic of charge motion as proposed by Davis (Davis, 1919)

In this model, *W* is the weight of the charge in pounds and r_1 is the inner radius of the mill. *K* is the ratio of the inner charge radius r_2 to r_1, derived to be a function of the volumetric filling *J* as given in Equation 2.2:

$$K = \left(\frac{39}{100}\right) \cdot \sqrt{7 - 10 \cdot J} - \left(\frac{2.4}{100}\right) \qquad \textbf{Equation 2.2}$$

Davis tested his power equation using data from a 3 inch diameter mill, and found that it gave good predictions at a rotational speed he termed the 'optimum speed'. This was defined to be the speed at which departing particles in free fall impacted at the maximum kinetic energy.

Hogg and Fuerstenau found that Davis' power draw model was highly simplified, and fitted a very specific case of operation (Hogg and Fuerstenau, 1972). The expression for the Davis circle was also not adequate to correctly describe the behaviour of particles as it assumed that all the charge would descend in free flight. It also ignored many significant contributing factors to mill power draw such as charge density, particle size and lifter shape (Austin, 1990, Morell, 1993).

The model put forward by Rose and Evans in 1956 (Rose and Evans, 1956a, Rose and Evans, 1956b) took into account most of the variables that were known to affect power draw. These researchers conducted experiments using a ball charge in water, as well as powder

mixed with fluid at different solids concentrations, in different mill sizes of up to 3 inches in diameter. By measuring the power draw, they used dimensional analysis to graphically determine the effect of each operating variable. The developed equation was simplified until the function for mill power draw in Equation 2.3 was derived:

$$\frac{P}{D^5 N^3 \rho} = \left(1 + \frac{4 \cdot \sigma}{10 \cdot \rho}\right) \cdot \left(\frac{L}{D}\right) \cdot \left(3.13 \cdot \left(\frac{N_c}{N}\right)^2\right) \cdot \emptyset_3' \cdot J \qquad \textbf{Equation 2.3}$$

Here, *D* is the internal mill diameter, *N* is the mill speed in revolutions per second, and ρ is the ball density. σ is the effective density of the fluid powder mixture, while *L* is the internal mill length. N_c is the mill critical speed, defined as the speed at which charge at the liner surface centrifuged, and could be determined (in rpm) using Equation 2.4

$$N_c = \frac{42.3}{\sqrt{D}} \qquad \textbf{Equation 2.4}$$

The model was tested using data from a pilot scale mill for speeds of up to 75% of critical. It was found that while the model followed trends consistently, it underestimated the power draw, and showed a significant variance. Further, according to their model, the ball size was stated to have little effect on mill power draw which later work would show was not the case (Morell, 1992).

The work of Bond in 1961 (Bond, 1961) developed a model which became among the most widely used in industry to date. Bond used empirical data from a 0.3m mill to develop a model for power draw given as:

$$P = 12.262 \cdot \rho \cdot L \cdot D^{2.3} \cdot J \cdot (1 - 0.937 \cdot J) \cdot \left(\frac{1 - 0.1}{2^{9-10\emptyset}}\right) \qquad \textbf{Equation 2.5}$$

The density ρ used is the bulk density of steel balls, while *L* and *D* are the mill internal length and diameter respectively. J is the mill volumetric filling and ϕ is the fraction of mill critical speed.

The model was found to scale well for up to industrial size mills, and thus gained popularity. However, as it was based on empirical data its predictive capabilities were limited to the range for which it was designed (Morell, 1993).

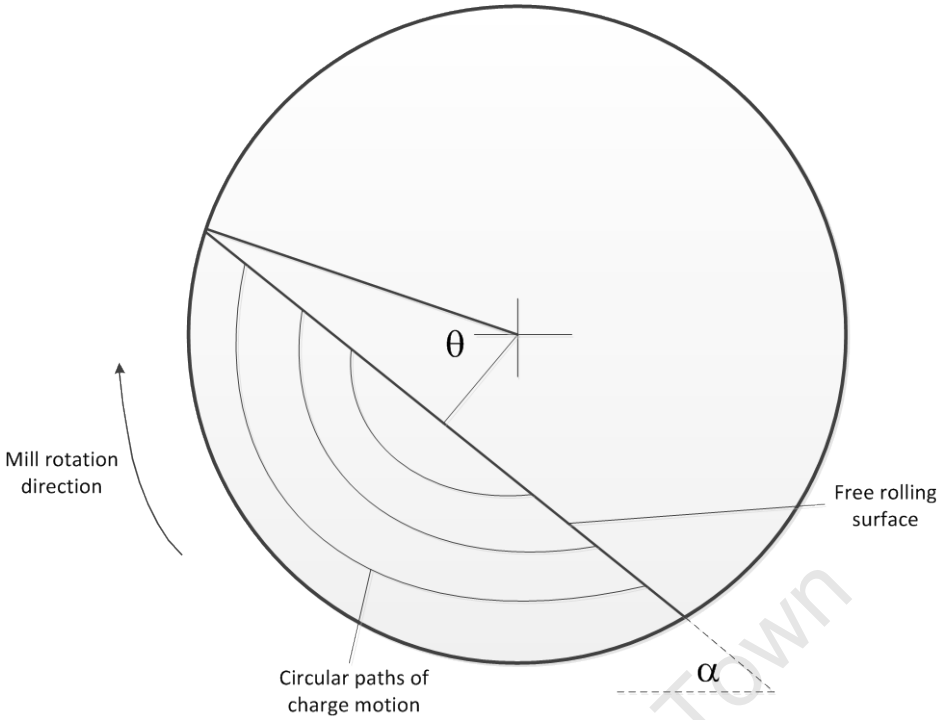

Figure 2.5: Schematic of charge motion as proposed by Hogg and Fuerstenau (Hogg & Fuerstenau, 1972)

Hogg and Fuerstenau applied a simplified description of charge shape and motion to model power draw (Hogg & Fuerstenau, 1972). In their model, particles moved in the bulk region along fixed concentric paths with the rotating mill, similar to the approach by Davis (Davis, 1919). At the free surface the particles were then proposed to descend by rolling down to the base of the mill, whereupon the cycle would recommence. In this study, the angle of repose α was described as the angle made by the free surface and the horizontal, as shown in Figure 2.5. Hogg and Fuerstenau also incorporated a region proposed by Barth (Barth, 1930) known as an equilibrium surface, a path separating the rising charge from the falling material. In this instance, this was a straight line joining the point of impact at the base of the mill (toe) to the point of departure from the mill shell (shoulder), slanted at the angle defined by the angle of repose.

The expression for the potential energy was integrated to derive an expression for power draw in Equation 2.6:

$$P = K \cdot sin(\alpha) \cdot sin^3(\theta) \cdot \emptyset \cdot \rho \cdot L \cdot D^{2.5} \qquad \textbf{Equation 2.6}$$

K is a fitted constant, while ϕ is the fraction of mill critical speed. *L* and *D* are mill dimensions as before while charge density ρ in this case is taken to be the mean bulk density. θ is the

angle between a radial line to the departure shoulder and another bisecting the equilibrium surface line.

While the model by Davis assumed that all the charge descended in free fall, Hogg and Fuerstenau proposed that all the charge cascaded down along the mill surface. This was an oversimplification as it neglected a significant portion of charge motion. Further, the model assumed that all the energy took the form of potential energy whilst neglecting any influence of kinetic energy.

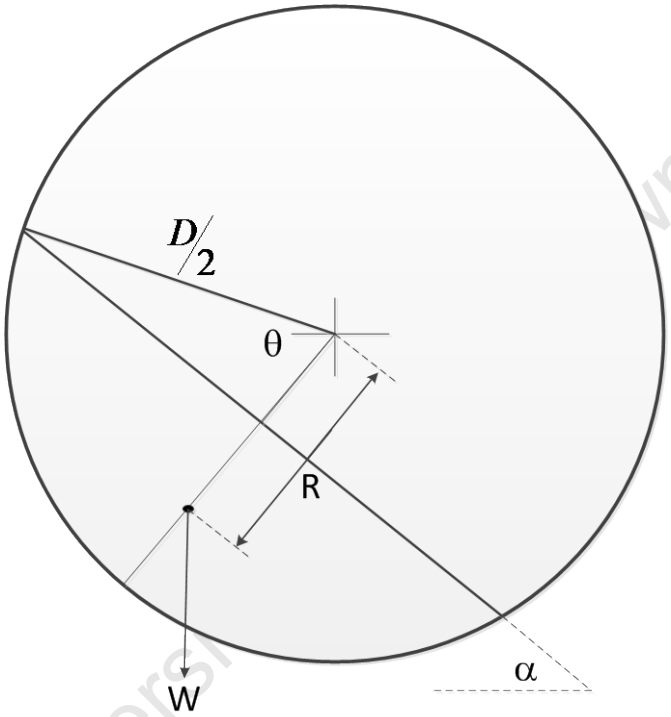

Figure 2.6: Schematic of charge motion as proposed by Arbiter and Harris (Arbiter and Harris, 1982)

Arbiter and Harris modified the charge motion model by Hogg and Fuerstenau to obtain a power model based on the principle of a lever arm (Arbiter and Harris, 1982). For this method, as depicted in Figure 2.6, the total charge was approximated to have a mass *W* which formed a torque about the mill centre rotating with the rotational speed of the mill.

The mill power draw was the product of the torque and rotational speed as given in Equation 2.7:

$$P = \frac{1}{6} \cdot \pi \cdot \rho \cdot N \cdot L \cdot D^3 \cdot sin^3(\theta) \cdot sin(\alpha) \qquad \textbf{Equation 2.7}$$

The function obtained was similar to that suggested in Hogg and Fuerstenau's model. This was because the derivation using torque and rotational speed amounted to a calculation of the work done against gravity or gain of potential energy.

By simplifying this equation, Harris and Scknock (1985) later developed a general equation to relate the power draw for various operating conditions, given by Equation 2.8:

$$P = K \cdot D^n \cdot L \cdot f \cdot Y \cdot \lambda \cdot F \cdot (1 - a \cdot F) \qquad \textbf{Equation 2.8}$$

Here, *K, n* and *a* are fitted parameters while *f* and λ are the fraction of critical speed and charge density respectively. F is the fractional filling by load. The model included a value *Y*, which was determined as a speed correction factor for different conditions.

Liddel (Liddel, 1988) used a 0.3m diameter mill to develop his expression for power draw using high speed filming to define his charge motion shape. He observed that the motion could be divided into distinct regions as illustrated in Figure 2.7. In region 1, balls moved in a circular motion from the base of the mill to the shoulder. In region 2, balls continued to rise with a velocity equal to a fraction of the mill speed. Balls in region 3 then descended either in free fall or along the top of the charge surface, where they impacted in a random manner against the toe in region 4.

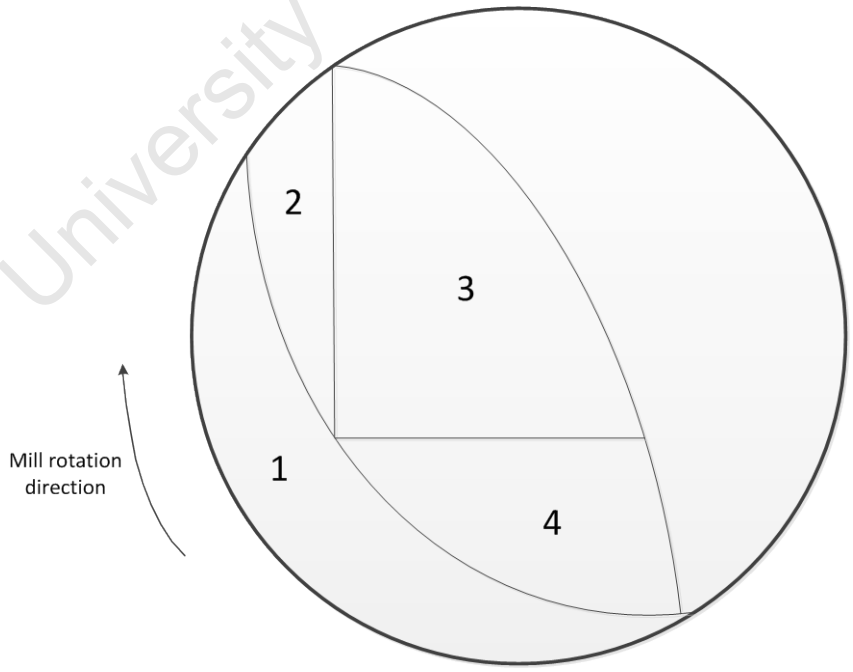

Figure 2.7: Schematic of charge motion as proposed by Liddel (Liddel, 1988)

Liddel did not use his prescribed charge motion model to develop a relationship for mill power draw. Instead, using Harris' equation and his own speed correction function *Y*, the expression in Equation 2.9 was derived:

$$P = 9.69 \cdot \rho \cdot \phi \cdot L \cdot D^{2.5} \cdot J \cdot (1 - 1.06 \cdot J) \cdot Y \qquad \textbf{Equation 2.9}$$

In 1990, Fuerstenau et al. developed a model which incorporated slurry viscosity by dividing the charge into cascading and cataracting fractions (Fuerstenau et al., 1990). As shown in Figure 2.8, the cascading portion was given by Arbiter and Harris' charge form, and was stated to be unaffected by viscosity. The cataracting fraction was determined using a lever arm relation and was described as the region most affected by the charge viscosity.

Fuertenau's power draw equation was expressed as a sum of three separate components, the cascading power fraction (P_{cs}), the cataracting power fraction (P_{ct}), and an internal friction component (P_f). These equations were given as instantaneous properties at time t, with the three components given in Equation 2.10, Equation 2.11 and Equation 2.12 respectively.

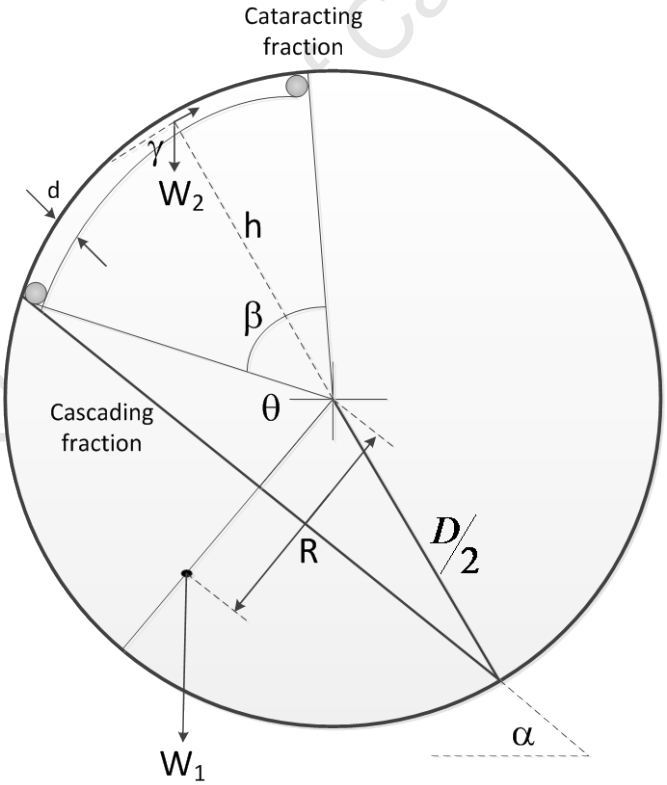

Figure 2.8: Schematic of charge motion as proposed by Fuerstenau et al. (Fuerstenau et al., 1990)

$$P_{cs}(t) = \frac{2 \cdot N \cdot W_1 \cdot g \cdot (D-d)}{3 \cdot J_1} \cdot \emptyset(J_1) \cdot sin(\alpha)$$ **Equation 2.10**

$$P_{ct}(t) = 2 \cdot \pi \cdot N \cdot W_2 \cdot g \cdot h \cdot cos(\alpha)$$ **Equation 2.11**

$$P_f(t) = C \cdot e^{(-k \cdot t)}$$ **Equation 2.12**

Although the model was a comprehensive approach to describing power which took viscosity into account, the overall equation required six parameters to be fitted using empirical data. This limited its practicality, particularly for industrial data for which it was difficult to accurately quantify parameters such as the angles and charge motion fractions in the absence of sensors that could provide such information.

Moys developed an equation which considered viscosity effects by dividing charge into two fractions, termed a 'centrifuging layer' and a 'non-centrifuging layer' (Moys, 1990). Only the non-centrifuging portion of the charge was taken into account in modelling the mill power draw. This fraction, which constituted the expression for the total power draw was derived by modification of Bond's equation to obtain Equation 2.13:

$$P(t) = K_2 \cdot \left(D_{eff}\right)^{2.3} \cdot sin(\alpha) \cdot \rho \cdot J_{eff} \cdot \left(1 - \beta \cdot J_{eff}\right) \cdot N_{eff}$$ **Equation 2.13**

K_2 is a fitted constant, while D_{eff} and J_{eff} are the effective diameter and volumetric filling respectively. These are functions of the thickness of the centrifuging layer, given by an equation which is a function of the slurry viscosity and fitted parameters. N_{eff} is the effective speed. The parameters for this model were fitted from experimental data using a 0.3m diameter laboratory mill.

$$P(t) = K \cdot D^{2.5} \cdot L \cdot (1 - 1.03 \cdot J) \cdot \left[\frac{\rho_c}{w_c} \cdot (1 - E_B) \cdot J + 0.6 \cdot J_B \cdot \frac{\rho_b - \rho_s}{w_c}\right] \cdot \emptyset_c \cdot \left[1 - \frac{0.1}{2^{9-10 \cdot \emptyset_c}}\right] \cdot (1 + f_3)$$

Equation 2.14

Austin developed a model for SAG mills based on Hogg and Fuerstenau's function (Austin, 1990). He modified this equation to include the kinetic energy of particles in the charge. In this derivation, the charge density was determined using a function that incorporated the effective porosity, and included an additional term for the power draw of conical sections at the mill feed or discharge end. The overall equation for power draw from this approach is given in Equation 2.14.

K is a constant related to the angle of repose, while E_B is the effective porosity of the rock bed, assumed to be 0.3. W_b is the weight fraction of rock to the total weight, and ρ_b and ρ_s are the ball density and rock density respectively. J_B is the volume fraction of balls in the cylindrical section of the mill. Austin validated this model by fitting it against industrial data, but in a later review by Morell the model was stated to be too complex to implement effectively in normal operation (Morell, 1993).

Following the development of DEM with application to tumbling mills (see Section 2.2), Mishra and Rajamani (Mishra and Rajamani, 1992) used the technique coupled with experiments on a 0.9m diameter mill to analyse charge motion and develop a methodology to derive the power draw.

The linear spring and dashpot contact model was used to calculate interaction forces and energy losses between colliding bodies (See Section 2.2). The total energy losses to collisions were calculated as a sum of global damping forces and dashpot forces using Equation 2.15.

$$E_{loss} = E_{global} + E_{dashpot} \qquad \textbf{Equation 2.15}$$

Where the global energy losses were given by Equation 2.16 and the dashpot energy losses were given by Equation 2.17.

$$E_{global} = \sum_{i=1}^{nsteps} \sum_{j=1}^{nballs} \left(C_t \cdot v_{j,i}\right) \cdot \left(v_{j,i} \cdot \Delta t\right) + \left(C_r \cdot \dot{\theta}_{j,t}\right) \cdot \left(\dot{\theta}_{j,i} \cdot \Delta t\right) \qquad \textbf{Equation 2.16}$$

$$E_{dashpot} = \sum_{i=1}^{nsteps} D_{n,j,i} \cdot \left(v_{n,j,\frac{i-1}{2}\Delta t} \cdot \Delta t\right) + D_{s,j,i} \cdot \left(v_{s,j,\frac{i-1}{2}\Delta t} \cdot \Delta t\right) \qquad \textbf{Equation 2.17}$$

Here, C_t and C_r are global damping constants for translational and rotational damping, while D_n and D_s are contact forces in the normal and shear direction. With the simulated tumbling mill taken to be at steady state, Mishra and Rajamani equated the sum of energy losses in Equation 2.15 to the energy supplied by the mill. The energy loss in Equation 2.15 divided by the simulation time then provided the predicted mill power draw.

The model was validated by comparing the power draw predictions to measurements on an experimental scale tumbling mill. In addition, still images of the charge motion were compared to the simulated motion to verify the computational results. In their work, it was

noted that a more comprehensive validation would entail measurement of the charge packing density and velocity distribution. This was not done because at the time there were no feasible methods of making such a comparison (Mishra et al., 1990).

Morell developed a power draw model based on empirical data from several industrial mills, which is among the most highly regarded in comminution research (Napier-Munn et al., 1999). In his work, the region of the mill charge which drew power was represented using an annular ring as depicted in Figure 2.9.

By segmenting the mill into radial and angular elements, Morell integrated the lever arm contributions from the inner radial layer to the internal mill radius, and the toe angle to the shoulder. This expression equated to the potential energy contribution of the charge and was given by Equation 2.18:

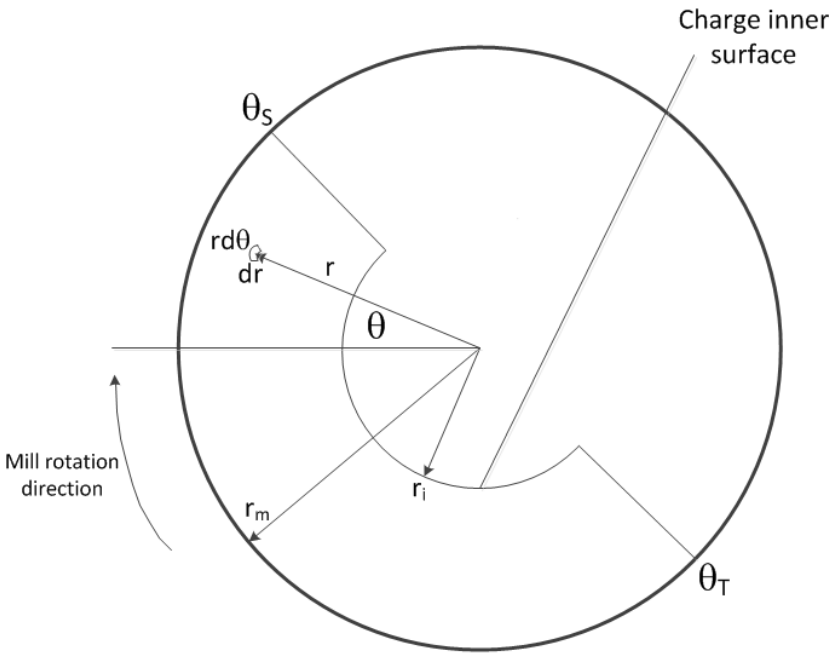

Figure 2.9: Schematic of charge motion as proposed by Morell (Morell, 1993)

$$P_{pot} = \frac{\pi \cdot g \cdot L \cdot \rho_c \cdot N_m \cdot r_m}{3 \cdot (r_m - z \cdot r_i)} \cdot \{2 \cdot r_m^3 - 3 \cdot z \cdot r_m^3 + r_i^3 \cdot (3 \cdot z - 2)\}\{sin(\theta_s) - sin(\theta_t)\}$$

Equation 2.18

As the derived expression was found to equate to only the potential energy, Morell added a term to include the kinetic energy contribution, given in Equation 2.19.

$$P_{kin} = L \cdot \rho_c \cdot \left\{\frac{N_m \cdot r_m \cdot \pi}{r_m - z \cdot r_i}\right\}^3 \cdot \left\{(r_m - z \cdot r_i)^4 - r_i^4 \cdot (z-1)^4\right\}$$

Equation 2.19

The net power draw is the sum of the potential and kinetic energy equations. N_m is the mill rotation speed rate, while ρ_c is the charge density.

The model was tested against industrial data and found to be in good agreement. It gained wide acceptance as a method for predicting the power required for the design and operation of SAG mills because it relied on parameters that could be measured on an industrial scale and gave reasonably accurate predictions (Napier-Munn et al., 1999).

Based on DEM (see Section 2.2), Cleary proposed a method for the determination of power draw that could be used to validate numerical simulation data (Cleary, 2001). As depicted in Figure 2.10, particles in the mill exerted downward forces on the mill due to their weight. To counter act this force and keep the mill under steady state rotation, the mill geometry would have to supply an equal and opposite force. As the mesh developed for DEM simulations modelled the mill geometry as a system of inter-connected nodes, the accumulated sum of forces at these nodes equated to the total force that would need to be supplied by the mill to lift the charge and keep the geometry under the specified rotational speed. Using this approach, the sum of these forces multiplied by the velocities of each node equated to the mill power draw, as derived in Equation 2.20

$$P_{GEOM} = \sum_{1}^{N_{geom}} \left|\overrightarrow{F_g} \cdot \overrightarrow{V_g}\right| \qquad \textbf{Equation 2.20}$$

N_{geom} is the number of nodes in the simulated mill geometry. Vector forces F_g (F_x, F_y, F_z) and V_g (V_x,V_y,V_z) represent the forces and velocities at each node respectively. The model was tested against measurement for both laboratory and industrial scale mills and found to be in good agreement.

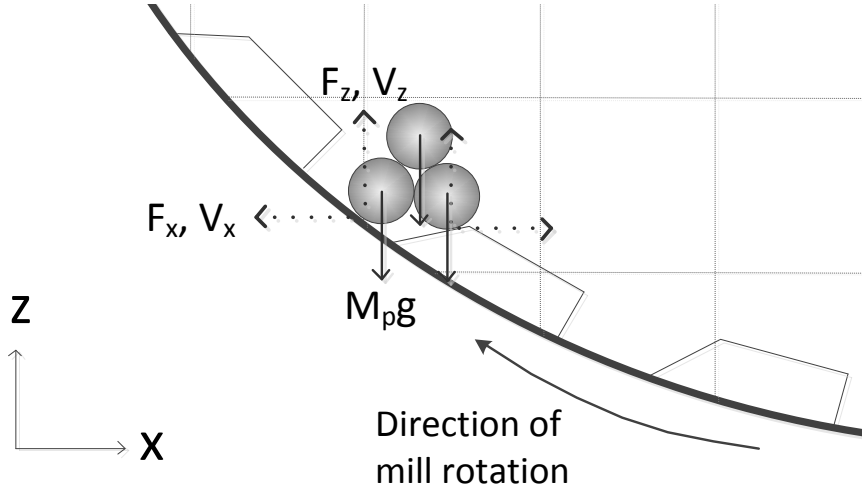

Figure 2.10: Schematic approach taken to determine mill power using force balance against the mill shell

Govender and Powell developed an empirical model based on particle tracking experiments using a bi-planar angioscope (Govender and Powell, 2006). A 142mm diameter mill was used to track charge particles and determine the centre of circulation (CoC). The radial and angular positions of the charge centre of mass were subsequently calculated relative to the CoC. Least squares regression was used to fit a polynomial to the variation of the CoC radius with mill speed. A similar approach was followed using straight lines to fit the variation of the angular position of the CoC with mill speed. The power draw could then be determined as a product of the torque and mill rotational speed as given in Equation 2.21:

$$P = M \cdot g \cdot R_{COM} \cdot cos(\theta_{COM}) \cdot \omega \qquad \textbf{Equation 2.21}$$

Where *M* is the total charge mass, *g* the acceleration due to gravity, and R_{COM} and θ_{COM} the radial and angular positions of the charge centre of mass. Although the model was not validated against any measurement, it was benchmarked against power predictions based on lever arm calculations using the average centre of mass and found to be in good agreement.

Kallon et al. proposed a variation of this approach and used PEPT data to develop a power draw model which incorporated charge circulation rate (Kallon et al., 2011). It had been assumed in prior work that as the mill rotated once over a whole revolution, so did the charge. This implied that a full rotation of the bulk body occurred once per mill revolution. Research work on tumbling mill motion indicated that this was not the case, as mixing would therefore not occur (Powell and McBride, 2004). In order to address this shortcoming, the work of Kallon et al. developed a methodology to determine the charge circulation rate for a

tumbling mill. This study was performed using an experimental scale mill operated with a mono-sized charge body.

Figure 2.11 shows a schematic of this approach. Kallon proposed that the lever arm for the torque determination pivoted not about the centre of the mill, but about the centre of circulation (CoC). The power draw was calculated using the torque arm about the CoC multiplied by the charge circulation rate, as given in Equation 2.22.

$$P = M \cdot g \cdot C_{media} \cdot [x_{CoM} - x_{CoC}] \qquad \textbf{Equation 2.22}$$

Here, C_{media} is the charge circulation rate while x_{CoM} and x_{CoC} are the horizontal distances of the centre of mass and centre of circulation from the mill centre. The model was tested against PEPT data obtained from experiments with a 0.3 diameter mill and found to marginally under predict mill power.

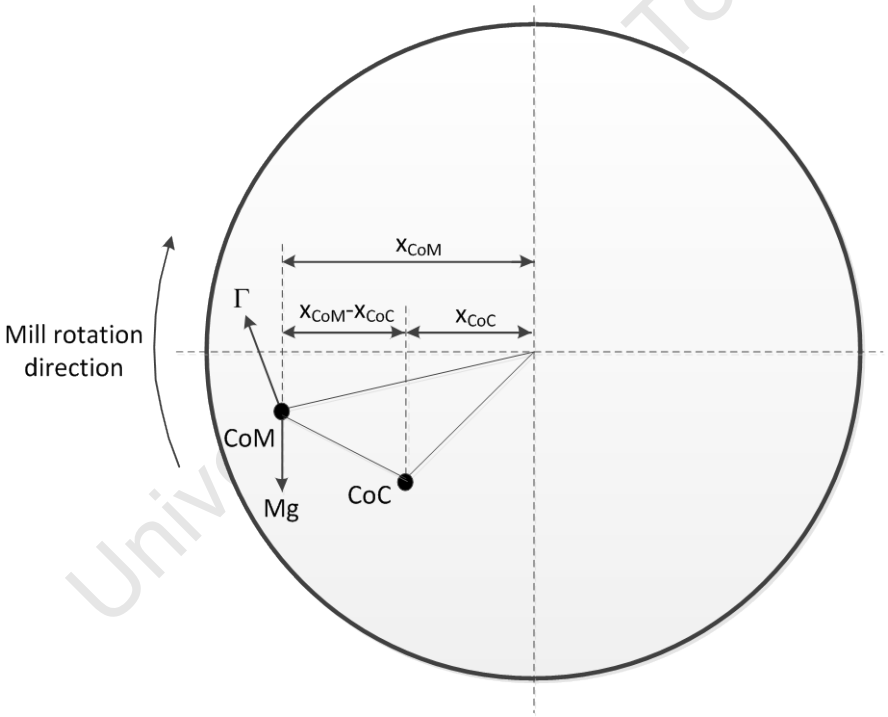

Figure 2.11: Schematic of approach taken to determine mill power by Kallon et al. (Kallon et al., 2011)

The work of Mishra and Rajamani (Mishra and Rajamani, 1992), and that of Cleary (Cleary, 2001) demonstrated that DEM could be used to analyse the charge motion behaviour in a tumbling mill and determine the power draw. The next section discusses the approach that has been followed to model the tumbling mill environment using this technique.

2.2 A mechanistic approach to mill modelling using The Discrete Element Method (DEM)

As discussed in the previous section, studies on power draw have traditionally followed simplified descriptions of charge motion. This is mainly due to the complexity associated with accurately describing the tumbling mill environment mathematically at a fundamental level.

The Discrete Element Method (DEM) however emerged in the early nineties as a means to investigate particle motion and interaction in tumbling mills. DEM is a numerical technique by which finite rotations and displacements of numerous rigid bodies can be determined along with a complete history of contact information for every calculation cycle. Although initially pioneered by Cundall and Strack to study the motion of soil particles (Cundall and Strack, 1979), this method has been adapted to suit systems such as the tumbling mill environment (van Nierop et al., 2001. Venugopal and Rajamani, 2001. Cleary et al., 2003). A typical visualization of a DEM simulation with 2-8mm particles rotating in a 300mm mill is given in Figure 2.12.

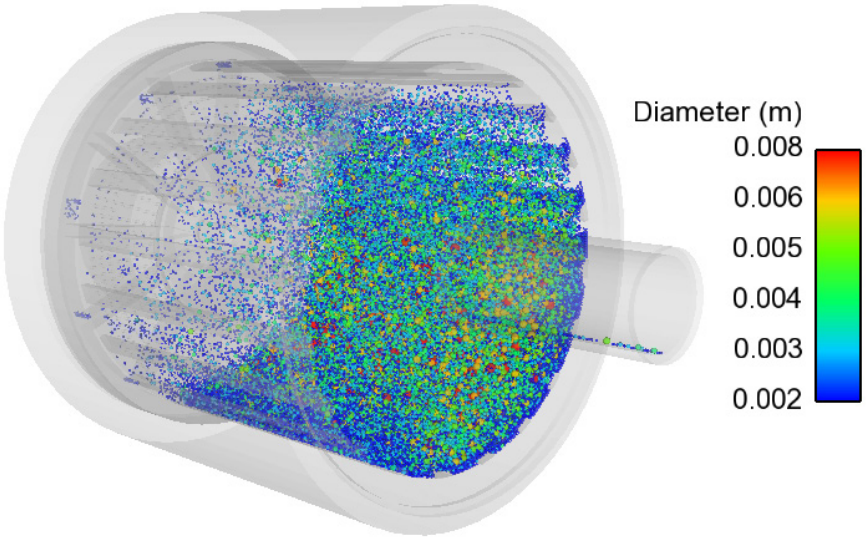

Figure 2.12: DEM visualization of charge revolution in a tumbling mill

Trajectories of individual charge bodies are computed incrementally by applying Newton's second law of motion. Although steel balls and rock particles are defined to be rigid spheres, collisions between them and the mill shell are considered to be deformable single point contacts. A contact model specified in the simulation is therefore introduced to govern the

relationship which determines the deformation between contacting bodies given the contact force and predetermined material properties.

In DEM it is assumed that the incremental time scale is sufficiently small so that any forces between contacting bodies do not propagate to any adjacent particles. The governing equation at each time-step is thus a calculation of the resultant force for every particle *i* in the system, given by Equation 2.23:

$$m_i \frac{dv_i}{dt} = \sum_{j=1}^{k_i} \left(F_{c,ij} + F_{d,ij}\right) + m_i g + F_i \qquad \textbf{Equation 2.23}$$

In this equation, m_i and v_i are the mass and translational velocity of the particle at time *t*, while *k* is the total number of particles in contact with particle *i*. The total force on the particle is calculated as a sum of four forces, with F_c and F_d representing the contact force and damping forces respectively. The force F_i is calculated in the event that there are any other forces acting on the particle such as drag, cohesion or magnetic fields. The remaining force is gravity. A similar form of equation is used to determine the rotational force on each particle.

Contact model

Given that forces at the formation of contacts are determined from incident velocities and elasticity of the colliding bodies, the contact model dictates whether or not the collision mechanics are an accurate representation of the physical system. Although numerous contact models have been proposed for use in DEM simulations, the majority are minor variations of three approaches:

- Linear spring and dashpot
- Hertz-Mindlin
- Walton and Braun

The approach behind each of these contact models was well summarized by Zhu et al. (Zhu et al, 2007). The basic premise and information about each contact model is given in Table 2.1

Table 2.1: Summary of contact force and torque models (taken from Zhu et al., 2007)

Contact force and torque models

Force models	Normal force	Tangential force	References
Linear spring–dashpot model	$\mathbf{f}_n = -K_n\delta_n\mathbf{n}_c - C_n(\mathbf{v}_c\cdot\mathbf{n}_c)\mathbf{n}_c$	$\mathbf{f}_t = -K_t\mathbf{v}_c^t + C_t(\mathbf{v}_c\times\mathbf{n}_c)\times\mathbf{n}_c$	Cundall and Strack (1979)
Simplified Hertz–Mindlin and Deresiewicz model	$\mathbf{f}_n = -\frac{4}{3}E^*\sqrt{R^*}(\delta_n)^{3/2}\mathbf{n}_c$ $-C_n(8m^*E^*\sqrt{R^*\delta_n})^{1/2}$ $\cdot(\mathbf{v}_c\cdot\mathbf{n}_c)\mathbf{n}_c$	$\mathbf{f}_t = -\mu\lvert\mathbf{f}_{n,e}\rvert(1-(1-\lvert\mathbf{v}_c^t\rvert/\delta_{\max})^{3/2})\hat{\mathbf{v}}_c^t$ $+2C_t(1.5\,\mu\text{m}*\lvert\mathbf{f}_{n,e}\rvert$ $\cdot\sqrt{1-\lvert\mathbf{v}_c^t\rvert/\delta_{\max}}/\delta_{\max})^{1/2}$ $\cdot(\mathbf{v}_c\times\mathbf{n}_c)\times\mathbf{n}_c$	Langston et al. (1994, 1995a,b), Zhou et al. (1999) and Zhu and Yu (2002)
Walton and Braun's model	$\mathbf{f}_n = \begin{cases} -k_1\delta_n\mathbf{n}_c,\ \dot{\delta}_n \geqslant 0 \\ \text{(loading)} \\ -k_2(\delta_n-\delta_{n0})\mathbf{n}_c,\ \dot{\delta}_n < 0 \\ \text{(unloading)} \end{cases}$	$\mathbf{f}_t = \begin{cases} \mathbf{f}_t' + k_t^0\left(1-\frac{f_t-f_t^*}{\mu f_n-f_t^*}\right)^{1/3}\Delta\mathbf{v}_c^t \\ \text{if } \dot{\mathbf{v}}_c^t \text{ in initial direction} \\ \mathbf{f}_t' + k_t^0\left(1-\frac{f_t^*-f_t}{\mu f_n+f_t^*}\right)^{1/3}\Delta\mathbf{v}_c^t \\ \text{if } \dot{\mathbf{v}}_c^t \text{ in opposite direction} \end{cases}$ where $f_t = \lvert\mathbf{f}_t\rvert,\ f_n = \lvert\mathbf{f}_n\rvert$.	Walton and Braun (1986a), and Walton (1993)
Torque models	Rolling friction torque	Torque from tangential forces	References
Method 1	$\mathbf{m}_r = -k_r\theta_r - C_r\,\mathrm{d}\theta_r/\mathrm{d}t$	$\mathbf{m}_t = \mathbf{R}\times\mathbf{f}_t$	Iwashita and Oda (1998, 2000)
Method 2	$\mathbf{m}_r = -\min\{\mu_r\lvert\mathbf{f}_n\rvert, \mu_r'\lvert\omega_n\rvert\}\hat{\omega}_n$		Zhou et al. (1999), and Zhu and Yu (2002)

The linear spring-dashpot model has been the most widely used in DEM analyses of tumbling mills (Agrawala et al., 1997. Cleary and Morrison, 2011. Mishra and Rajamani, 1992. van Nierop et al., 2001). With this principle, particle collisions are modelled using a simple linear spring and damping dashpot system resolved into normal and shear contact components. A schematic of this approach is given in Figure 2.13.

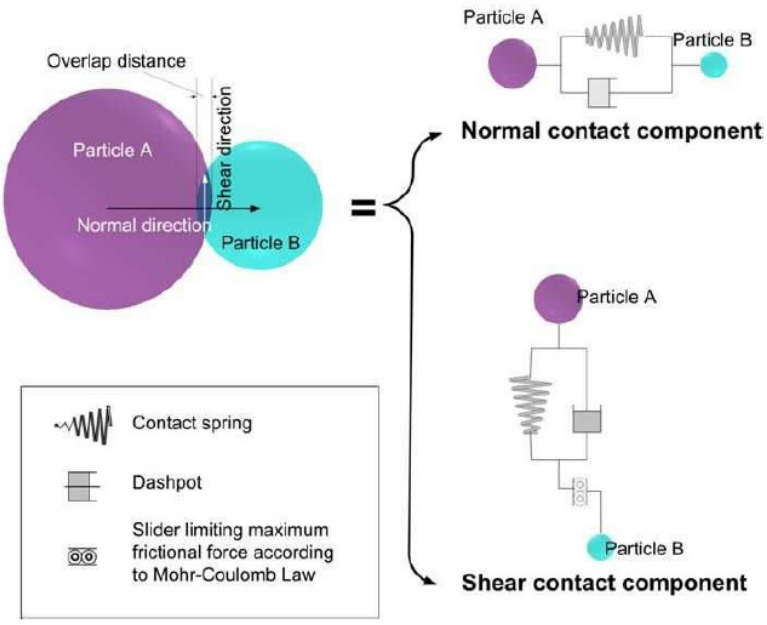

Figure 2.13: Schematic of approach taken with the linear spring and dashpot contact model (taken from Govender et al., 2004)

The contact model calculates the normal force as a sum of contact and dashpot forces as given in Equation 2.24:

$$F_n = k_n \cdot \alpha_n - b_n \cdot V_n \qquad \textbf{Equation 2.24}$$

The first term in this equation is the contact force. This is determined using Hooke's law as directly proportional to the displacement α_n between particles. The quantity k_n which defines the relationship is an artificial quantity known as the spring stiffness of a material. The second term in the equation is the damping force, defined to be directly proportional to the relative velocity between particles V_n via a damping constant b_n (Cundall and Strack, 1979).

The tangential relationship follows this same principle, except that the shear force is limited to a maximum set by the Mohr-Coulomb law, which states that it cannot exceed the product of the coefficient of friction and normal force (Juvinall and Marshek, 2006).

While the linear spring-dashpot model has successfully been applied to predict charge motion characteristics and determine power draw, it is apparent that it is unphysical as a model for particle collisions. The linear spring is often calibrated to simulate environments accurately by modification of the stiffness constant and friction coefficient (Mishra and Murty, 2001). Fundamental theories of elastic contact have determined that the force-displacement relationship between colliding bodies is not linear (Johnson, 1985). For the force calculation using the linear model, the assumption that contact and damping forces increase linearly with displacement and relative velocity respectively is thus an oversimplification. The linear model also assumes that viscous damping is at a maximum when the overlap between particles is small, which is unrealistic. Damping should be at a minimum when particles come into contact and at the point when they depart (Kulya, 2008). The work of Sarracino concluded that due to the unphysical nature of the linear-spring contact model, the impact energy of collisions would not be accurately predicted (Sarracino et al., 2004).

The Hertz-Mindlin contact model has been used by a number of researchers to conduct DEM simulations of tumbling mills (Khanal and Morrison, 2009. Misra and Cheung, 1999. Yang et al., 2003). Unlike the linear spring, this model uses Hertzian theories of elastic contact to determine forces between particles, which do not vary linearly with displacement. The parameters used to ascertain collision forces are based on material properties such as Young's Modulus and density. This model is well suited to engineering applications and relies on physical parameters which can be measured to calculate contact forces (EDEM, 2006). A schematic of this approach is given in Figure 2.14.

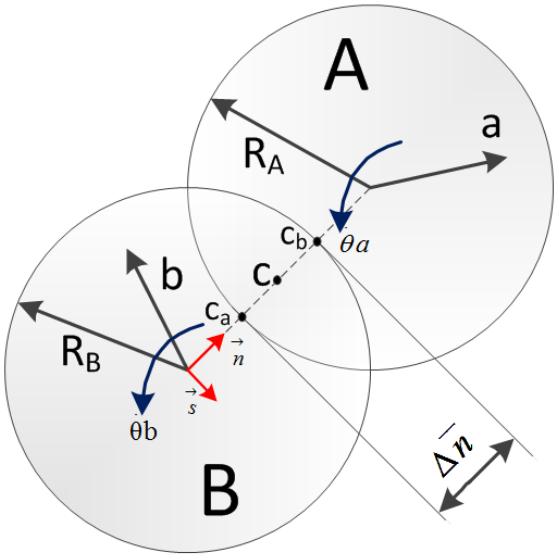

Figure 2.14: Schematic of the approach used for the Hertz-Mindlin contact model

Hertzian theory (Hertz, 1882. Johnson, 1985) dictates that the contact force varies non-linearly as a function of normal displacement *n* between particles by Equation 2.25:

$$F_c = -\frac{4}{3} \cdot E^* \cdot \sqrt{R^*} \cdot \Delta\bar{n}^{\frac{3}{2}} \qquad \textbf{Equation 2.25}$$

In this equation, the terms preceding the displacement are often combined and presented as a Hertz spring stiffness k_n. The effective Young's modulus E^* of the contacting bodies *A* and *B* is given by Equation 2.26:

$$\frac{1}{E^*} = \frac{1-\gamma_A^2}{E_A} + \frac{1-\gamma_B^2}{E_B} \qquad \textbf{Equation 2.26}$$

Where E_A and E_B and γ_a and γ_b are the Young's Moduli and Poisson's ratios of the colliding bodies respectively, while effective radius R^* is found using Equation 2.27:

$$\frac{1}{R^*} = \frac{1}{R_A} + \frac{1}{R_B} \qquad \textbf{Equation 2.27}$$

In a similar manner, the tangential contact force is calculated using Equation 2.28 as a product of the displacement and the shear contact stiffness k_s, prescribed by the theory by Mindlin and Deresiewicz (Mindlin and Deresiewiscz, 1953).

$$k_s = \frac{E^* \cdot \sqrt{2 \cdot R^*}}{(1+\gamma)(2-\gamma)} \cdot \sqrt{\Delta \bar{n}} \qquad \textbf{Equation 2.28}$$

Where viscous damping is incorporated, both the normal and tangential forces have a damping force determined as the product of an arbitrary parameter ζ and the relative velocity of the colliding bodies. This parameter has been implemented in various forms (Mishra, 2003. Tsuji et al., 1993. DEM Solutions, 2006), but is usually a function of the damping constant. The software package EDEM applies this parameter in the form of Equation 2.29:

$$\zeta = 2 \cdot \left(\frac{5}{3}\right)^{\frac{1}{2}} \cdot b \cdot \left(m^* \cdot 2 \cdot E^* \cdot (R^*)^{\frac{1}{2}}\right)^{\frac{1}{2}} \qquad \textbf{Equation 2.29}$$

The Walton and Braun model is a modified form of the Hertz-Mindlin model (Walton and Braun, 1986). In the normal direction, a partially latched spring is used to model the force as a function of particle overlap, resulting in two different loading and unloading stiffness values as given in Equation 2.30.

$$F_n = \begin{cases} K_1 \cdot \alpha & (loading) \\ K_2 \cdot (\alpha - \alpha_0) & (unloading) \end{cases} \qquad \textbf{Equation 2.30}$$

In this equation α_0 is the relative overlap at the point of complete unloading caused by inelastic deformation of the surface. The strain energy lost by the relative difference loading and unloading forces governs the energy loss.

In the tangential direction a simplification of the Mindlin-Deresiewicz model is applied, where the effective tangential stiffness is calculated by Equation 2.31:

$$K_t = \begin{cases} K_0 \cdot \left(1 - \frac{T - T^*}{\mu \cdot F_n - T^*}\right)^{\gamma} & (for\ T\ increasing) \\ K_0 \cdot \left(1 - \frac{T^* - T}{\mu \cdot F_n + T^*}\right)^{\gamma} & (for\ T\ descreasing) \end{cases} \qquad \textbf{Equation 2.31}$$

K_0 is the initial slope of the tangential force-displacement curve, where T is the tangential force. T^* is the tangential force at an existing path, while γ is a fixed parameter.

Calibration and validation of DEM results

As numerical modeling of tumbling mills using DEM has gained acceptance, it has become imperative that the results are verified against experimental data. For tumbling mill

simulation studies, calibration of the parameters used for the contact model normally involves experimental measurement of a simplified system, while validation of the results entails mainly three approaches:

- High speed filming/photography
- Online sensor measurement
- X-ray and PEPT imaging

To calibrate the parameters used for the contact model, a simplified experiment is designed to examine the collision behaviour of a typical particle, such as that illustrated in Figure 2.15. These tests have mainly taken place in the form of dropping particles on a flat bed or firing them against a target (Chandramohan and Powell, 2005. Mishra and Rajamani, 1992. Kharaz et al., 2001). For these tests, velocity and trajectory measurements are captured and compared against those from numerical simulation of an identical system. Properties for the mill simulation such as coefficient of friction, restitution, and spring stiffness are then selected based on values which closely match those of experiment.

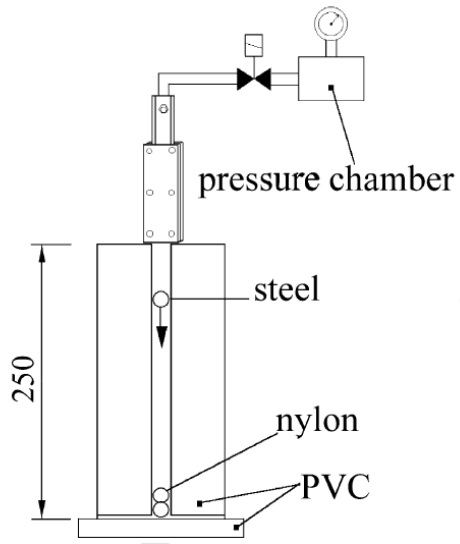

Figure 2.15: Schematic of experimental set up used to determine damping coefficient by Tanaka et al. (Tanaka et al., 2002)

An advantage of this method is that it is simple to implement and allows for rapid testing of a variety of conditions over which the contact model can be calibrated (Chandramohan, 2005). However this method has the disadvantage that it is highly simplified, and does not consider the types of force interactions that lead to the packing and mixing characteristics exhibited by real charge. Further, particularly in the case of the linear spring contact model, because an unphysical material property such as spring stiffness is fitted to experimental data, the

calibrated properties may not necessarily provide a true reflection of the contact forces when used in the simulation (Sarracino et al., 2004).

For validation studies of DEM simulations using high speed filming, a laboratory scale mill with a transparent end face and a mounted camera have been used (Venegopal and Rajamani, 2001. Perez-Alonso and Delgadillo, 2012). The high speed camera, shown in Figure 2.16, captures snapshots or video of the moving charge under different conditions. These videos or captured still images are then compared to DEM simulations at identical conditions. Based on comparisons of the charge shape and distinguishing features such as the toe and shoulder, the accuracy of the simulation is then verified.

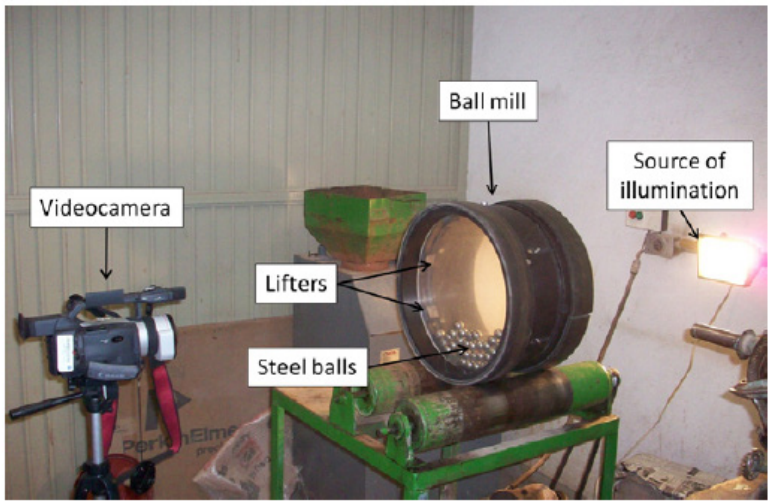

Figure 2.16: Experimental setup used for validation of 2D DEM experiment by Perez-Alonso and Delgadillo (Perez-Alonso and Delgadillo, 2012)

The advantage of this system is that it is actual charge motion that is compared against computational simulations. Conditions that influence charge behaviour in the real system can thus be studied and related to those from simulations. However, a short coming of this approach is that it is a qualitative measure of the accuracy of DEM, and as a consequence is highly subjective as the images can be selectively captured such that they match the simulation. As a result, while this method is a good measure of observable features of charge motion, such as the head and toe positions, it does not provide a basis to evaluate the inter-particle forces or energy environment in the mill in any detail.

To provide a quantitative means of validating DEM simulations, the power draw of tumbling mills is typically measured (Mishra and Rajamani, 1992. Cleary, 2001). As it is not currently feasible to measure every inter-particle force interaction and collision energy loss inside tumbling mills, the measured net power draw of the mill is compared to the overall charge power predicted by the DEM simulation, which may be derived using several approaches

(see Section 2.1: Power Draw models). The main advantage of this approach is that it is a quantitative measure that is used to validate the energy environment predicted in a DEM simulation, which is directly calculated from contact model laws and material parameters. A disadvantage of this approach is that it provides a single measure that is used to validate DEM results without an evaluation of the charge motion and interaction at the inter-particle level. It has been stated in previous work that particle kinematics and energy losses may thus be falsely represented by the contact model although the DEM simulation approximates the correct power draw (Kulya, 2008).

Another form of validation by online measurement is the use of an instrumented ball in laboratory scale tumbling mills, as performed by Martins et al. (Martins et al., 2008). With this approach, the instrumented ball (see Figure 2.17) is fitted with accelerometers, rotation rate sensors and temperature sensors and run in the mill. This is done in conjunction with a high speed camera which records the charge motion. The first and second moments of the kinetic energy (Freund and Walpole, 1987), potential energy and energy losses are then calculated and compared to results of DEM simulations to validate the predicted forces and energy losses from the contact model.

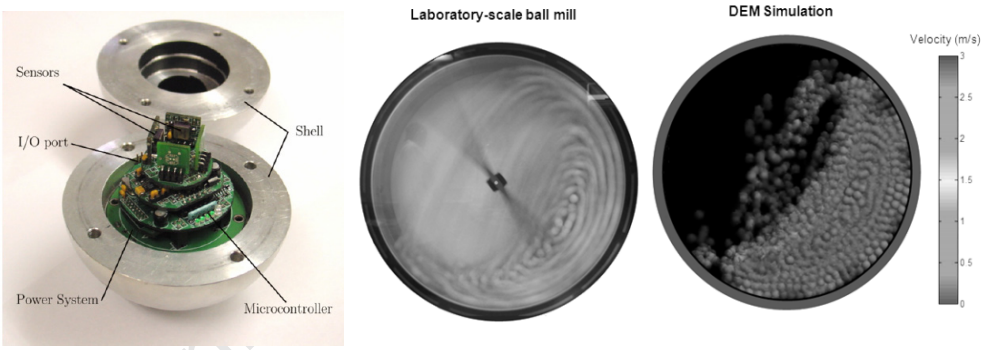

Figure 2.17: Opened instrumented ball displaying sensors and comparison of laboratory scale mill data with DEM (taken from Martins et al., 2008 and Martins et al., 2012)

This method has the advantage of being a quantitative physical measurement of the actual system which is used to compare to DEM simulation results. The forces and kinetics of the ball are used to compare particle interaction properties while the video capture information is used for a comparison of the overall charge dynamics. The instrumented ball used in the work by Martins et al. (Martins et al., 2012) comprised of an electronic data acquisition system embedded in a protective shell with an outer diameter of approximately 100mm. A disadvantage of using this approach to validate DEM simulations was that the particle size that could be investigated was limited to that of the instrumented ball. At present, the method therefore cannot be used to investigate the effect of charge properties such as particle size.

Another approach which has been demonstrated to be a means of validating DEM simulations is imaging of the internal tumbling mill environment through X-ray or PEPT measurement (Govender et al., 2001a, Yang et al., 2003). For these methods, the motion of particles inside the tumbling mill environment is traced and used to ascertain information regarding the overall charge behaviour. While it does not provide details regarding inter-particle forces and collision energy losses, kinematic information is obtained for particles which are subject to these forces, thus providing a quantitative measure of in situ charge behaviour under these conditions. A photograph of this system is given in Figure 2.18.

Figure 2.18: Photograph of bi-planar angioscope used for validation studies by Govender et al. (Govender et al., 2001b)

The advantage of this method is that it is a quantitative measure of charge motion in the environment which is being validated. Comparisons of kinematic properties of the charge such as packing fraction and velocity distribution can be directly compared against DEM data to verify that the physics from the simulation is accurate. A disadvantage of using the bi-planar angioscope is that it requires the use of equipment that permits the penetration of X-ray beams, such as perspex (Govender, 2001a). For PEPT, a limitation is that the equipment has to fit within the field of view of the camera system (shown in Figure 2.29). This means that the size of mill that can be tested is limited to that permitted by the instrumentation.

The PEPT method offers a unique opportunity to quantitatively evaluate the influence of particle properties such as size on the charge motion. These kinematic properties can be directly compared against DEM simulations as a means of validating the predictions of

particle motion. The PEPT technique, which is utilized in this study, is discussed in more detail in Section 2.3.

Outputs from DEM simulations

DEM has been demonstrated to be a valuable tool through which the internal environment of a tumbling mill can be studied (Zhu et al., 2008). Several important characteristics of charge motion have been identified through study of numerical simulation data, with the method allowing researchers to study the mechanisms underpinning this behaviour in detail.

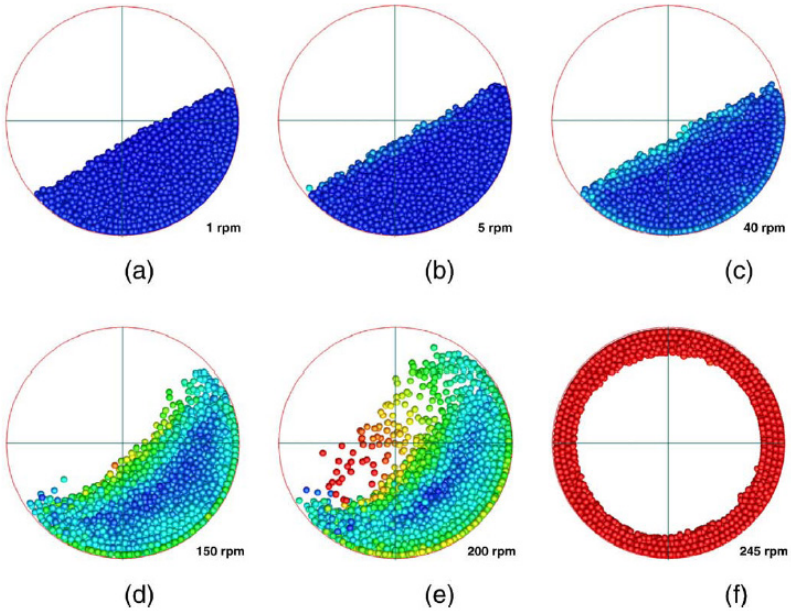

Figure 2.19: Particle flow patterns at different flow regimes (taken from Yang et al., 2008)

For example, in Figure 2.19, from the work of Yang et al. (Yang et al., 2008) the different regimes of flow with increase in mill speed were demonstrated from DEM results, from slumping in (a) to centrifuging in (f) for a mono-sized charge. Velocity values of every particle were extracted and used to plot probability distributions for the charge velocity at each speed. The results indicated that the distributions of flow velocities at different speeds, when normalized against the mean mill velocity all followed a log-normal distribution, given by Equation 2.32.

$$\mathrm{P}(v^*) = a \cdot e^{\left(-b \cdot \left[ln\left(\frac{v^*}{v_0^*}\right)\right]^2\right)} \qquad \textbf{Equation 2.32}$$

In this equation, v^* is the particle velocity and $v_0{}^*$ is the normalized mill speed. Parameters *a* and *b* are fitted constants. In the work by Yang et al., it was concluded that the charge

velocity distribution at each speed could be expressed through a scaling rule as a function of the mill velocity, virtually independent of the regime of particle flow. The results of the DEM simulations were verified by comparison with experimental data from PEPT, such as spatial velocity fields.

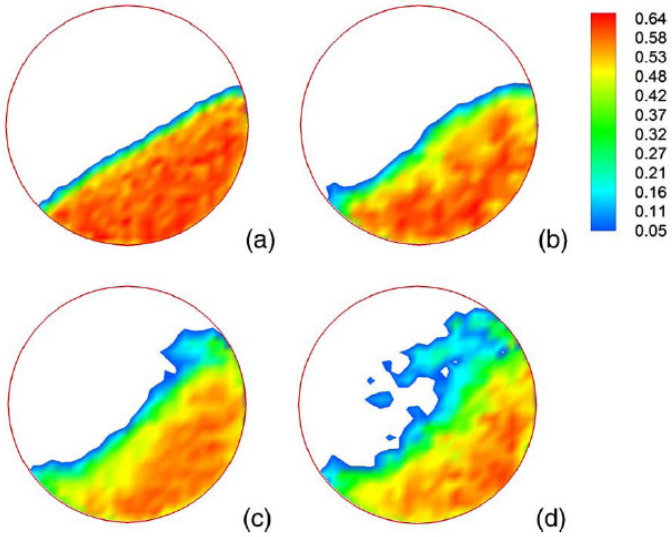

Figure 2.20: Spatial distribution of packing density at different speeds (taken from Yang et al., 2008)

In the article, the solidicity or packing density in each region of the transverse mill face was also determined, as shown in Figure 2.20. It was found that the charge packing in the bulk region was not uniform, and that the distribution changed with increasing speed from (a) to (d), particularly at speeds where cascading and cataracting regimes occurred. Yang et al. concluded that this was because at higher speeds particle flows dilated as more charge was lifted and the charge began to occupy more volume regions of the mill. Probability distributions for the packing density were used to demonstrate that the mean packing density progressively decreased from that of a random loose packing state at low speeds to a more porous and dilated distribution at higher speeds. This was concluded to have a significant effect on the mass and heat transfer in the packed bed.

While the work of Yang et al. considered a mono-sized charge, in the study by Cleary (Cleary, 1998), the effect of speed was investigated using charge consisting of particles of different sizes, as depicted in Figure 2.21. In Cleary's work, DEM was used to confirm the observation put forward by Powell and Nurick (Powell and Nurick 1996b) that radial segregation by particle size occured about the transverse face of the mill at different speeds. Cleary found that the mill speed dictated the mode of segregation that the charge exhibited. In the cascading and cataracting regime, it was found that the larger particles tended to

circulate around the central core of the charge while the smaller particles moved to the periphery and tended to cataract. At lower speeds the reverse of this behaviour was noted.

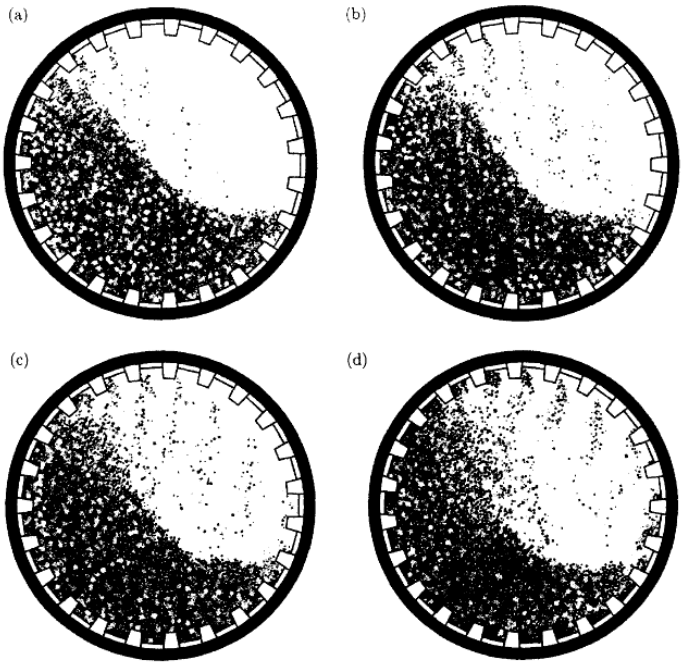

Figure 2.21: Plots of charge motion at different speeds (taken from Cleary et al., 1998)

Two mechanisms were stated to influence this phenomenon. At low speeds, smaller particles permeated the interstices between slumping layers of charge, causing larger particles to sink to the outer periphery of the charge body. At higher speeds, centrifugal forces drove smaller particles radially further away from the mill centre, while larger particles moved to the centre of the charge, meaning that smaller particles became more prone to cataracting (Cleary, 1998).

While there are a great deal of other properties that can be investigated with DEM (Zhu et al., 2008), such as lifter wear, grate design and axial transport, the collision energy distribution is frequently examined as an output from simulations of tumbling mills. For instance, Figure 2.22 and Figure 2.23 show the spatial distribution of dissipated collision energies from the work of Powell and McBride (Powell and McBride, 2004) and Nordell and Potapov (Nordell and Potapov, 2011) respectively. In these plots, the magnitude and locations of highest energy dissipation, and consequently the highest grinding regions about the mill are highlighted using the yellow to red hues. Changes in the milling conditions such as charge particle size, mill speed, filling and lifter geometry play an influence on these distributions, which can be investigated by use of DEM (Powell et al., 2008. Cleary and Morrison, 2011).

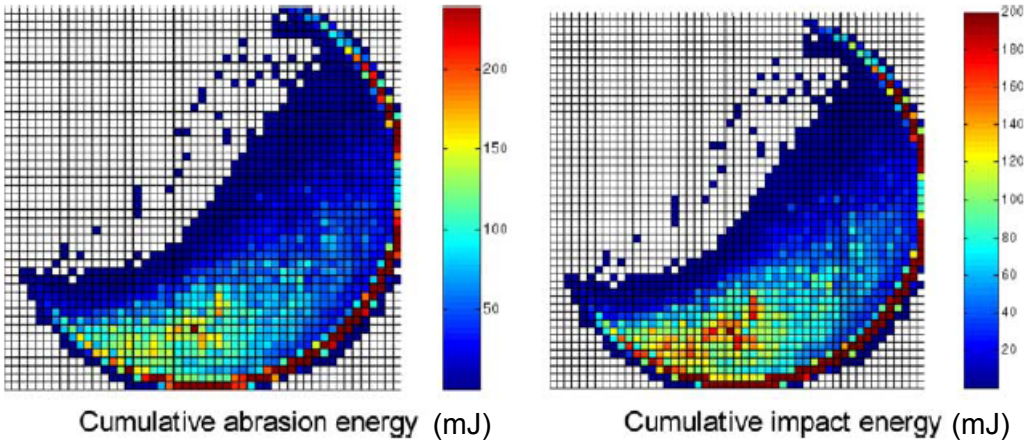

Figure 2.22: Spatial distribution of dissipated collision energies (taken from Powell and McBride, 2004)

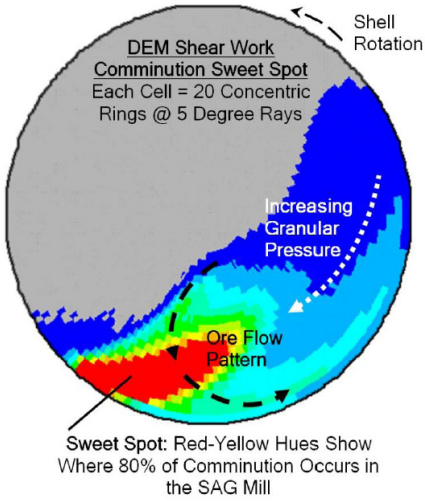

Figure 2.23: Spatial distribution of contact energies in a SAG mill (taken from Nordell and Potapov, 2011)

While distributions such as those in Figure 2.22 and Figure 2.23 demonstrate that the highest energy dissipation in the mill occurs in the toe region, an important characteristic also observed from DEM data is the frequency with which collision events occur. DEM simulations quantify the energy losses associated with every collision. Distributions showing the collision frequencies against the energy ranges in which they occur are thus commonly plotted from computational modelling data, as illustrated in Figure 2.24 to Figure 2.28.

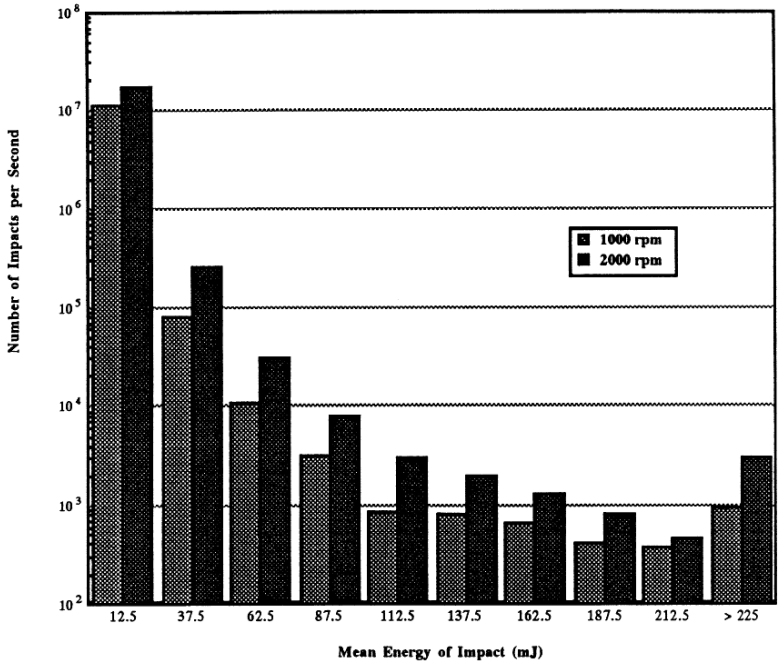

Figure 2.24: Collision energy distribution demonstrating mean impact energies at different speeds (taken from Rajamani et al., 2000)

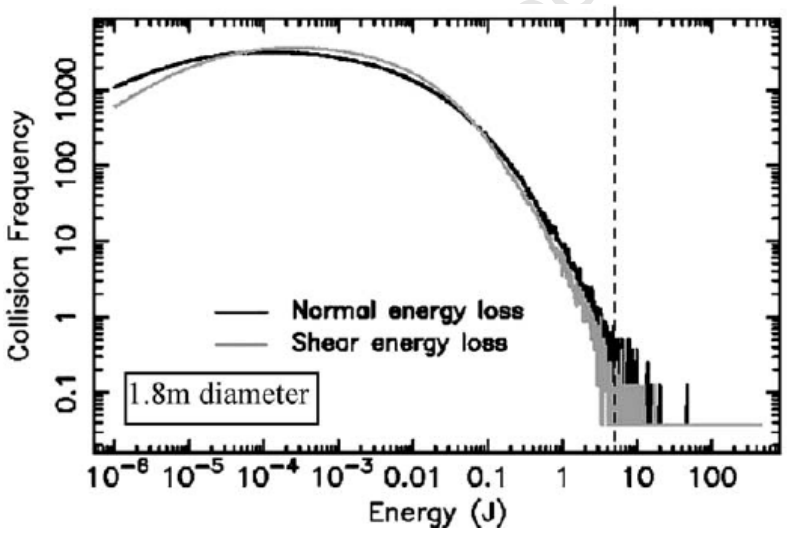

Figure 2.25: Collision energy spectra highlighting normal and tangential energy losses (taken from Cleary and Morrison, 2004)

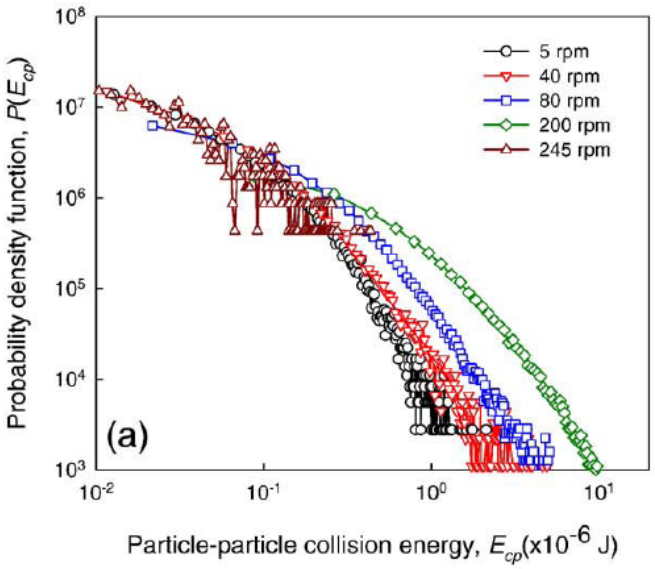

Figure 2.26: Energy spectra plotted as probability density function for different speeds (taken from Yang et al., 2008)

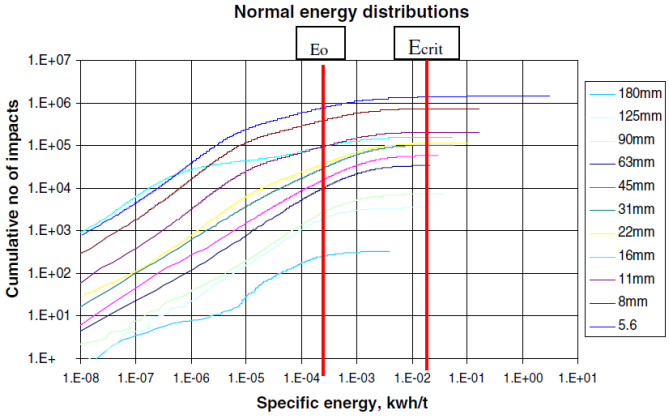

Figure 2.27: Energy spectra plotted as cumulative distribution for different particle sizes (taken from Powell et al., 2008)

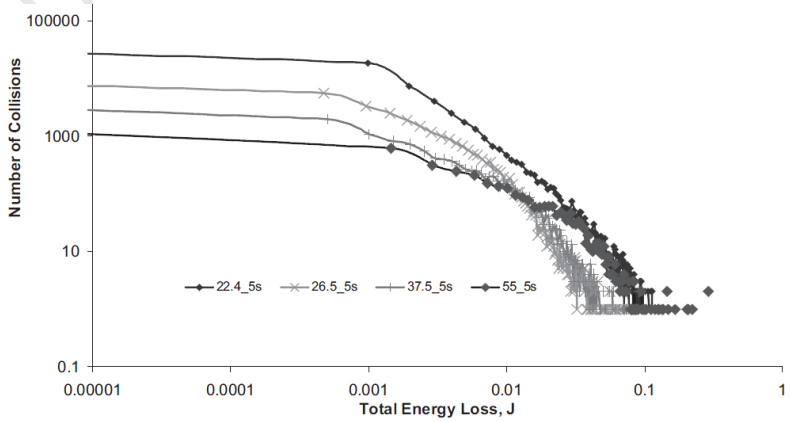

Figure 2.28: Energy spectra plots for different size classes in a charge distribution (taken from Khanal and Morrison, 2009)

These distributions have allowed researchers to examine different aspects of particle collision behaviour in tumbling mills. Rajamani et al. (Rajamani et al., 2000) studied the energy distributions in Figure 2.24, where it was highlighted that the low energy impact events dominated the distribution while relatively high energy collisions occurred much more infrequently. It was also demonstrated that an increase in speed led to a higher number of impact events at the higher end of the scale.

In Figure 2.25, Cleary and Morrison (Cleary and Morrison, 2004) extracted the normal and tangential DEM collision energy spectra for a 1.8m diameter pilot mill and compared it against a slice of an 11m diameter full scale mill. The results were found to follow a similar trend, and a linear relationship with mill length and diameter raised to the power of 2.5 was proposed as a scaling factor between these mills.

For Figure 2.26 it was shown in the work by Yang et al. (Yang et al., 2008) that the collision energy spectra could be plotted as a probability density function. The probable collision energies that resulted at each speed were plotted and it was found that an increase in mill speed tended to shift the distribution toward higher energies until a limit was reached at the point where the charge began to centrifuge. Thereafter, with increase in speed to the collision energies decreased.

In Figure 2.27, Powell et al. (Powell et al., 2008) plotted the collision energy spectra as a cumulative distribution for different particle sizes. This was done to correlate the simulation data with existing theories of impact breakage (see Section 2.4: The t_{10} breakage model), and to investigate whether the cumulative impact energies extracted from DEM could be used as the input to breakage probability functions which could predict the likely product.

In the work by Khanal and Morrison (Khanal and Morrison, 2009), depicted in Figure 2.28, the energy spectra was plotted for different size classes of a charge distribution used in a 0.3m diameter laboratory scale mill. It was noted that the smaller particle sizes dominated the lower end of the energy scale generating a great deal more impacts than larger sizes. At higher energies however the larger sizes had higher collision frequencies, indicating that impact breakage in tumbling mills at higher energy levels was dominated by coarser size fractions. A relatively large difference was found in the energy spectra curves of different sizes to those at different speeds. This suggested that the particle size had a greater influence on the resulting energy distribution than the mill speed at the ranges investigated.

Plots of the energy spectra have played a crucial role in elucidating the mechanisms behind the observed behaviour of charge in tumbling mills (Mishra, 2003). These distributions have provided a basis for understanding the energy utilization in the tumbling mill.

The PEPT method has been demonstrated to be a unique method of verifying the results of DEM simulations (Yang et al., 2003. Laurent and Cleary, 2012). This technique, which is utilized in this study, is discussed in the next section.

2.3 Positron Emission Particle Tracking (PEPT)

Positron Emission Particle Tracking (PEPT) is a technique for measuring the flow trajectory of a radioactive particle in a granular or fluid system such as a rotating drum (Parker, 2008). This technique was originally introduced in the medical field as Positron Emission Tomography (PET), and has been modified to suit engineering applications (Parker et al., 1997).

The premise of the PEPT method is the positron annihilation of a "tracer", a particle tagged with a radionuclide. Positron-emitting tracers are normally labelled using radionuclides such as ^{18}F, ^{64}Cu and ^{68}Ga. These radionuclides decay by emission of back to back gamma rays of 511 keV. Simultaneous detection of the two gamma rays in an array of detectors (a PEPT "camera") defines a straight line along which the particle position lies. Based on a series of lines within a discrete time period, the position of the particle can be triangulated in three dimensions. Figure 2.29 shows a picture of a PEPT camera system in a parallel plate configuration (Positron Imaging Centre, University of Birmingham), along with a schematic describing the method used to detect and triangulate particle positions.

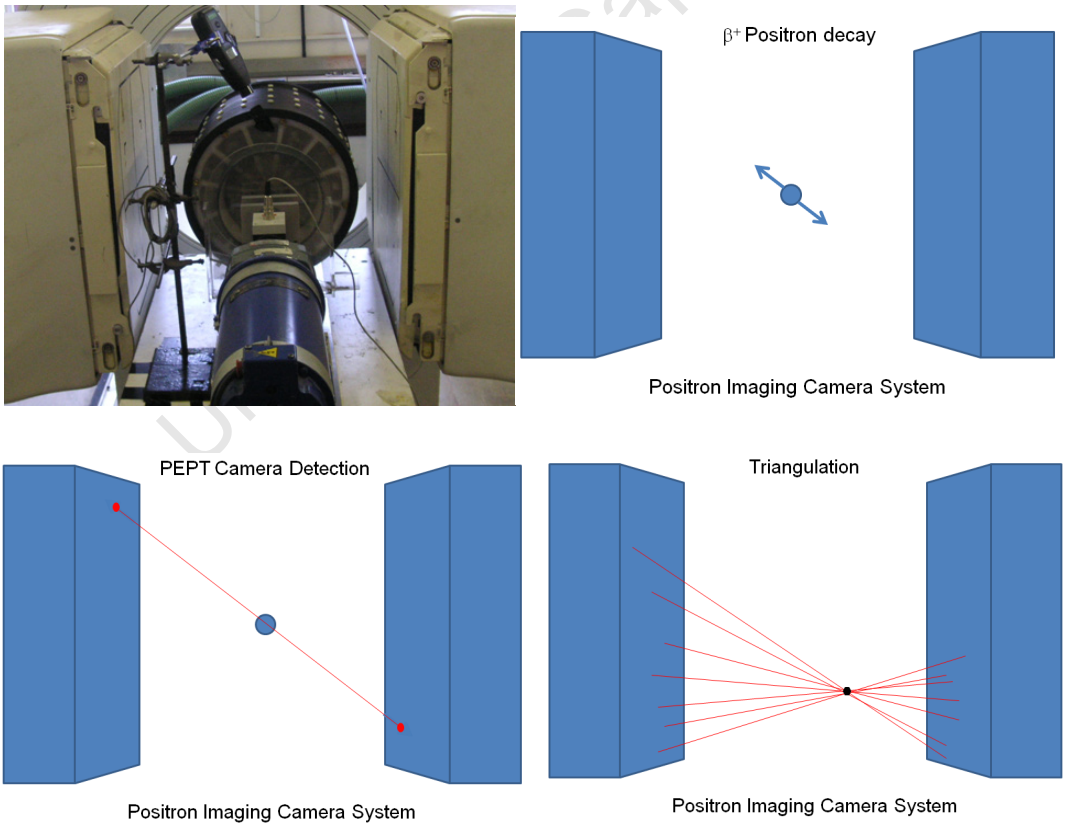

Figure 2.29: Laboratory scale tumbling mill in parallel plate PEPT camera and schematic of its operation

The accuracy of the method depends on the radioactivity and speed of the tracer particle, as well as the attenuation of the medium in which it travels. Based on the theory of back to back gamma ray emissions, few lines would be necessary to triangulate the position. However, due to numerous simultaneous gamma ray emissions, random pairings and scatter from the camera often occur. Therefore, in order to determine the true position, the raw data from the PEPT technique has to be filtered to remove false pairings from the reconstruction. A methodology to accomplish this is detailed in the work by Parker et al. (Parker et al., 1997). In summary, the centroid of a selected number of sequential lines of response is initially used to triangulate the particle position. The lines furthest from the centroid of these lines are then discarded in an iterative manner until the desired level of accuracy is reached.

For particles containing oxygen, a tracer can be produced by either direct bombardment or ion exchange (Parker and Fan, 2008). Direct activation involves the use of a proton beam to bombard the oxygen carrying particle. For a ^{3}He beam, some oxygen particles acquire some protons and are converted to ^{18}F according to Equation 2.33

$$^{16}_{8}O + ^{1}_{1}H \rightarrow ^{18}_{9}F + ^{1}_{0}n \qquad \textbf{Equation 2.33}$$

The unstable Flourine-18 subsequently decays via positron decay, initiating annihilation events with electrons that produce the back to back gamma rays detected by the PEPT camera (Parker, 1997). Flourine-18 has a half-life of approximately 110 minutes.

The PEPT technique offers a distinct advantage to other methods of examining charge dynamics as it provides an in situ measurement of particle motion in the system under investigation. Trajectory histories can then be used to calculate the kinematics of particle flow, and use it to discern characteristics of the whole body (Parker, 1997).

The main assumption underpinning the use of PEPT in determining characteristics of the whole charge is that the system is ergodic. Ergodicity refers to the assumption that the time average of a single realization of a system can be used to determine the ensemble average (Conway baker et al., 2002. de Oliviera and Werlang, 2007). This hypothesis was first put forward by Boltzmann in 1884 (Boltzmann, 1884), simply stated in English translation as:

'For large systems of interacting particles in equilibrium, time averages are close to the ensemble, or equilibrium average.'

This theory forms underlying principle on which statistical mechanics is based. For PEPT, the theory can be used to relate statistical data from single particle tracking experiments to

the behaviour of the whole charge in a mono-sized system. (Castagnino and Lombardi, 2009).

For instance, the work by Parker et al, 1997 (Parker et al., 1997) demonstrated that data from PEPT could be used to obtain spatial distributions of porosity in a rotating drum. Using a single particle tracer, the packing density was calculated as a fraction of the total time, or residence time distribution, spent in each region.

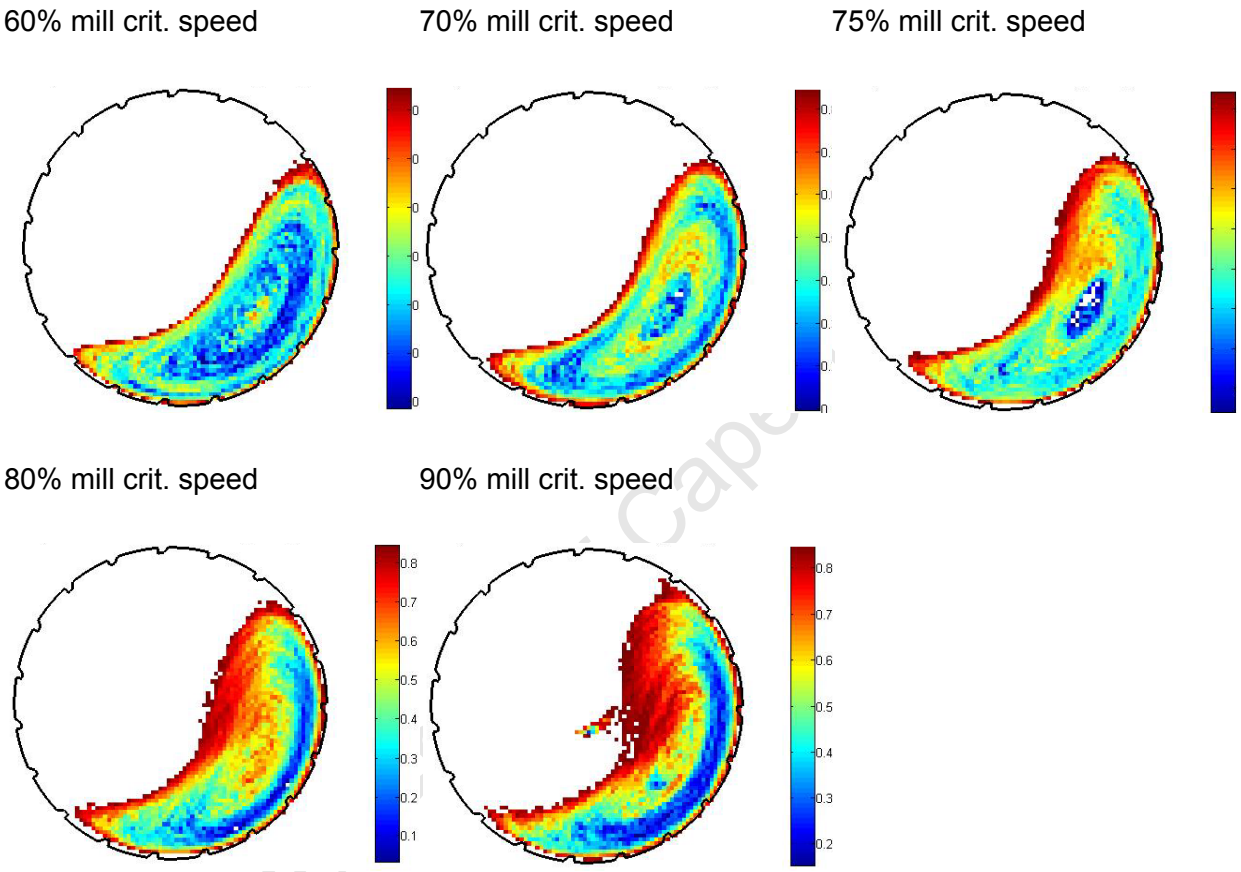

Figure 2.30: Spatial distribution of porosity at different speeds (taken from Sichalwe et al., 2011)

The work by Sichalwe et al. (Sichalwe et al., 2011) followed this methodology, by initially determining the residence time fraction F_{ij} spent in each voxel of a grid in the transverse mill plane. The number of particles in the voxel is then determined by Equation 2.34:

$$N_{ij} = N_i \cdot F_{ij} \qquad \textbf{Equation 2.34}$$

Here, N_i is the total number of charge particles. The total solid volume in the voxel is calculated using Equation 2.35, using d_i, the diameter of the particle.

$$V_{ij} = \frac{N_{ij}}{6} \cdot \pi \cdot d_i^3$$ **Equation 2.35**

The solidicity or packing fraction is subsequently determined as this solid volume divided by the voxel volume. The porosity is the difference between this value and unity. Spatial distributions were obtained as shown in Figure 2.30, indicating the influence of mill speed on charge porosity. Sichalwe observed that as mill speed increased, the bulk region became more porous due to increasing centrifugal forces on the charge body (Sichalwe et al., 2011). The porosity of the rising bulk charge at the mill periphery was also noted to decrease with increasing speed. Sichalwe speculated that this was due to an increase in packing density against the mill shell as more particles were prone to cascading and cataracting at higher speeds.

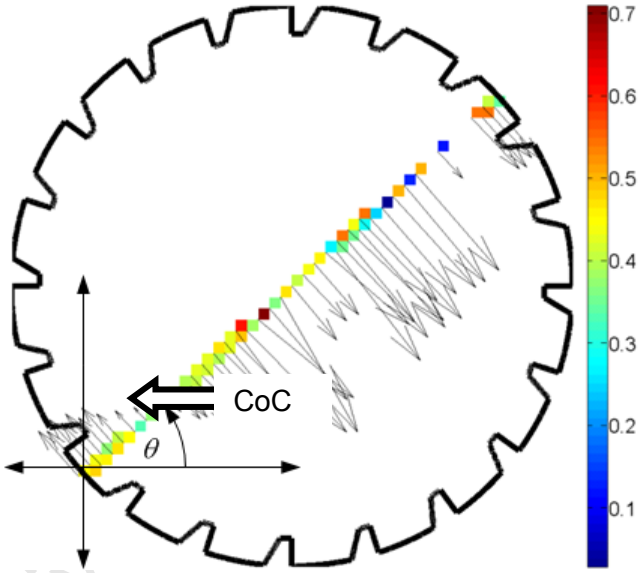

Figure 2.31: Tangential velocity profile for a 1mm particle in 30%wt slurry at 75% critical mill speed (taken from Govender et. al., 2011)

The work of Govender et al. showed that PEPT data could also be used to estimate shear rates in tumbling mills (Govender et al., 2011). As a proxy for shear rate, a spatial map of tangential velocities in different regions was determined. The tangential velocity in voxels of the mill along a diametrical line through the Centre of Circulation was determined as illustrated in Figure 2.31. Along this selected profile, it was found that the tangential velocity could be modeled using Equation 2.36:

$$V(r,\theta) = a_1 \sin(b_1 r + c_1) + a_2 \sin(b_2 r + c_2)$$ **Equation 2.36**

As discussed in Section 2.1, PEPT data could also be used to investigate charge power draw in tumbling mills (Kallon et al., 2011). The calculation of power draw from PEPT data

provides a quantitative measure to compare against measurement. To ensure that the bulk charge motion data determined from particle tracking experiments using PEPT is consistent with that of the actual tumbling mill charge, the PEPT power draw should be a close approximation of the measured power draw. The unique value of PEPT data is that the average kinematic properties can then be directly compared against DEM simulations of an identical system to validate the predicted charge motion from the computational system.

2.4 Additional relevant theory

The analysis in this thesis utilizes a number of existing techniques which have been used to represent data and solve mathematical and engineering problems. This section summarizes several relevant approaches that are relevant to this work.

The t_{10} breakage model

A measure of efficiency for a tumbling mill is its use of the supplied energy in causing breakage (Fuerstenau and Abouzeid, 2002). Breakage occurs via three mechanisms: impact, abrasion and attrition, where it is known that impact dominates breakage behaviour at the coarse size range (Napier-Munn et al., 1999).

In the software package JKSimMet (JKTech, 2013) the use of comminution energy for impact in AG/SAG mills is modelled as a function of a parameter known as the t_{10} (Shi and Kojovic, 2007). The t_{10} is an indicator of the degree of breakage, defined as the percentage of material passing through a screen size one tenth of the original particle size. Using probability theory, the relationship for the t_{10} as a function of impact energy is derived as given in Equation 2.37:

$$t_{10} = M \cdot \left[1 - e^{\left(-f_{mat} \cdot x \cdot k \cdot (E_{cs} - E_{min})\right)}\right] \qquad \textbf{Equation 2.37}$$

In this equation, f_{mat} is defined as a material specific parameter which influences the amenability of the material to fracture. The particle size x is explicitly given in this model as the breakage behaviour is known to be size dependent. The quantity k represents the successive number of impacts at the energy level that achieves the given breakage degree. This is required as the continuum mechanics based derivation for the probability of breakage shows that incremental damage occurs with each impact even at relatively low energy levels which leads to eventual breakage (Tavares and King, 2002. Vogel and Peukert, 2003). Consequently, breakage is modelled as a failure event that occurs cumulatively with impact energy.

The quantity E_{min} is also included in the model, defined to be the theoretical minimum value below which negligible damage occurs. This quantity, also written as E_0, has been found by impact breakage tests to be a material specific parameter which is influenced by particle shape and size (Bbosa et al., 2006. Whyte, 2005). E_{cs} is the specific comminution energy (kWh/t) or available energy to cause fracture per mass present.

Graphically, results of fitting this model to particle breakage data show good agreement as shown in Figure 2.32. From DEM simulations of tumbling mills, the cumulative form of the collision energy spectra can be plotted as given in Figure 2.27. As the form of the curve is similar to the t_{10} function, it has been hypothesized that the cumulative energy distribution from DEM can be directly correlated with this breakage model (Powell et al., 2008). Using this approach, the quantity E_0 has been determined from DEM energy spectra data of spherical particles in a pilot scale tumbling mill (Kulya, 2008).

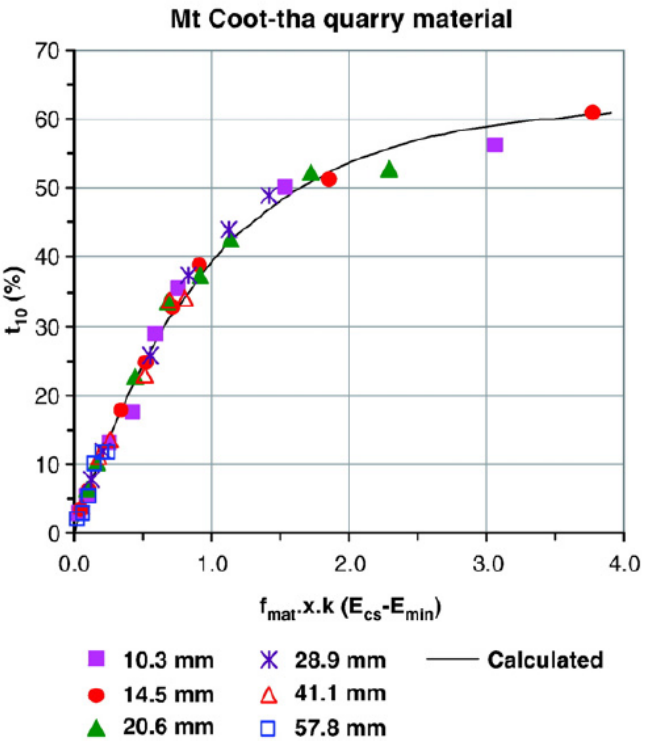

Figure 2.32: Example of t_{10} function fitted to breakage data (taken from Shi and Kojovic, 2007)

In this thesis, DEM energy spectra data is used to determine E_0 in Section 5.4. The cumulative form of the energy spectra model developed in this work is also compared with the t_{10} function in Section 8.3.

Probability theory

The primary focus of this work, the power draw and subsequent collision energy distribution in a tumbling mill, is based on random distributions of particles and chaotic events. However, principles from probability theory were applied to present results in ways that demonstrate key trends.

The relative frequency, that is the frequency of a particular event divided by the total events, can be exhibited as a distribution. Although the events may be stochastic, through a principle known as statistical regularity, the relative frequency of an event stabilizes with increase in the number of events that is used to determine it (Helstrom, 1984). This assumption signifies that, if sufficient statistics are accumulated at a particular set of conditions, the relative frequencies of events associated with that configuration converge to values which can be taken to be the probability that those events will occur.

The significance of relative frequencies is aptly described in the work of von Mises who stated that the standard interpretation of probability is the limit of its relative frequency in a large number of trials (von Mises, 1981). Relative frequency distributions from experimental and simulation data can therefore be used to compute empirical estimates for probability distributions. Probability distributions, essentially the likelihood that certain events will occur under specific conditions, are the basis on which most modelling relationships in engineering practice are built.

Another important concept in probability theory is that of conditional probability. This is a method used to calculate probabilities for which some partial information about the system or experiment is known. It can also be described as a simplified means of determining probabilities as a known event associated with the system conditions the likely range of the outcome (Ross, 2009). In mathematical notation, the probability of an event *P(B)* given that the outcome of another probability event *P(A)* has occurred is denoted by $P(B|A)$.

The formula for calculating this probability is based on the reduced sample space for the event A, such that it is given by Equation 2.38:

$$\mathrm{P}(B|A) = \frac{P(BA)}{P(A)} \qquad \textbf{Equation 2.38}$$

Here, *P(BA)* is the combined probability that both events *A* and *B* will occur. This formulation is consistent with the interpretation of probability as the limit of relative frequency.

In this thesis, probability distributions based on PEPT and DEM data are used to develop a model for the power draw of a tumbling mill in Chapter 6. In Chapter 7, energy spectra data from DEM simulations is used as a basis to develop probability distributions for the collision energy loss.

Numerical Quadrature using the Tanh-Sinh method

In mathematics, the fundamental theorem of calculus is well known to be a means of evaluating the definite integral of a function (Stewart, 2010). For a function which is continuous over a closed interval *[a,b]*, this theorem can be written in the form of Equation 2.39.

$$\int_a^b f(x)dx = F(b) - F(a) \qquad \textbf{Equation 2.39}$$

In different areas of research, including engineering, a problem often arises that the integral *F(x)* cannot be determined in terms of elementary functions (Press et al., 1986). For such cases, the solution to the definite integral is often determined numerically. The approximation *A(f)* that provides a numerical solution to the integrand is known as a quadrature rule, expressed mathematically as Equation 2.40

$$\int_a^b f(x)dx \approx A(f) \qquad \textbf{Equation 2.40}$$

Here, the approximation *A(f)* may take a completely different form to the original function to determine the integral without considering the integral *F(x).* For what is known as an *n*-point approximation *A(f)* can be expressed as a weighted sum in Equation 2.41

$$A(f) = \sum_{i=1}^{n} w_i \cdot f(x_i) \qquad \textbf{Equation 2.41}$$

Here, values of x_i are called abscissas, point values where the function is calculated, while values of w_i are the weights associated with each point.

Several methods of numerical quadrature have been proposed by researchers to address complex problems with different practical applications (Bailey et al., 2005). Among these, interpolatory quadrature using Newton-Cotes formulas and Gaussian rules are the most common (Heath, 1997).

The Tanh-Sinh method was developed by Takahashi and Mori (Takahashi and Mori, 1974) to evaluate integrals with end point singularities, but was also found to give solutions to double exponential integrals with high precision. It is based on a Euler-Maclaurin summation formula, and employs a transformation of a function *f(x)* over a finite interval *[a,b]* to an integral over $(-\infty, \infty)$ by using a change of variable.

Considering that the integral to be evaluated has the form given in Equation 2.42:

$$I = \int_a^b f(x)dx \qquad \textbf{Equation 2.42}$$

The variable transformation occurs using Equation 2.43:

$$x = \emptyset(t), \qquad a = \emptyset(-\infty), \;\; b = \emptyset(\infty), \qquad \textbf{Equation 2.43}$$

The function ∅(t) is chosen such that it can be determined on $(-\infty, \infty)$. Consequently, the new integral *I* is given by Equation 2.44

$$I = \int_{-\infty}^{\infty} f(\emptyset(t) \cdot \emptyset'(t))dt \qquad \textbf{Equation 2.44}$$

The function ∅(t) is also selected such that after the transformation the decay of the integrand is double exponential or represented by Equation 2.45

$$|f(\emptyset(t) \cdot \emptyset'(t))| \approx e^{-c \cdot e^{|t|}}, \;\; |t| \to \infty \qquad \textbf{Equation 2.45}$$

The simple trapezoidal formula can then be applied with an equal mesh size *h* (Mori and Sugihara, 2001), to give Equation 2.46

$$I = h \cdot \sum_{k=-\infty}^{\infty} f(\emptyset(kh) \cdot \emptyset'(kh)) \qquad \textbf{Equation 2.46}$$

For calculations, *k* is truncated at some value *P* to evaluate the summation depending on the level of accuracy that is required. Thus, *2k+1* terms are accumulated for the numerical solution.

Thus the transformation given in Equation 2.47:

$$x = \emptyset(t) = tanh\left(\frac{\pi}{2} sinh(t)\right) \qquad \textbf{Equation 2.47}$$

gives the double exponential formula in Equation 2.48:

$$I = h \cdot \sum_{k=-M}^{M} f\left(tanh\left(\frac{\pi}{2} sinh(k \cdot h)\right) \cdot \left(\frac{\frac{\pi}{2} \cdot \cosh(k \cdot h)}{cosh^2\left(\frac{\pi}{2} \cdot \sinh(k \cdot h)\right)}\right)\right) \qquad \textbf{Equation 2.48}$$

This method has been found to be the most accurate determination of double exponential integrals for the least number of function evaluations (Bailey et al., 2005).

Tanh-Sinh quadrature is used in Chapter 7 of this thesis to calculate the total energy loss by integrating the function used to model the energy spectra. This technique is also used in the same chapter to develop a probability density function for the collision energy loss as a function of mill operating parameters.

2.5 Discussion of reviewed literature

Based on the broad spectrum of work considered in this chapter, the following observations are made which define the basis for this thesis.

Modelling and optimizing the power draw and utilization in tumbling mills is a significant challenge that has been addressed using a variety of methods for almost a century. Such devices typically operate in the cascading and cataracting regime, for which the dynamic charge motion is complex. As a result, empirical models designed to predict power draw have often relied on simplifications of the charge motion behaviour. While these methods has been found to be effective for the range over which they are defined, they have been found to be limited to static cases and perform poorly outside of their design ranges.

It has been emphasized in modelling the power draw that a correct depiction of charge motion is imperative to providing accurate predictions. This is because under any mill operating regime, the motion of the charge is responsible for the torque requirements that drive the mill at the specified speed. Under steady state conditions the charge motion for specified operating conditions demonstrates a number of features, such as the toe and shoulder position, that have been used as the basis for most models.

The simplified depictions of the charge body as a solid mass with various features that alter under different conditions has been a successful approximation of mill behaviour with regards to predicting power. However, such simplifications have not been able to capture the finer details of charge behaviour, such as the radial segregation patterns that occur within the charge size distribution which influence the motion and affect mill power. The distribution of the charge and its influence on power draw is an avenue to the understanding of how energy harnessed by the body is subsequently utilized in causing collisions between particles.

For the development of power draw models which scale up between laboratory, pilot and industrial scales, 0.3m diameter tumbling mills have often been used at the laboratory scale. The laboratory scale mills have been found to provide an ideal basis for predicting the behaviour of the other relative scales. For the model to have meaningful application, it has been noted that the parameters used to define the power draw need to be measurable quantities related to the mill geometry and charge.

DEM has been demonstrated to be a means of studying the mechanisms of charge motion that influence power draw and energy utilization. For this method to accurately depict the

tumbling mill environment, the contact model has to be configured and assessed to be a representative of dynamic charge motion behaviour. For this purpose validation cannot be quantitative or qualitative alone, but needs to be a combination of both to have a comprehensive examination of simulation behaviour.

PEPT has been demonstrated to be a means of investigating charge power draw in tumbling mills. The calculation of power draw from PEPT data provides a quantitative measure to compare against measurement. To ensure that the bulk charge motion data determined from particle tracking experiments using PEPT is consistent with that of the actual tumbling mill charge, the PEPT power draw should be a close approximation of the measured power draw. The unique value of PEPT is that the average kinematic properties can then be directly compared against DEM simulations of an identical system to validate the predicted charge motion from the computational system.

From the power draw models proposed, the torque arm based methods have often proved successful as they rely on the mechanism through which energy is transmitted to the charge, the torque and angular velocity of the drive shaft. Prior models have relied on simplifications of the charge distribution that generates the required torque as well as the charge velocity distribution. This has primarily been due to the absence of feasible methods of measuring the actual charge motion in tumbling mills. PEPT and DEM kinematic data offers a means of addressing this shortcoming, such that the actual charge motion behaviour obtained from these techniques can be used as the basis to predict the mill power draw.

Particle motion information from PEPT and DEM data can be used to describe the motion of the overall charge. The conditions for this assumption to hold, for both DEM and PEPT are two-fold. First, steady state conditions have to exist in the tumbling mill over the period for which the statistics are acquired. Second, the number of accumulated statistics for the particles has to be sufficiently high that the relative frequencies represent reasonably close approximations of the behaviour of the overall charge.

In this thesis, this is accomplished with DEM by calculating relative frequencies using data from every single particle in the charge over all the discrete time intervals that constitute a single revolution at steady state. The higher the particle count in the simulation, and the longer the periodic time, the more accurate the theoretical probability based on relative frequency tends to be.

For PEPT, using the ergodic principle (see Section 2.3), data from a single particle is used to accumulate sufficient statistics to represent the ensemble average, and consequently its

relative frequencies. For this to be possible, the tracking period has to be sufficiently long enough under steady state conditions that the data becomes statistically representative.

The energy spectra plots from DEM characterize the power utilization of tumbling mills in causing collisions. These distributions, which can be expressed in a variety of forms, depict trends which are a direct consequence of the charge motion under specific mill operating conditions. Mill operating parameters such as the particle size and mill speed have been noted to have a significant influence on the energy spectra. Plots of the energy spectra at different speeds have been used to demonstrate that the distributions can be modelled as a scalar multiple of the mill speed. In addition, energy spectra curves of different particle sizes in a charge body have indicated identical trends, suggesting that the relationship can be modelled.

The research reviewed for this thesis has found that there is no existing model for the energy spectra of a tumbling mill as a function of the operating variables that influence it, particularly particle size. Energy spectra plots are frequency distributions for collisions in the mill at discrete energy ranges over a single mill rotation at steady state. The probability that collisions in a mill occur at a particular energy range is a direct consequence of the operating parameters. For this thesis, collision data from DEM is used to model the energy spectra and develop a probability distribution for the collision energy loss of each particle size class.

CHAPTER 3

METHODOLOGY

Overview
This chapter describes the approach that was taken to address the objectives put forward in the introduction. The experimental work in this thesis involved particle tracking using PEPT and computational simulations using DEM. A summary of the methodologies behind the conducted PEPT experiments and DEM simulations is laid out.

3.1 Experimental framework

The ADAC Forte parallel plate camera at the Positron Imaging Centre, University of Birmingham, was used to conduct the Positron Emission Particle Tracking (PEPT) experiments in this study. An experimental rig comprising of a laboratory scale tumbling mill with a diameter of 300mm and length of 270mm was designed and manufactured for this work. A picture and schematic of this mill is provided in Figure 3.1.

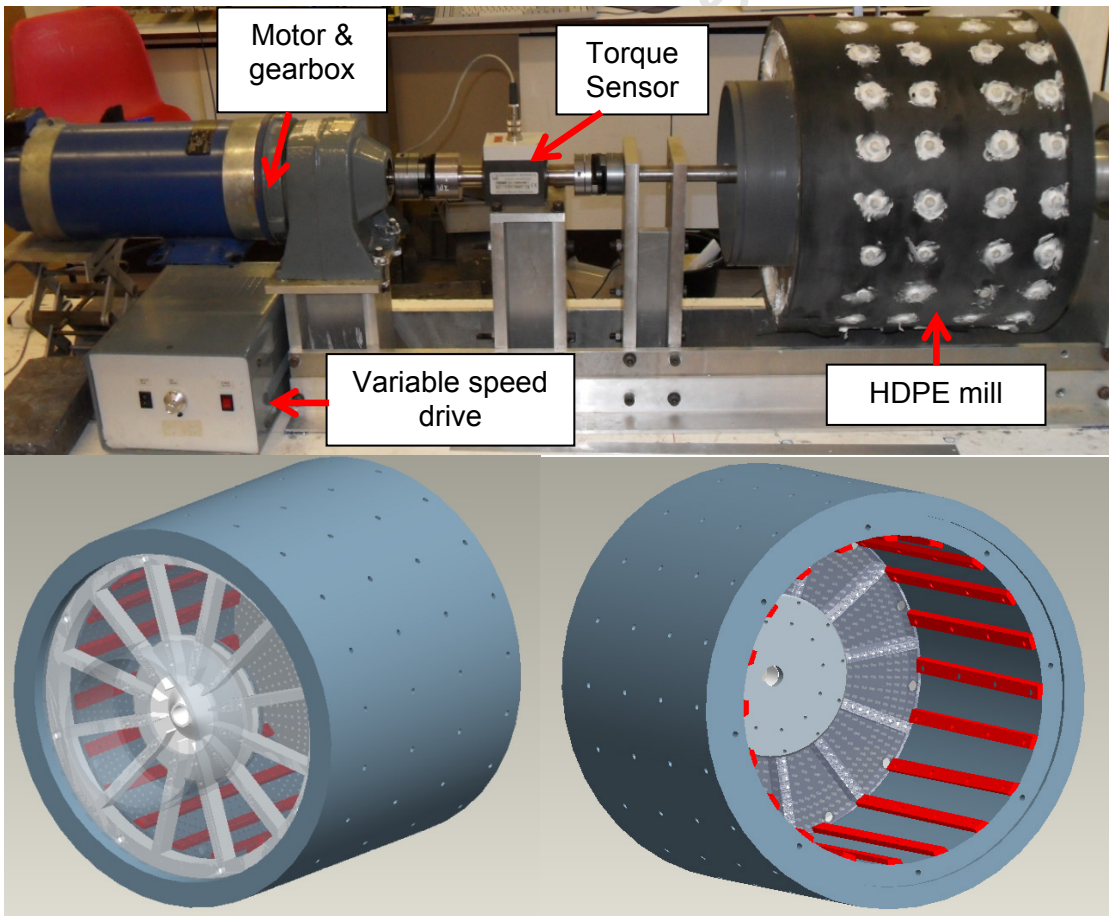

Figure 3.1: Picture and schematic of 300mm tumbling mill used for PEPT experiments

The mill shell was machined out of high density polyethylene (HDPE), with an end face and support plate of mild steel at the inlet and discharge ends respectively. This support plate housed HDPE discharge panels with holes of 1mm diameter. The mill was fitted with 20 evenly spaced nylon lifters with a height of 5mm, width of 20mm, and 60 degree face angle. A 100Nm torque transducer was mounted between the mill and the drive motor which output voltage signals at 1000Hz to a computer. The motor and step-down gearbox were controlled by a variable speed drive which could be set to run the mill over a speed range of 0 to 90 rpm (117% critical speed).

Spherical glass beads of 2-8mm were used as the dry charge in batch mode. A mill volumetric filling (*J*) of 31.25% was used for experiments. The total charge mass (M_c) required was determined using Equation 3.1.

$$M_c = \frac{J}{V_m} \cdot 100 \cdot (1 - \varepsilon) \cdot \rho \qquad \textbf{Equation 3.1}$$

V_m is the volume of the mill, while ε and ρ are the charge porosity and charge density respectively. There are various models for the close sphere packing of monodispersed spheres (Dullen, 1992). As the motion of spherical particles in the tumbling most closely resembled that of poured random packing, a charge porosity of 0.375 (packing fraction of 0.625) was assumed. The glass bead density was 2500 kg/m^3.

Experiments were distinguished into two types which were named as follows:

Mono-size distribution experiments

For these tests the mill was run consisting of charge composed entirely of glass beads of a single size. 3mm and 5mm beads were used, which provided a basis for comparison of simplified motion at two mid-range particle sizes. These tests further allowed for an investigation of motion behavior for distinct sizes, and were used as the initial platform for the validation of DEM simulations.

Full size distribution experiments

In these experiments, a size distribution of glass beads from 2-8mm was selected based on a Weibull distribution, whose form is given in Equation 3.2. Values of 4.41 and 2.41 were used for parameters a_1 and a_2 respectively, which resulted in the distribution plotted in Figure 3.2. These values were selected such that the curve reflected the ‘S-shape’ that is

typically associated with charge size distributions in tumbling mills (Wills and Napier-Munn, 2006).

$$y = 100\left(1 - e^{\left(-\left[\frac{x}{a_1}\right]^{a_2}\right)}\right) \qquad \textbf{Equation 3.2}$$

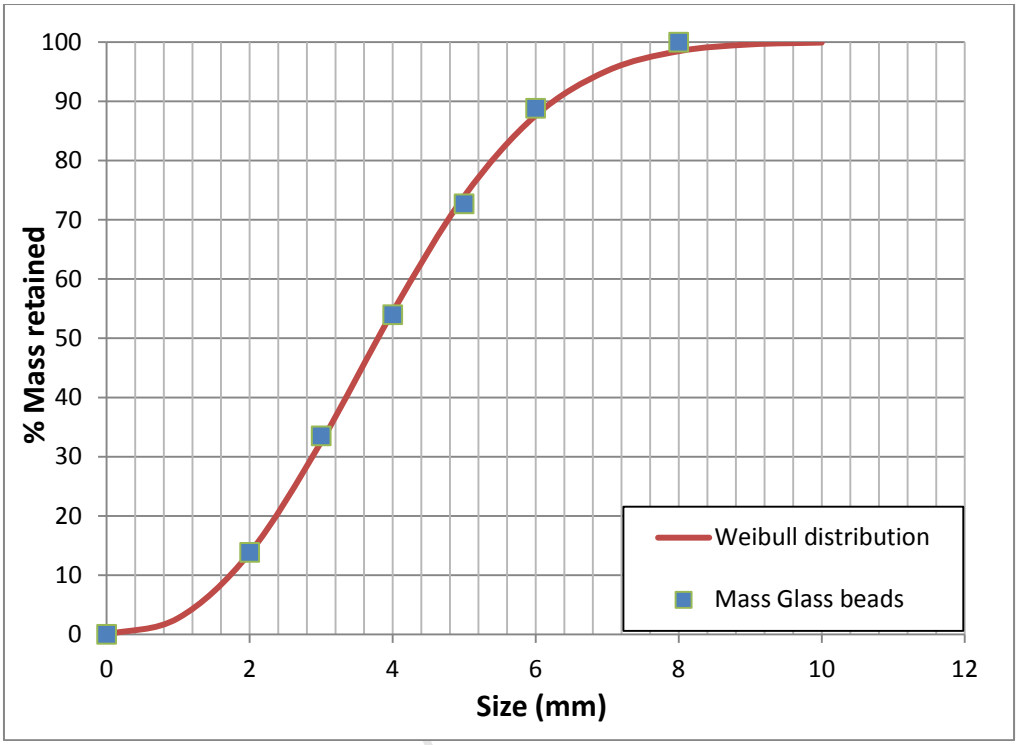

Figure 3.2: Size distribution of glass beads used for PEPT experiments

Table 3.1: Summary of mill specifications and conditions investigated with PEPT

PEPT Mill		
Internal diameter (m)		0.3
Internal length (m)		0.27
% Filling by volume		31.25
Number of lifters		20
Glass bead size (mm)	**Charge Mass (kg)**	**Mill Speeds (%crit)**
Mono-size experiments		
3	9.66	60, 75
5	9.66	50, 60, 75
Full size distribution experiments		
2	1.34	60, 75
3	1.9	60, 75
4	1.98	60, 75
5	1.81	60, 75
6	1.56	60, 75
8	1.08	60, 75
Sum of Full size dist. Mass	9.67	

Table 3.1 provides a summary of the mill specifications and the charge compositions and mill speeds investigated using PEPT. Tumbling mills are typically operated at between 20-45% filling (Kawatra, 2006). The volumetric filling of 31.25% was selected for this work as a mid-range value of typical mill operation. The mill speed of tumbling mills is normally between 60-83% of the critical speed, which is given by Equation 2.4 (Napier-Munn et al., 1999). For the 5mm glass beads, three mill speeds were investigated to examine the behaviour of the glass beads in the transition from a purely cascading to a cascading and cataracting regime (see Section 2.1). As the focus for this work was the cascading and cataracting regime which was typical of industrial application, the remainder of the experiments were carried out at 60% and 75% mill critical speeds.

Glass beads of each particle size were subjected to direct activation using a 33MeV ^{3}He beam for use as radioactive tracer particles. Following the methodology described by Parker (Parker et al., 1997), the beads were labelled with ^{18}F, which has a half-life of approximately 110 min. Before and after each test, the radioactivity of the tracer particle was measured using a Geiger counter. This was done to ensure that the level of radioactivity on the tracer was at least 300 μC, which was the recommended minimum for the parallel plate PEPT camera (Parker and Fan, 2008).

The activated glass bead was added to the charge in the mill and tracked at each investigated speed. Based on the ergodic assumption discussed in Section 2.3, it was found that running at each condition for an hour was adequate to determine the average motion properties of particles of a given size from the motion of the tracer (Mangesana, 2011). In this work, each condition listed in Table 3.1 was tested by tracking the motion of the tracer particle for an hour. For the full size distribution experiments, each size was tracked separately.

The charge power draw at each condition was measured using a torque transducer and tachometer. The methodology followed to determine the mill power is discussed in the next section.

3.2 Determination of measured power

A T2OWN torque transducer (HBM, 2012), pictured in Figure 3.3, was used to measure the dynamic load applied to the mill shaft during rotation. This sensor was rated up to 100Nm which was more than adequate for the load range in this work (~ 0 to 40Nm). The torque sensor output voltages at a frequency of 1000Hz in a range from 0 to 10 volts. This voltage was directly proportional to the torque applied to the shaft.

Figure 3.3: Torque transducer used for determining load

The output signal from the torque transducer was fed into an amplifier which in turn was read into a computer. LabView Signal Express (National Instruments, 2012) was then used to display the real time signal, which could also be recorded. Figure 3.4 provides a screen capture of the LabView software interface, which shows a graph of the real time voltage at a given time recorded from the transducer.

Figure 3.4: Screen capture of LabView Signal Express interface

To determine the torque on the shaft, the sensor required calibration. A clamp was designed for this purpose, which is pictured in Figure 3.5. The clamp was fastened to one end of the torque sensor shaft with the other end tightened. Two lever arms could then be screwed into the sides of the clamp, one at either end to counter balance the weight. A spirit level would be used to ensure that the lever arms were horizontal to the mill shaft axis.

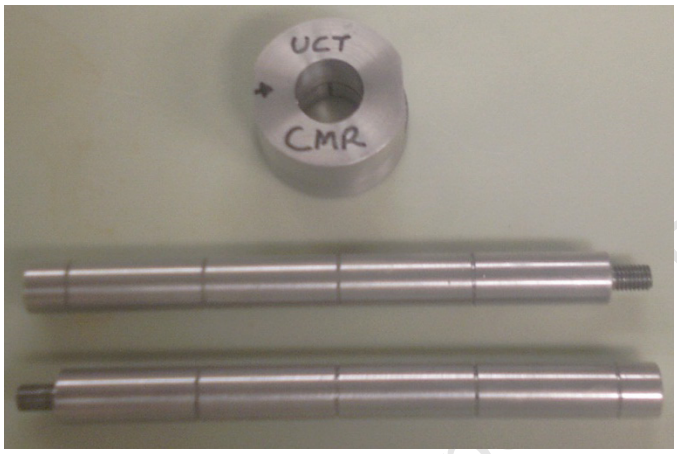

Figure 3.5: Picture of clamp used to calibrate torque sensor

The real time voltage from the torque sensor was initially set to zero. A known weight would then be attached to a string and hung on the clamp at one of the grooves along its distance. This would generate a fixed static torque about the mill shaft, with the change in voltage on the sensor being directly proportional to the torque on the shaft. By taking readings using different weights and distances along the calibration clamp, data points for a Torque vs. Voltage relationship could then be plotted as shown in Figure 3.6.

The plot yielded that the best fit line through these data points was a straight line through the origin. The gradient of this line represented the calibration factor K_c which was the relationship between the measured voltage and torque for the set gain value on the amplifier.

The mill was initially run empty to establish the no load power. Once the particles were fed to the mill, the zero on the torque sensor would then be reset such that the changes in voltage would reflect the power draw of the particles alone. These recorded voltage readings were captured for 15 minutes of each experimental run.

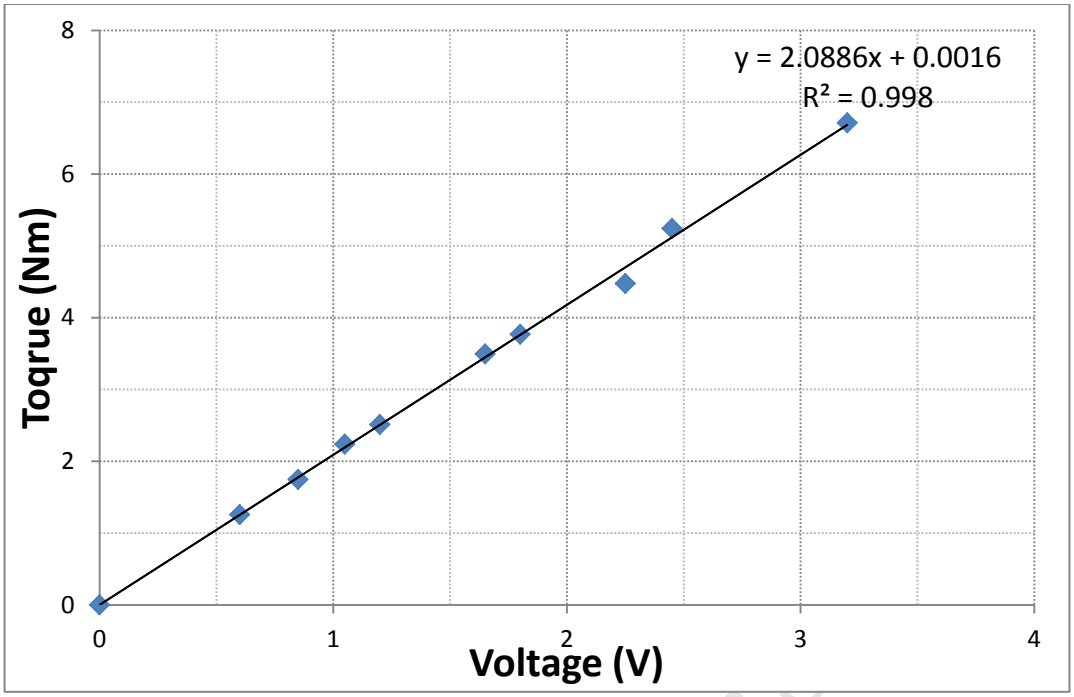

Figure 3.6: Data points and calibration line for torque sensor

The angular speed of the mill in radians per second (ω) was measured during each test using a tachometer. Given the determined calibration factor, measured voltage and angular speed, the mill power draw could then be determined using Equation 3.3.

$$P_{MEAS} = K_c \cdot \bar{V} \cdot \omega \qquad \textbf{Equation 3.3}$$

In this equation, the voltage used was the average over the duration of the power draw measurement. Fluctuations in the voltage and speed readings contributed toward uncertainties in the power measurement. To determine the uncertainty for each mill power draw measurement, Equation 3.4 was used.

$$\Delta P_{MEAS} = \sqrt{\left(\frac{\Delta V}{V}\right)^2 + \left(\frac{\Delta \omega}{\omega}\right)^2} \qquad \textbf{Equation 3.4}$$

Where ΔV and $\Delta \omega$ are the variances in the voltage and angular speed readings respectively.

3.3 Numerical modelling

The Discrete Element Method (DEM), as described in Section 2.2, was used to simulate the mechanical environment of particle motion in the tumbling mill. The mill geometry, including lifters and endplates, was imported from the computer aided design (CAD) drawings into the DEM package. In order to reduce the computational expense in meshing the mill geometry, these drawings were simplified by removing all bolts and holes in the mill shell.

EDEM, a commercially available software package developed by DEM Solutions (DEM Solutions, 2006), was selected to carry out the simulations in this study. A screenshot of the Graphical User Interface (GUI) for this software is shown in Figure 3.7. The DEM simulation parameters, including the mill material, charge properties and interaction coefficients had to be specified to represent those of the actual particles and mill. The required parameters were selected based on an existing database of experimental work on different materials (Chandramohan, 2005) as well as the software's material database for the relevant interacting elements.

The properties required were the Poisson's ratio, shear modulus and density of the HDPE mill shell, mild steel support plates, nylon lifters and glass beads. In addition, the restitution and friction coefficients of the glass beads against each of the other materials had to be specified. Gravity was turned on and set to the default 9.81 m/s^2. Table 3.2 summarizes the list of parameters that were used for performing the DEM simulations in this work.

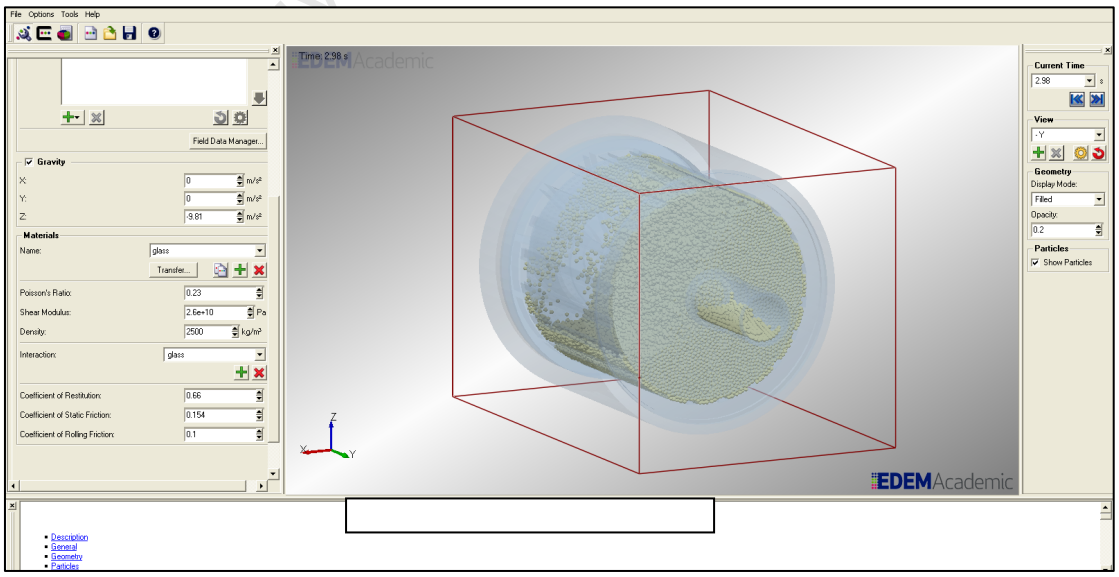

Figure 3.7: Screenshot of the EDEM interface

Table 3.2: Summary of the parameters specified for DEM simulations

Item	Material	Density (kg/m^3)	Shear Modulus (GPa)	Poisson's ratio
Mill shell, Discharge grate support plate, Discharge panels	HDPE	950	0.31	0.42
Lifters	Nylon	1100	0.76	0.76
End face, Feed pipe, Exit plate	Mild steel	7800	76	0.29
Beads	Glass	2500	26	0.23
Coefficients for glass beads				
	HDPE	Nylon	Mild steel	Glass
Friction	0.29	0.53	0.42	0.4
Restitution	0.70	0.28	0.65	0.66

EDEM allowed the importation of geometries saved in either STEP (.stp) or IGES (.igs) format. The PRO/ENGINEER WildFire 5.0 (PTC, 2009) 3D design drawings of the tumbling mill were thus simplified, saved in the 'iges' format and imported into the software. The default properties for facet sag, length and minimum number were used, while the option to mesh the geometry as a single body was un-checked to preserve the individual material components of the mill.

Particles in EDEM were by default defined as spheres, and as such the glass beads used as the mill charge could be created directly. Figure 3.8 illustrated a snapshot of the particle definition stage. Here, each glass bead size from 2 to 8mm was created individually, after which its properties (mass, volume, moments of inertia) were calculated automatically based on the specified material parameters. The option to specify a contact radius for each particle size was left unchecked.

The Hertz-Mindlin (no slip) contact model, described in Section 2.2, was used to simulate interaction between colliding particles and to calculate energy losses. This was the default model in the software as recommended by the designers, and had been found in prior research to provide an accurate representation of the tumbling mill collision environment (Kulya, 2008. Djordjevic et al., 2006. Khanal and Morrison, 2009).

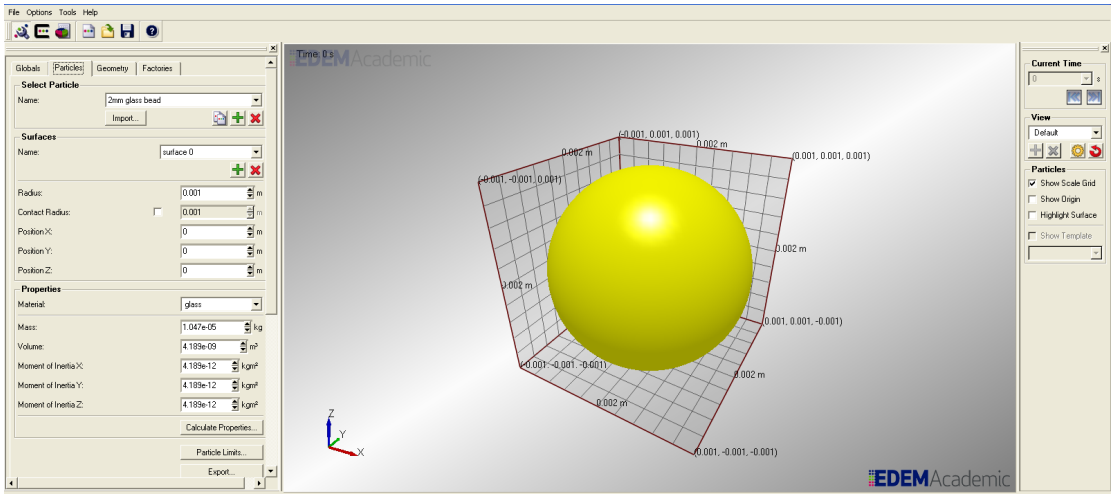

Figure 3.8: Screenshot of particle definition stage in EDEM

The number of particles in each size class (P_i) required was determined using Equation 3.5,

$$P_i = roundup\left(\frac{J \cdot (1-\varepsilon) \cdot V_m}{V_i \cdot 100}\right) \qquad \textbf{Equation 3.5}$$

where J is the fractional volumetric mill filling, ε the charge porosity and V_m and V_i are the mill and particle volumes respectively. As discussed in Section 3.1, the porosity of poured random packing of 0.375 was assumed for the charge body (Dullen, 1992).

The rounded up whole number of particles was multiplied by the calculated particle mass to obtain the total charge mass. This was verified against the experimental mass to ensure that the charge in DEM simulations was consistent with experiment. Table 3.3 and Table 3.4 showed the comparison of particle masses for mono-size and full size distributions for the DEM and PEPT experiments. The mass values between the two were consistently close, indicating that the charge body used for all PEPT experiments and DEM simulations were similar.

Table 3.3 : Comparison of experimental and calculated masses for mono size DEM simulations

Mono-size distribution		
Particle diameter (mm)	3	5
PEPT experimental mass (kg)	9.662	9.662
No. of DEM particles created	274,219	59,232
DEM Mass	9.691	9.690

Table 3.4: Comparison of experimental and calculated masses for full size distribution DEM simulations

Full size distribution							
Size (mm)	2	3	4	5	6	8	Total
PEPT expt. mass (kg)	1.34	1.90	1.98	1.81	1.56	1.08	9.670
No. of DEM particles	127,596	53,676	23,595	11,080	5,532	1,606	223,085
DEM Mass	1.336	1.897	1.977	1.813	1.564	1.076	9.663

The dynamics of individual components in the mill geometry were set according to the rotational speed of the mill in radians per second. This was to ensure that the mill revolved as a solid body about its axis to match the conditions of the experiment.

In addition to the imported mill geometry, a cylindrical volume was created inside the mill to act as a particle creation section. EDEM required a geometry section for its particle creation factories which determined where, when and how particles appeared into a simulation. A virtual cylinder, as displayed in Figure 3.9, was created to act as a creation section and was configured such that it did not interfere with the motion of particles.

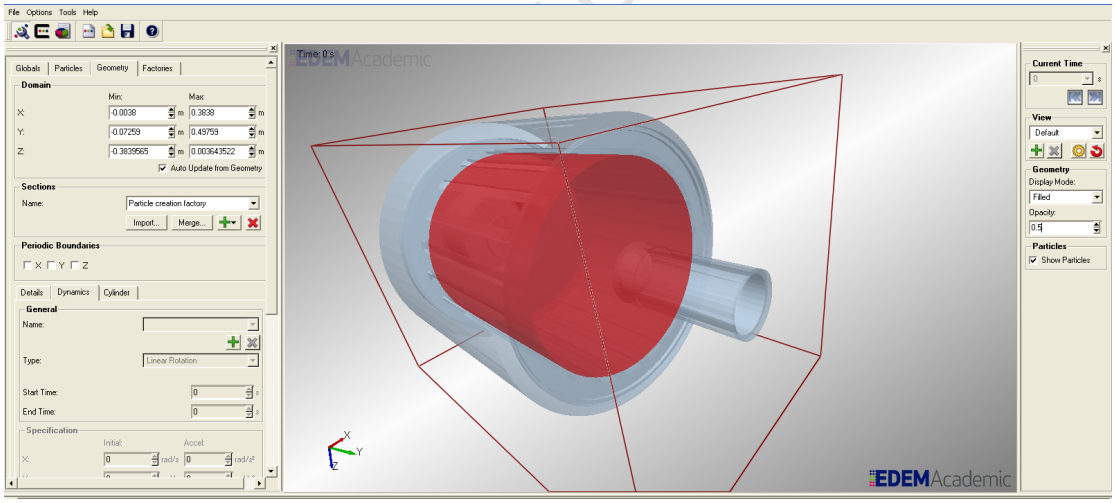

Figure 3.9: Screenshot of virtual geometry created in EDEM

A particle creation factory for each glass bead size would then be created depending on the requirements for the given simulation. For each factory, the number of particles to be created, creation rate, spatial position and material had to be specified. The dynamic particle creation option was selected as it was more efficient in promoting mixing and avoiding packing complications than the static method (Kulya, 2008). In every simulation conducted, the creation rate was set such that all particles would be placed in a random location inside

the creation domain within the first mill revolution. This was done in order to reduce the amount of time the mill would require to reach steady state.

The amount of time between successive iterations in the simulator, or the time step, was set prior to initiating the simulation. The Rayleigh time step is defined as the time taken for a shear wave to propagate through a solid particle (DEM Solutions, 2006). If the time step set in the simulation exceeded this value, incorrectly calculated particle contact forces could lead to abnormal particle physics. To ensure stability, every DEM simulation time step was therefore set to at least half the critical (or Rayleigh) time step (Malone and Xu, 2008).

CHAPTER 4

PEPT EXPERIMENTAL RESULTS

Overview
This chapter presents the results of the PEPT experiments carried out in this work. The charge location probability distribution, velocity, porosity and power draw are calculated from experimental data.

4.1 PEPT data reconstruction

The data recorded by the computer during PEPT experiments was produced in the form of text files which contained sequential coordinates of end points for the lines of response from the PEPT camera. As described in Section 2.3 of the literature review, the original locations of the radioactive tracer could be determined by triangulation of such lines. To this end, TrackC, an executable program developed in C++ by the Positron Imaging Centre (University of Birmingham) was used to reconstruct tracer locations from the raw data. Two input parameters were required for this software, termed N-*events* and f-*opt.* N-*events* represented the number of sequential lines of response utilized to perform the triangulation, while f-*opt* was the percentage of these lines that would be used, after discarding lines furthest away from the centroid, to calculate the tracer position. For this work, values of N-*events* and f-*opt* were kept at their default values of 200 and 15 respectively.

```
300Mill_5mm_31.25Load_60Speed

Separation=642

f(opt) :  0.150      Displacement parameters :    300,   400,  1500

Fixed slices:    200 events/slice,    1 locations/slice

      t        x          z          y         e

     12.0     387.0     429.3     445.3       2.7       0.0       0.00
30
     37.5     387.0     433.0     443.1       2.1       0.0       0.00
23
     59.9     386.2     436.9     442.2       2.0       0.0       0.00
24
     78.2     387.2     433.6     442.5       2.4       0.0       0.00
24
     96.5     388.3     441.1     441.6       1.8       0.0       0.00
24
```

Figure 4.1: Screenshot of the text file output from the TrackC software

The output of the triangulation algorithm was a text file which contained the Cartesian coordinates of the PEPT tracer for the duration of the experiment. A screenshot of the text output from the TrackC software is given in Figure 4.1. The 3-d [*x,y,z*] data points in millimetres along with the logged time *t* in miilliseconds were then imported into MATLAB (Mathworks, 2011), which was used to carry out the PEPT analysis in this study.

4.2 Determination of kinematic quantities from PEPT data

The coordinates extracted from the triangulation information could be expressed in parametric terms as positions *x, y* and *z* with respect to time *t*. For convenience, the origin is specified as the mill centre, with coordinates *x* (horizontal) and *y* (vertical) in the transverse plane, while *z* runs along the axial mill length with its zero at the inlet. Plots of the tracer particle's position along each axis (in m) against time (in min) could thus be plotted as given in Figures 4.1 to 4.3. These plots depicted the motion over the first ten minutes of the experiment for a 5mm mono-size particle tracked at 60% mill critical speed.

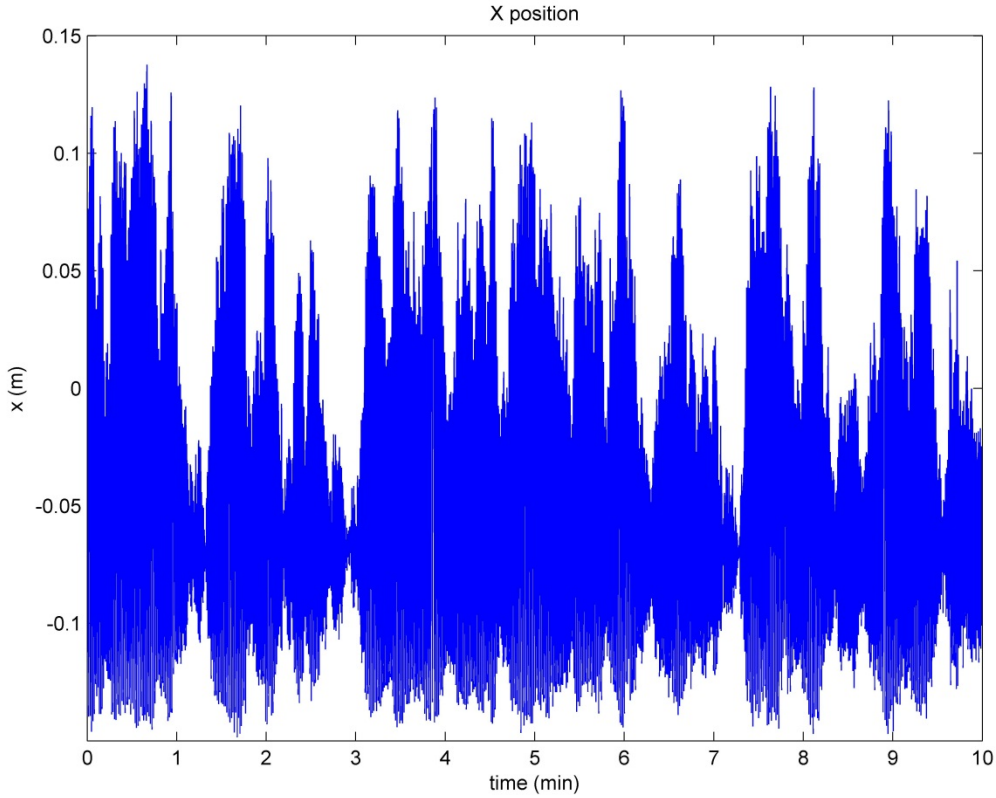

Figure 4.2: Plot of PEPT tracer's position along x-axis against time

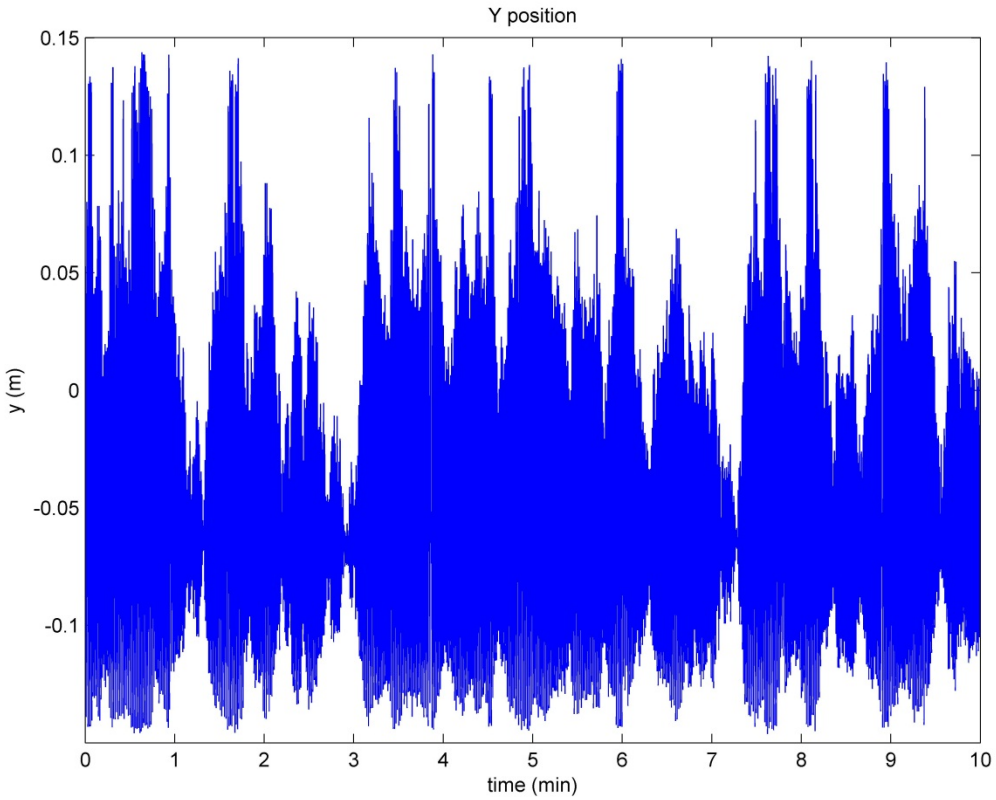

Figure 4.3: Plot of PEPT tracer's position along y-axis against time

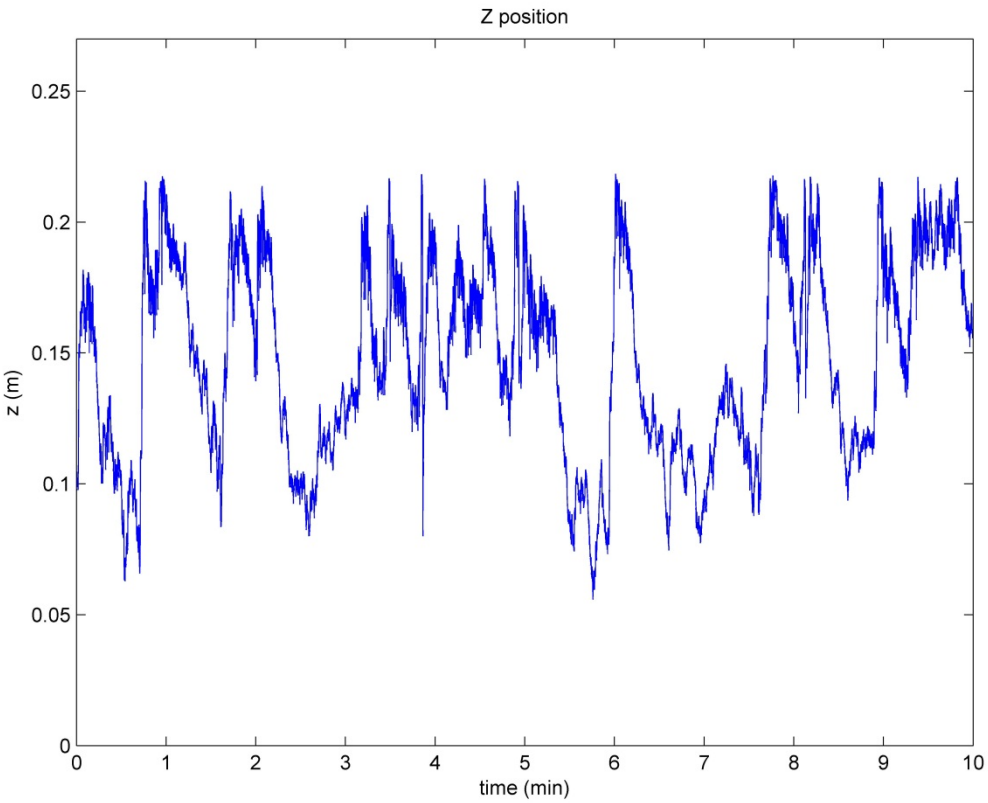

Figure 4.4: Plot of PEPT tracer's position along z-axis against time

It was observed that the particle's position followed an oscillating pattern with time. In the *x* and *y* planes, the amplitude represented the range of particle locations over the diametrical span of the 0.3m mill. For both these plots, Figure 4.2 and Figure 4.3, it was observed that although the particle trajectory covered virtually the entire span of the mill diameter, majority of the coordinates were found in positions lower than the mill centre. Relative frequency distributions of the tracer coordinates could be used to highlight this trend, as given in Figure 4.5. Here, the relative number of occurrences that coordinates fell into discrete intervals along the respective axes was given, from the mill shell (at -0.15) through the mill centre (at 0) to the other end of the mill (at 0.15). The peaks of these plots were the horizontal and vertical positions where the particle spent the greatest time, or the mode of the distributions. Further, the left-skewed form of the distribution meant that the mean particle position would similarly be located in the bulk region, which could be approximated as the centre of mass of the entire charge body for mono-size experiments (Bbosa et al., 2011). This meant that while the particle was lifted and rotated throughout the transverse area of the mill, the position where it spent the greatest time, and consequently the most probable particle location was in the bulk region.

As the mill was operated in batch mode, it was found that the position along the *z*-axis did not tend to any particular region. Plots of the axial motion of the particle such as Figure 4.4 showed that its location oscillated about the centre of the mill length (at 0.135) with relatively equal amounts of time spent at the inlet and discharge ends.

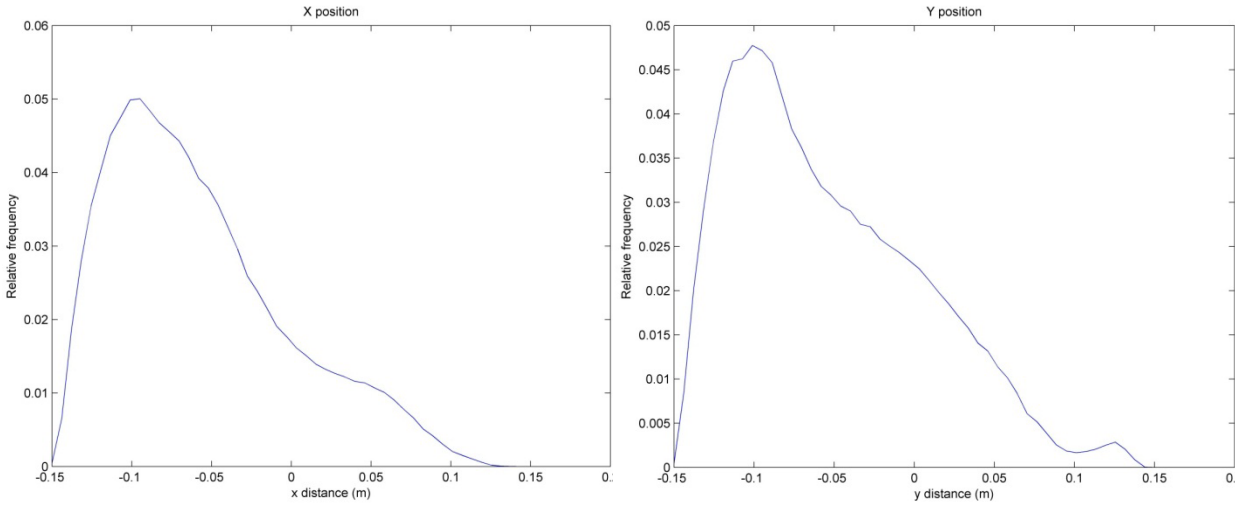

Figure 4.5: Plots of relative frequencies for particle positions along the *x* and *y* axes

Figure 4.6(a) illustrated a 2-d plot of the mill in the x-y transverse mill plane with all particle coordinates obtained for the 5mm glass bead tracer at 60% critical speed. In Figure 4.6(b) a

smoothed line with a three-point moving average to each pair of sequential points was fitted to obtain the particle trajectory. It was noted that, over the duration of the experiment, the single tracer depicted the typical motion of the full charge (Mellmann, 2001). The particle was observed to rise by the action of the rotating mill and lifters until a point of departure (shoulder) where it either cascaded along the charge free surface or cataracted in free flight into the toe region, before mixing into the bulk charge and reinitiating the repeating cycle (Powell and McBride, 2004).

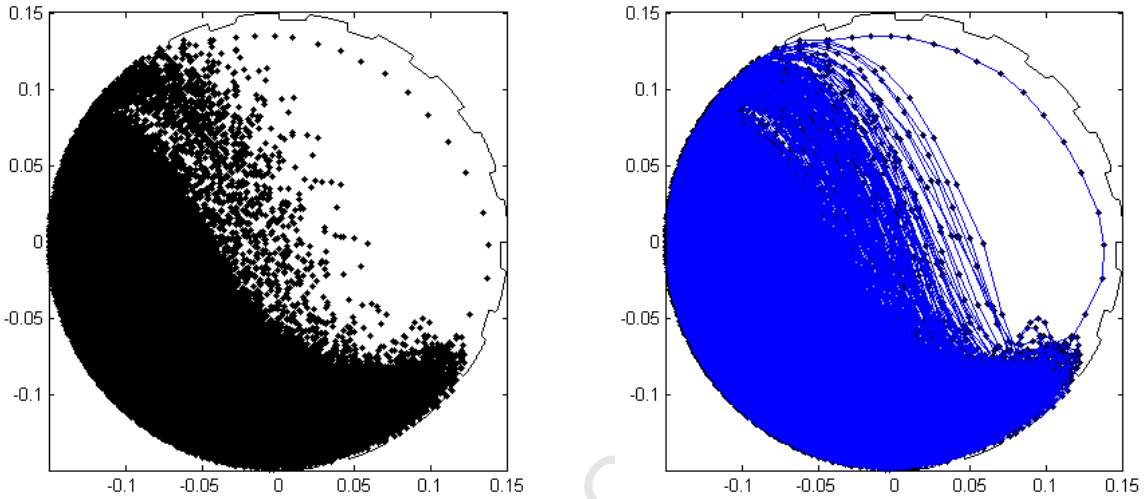

Figure 4.6: Plots of PEPT tracer coordinates and a fitted trajectory path for data obtained from the 5mm mono-size experiment at 60% mill critical speed

To eliminate effects introduced by inconsistencies in time between each data point, a shape preserving piecewise cubic Hermite interpolation polynomial was used to calculate points with even time intervals along the tracer path (Kahaner et al., 1989). The velocity and acceleration of the particle could then be calculated by taking first and second order derivatives of this function.

Time averaged spatial distributions of the tracer's motion in different regions of the transverse face were then obtained by discretizing the plane into a square grid with the origin at the mill centre. A grid with 50 x 50 cells was used such that the length of each grid square was close to the diameter of the tracer particle. This was important when calculating quantities such as packing fraction as it was assumed that if the tracer's coordinates fell into a particular cell, the entire particle volume was contained in the voxel defined by the square and mill length. As the mill was run in batch mode, particle data along the length of the mill was thus assumed to be axially symmetric.

Based on the ergodic hypothesis discussed in Section 2.3, the average quantities determined for the tracer over the one hour duration of each experiment were considered to be a representation of the charge behaviour of the tracked size class. Kinematic properties for PEPT in this work were calculated on this basis. The algorithms utilized to carry out this analysis are provided in Appendix A1.

Location probability distribution and velocity

Spatial distributions of location probability for each size class were determined by accumulating and normalizing the frequencies with which tracer coordinates fell within each voxel in the grid. For PEPT data, these distributions provided an indication of the relative time spent in each cell as time intervals between binned coordinates were consistent. As the PEPT experiments were conducted under steady state conditions, the location probability distributions of the single tracer particle could be interpreted as probability distributions for the entire charge body of the given size (Mangesana, 2011). Based on this assumption, each normalized grid was scaled by the charge mass in its size to obtain a mass distribution. Figure 4.7 (left) shows the location probability distributions that were obtained for 5mm mono-size tests.

The binning algorithm was also utilized to obtain distributions of the average absolute velocities at each grid location. These plots were given on the right hand side of Figure 4.7. Colour bars alongside each distribution indicated the value in a voxel, with the range of low to high quantities depicted using hues from blue to red respectively.

Charge descriptions that are routinely used to define charge motion behaviour (see Section 2.1) were evident from location probability and velocity plots, such as the head, departure shoulder, impact toe and bulk toe (Powell and McBride, 2004). From location probability distributions, the outline of the charge free surface could also be identified as a curved, bean like shape above which was a region of low probability marked by a blue hue. This curved charge profile separated the bulk charge from the material that was in free flight.

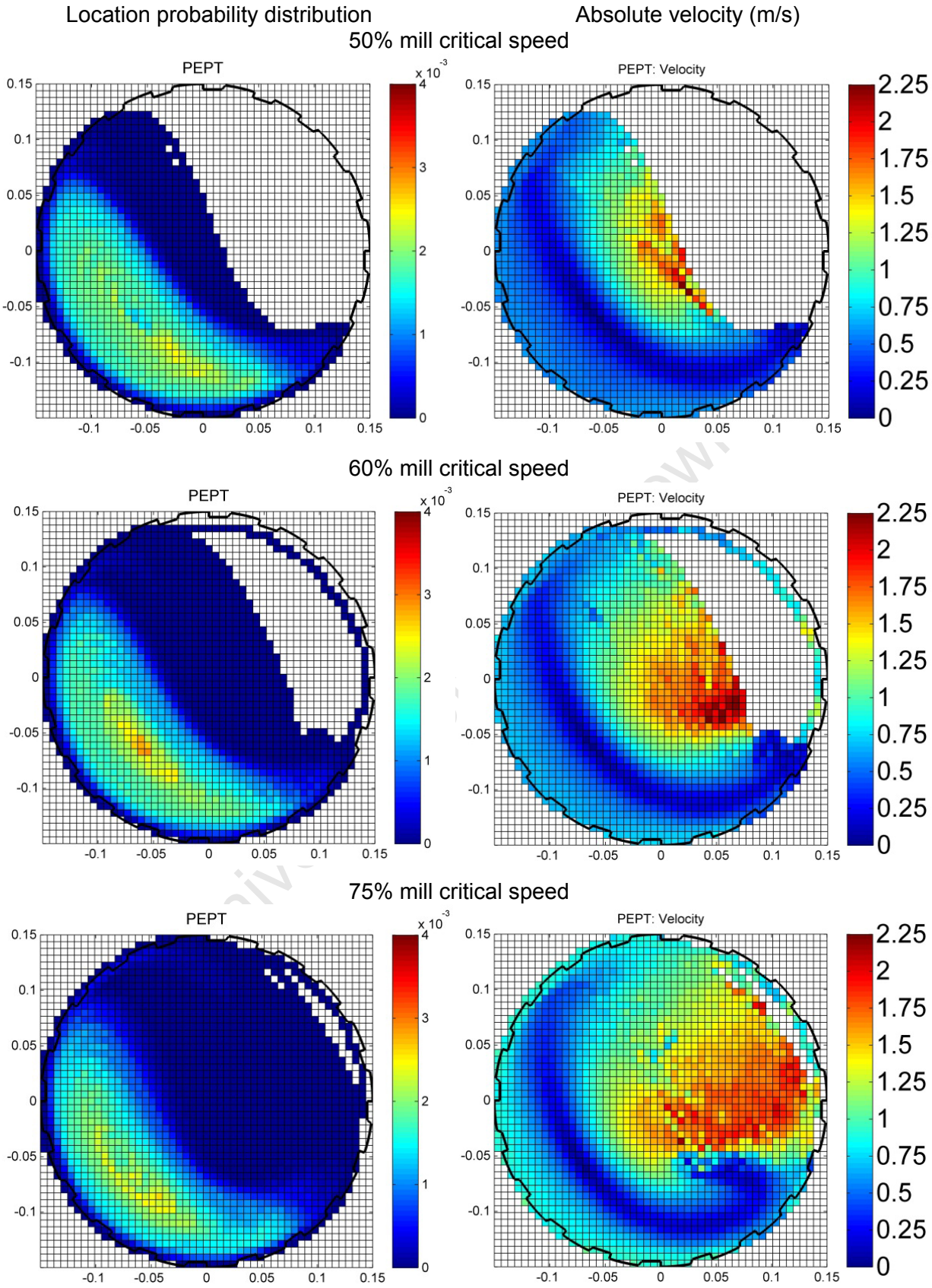

Figure 4.7: Spatial plots of location probability and absolute velocity for 5mm glass beads tracked with PEPT

In addition, Figure 4.7 highlighted a transition in the charge motion regime with mill speed. At 50% critical speed the charge largely consisted of cascading motion, while majority of the charge remained in the bulk mixing region. As the mill speed increased the bulk region began to thin out as more material was lifted by the mill. As a consequence, at 60% and 75% critical speeds, the charge particles were lifted by the mill such that more cataracting behaviour was observed. Such a charge pattern promoted charge mixing while encouraging particle impact, which was the typical operating regime for most industrial tumbling mill applications (Mellmann, 2001), which was the regime of interest for this work.

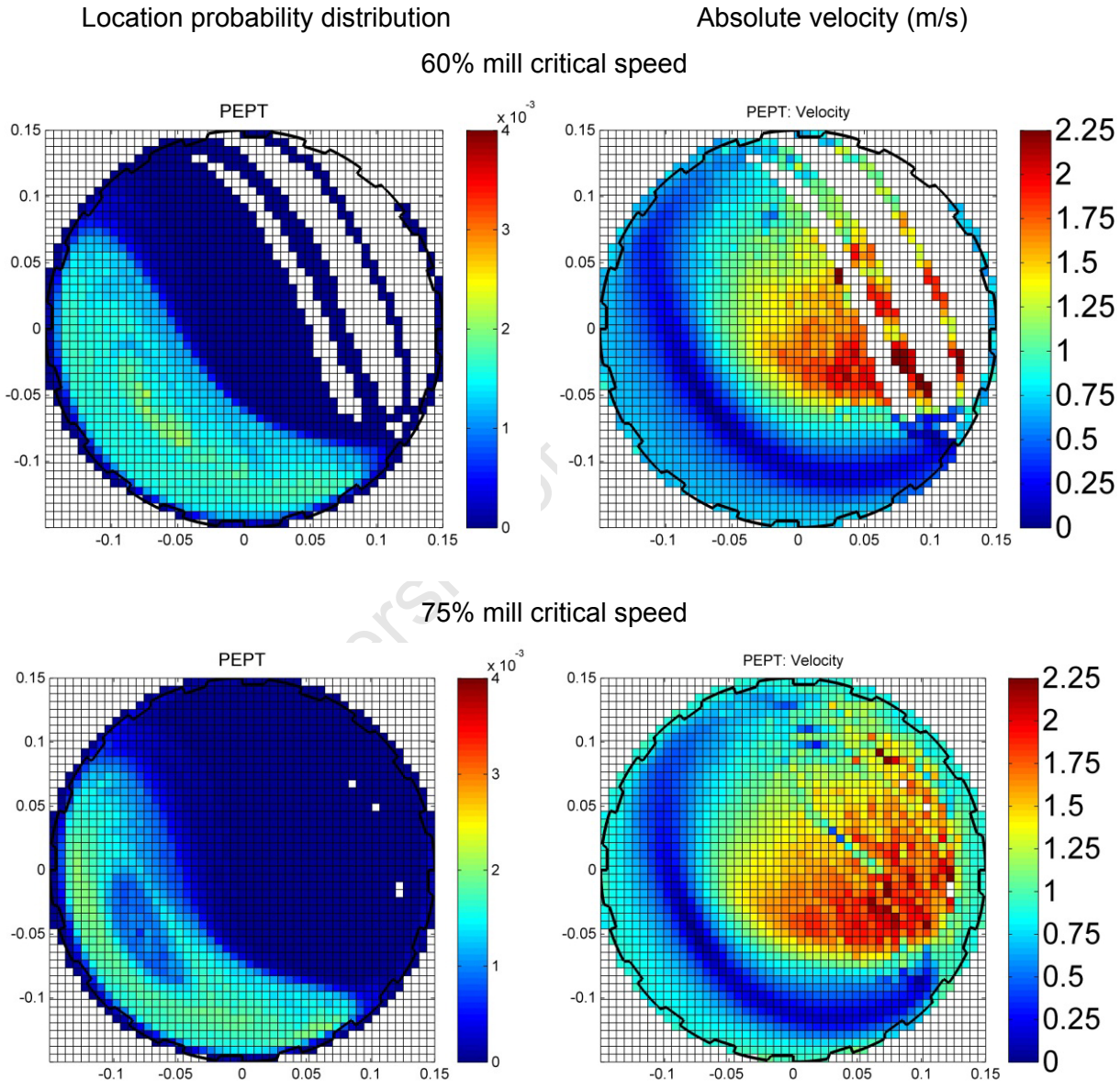

Figure 4.8: Spatial plots of location probability and absolute velocity for 3mm glass beads tracked with PEPT

Figure 4.8 depicted spatial distributions of location probability and absolute velocity for mono-size experiments with 3mm particles at 60% and 75% critical speed. It was noted from the corresponding plots in Figure 4.7 that the smaller 3mm charge cataracted more readily at both speeds than the larger 5mm charge. This was highlighted at 75% critical speed, where a low probability region was observed in the bulk region of the charge for 3mm particles, indicating that the smaller 3mm tracer cataracted a great deal more compared to the larger size.

To further investigate this trend, Figure 4.9 reproduced the spatial plots for mono-size tests in the form of relative frequency distributions along each transverse axis. These distributions indicated that the particle location probability followed a similar trend for both sizes, skewed to the rising end of the charge with a distinct peak, or mode.

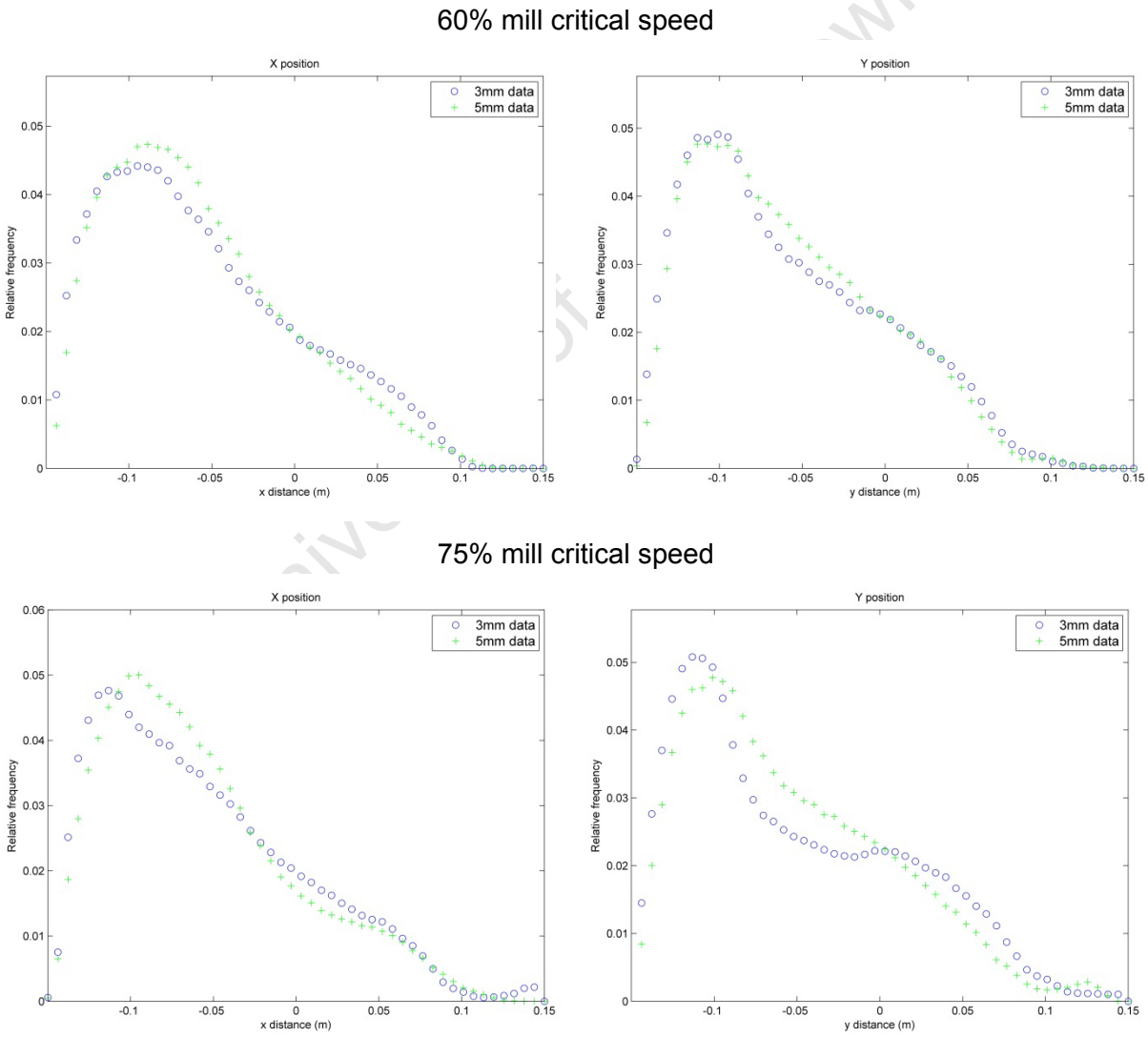

Figure 4.9: Comparison of relative frequency plots of *x* and *y* positions between 3mm and 5mm data

This mode represented the maximum probability, or the most likely position that the particle of either size would occupy along each axis of the mill. For the *x*-axis, it was noted that the mode of the 3mm tracer was closer to the mill periphery than the 5mm bead, with the difference becoming more apparent at the higher speed. This meant that the smaller sized particle tended to shift horizontally further toward the rising end of the mill with increasing speed. In the y direction, the 3mm distributions demonstrated a noticeable reduction in frequencies in the mid-region of the mill slightly below the mill centre relative to those of 5mm distributions, particularly for the higher speed. For the higher 75% critical speed, the smaller 3mm particles were observed to have higher frequencies above the centre of the mill. The information from the distributions in the *x* and *y* planes thus indicated that the smaller particle was more prone to cataracting at the compared speeds.

Based on the ergodic assumption, the overall distribution of granular particles in either size would similarly follow this behaviour. This meant that in the cascading and cataracting regime, smaller charge particles would be more prone to be lifted with the rising mill, and consequently cataracting more as observed. Time averaged velocity distributions could also be represented as vector field plots. In these, the length of each arrow represented the relative magnitude of the velocity in a voxel, while the average direction of motion was indicated by the arrowhead. Figure 4.10 provided vector field plots for 3mm and 5mm mono-size experiments at 75% mill critical speed. It was observed that the charge motion followed a pattern that distinctly highlighted turning points and regions of high and low velocity.

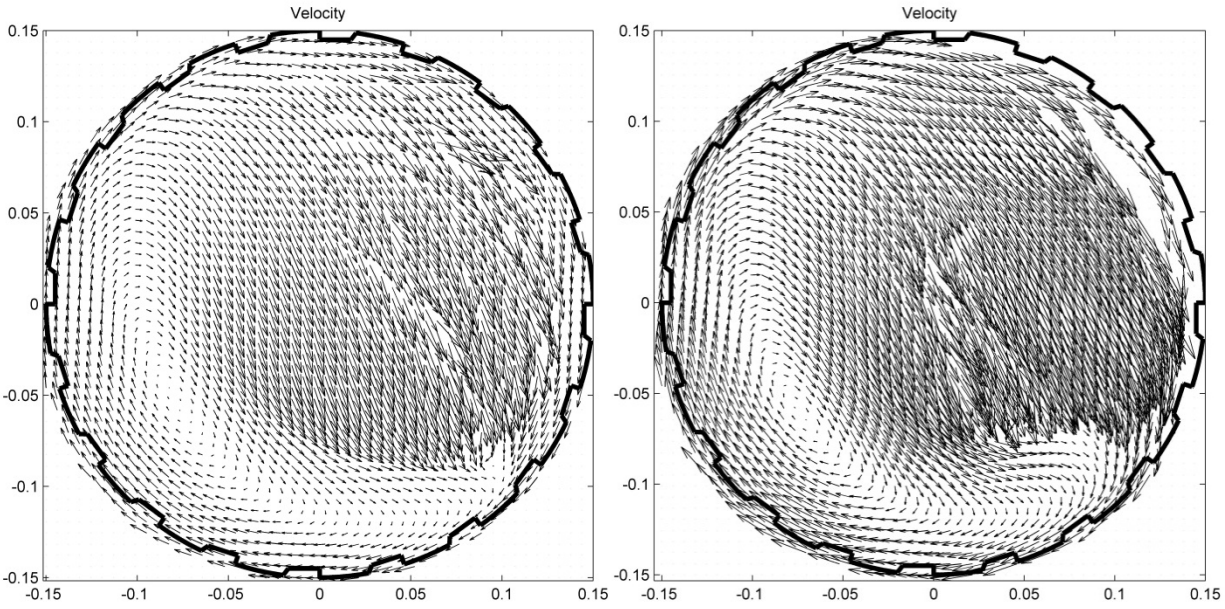

Figure 4.10: Plots of velocity fields at 75% critical speed for 3mm and 5mm glass beads respectively

The Centre of Circulation (CoC) is defined as the point about which all the charge in the mill revolves (Powell and Nurick, 1996). By inspection, the CoC of the charge could be pinpointed from velocity field plots such as Figure 4.10. The CoC locations for 3mm and 5mm data were determined and listed in Table 4.1. It was found that horizontal positions of the CoC for the smaller 3mm glass beads were closer to the mill shell, while vertical positions were higher than those of the 5mm charge at identical speeds. This supported the observed trend from the relative frequency distributions in Figure 4.9 which indicated that the smaller beads were lifted more readily at similar speeds.

Table 4.1: Comparison of CoC coordinates for 3mm and 5mm mono size tests

	CoC coordinates (*x*,*y*)	
Particle size (mm)	60 % mill crit.	75 % mill crit.
3	(-0.075, -0.059)	(-0.085, -0.044)
5	(-0.067, -0.062)	(-0.080, -0.055)

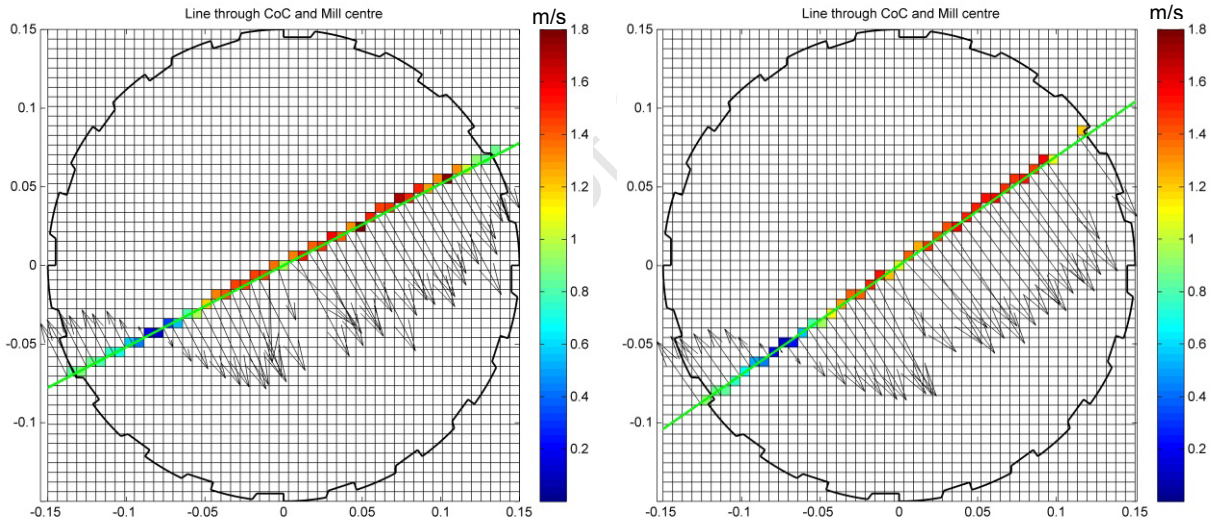

Figure 4.11: Plot of radial lines through the Centre of Circulation for the 3mm and 5mm mono-size experiments at 75% critical speed

An analysis routine was developed to examine a profile of the tangential velocity along a diametric line through the CoC, following the methodology applied by Mangesana (Mangesana, 2011). This line through the CoC was chosen for this profile as it represented a unique location in the charge specific to the particular operating condition. Figure 4.11 shows the tangential velocity profile through the CoC for 3mm and 5mm mono-size experiments at 75% critical speed. The average tangential velocities in the voxels (in m/s) that the radial line

passed through were indicated by the colour bars alongside, while their magnitude and direction were represented by the vector arrows.

Considering this profile from left to right, the tangential velocity followed a rising motion which decreased to zero and then increased in the descending direction. In the rising direction, the tangential velocity was at its highest at the mill periphery. As described by Yamane et al. (Yamane et al., 1998), in this region the relative velocity differences of rising charge particles created slip effects between successive layers of charge. This led to decreasing charge tangential velocities along the diametric line until a value of zero was reached at the CoC, where the sliding velocity was equal to that of the mill. Beyond this point, the charge tangential velocity progressively increased in the descending direction, where the particles in free fall above the charge free surface cataracted at the highest tangential velocities.

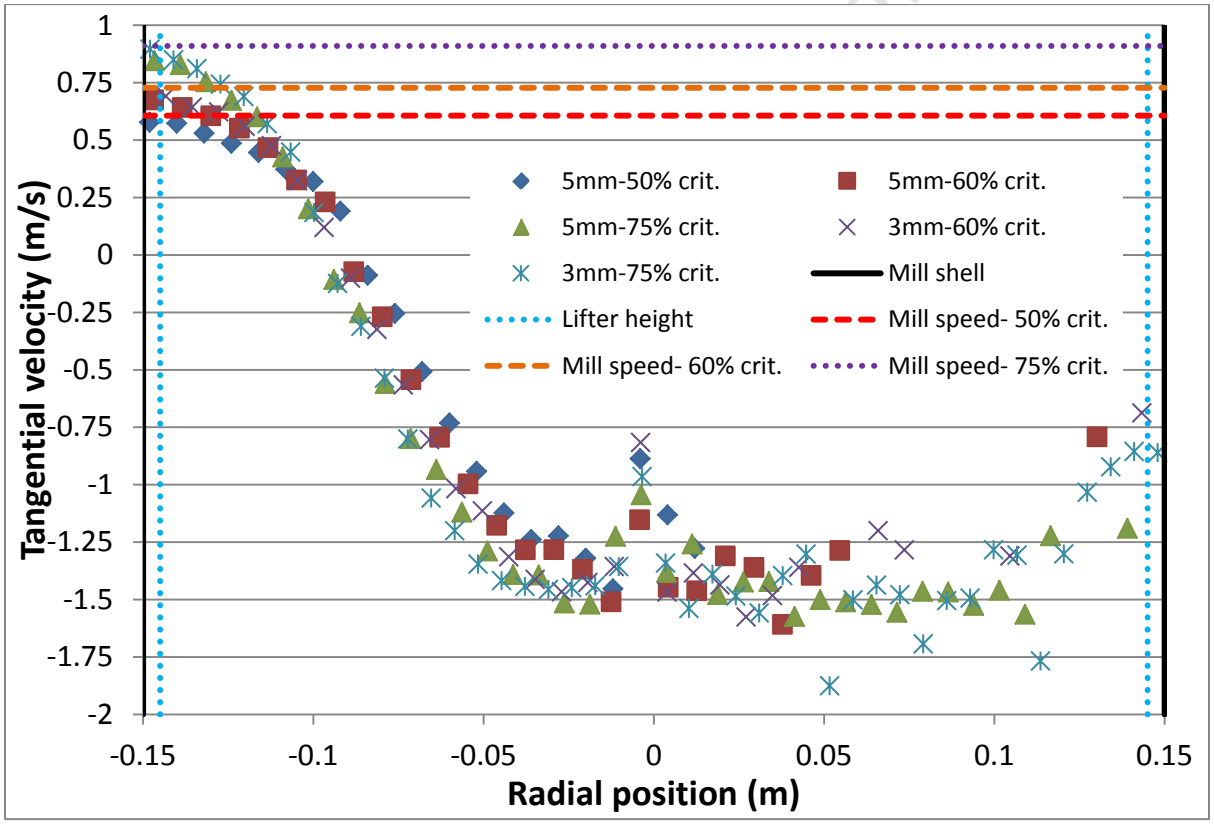

Figure 4.12: Graphical plot of PEPT tangential velocities along diametrical lines through the CoC for 3mm and 5mm mono-size experiments

The tangential velocity profile along this line could also be represented in graphical form as given in Figure 4.12. Similar trends were observed for all mono-size experiments. It was found that the tangential velocity of the charge at the mill shell was approximately equal to that of the mill. The velocity then decreased to the zero value at the CoC, and into the

opposite direction of flow beyond the charge free surface and into the cataracting region in which the velocity values were highest.

In the work by Govender et al. (Govender et al., 2011), it was shown that the tangential velocity V_T at position *r* along the line, for a fixed angle of repose θ, followed a function of the form given in Equation 4.1,

$$V_T(r,\theta) = a_1 \cdot \sin(b_1 \cdot r + c_1) + a_2 \cdot \sin(b_2 \cdot r + c_2) \qquad \textbf{Equation 4.1}$$

In this model, a_n, b_n and c_n, (with n=1, 2) were fitting parameters used to describe the motion of the charge. Figure 4.13 provided an example of the function fitted to the 5mm mono-size PEPT data at 75% critical speed. It was found that the equation showed good agreement with the data, as demonstrated by the list of parameters and their R^2 values in Table 4.2. The differences between the fitted function and the data in the cascading and cataracting region above the free surface were attributed to the inconsistent trends in the tangential velocity in these regions.

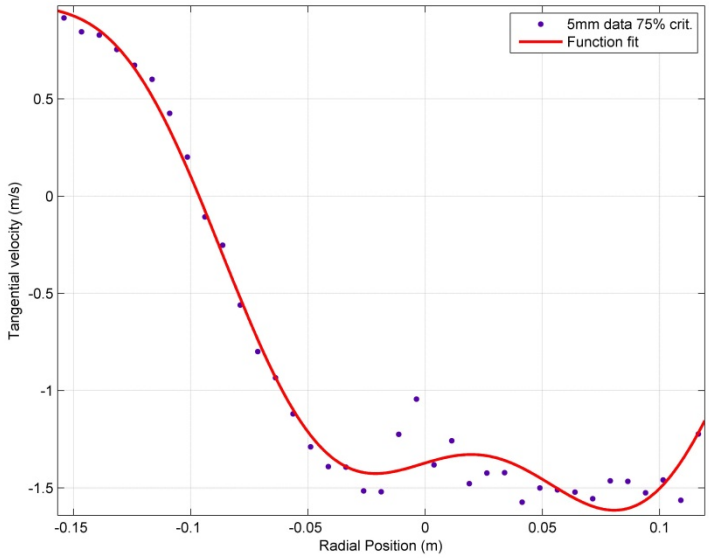

Figure 4.13: Tangential velocity function fitted to 5mm charge data at 75% mill speed

Table 4.2: List of fitted parameters for tangential velocity function to PEPT data

Size (mm)	% Mill crit.	a_1	b_1	c_1	a_2	b_2	c_2	R^2
3	60	1.498	14.8	-1.667	0.22	62.37	1.571	0.988
3	75	1.667	11	-1.994	0.294	39.97	0.285	0.966
5	50	0.254	57.15	0.818	1.49	11.9	-1.993	0.985
5	60	1.568	11.63	-1.971	0.227	47.83	0.268	0.988
5	75	1.63	11.29	-1.972	0.286	42.31	0.466	0.986

The procedure for obtaining location probability distributions was applied to Full size distribution experiments. These distributions, as given in Figure 4.14, reflected a similar trend that the smaller particles dominated the cascading and cataracting region while the larger sized largely remained in the bulk region, even at the higher speed. This result followed the evidence of radial segregation put forward in the work by Cleary et al. (Cleary et al., 1998), and similarly Powell and Nurick (Powell and Nurick, 1996c), who observed that under the cascading and cataracting regime smaller size particles tended to shift further away from the mill centre while larger particles dominated the zone about the mill centre.

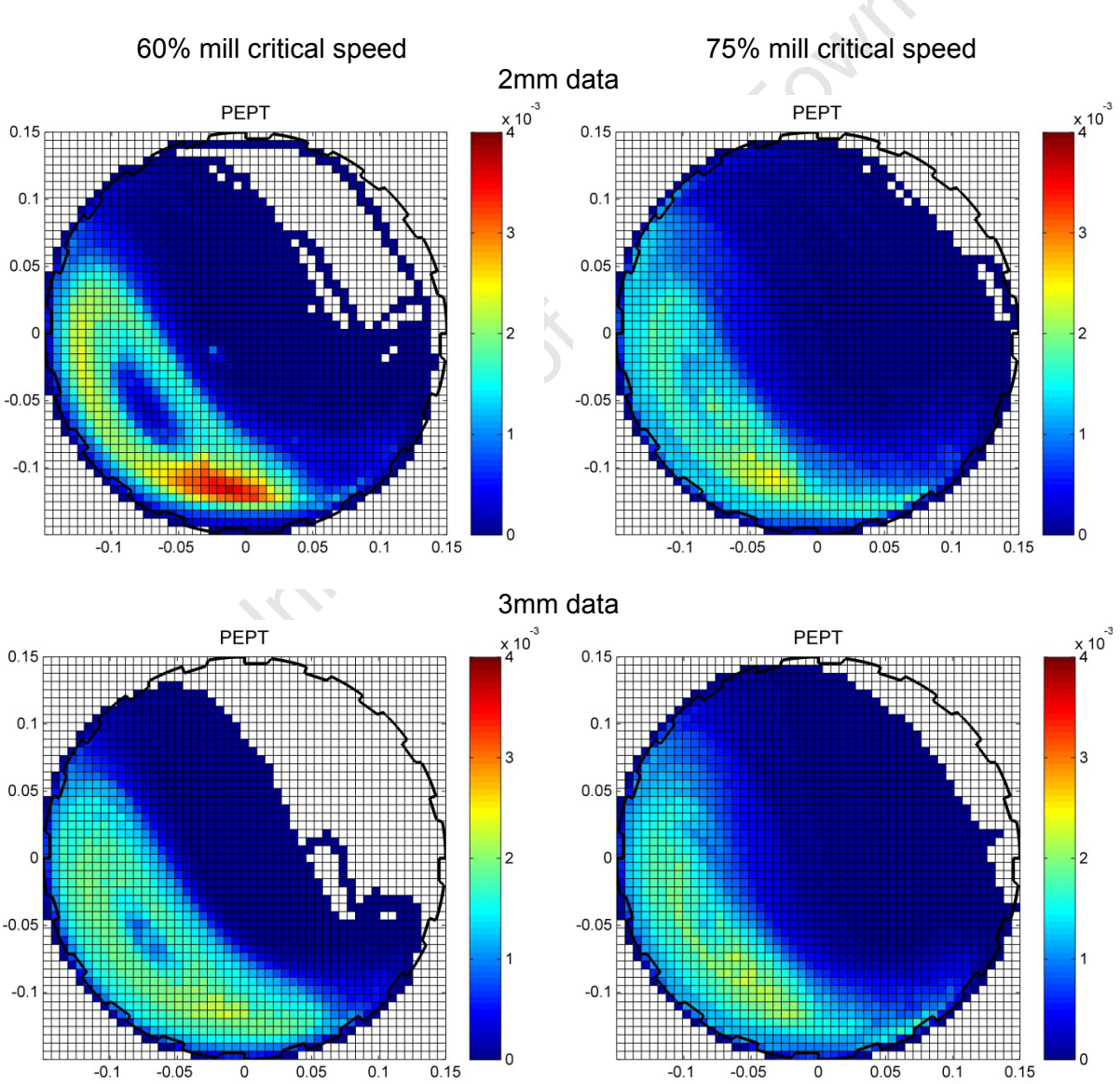

4mm data

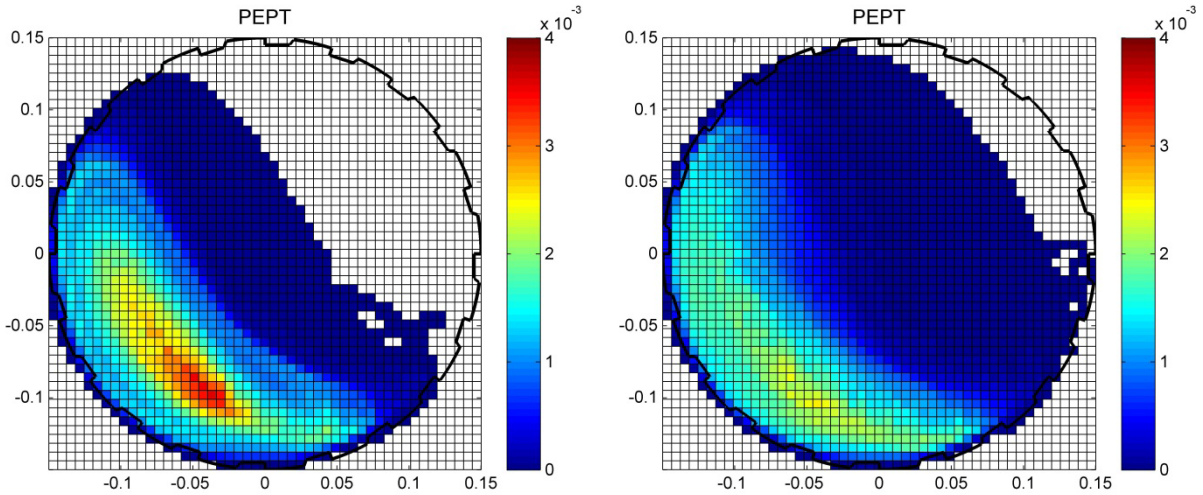

5mm data

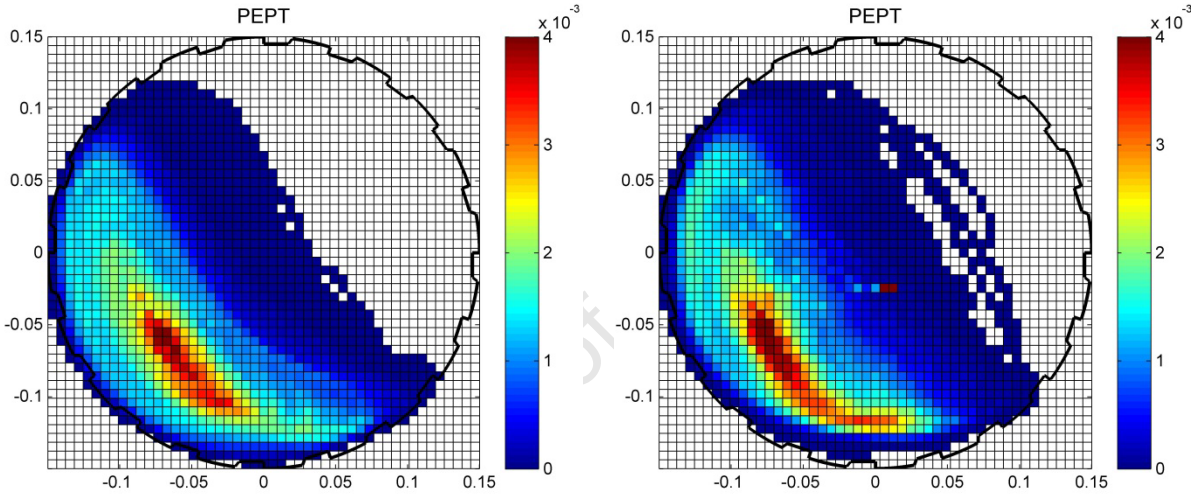

6mm data

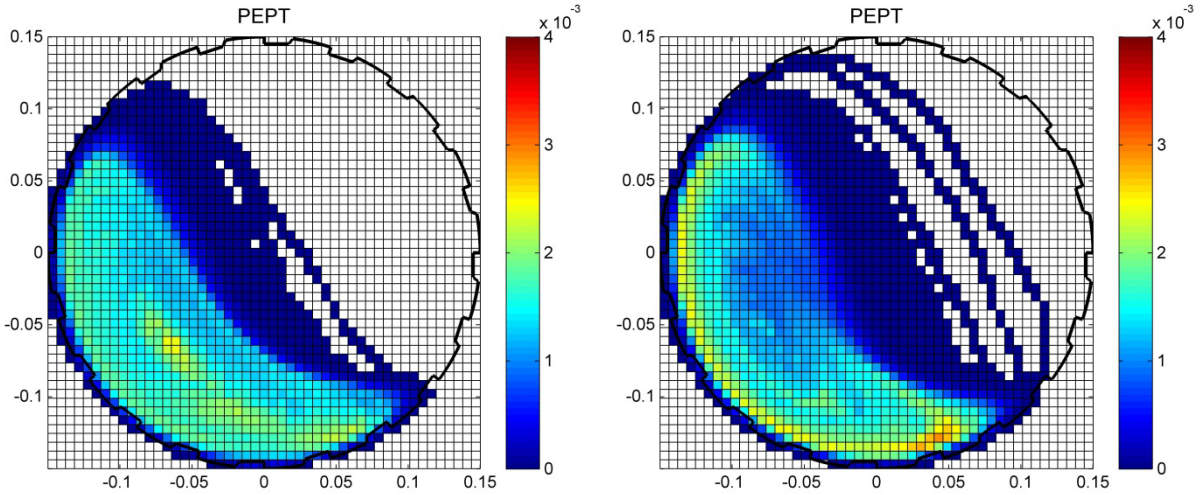

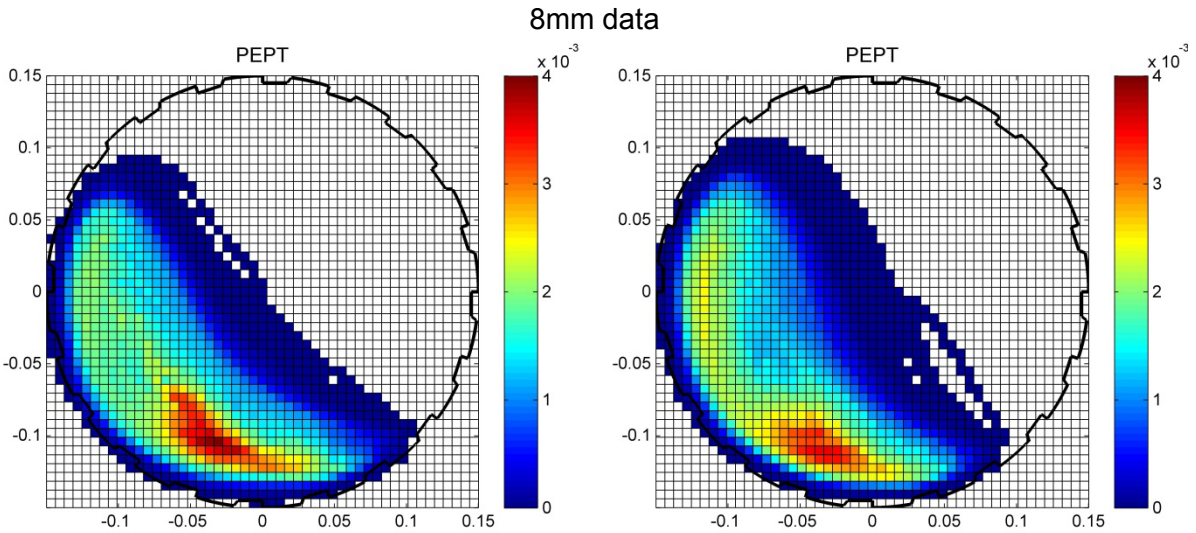

Figure 4.14: Spatial location probability distributions for Full size distribution experiments

Packing fraction/Porosity

The packing fraction was determined according to the methodology prescribed by Sichalwe et al., (Sichalwe et. al., 2011). The frequency of particle locations in each voxel was multiplied by the particle volume, which was then divided by the voxel volume. The result was the packing fraction in the voxel, and thus the porosity in the location was the difference between this value and unity. This procedure to determine charge porosity only applied to monosize PEPT experiments as the relative frequencies of the single tracer represented the behaviour of the entire charge. Figure 4.15 provides an example of a spatial plot of porosity for the mono-size PEPT experiment at 50% mill critical speed.

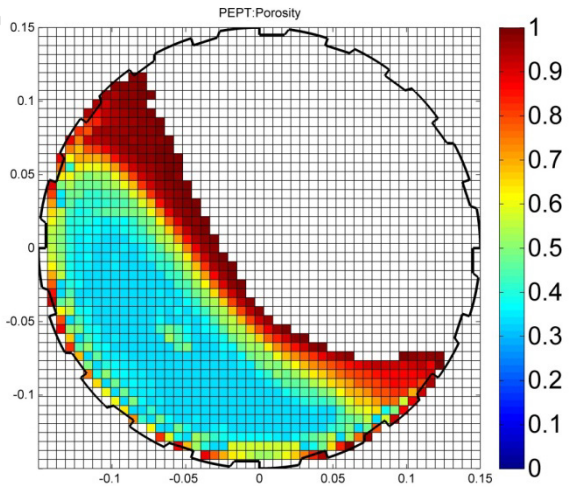

Figure 4.15: Porosity distribution for 5mm mono-size tests at 50% crit. speed

The colour bar alongside portrayed that blue hues were voxels of low porosity (high packing fraction) while red hues were voxels of high porosity (low packing fraction). This plot indicated that the charge was most densely packed in the bulk region, with porosities increasing in distinct bands until the free surface, whose profile could be identified by the red hue above the charge. Along the mill periphery, the tracer particle could only occupy the spaces between the mill lifters. As the mill rotated, the volumes covered by the lifters occluded the tracer from occupying the regions in the mill periphery for significant periods of time relative to other regions. Due to the relatively low frequencies of tracer coordinates in this region, porosity values were found to be relatively high along the outer mill periphery. To compensate for this, porosity values in these regions were determined according to a reduced volume which accounted for the number and geometry of the lifters. Nevertheless, the nature of the PEPT data was such that the reduced residence times, and consequently the frequencies of tracer counts in these regions generated artificially low porosity values along the mill shell. This was a limitation of the PEPT technique that was similarly encountered in the porosity distributions generated in the work by Sichalwe et al. (Sichalwe et al., 2011) and Govender et al. (Govender et al., 2012).

Porosity distributions for other mono-size experiments were displayed in Figure 4.16. In these plots, particularly at the higher speed it was found that that the smaller 3mm charge had a lower porosity (higher packing) in the bulk region. As more material was located against the outer perimeter of the mill, the smaller size beads tended to get lifted higher and appeared to cataract more freely than the larger charge. This was consistent with the trend noted from location probability distributions in Figure 4.7 and Figure 4.8.

It was observed that porosity values, particularly in the cascading region of the charge, increased with mill speed. This was to be expected as at higher speeds centrifugal forces became more dominant, leading to more cataracting behaviour. As a consequence, less material was cascading, resulting in higher voidage in this region. This was particularly evident for the smaller 3mm charge material which depicted that the porosity in the cascading region was markedly lower at 75% critical speed.

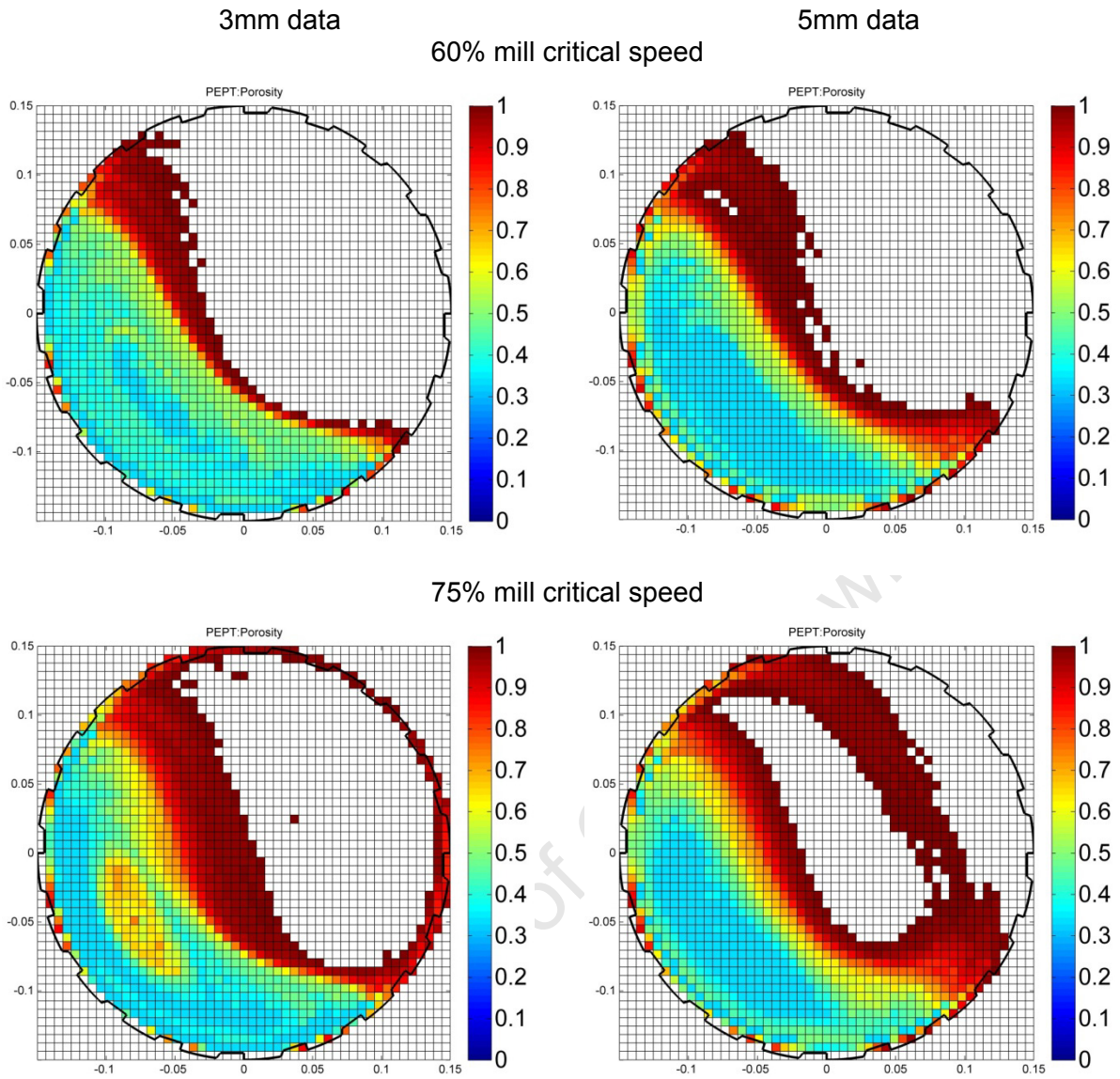

Figure 4.16: Spatial distributions of Porosity for mono-size experiments

These results were in agreement with prior work which demonstrated that the porosity in tumbling mills was not uniform, especially for the operating speed range for most industrial applications (Sichalwe et al., 2011. Yang et al., 2008). While this would primarily affect the material transport, the porosity was also important to the power draw as the charge packing distribution would affect the torque on the drive shaft.

Power draw

As described in the experimental methodology (see Section 3.2), the actual power drawn by the mill was measured for all experiments using a torque transducer attached to the drive shaft. Several methods could be investigated to determine the charge power draw from PEPT data for comparison against measured values (Bbosa et al., 2011. Kallon et al., 2011).

A methodology was developed for this thesis to calculate power draw from spatial location probability and velocity data from PEPT. For this approach, the charge distribution was simplified to be a spatial distribution of granular material of varying mass fractions in each region. The spatial charge location probability distributions of each size were scaled by the mass present in that size to determine the mass contribution of each voxel. Spatial distributions of the average angular velocity in each voxel were also determined. The mass distribution and average angular velocity distribution were then used to calculate the mill power draw as a sum of the products of the torque and angular velocity contributions of every region of the mill about the centre. The power draw, P_{PEPT}, by this means was derived to be given by Equation 4.2.

$$P_{PEPT} = \sum_{i=1}^{2500} M_i \cdot g \cdot x_i \cdot \overline{\omega_i} \qquad \textbf{Equation 4.2}$$

In Equation 4.2, M_i is the mass in each voxel as determined by the particle location probability in the voxel *i* multiplied by the charge mass in the given size. The acceleration due to gravity is denoted by *g* while the distance from the mill centre to the voxel is x_i. $\overline{\omega_i}$ is the average angular velocity in the voxel.

Figure 4.17 shows a schematic of the described approach to calculate the power contribution of each voxel from mass distribution and angular velocity data. In this diagram it is shown that while *R* is the radial distance to the voxel, the lever arm length used to determine the torque can be simplified to give the horizontal ordinate distance *x* from the mill centre.

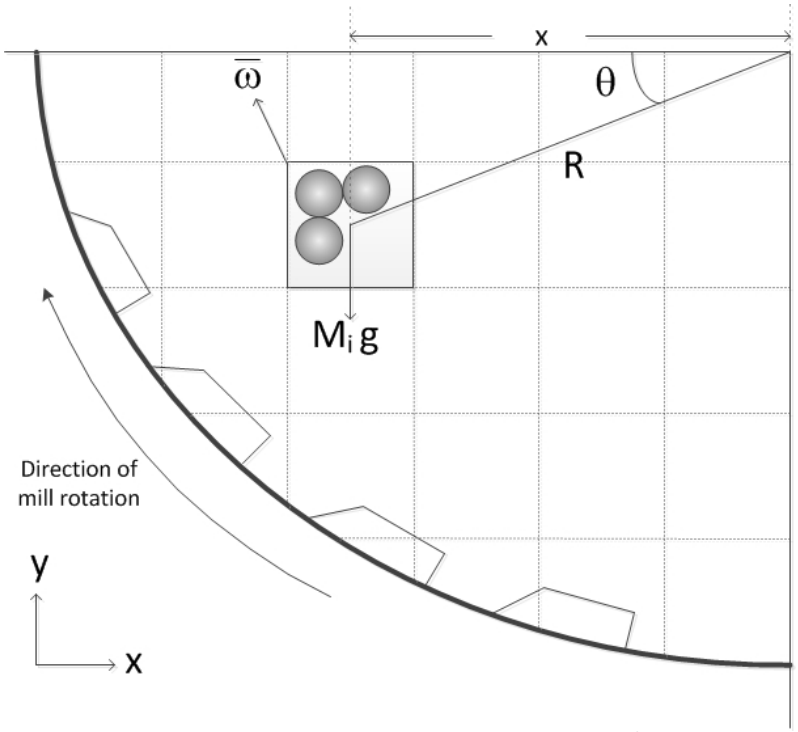

Figure 4.17: Schematic of approach taken to determine mill power using spatial location probability and average angular velocity distributions

Bar graphs in Figure 4.18 and Figure 4.19 provide values of the measured power draw (P_{MEAS}) for mono-size tests, as well as the calculated error. The power draw for the smaller sized 3mm particles was found to be higher at similar speeds than the 5mm charge. This meant that for the same mill speed, with an identical volumetric filling, the torque generated about the drive shaft by the smaller size particles was higher.

In these bar graphs, the measured power was compared to that calculated from PEPT (P_{PEPT}). Values determined from PEPT were consistently found to be within agreement with measurement. Because the PEPT power draw was directly calculated from particle location probability and velocity data, this meant that this information could be used to investigate differences in charge motion behaviour that influenced the mill power.

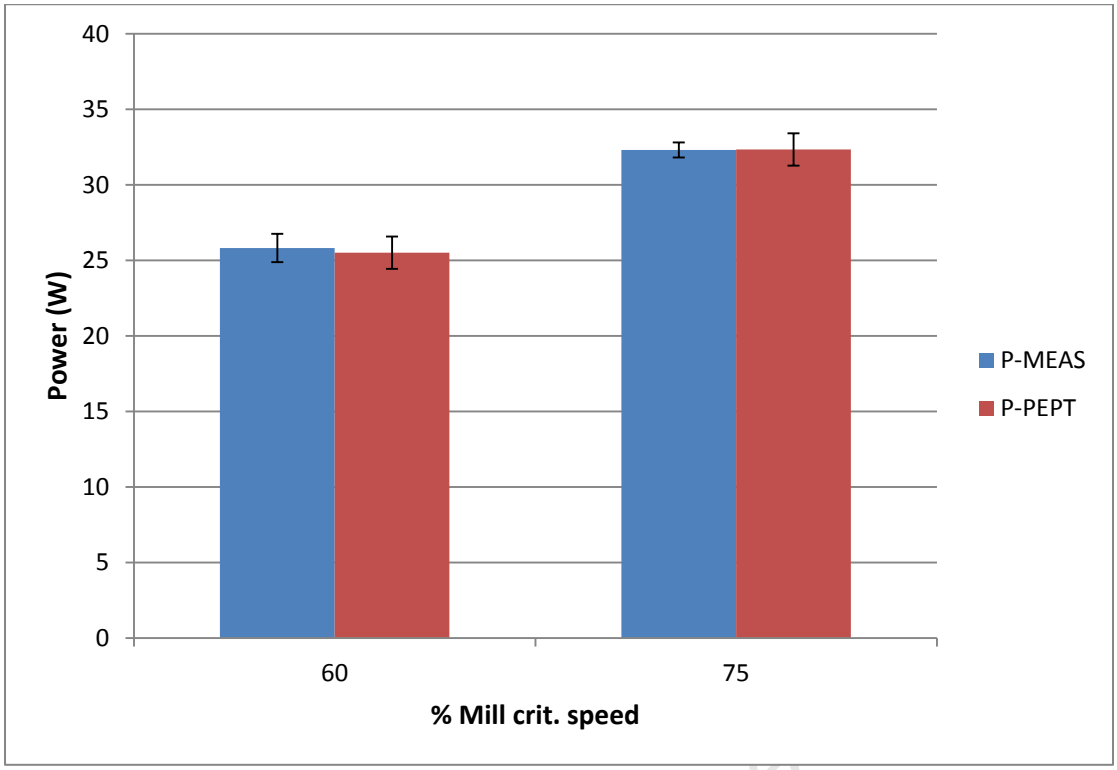

Figure 4.18: Comparison between measured power draw and calculated power draw from PEPT (3mm charge)

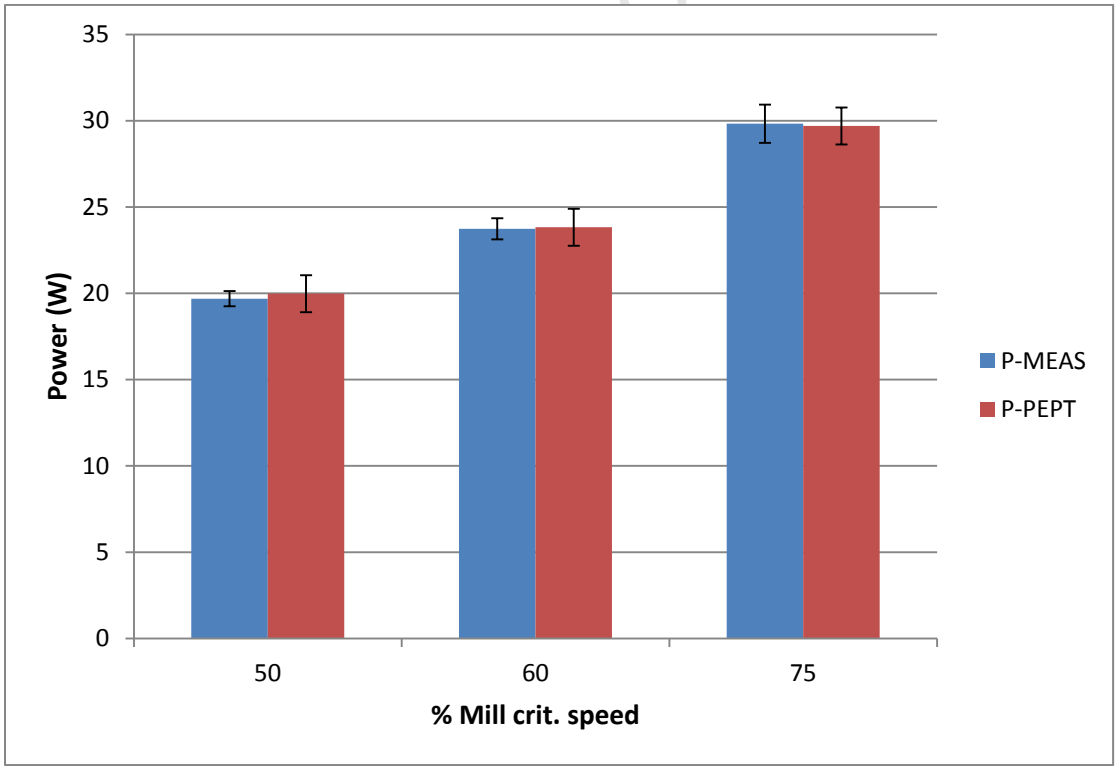

Figure 4.19: Comparison between measured power draw and calculated power draw from PEPT (5mm charge)

$$\Delta P_{PEPT} = \sqrt{\sum_{i=1}^{2500} \sqrt{\left(\frac{\Delta x_i}{x_i}\right)^2 + \left(\frac{\Delta \overline{\omega_i}}{\overline{\omega_i}}\right)^2}^2}$$

Equation 4.3

The error from the PEPT power draw approach was determined using Equation 4.3. This error was found to be consistent as the spatial error in the calculation of the horizontal voxel location from the centre was a much higher source of uncertainty than that of average angular velocity. As the calculated power draw from tracking a single particle was consistently within agreement with that of the overall charge determined by torque measurement, the methodology followed for PEPT experiments represented an ergodic system.

From the binning method utilized, spatial distributions such as Figure 4.20 could be plotted to examine significant areas that contributed to the charge power draw. Because the voxel values were calculated using the mechanical energy per unit time of the particles, these plots represented the power required to cause the particular charge motion generated under the given operating conditions, as opposed to the areas where it was dissipated in particle contacts.

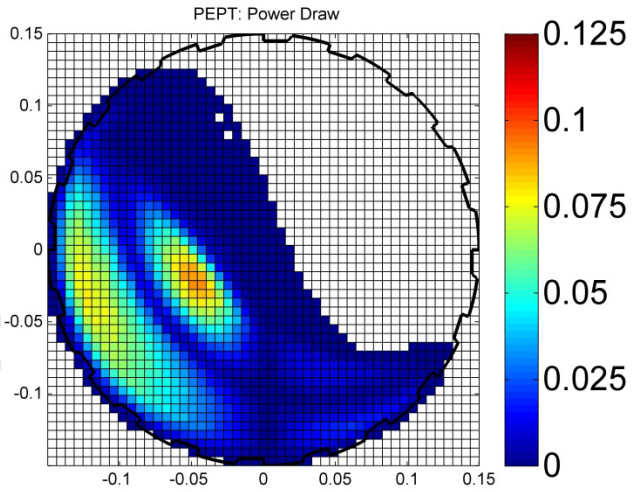

Figure 4.20: Spatial power draw distribution for 5mm mono-size test at 50% crit. speed

A consistent trend was evident for all spatial power draw distributions such as Figure 4.20 and Figure 4.21. The plots indicated that the highest contribution to the mill power draw was the bulk charge, with negligible power drawn by material above the free surface. This was consistent with power draw models such as those proposed by Hogg and Fuerstenau (Hogg and Fuerstenau, 1972), Austin (Austin, 1990) and Moys (Moys, 1990).

Equation 4.2 utilized the principle of a lever arm rule to calculate the mill torque, similar to the approach taken by Arbiter and Harris (Arbiter and Harris, 1985). While Arbiter and Harris' equation simplified the charge body such that the entire mass was treated as a continuum, this power draw calculation from PEPT considered the charge as a distribution of varying mass in different regions. This approach also differed in that the angular velocity which multiplied the torque was the average of that of the particles in each region, as opposed to the angular velocity of the mill. This method was thus a determination of the mechanical energy per unit time of the particles in each voxel caused by the rotation of the mill.

Morell's model (Morell, 1992) similarly determined mill power on the basis of mechanical energy by integrating the lever arm contributions in different regions. This model simplified the charge motion by considering the rising charge as an annular ring with a varying shoulder and toe position. According to Morell's model, only the rising charge of the bulk mass contributed to the mill power draw.

The spatial power draw distributions from the PEPT power draw methodology (Figures 4.20 and 4.21) indicated there were two zones that significantly contributed to the power draw. The first was the rising en masse region while the other was the cascading region of the bulk body. These two regions were separated by a band of low power. The approach thus differed from those such as Morell and Moys in that the effective charge which contributed to the power draw included the cascading charge mass. This was in agreement with prior work by Kasozi and Madala (Kasozi and Madala, 2008), which found that determining the mill power draw as a sum of the mechanical energy per unit time included the cascading charge.

The first zone of high power, in the rising bulk region, was a consequence of the lifting action of the mill and lifters. In this region, power was expended by the mill in lifting the granular packed bed of particles, causing charge in this region to have sufficient motion to overcome the effects of gravity and slip. These effects began to dominate inward from the mill periphery until the region of low power demarcated by the blue hue. This region demarcated the equilibrium surface (Powell and McBride, 2004), at which the slip velocity was equal to the rising velocity, constituting a turning point at which the charge transitioned from rising to descending motion. This was a zero velocity region that drew negligible power as observed from the distribution.

The second zone that significantly contributed to the mill power draw was located in the cascading bulk charge. Here, as the charge was descending, this represented the kinetic

energy per unit time of the descending mass of particles, which was concentrated in the cascading region of the mill for lower speeds as the bulk of the charge did not cataract.

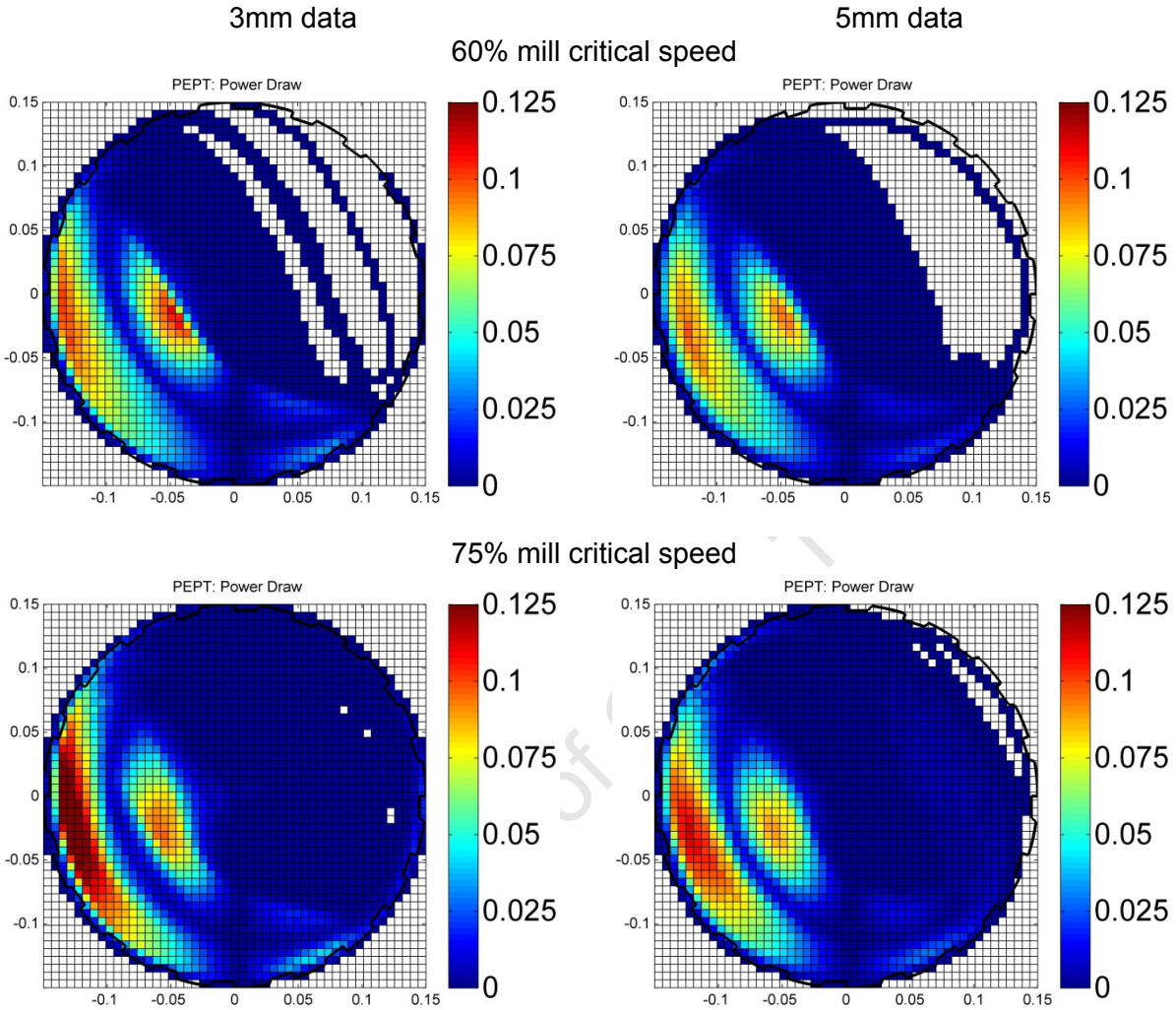

Figure 4.21: Spatial plots of power draw for mono-size PEPT experiments at 60% and 75% mill critical speed

Figure 4.21 demonstrated that with increase in mill speed, the power draw in the rising region increased. With more material cataracting at the higher speeds the amount of power drawn by the cascading region decreased. This highlighted that the noted increase in power draw with mill speed was primarily due to more energy being consumed by the mill in lifting the charge as mill speed increased. This was consistent with charge motion models such as Morell's (Morell, 1992) for which the shoulder position increased with speed to reflect more material being lifted, resulting in higher power draw.

Differences in power draw between particle sizes could also be examined on the basis of spatial power draw plots such as Figure 4.21. Plots of the average absolute velocity

distributions (Figure 4.7 and Figure 4.8) had indicated that both sizes had similar values in the rising and cascading regions that contributed most significantly to the power draw. The main contributing factor to differences in power between the two sizes was thus the mass distribution, or the charge packing density in each region calculated from the location probability distributions. It was demonstrated that the CoC of the 3mm charge was higher and radially further away from the mill centre than the 5mm charge (Table 4.1). From porosity distributions (Figure 4.16), it was further observed that the smaller charge had a lower porosity in the rising bulk region due to their higher packing density generated along the internal mill periphery. This was supported by the work of Powell and Nurick (Powell and Nurick, 1996b) and Cleary (Cleary, 1998) who found that in the cascading and cataracting regime smaller particles were more prone to segregate to the outer mill periphery.

The denser packing of the smaller granular body in the rising region for the same mill speed would thus generate a higher torque about the mill centre. As a consequence, as indicated by the spatial power draw distributions in Figure 4.21, the smaller size particles due to their tendency to shift further away from the mill centre drew more power in the rising region. In Section 5.2, this tendency was investigated with DEM simulations using a modified size distribution for which similar mass fractions were present in every size class. It was found that smaller particles tended to draw higher power draw than larger particles.

For Full size distribution experiments, each size was tracked separately for the one hour duration (See Section 3.1). Charge location probability and average angular velocity distributions were consequently determined for each particle size. The power draw of each size class was calculated with the cumulated torque per bin methodology using Equation 4.2, and the total charge power draw was then the sum of the individual contributions of each size.

As listed in Table 4.3, the total power draw was found to be within agreement with the measured power. This demonstrated that the cumulated torque per bin methodology could be used to isolate the individual power drawn by each size class within the charge body. The full size distribution tests did not indicate that the smallest particles drew the highest power. This was attributed to the mass fraction present in each size, which was set by the Weibull distribution used for the work. This result is discussed in more detail in Section 5.2.

Table 4.3: Summary of mean power draw measurements and calculations for full size distribution experiments

FULL SIZE DIST. TESTS		
Speed (%crit.)	60	75
	P_{PEPT} (W)	P_{PEPT} (W)
2mm	3.62	4.65
3mm	4.75	6.55
4mm	5.13	6.8
5mm	4.8	6.1
6mm	4.18	6.42
8mm	2.56	3.42
Total Power P_{PEPT} (W)	25.04	33.94
Error P_{PEPT} (W)	1.48	1.37
Measured power (W)	25.50	34.12

4.3 Summary of PEPT results

The following is a summary of the key results from the analysis of PEPT experiments:

Relative frequency distributions for the particle location showed that the most probable particle position, or mode, was in the rising bulk region, radially further away from mill centre than the mean centre of mass.

It was found from mono-size tests that the smaller charge particles cataracted more readily at similar speeds in the cascading and cataracting regime. The smaller charge particles tended to pack closer to the mill periphery, causing them to show a higher tendency to rise with the rotating mill and cataract. For Full size distribution experiments, a similar radial segregation pattern was observed whereby the smaller sizes tended to dominate the cascading and cataracting regions while the larger sizes remained close to the mill centre. This result was in agreement with that observed by Powell and Nurick (Powell and Nurick, 1996b).

It was also found from mono-size tests that horizontal positions of the CoC for the smaller 3mm glass beads were closer to the mill shell, while vertical positions were higher than those of the 5mm charge at identical speeds. This supported the notion that smaller particles were lifted more readily in the cascading and cataracting regime as observed by Cleary (Cleary, 1998).

Profiles of the tangential velocity along diametrical lines through the CoC were plotted to compare the motion pattern in the bulk region. These profiles showed consistent trends and followed the function form proposed by Govender (Govender et al., 2011).

Porosity distributions for mono-size experiments indicated that, particularly at higher speed, the smaller 3mm charge had lower porosity (higher packing) in the rising bulk region. This higher packing contributed to the smaller particles cataracting more freely, which led to higher porosity in the cascading region for the smaller particles. Porosities also tended to increase with mill speed, as the more the charge began to cataract at higher speeds, the more pores developed in the bulk region (Sichalwe et al., 2011. Yang et al., 2008).

The measured power draw for the smaller sized 3mm glass beads was found to be higher at similar speeds to the 5mm charge. The charge power draw was calculated from PEPT data using the cumulated torque per bin approach, and found to be within statistical agreement with the measured power for all experiments. This approach demonstrated that as the bulk of the smaller charge was radially closer to the mill shell, it generated a greater torque about the mill centre and ultimately a larger power draw.

Spatial plots of the power draw indicated significant areas where mechanical energy was acquired by the charge particles as a result of the rotation of the mill. These distributions displayed a consistent trend, with two zones of high power draw, one in the rising region and another in the cascading region. These two regions were separated by the equilibrium surface. The distributions indicated that the bulk charge drew the vast majority of the mill power draw, which was consistent with several of the power draw models discussed in Section 2.1 (Hogg and Fuerstenau, 1972. Moys, 1990. Morell, 1992). This approach however demonstrated that, particularly at lower speeds, the kinetic energy of cascading bulk charge provided a significant contribution toward the overall energy per unit time acquired by the particles. This meant that cascading charge had to be catered for when using the mechanical energy of the particles to determine the mill power, which was in agreement with the previous work conducted by Kasozi and Madala (Kasozi and Madala, 2008). For Full size distribution experiments, the total charge power draw could be determined by summing up the cumulated torque per bin mill power of the six sizes. This was found to be within agreement with the measured power, which demonstrated that this methodology could be used to isolate the individual power draw contribution of each size class within a charge body.

CHAPTER 5

DEM SIMULATION RESULTS AND VALIDATION

Overview
This chapter is a summary of the results obtained from the analysis of DEM simulations. Validation is carried out by comparison with kinematic quantities derived from PEPT data and measured power draw. Power dissipation and the collision energy spectra are then discussed.

5.1 Extraction of DEM Simulation data

EDEM, a commercially available software package developed by DEM Solutions (DEM Solutions, 2006) was used to carry out the numerical simulations in this work. All DEM simulations were carried out according to the methodology summarized in Section 3.3.

The Analyst tool in EDEM allowed selective extraction of specific components of the simulation. The following properties were extracted over the fourth mill revolution, which was found in prior work as a sufficient number of rotations to have reached steady state motion (Kulya, 2008):

- Particle position [*x,y,z*]
- Particle velocity [*x,y,z*]
- Particle Total Force [*x,y,z*]
- Collision Energy Loss
- Geometry Total Force [*x,y,z*]
- Geometry velocity [*x,y,z*]

These selections were exported from the software in the form of comma separated value (.csv) text files which listed quantities at 10 milli-second intervals. All data was then imported into MATLAB (Mathworks, 2011) which was used to carry out the subsequent analysis.

5.2 Kinematic quantities determined from DEM data and validation

Similar to the method followed for PEPT data (Section 4.2), spatial distributions of charge features were determined in a 50 x 50 square grid. Particle positions extracted from simulations were the coordinates of their centroids. It was consequently assumed that if the centroid fell into a given grid cell, the entire particle volume was contained in the voxel defined by the grid square and mill length.

Average kinematic quantities of all particles were therefore calculated over all the time increments that composed a single steady state revolution. A summary of these properties along with comparisons to those derived from PEPT follows.

Location probability distribution

For DEM data, spatial location probability distributions for the charge body were calculated by initially accumulating the frequencies of particle coordinates in all grid cells. The grid was then normalized to give a spatial distribution of the relative frequencies in different regions of the mill, as given in Figure 5.1.

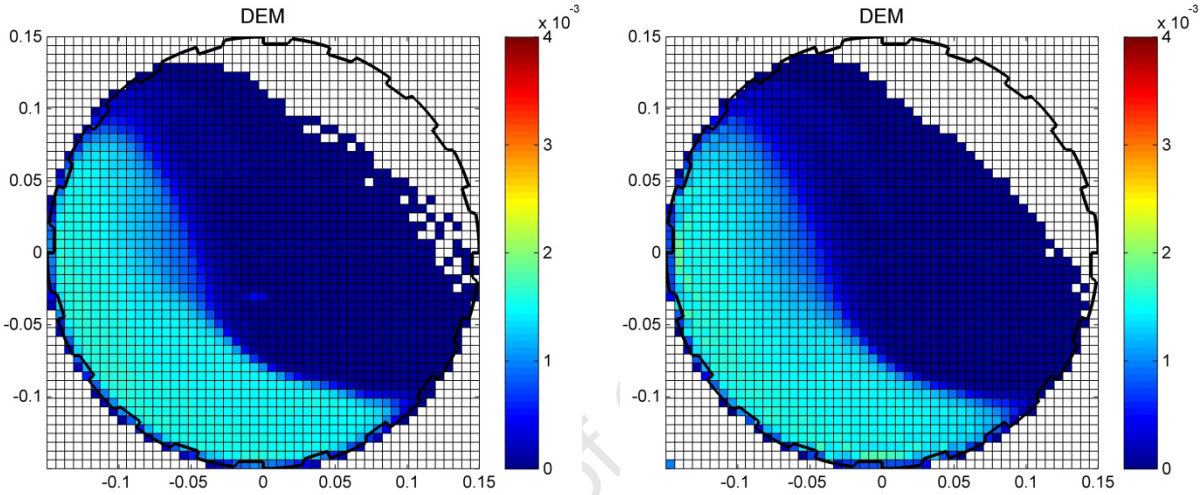

Figure 5.1: DEM plots of average position for 3mm and 5mm glass beads at 75% mill critical speed

All colour bars alongside the DEM location probability distributions were given an identical scale to those used for PEPT distributions, such that they could be directly compared. It was found that the DEM charge followed a similar overall pattern to location probability distributions from PEPT at similar speeds (See Section 4.2), whereby the bulk charge traced a distinguishable profile along the free surface above which particles descended from the departure shoulder in cascading or cataracting motion.

As indicated by the colour bars alongside, blue hues represented areas of low particle density while red hues represented high quantities. The plotted distributions for mono-size tests indicated that the bulk charge had a fairly homogeneous density, where the only notable distinctions were a marginally higher density in the rising charge region and the profile of the free surface. This was because unlike location probability distributions obtained from PEPT, those determined from DEM represented a snapshot of instantaneous particle positions without an indication of the time spent in the voxel. With PEPT, the relative

frequencies of the coordinates of the radioactive tracer were used to calculate the probability that a charge particle of a given size would be in a particular voxel. The frequencies of locations in each voxel would consequently be weighted by the amount of time the particle spent in a particular region. With DEM, the locations of every particle in the mill were used to determine the relative frequency, with the assumption that every particle had an equal likelihood of occupying a given position. Consequently, for mono-size simulations, the approach taken to determine location probability distributions from DEM averaged the bulk charge to virtually a continuum.

60% mill critical speed

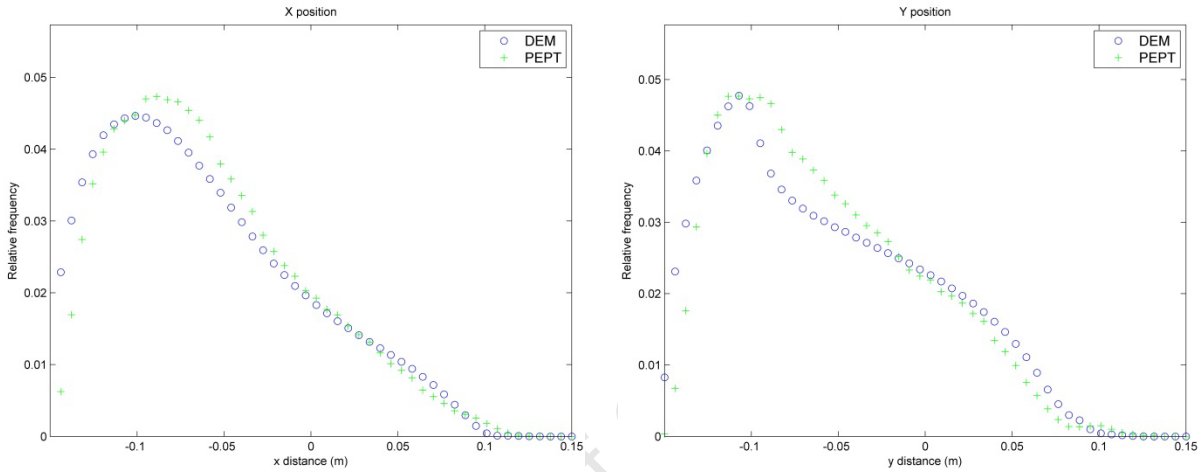

75% mill critical speed

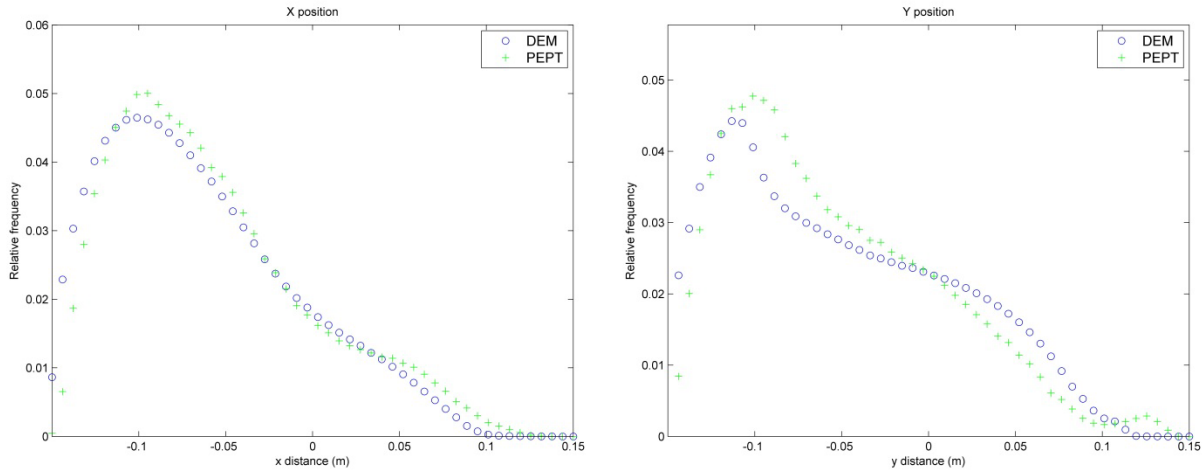

Figure 5.2: Plots of relative frequencies for particle positions along the *x* and *y* axes

Differences between location probability distributions based on averaged particle positions from DEM against distributions derived from single tracer data from PEPT could be highlighted using frequency distribution plots such as Figure 5.2. In this plot, a comparison of distributions in the transverse plane (*x,y*) from mono-size experiments of 5mm charge at

60% and 75% mill critical speed was shown. The points indicated the relative number of counts in cells along each axis from the mill shell (at -0.15) through the mill centre (at 0) to the other end of the mill (at 0.15). The peaks, or modes of these distributions indicated the most probable horizontal and vertical positions where particles would be found.

It was noted from these plots that while the trends were similar, DEM data generated higher frequencies at the rising mill periphery than PEPT, thus shifting the distributions marginally to the left. This was because, unlike DEM data, which provided relatively high statistics concerning every region, including material packed between rising lifters, the nature of PEPT data was such that relatively few counts were obtained from the tracer particles along the mill periphery. PEPT data therefore provided location probability distributions with lower readings at the mill shell than DEM. In the section of this chapter entitled Power draw and dissipation it was demonstrated that the differences between location probability distributions did not result in significantly different values for the mill power draw.

Spatial plots of location probability for full size distribution simulations were determined as depicted in Figure 5.3. These distributions followed a similar trend to that observed from PEPT data in that smaller size particles were lifted more readily and thus cataracted more freely than larger sizes, which largely remained in the bulk charge. A segregation pattern was also observed at both speeds, where mid-range particle sizes dominated the zone around the Centre of Circulation while larger particles circulated around this region, remaining in the bulk body and cascading along the free surface.

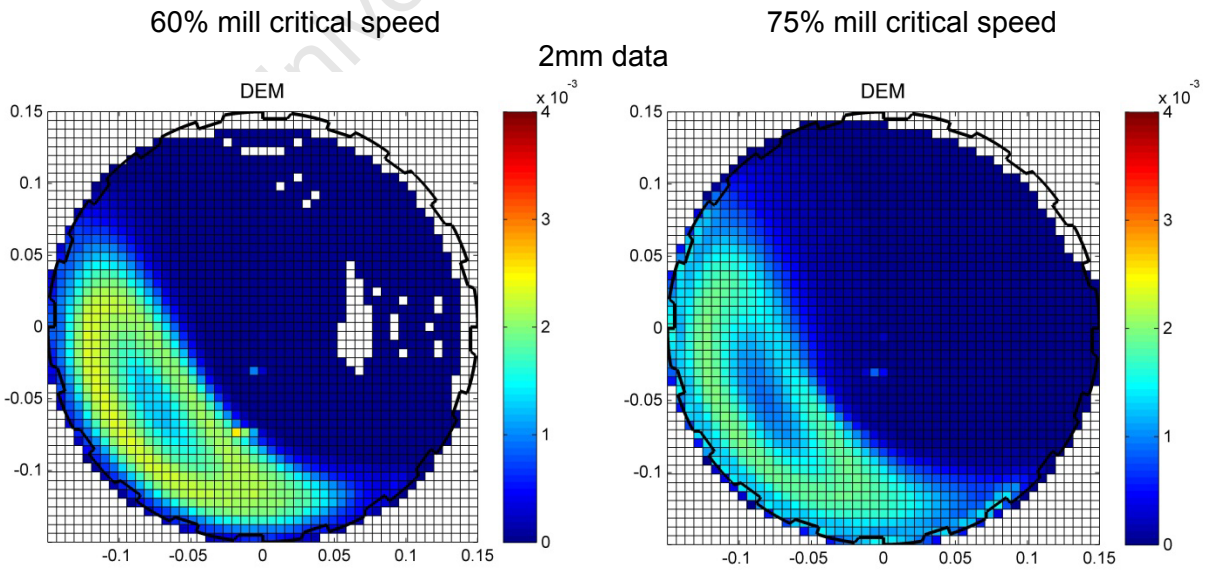

3mm data

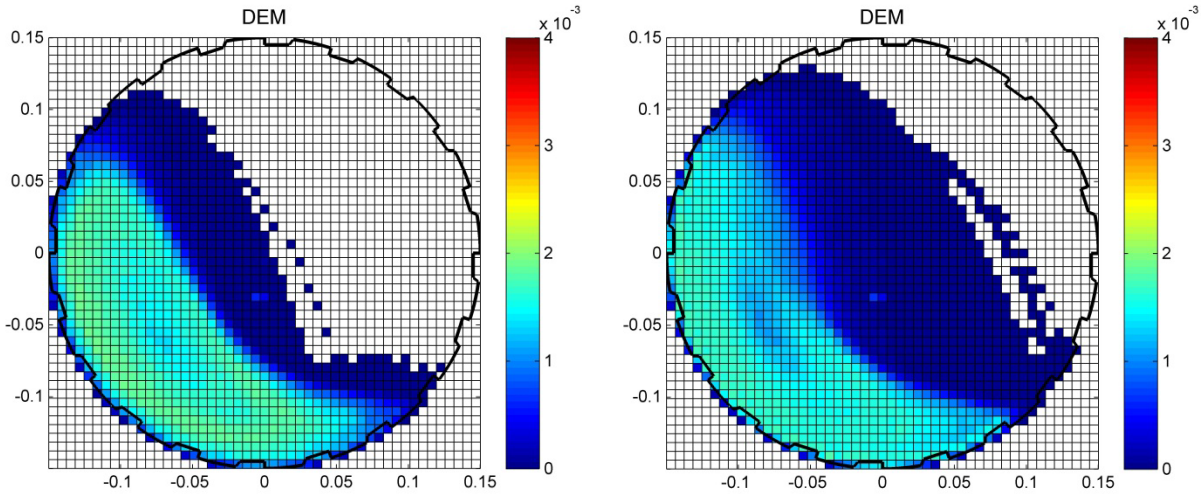

4mm data

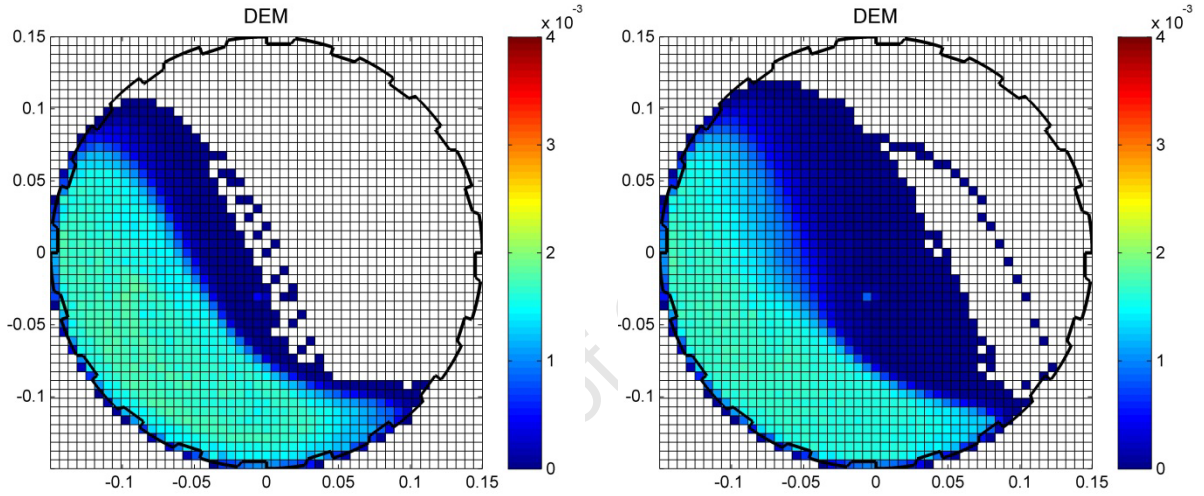

5mm data

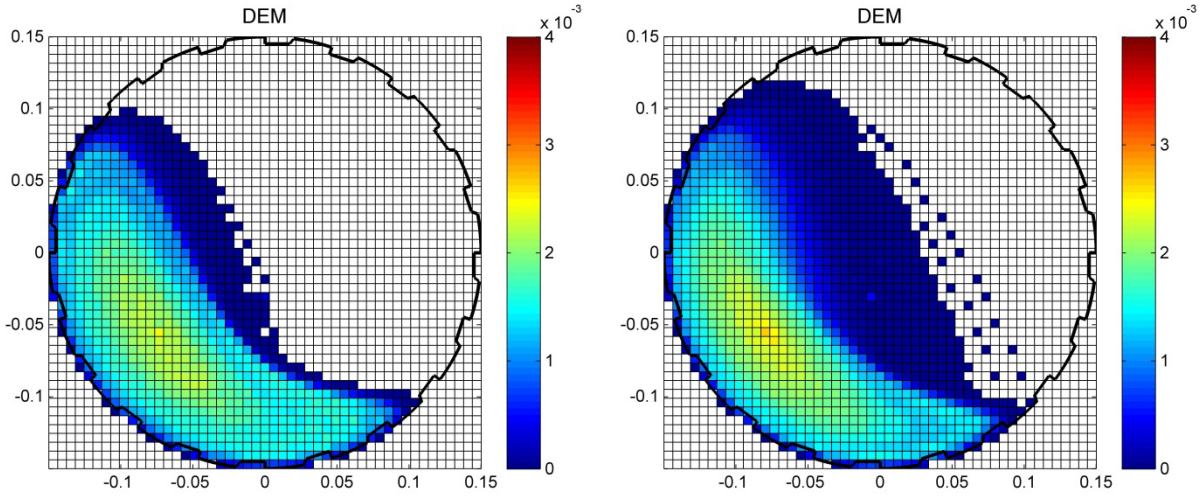

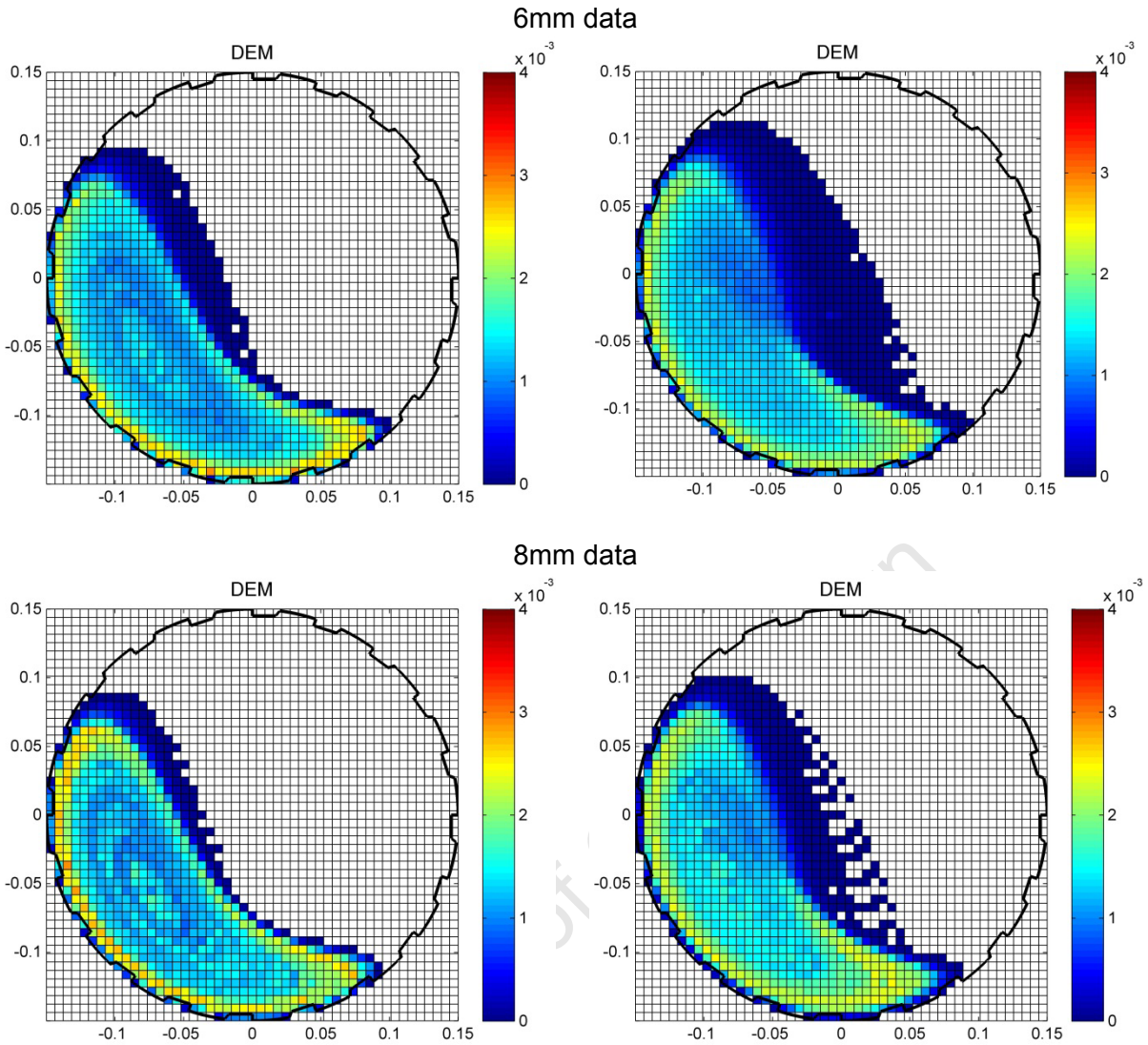

Figure 5.3: Location probability distributions from DEM for Full size distribution simulations at 60 and 75% mill critical speed

Velocity

Spatial plots of time averaged velocities calculated in PEPT (See Section 4.2) were compared to plots of average cell velocities determined from DEM. The 5mm mono-size experiments were compared in Figure 5.4, with DEM velocity plots on the left hand side, and the PEPT-DEM cell differences at corresponding mill speeds on the right hand side. The PEPT results used for this comparison are given in Figure 4.7.

Blue hues indicated positions where PEPT average velocities were notably higher than DEM while red hues indicated voxels where DEM averages were higher. It was found that PEPT and DEM average velocities were in agreement in most regions of the bulk charge body. The largest disparities occurred above the free surface in the cataracting region and impact toe.

PEPT averages tended to be higher in the cataracting region of the charge where particles entered free flight, while DEM averages were noted to be higher in the toe region. This was consistent with similar observations that were made for comparisons of DEM and PEPT data in tumbling mills by Govender et al. (Govender et al., 2012).

Reasons for these disparities were largely attributed to the differences in the nature of the two methods. Above the free surface, the cataracting behaviour of particles in flight has been noted to be aggressive and stochastic (Agrawala et al., 1997). DEM spatial plots were calculated by the averages of all the particle velocities in each voxel. Above the free surface, in the cataracting region, these averages included those of interacting particles. As demonstrated by Figure 5.6, these colliding particles altered the average particle trajectories from DEM causing lower velocities near the departure shoulder where particles entered free flight. For PEPT, this effect was not observed as the single tracer did not collide frequently with other particles as it entered the cataracting zone. Consequently, average velocities were higher in the cataracting zone for PEPT data. However, the erratic collision behaviour of the single particle and the unsteady nature of the motion in the toe region caused the trajectory to become unpredictable. This led to higher values in the average velocities of particles from DEM data, for which the averages were calculated from the motion data of all particles in the mill. In the Power draw and dissipation section of this chapter, it was noted that the charge material in the cataracting region had a negligible effect on power draw. The disparity in the velocity values in this region was thus considered to be of little consequence for this work.

Differences were consistently observed in voxels at the mill centre. These differences were caused by stationary particles from the DEM simulation that were present in the inlet chute. These particles reduced the DEM average velocities in voxels at the mill centre which led to PEPT velocities being found to be higher.

Table 5.1: Comparisons of mean and standard deviation obtained for PEPT and DEM velocity distributions

Test	Mean difference	Standard deviation
Mono-size 3mm 50 speed	0.01	0.13
Mono-size 3mm 60 speed	0.02	0.17
Mono-size 5mm 50 speed	0.01	0.15
Mono-size 5mm 60 speed	0.02	0.13
Mono-size 5mm 75 speed	0.02	0.14

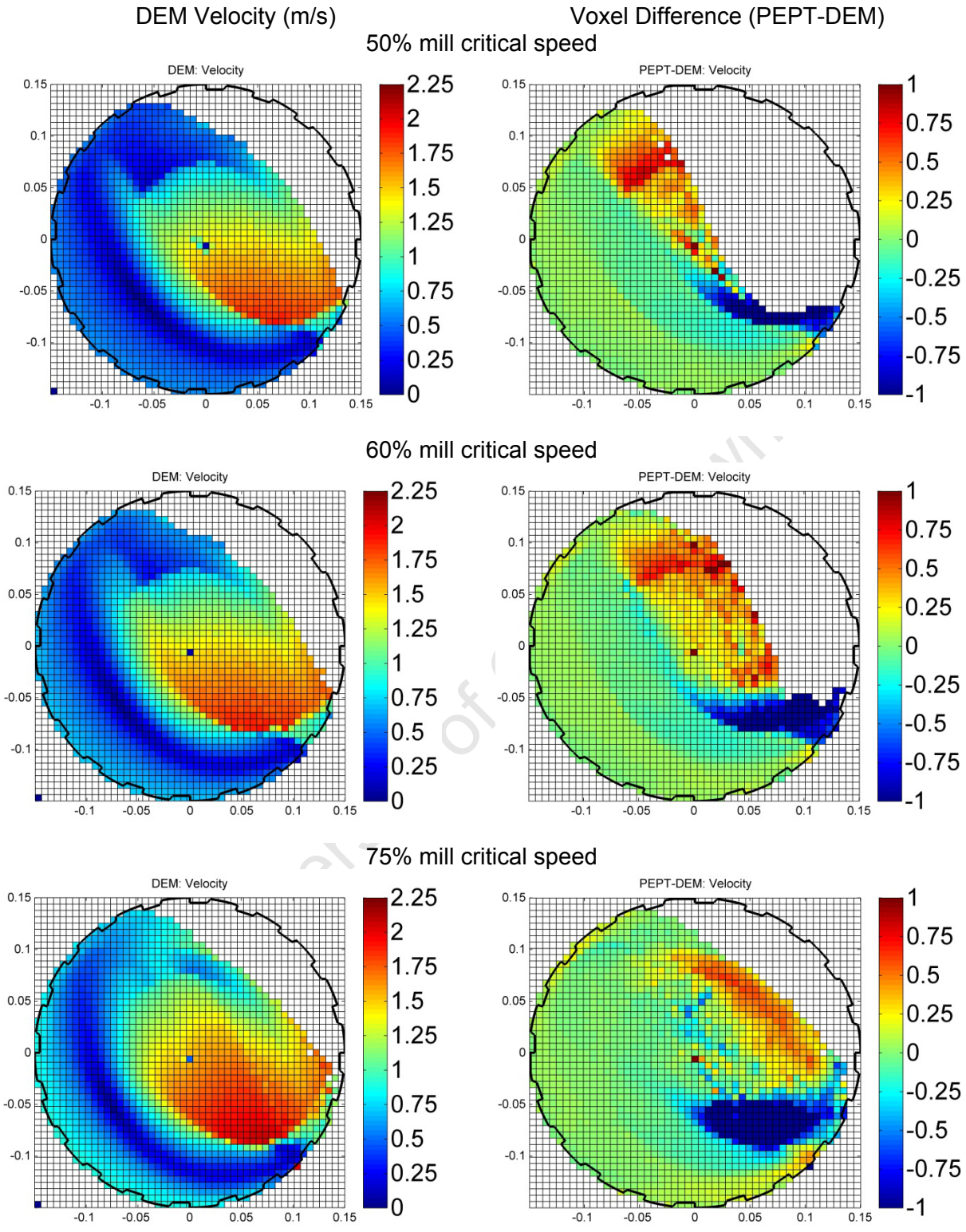

Figure 5.4: DEM absolute velocities for 5mm glass beads and difference from PEPT experiments

Table 5.1 showed the mean and standard deviations of differences between PEPT and DEM velocity plots. These values were calculated from only voxels for which both PEPT and DEM data registered counts, excluding those for which there were blank spaces. The results indicated that the disparity between average velocities from the two methods were minimal for all the conducted experiments. This signified that the average charge motion derived from particle trajectory data in PEPT was similar to that obtained from DEM. As PEPT velocity data was based on measurement of an actual system, DEM simulations could consequently be taken to be a quantitatively accurate representation of the charge motion. This was of importance as particle velocities were the key parameters in calculating interaction forces and collision energy losses from the contact model. An accurate simulation of charge motion was imperative to providing a platform for realistic collision mechanics.

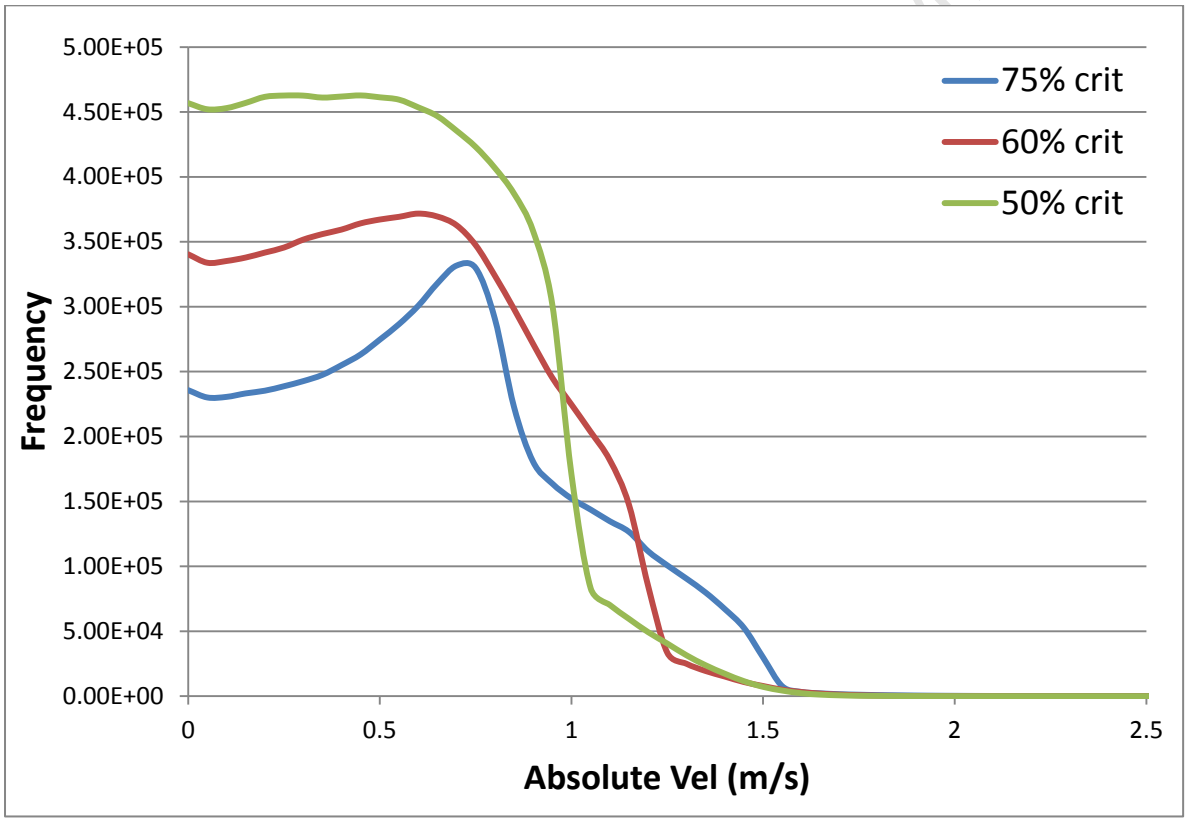

Figure 5.5: Plot of velocity distributions at different speeds for 5mm mono-size DEM simulations

Since DEM provided velocity information for all particles in the simulation, frequency distributions such as Figure 5.5 could be plotted which showed the number of occurrences of specific velocity ranges in the mill. For this plot of 5mm mono-size simulations, it was observed that for higher mill speeds, the distribution of particle velocities tended to shift further toward higher velocities. It was also found that the particles tended to have relatively low velocities, by either having a plateau of constant values or increase at the lower end until

a point at which occurrences in higher velocity bands decayed rapidly. This was consistent with results of DEM simulations by Yang et al. (Yang et al., 2008), which demonstrated that higher mill speeds in the cascading and cataracting regime led to a shift in the frequency distribution of particles toward higher velocities. This tendency was significant as it affected the collision energy losses in the mill as discussed in Section 7.4.

The average velocity plots from both DEM and PEPT could also be represented as velocity fields, as depicted in Figure 5.6. The direction and magnitude of velocities in each voxel were illustrated, while turning points in the charge motion and the Centre of Circulation (CoC) could be identified. In this comparison between PEPT and DEM data for 5mm mono-size data at 50% critical speed, the velocity fields were found to converge on an identical position for the CoC. Velocity field plots from DEM and PEPT data were found to be similar in the bulk region of the charge.

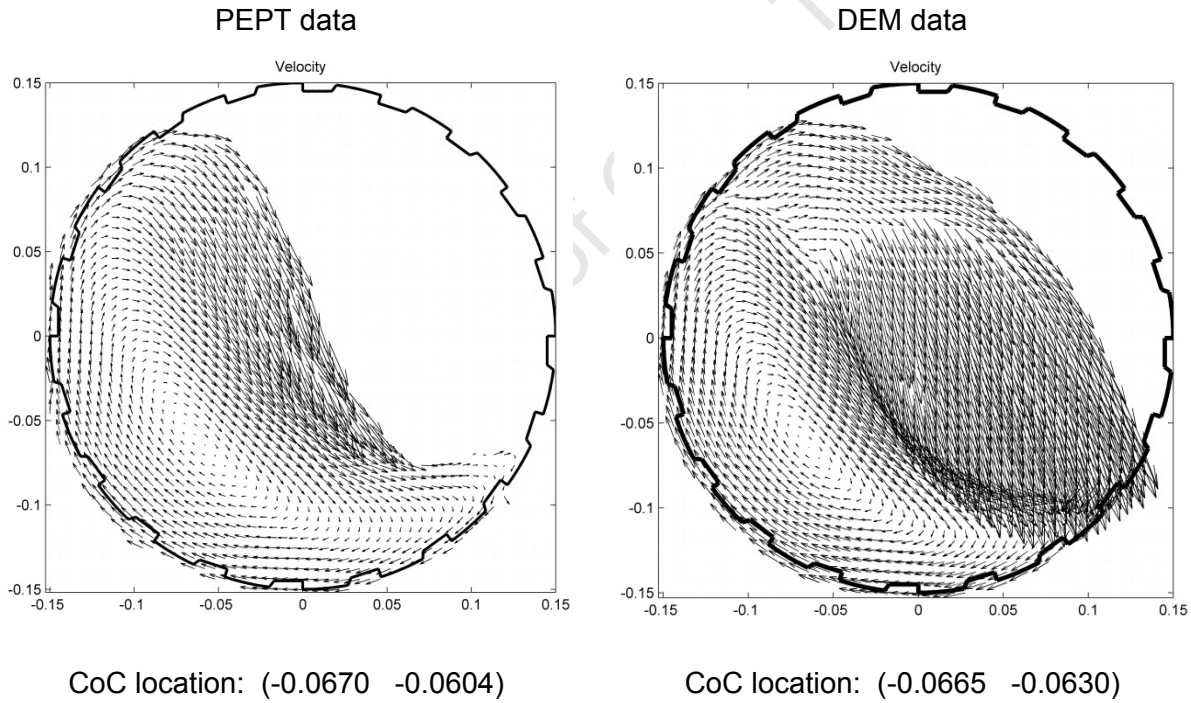

Figure 5.6: Velocity profiles of 5mm glass beads at 75% mill critical speed using DEM and PEPT respectively

Above the free surface, the pattern from the two plots differed. The PEPT data indicated that particles above the free surface cascaded from the shoulder in smooth concentric fields of flow. This was because the data from DEM considered average velocities from the instantaneous motion of all particles in this region and thus took account of any changes in trajectory resulting from collisions. For PEPT, the trajectory averages in this region were based on the motion of the single tracer. Due to the comparatively lower statistical data, the

velocity fields from PEPT did not capture the effects of particle interactions in the shoulder region. The velocity fields from PEPT data appeared to indicate an elevated toe compared to DEM data. However, as indicated from the location probability distributions in Figure 4.7, the position of the bulk toe could be observed as the intersection of the blue hue above the free surface with the mill shell. This position was in agreement with that of location probability plots from DEM in Figure 5.1. The PEPT velocity fields indicated the higher toe due to the stochastic collisions and rebounding of the tracer in the bulk impact zone. For velocity fields from DEM, the trajectories indicated a change of direction just above the free surface. This was due to the average motion of descending particles in this region which collided at the free surface before entering free flight. Unlike PEPT data from the single tracer, DEM simulations were the average motion of all particles in the system and captured this effect. The bulk toe could be observed from DEM velocity field plots as the region of the mill with the high concentration of interacting velocity fields.

Table 5.2 listed CoC values obtained for mono-size DEM experiments against those determined from PEPT. It was found that the values were closely similar between both methods, indicating that the simulated DEM particles and the PEPT tracer trajectories followed an identical circulating pattern.

Table 5.2: Comparisons of CoC values between PEPT and DEM data

	CoC (*x*-coordinate)		CoC (*y*-coordinate)	
	PEPT	DEM	PEPT	DEM
3mm mono-size 60 % crit.	-0.075	-0.079	-0.059	-0.052
5mm mono-size 60 % crit.	-0.067	-0.060	-0.062	-0.074
3mm mono-size 75 % crit.	-0.085	-0.081	-0.044	-0.048
5mm mono-size 75 % crit.	-0.080	-0.079	-0.055	-0.055

Profiles of tangential velocities along diametrical lines through the CoC were also determined for DEM simulations. As shown in Figure 5.7, similar trends to PEPT data were obtained for these plots (see Section 4.2). Equation 4.1 was fitted to this data, with the parameters obtained for each test listed in Table 5.3.

Table 5.3: List of fitted parameters for tangential velocity function to DEM data

Size (mm)	% Mill crit.	a_1	b_1	c_1	a_2	b_2	c_2	R^2
3	60	1.316	17.79	-1.298	0.301	61.86	1.683	0.962
3	75	1.607	14.62	-1.607	0.290	55.35	1.595	0.991
5	50	1.192	13.8	-1.729	0.206	50.93	0.724	0.978
5	60	1.347	14.61	-1.66	0.241	52.41	0.763	0.982
5	75	1.533	14.4	-1.679	0.228	50.87	0.949	0.979

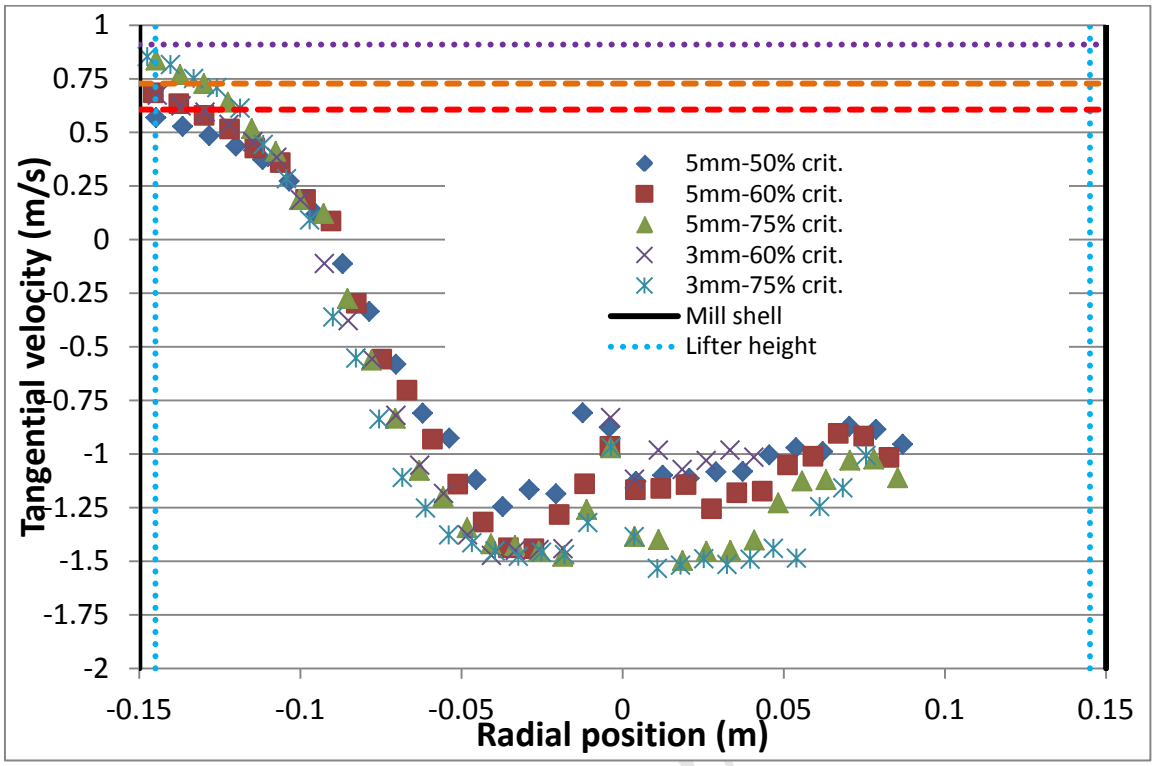

Figure 5.7: Graphical plot of DEM tangential velocities along diametrical lines through the CoC for 3mm and 5mm mono-size experiments

The tangential velocity profiles obtained from DEM and PEPT data could be directly compared by plotting the residuals between the methods along the mill diameter. In Figure 5.8, the mono-size 3mm and 5mm data was compared over this diametrical profile. It was found that below the CoC point, for which particles were rising with the mill, the tangential velocities between the two methods were closely similar.

In the cascading region, there were also marginal differences between PEPT and DEM data. This indicated that the velocity slip pattern in the rising bulk region was identical, and the cascading motion of the particles was also similar. This meant that the granular flow characteristics of the bulk charge predicted from the DEM simulation were in good agreement with the measured values from the PEPT experiment. Beyond the free surface, the residuals between the two methods deviated significantly due to the stochastic nature of velocity data in the cataracting region of the mill.

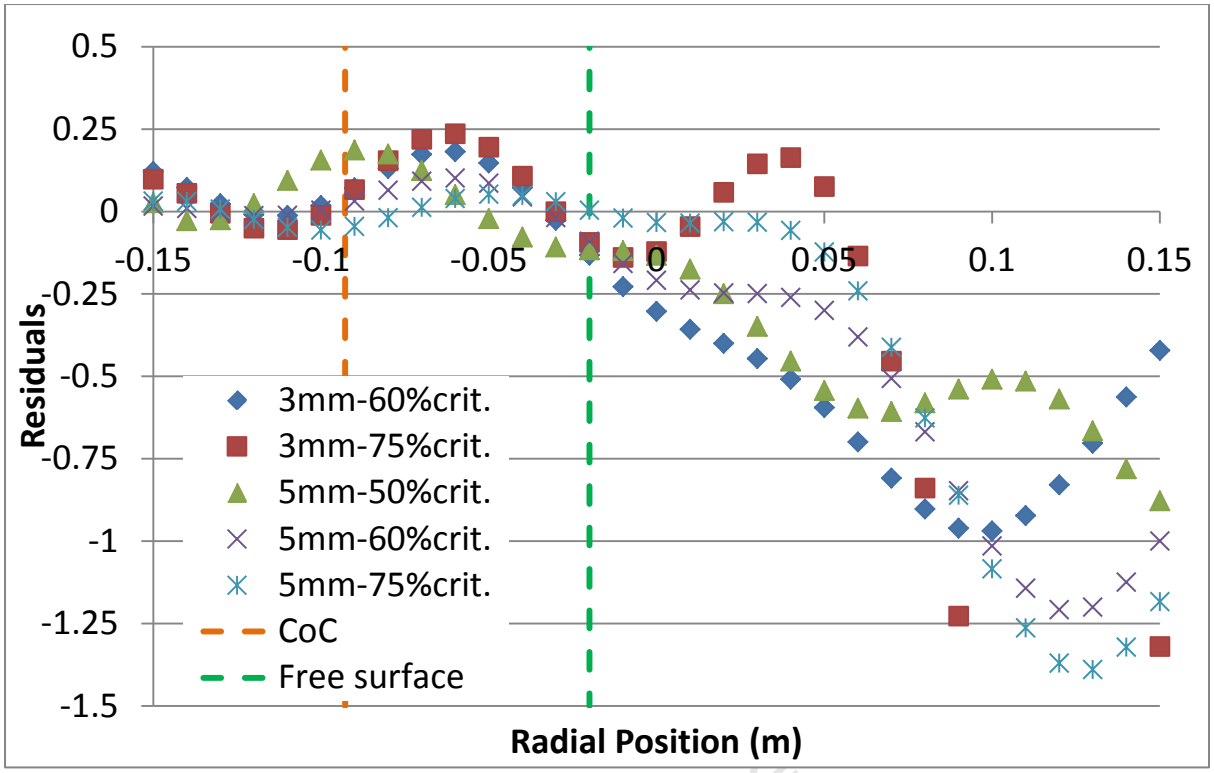

Figure 5.8: Plot of residuals between the fitted tangential velocity profiles of DEM and PEPT data

Packing Fraction/Porosity

Spatial distributions of the packing fraction were determined by multiplying the number of particles in each cell by the particle volume and subsequently dividing by the total voxel volume. The porosity in the voxel could then be determined by the difference between packing fraction and unity. Figure 5.9 showed the porosity distributions that were obtained for 5mm mono-size simulations on the left hand side, with differences between PEPT and DEM plotted on the right hand side.

Following the trend of PEPT porosity distributions, these plots showed that the charge was most densely packed in the rising region of charge with higher porosity gradually developing in the cascading region until the free surface, where the cataracting region was highly porous. Values of differences between PEPT and DEM porosity distributions were given in the colour bars alongside. Red hues indicated regions were PEPT porosities were higher (lower packing than DEM), while blue hues highlighted regions where DEM values were higher (higher packing fraction than DEM).

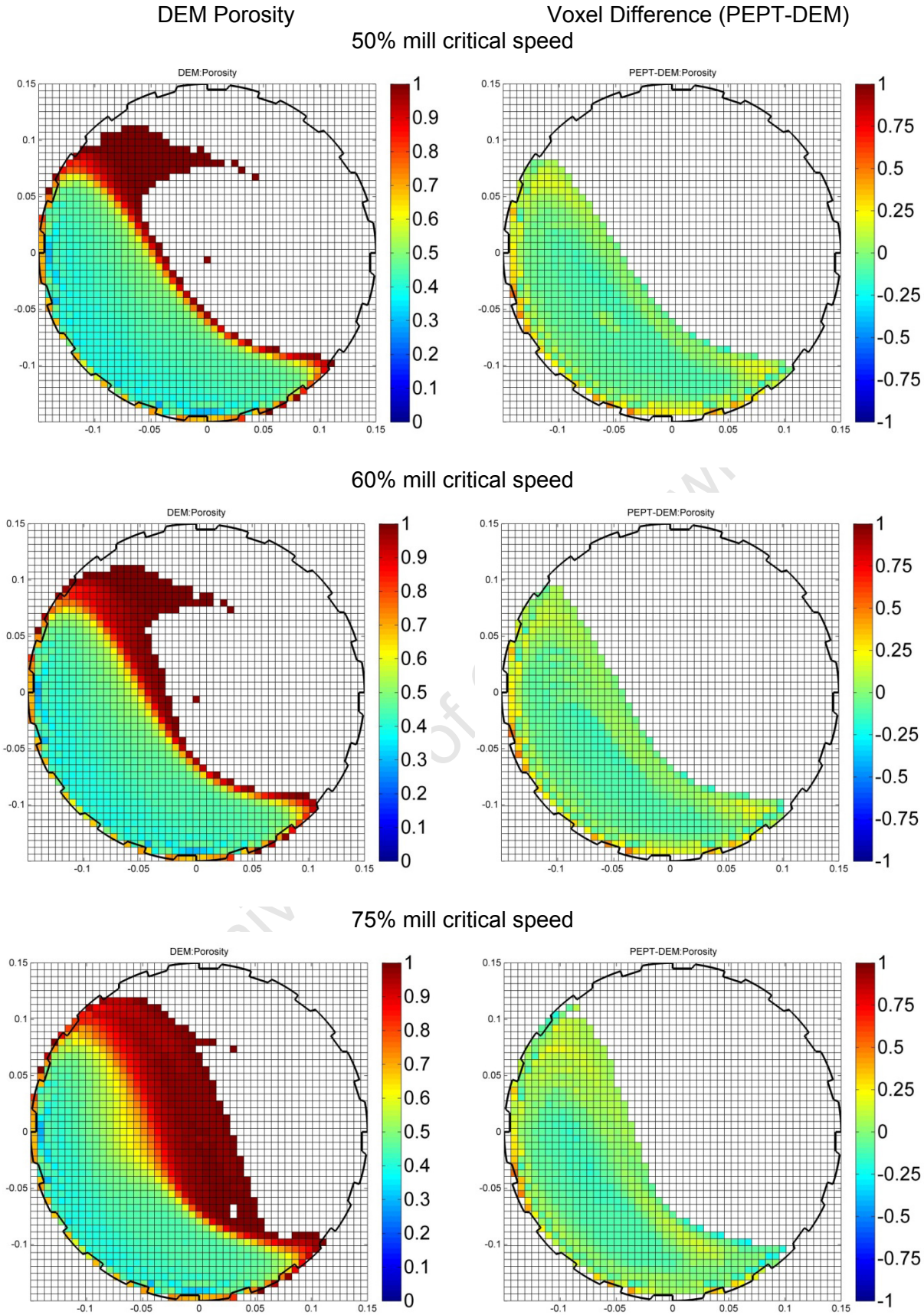

Figure 5.9: DEM porosity distributions for 5mm glass beads and difference from PEPT experiments

The largest differences between the data were observed along the outline of the mill periphery where PEPT data was found to have higher porosity (lower packing) than DEM data. As discussed in Section 4.2, this was due to the aliasing of PEPT data along the fringes of the mill in the spaces occupied by lifters, as similarly observed in the work by Govender et al. (Govender et al., 2012). This was

Marginal differences in porosity were also observed in the body of the bulk charge. This was due to the differences in the respective counts in each voxel in determining location probability distributions from PEPT and DEM, as illustrated in Figure 5.2. Based on location probability distributions from PEPT, the mean position of the charge body tended to be closer to the mill centre than for DEM, for which the location probabilities shifted the mean position marginally closer to the mill shell. This led to DEM porosities in the bulk charge being slightly higher (lower packing) than PEPT.

Table 5.4 listed the mean differences and standard deviations in porosities obtained between DEM and PEPT data. These values were calculated from only voxels for which both PEPT and DEM data registered counts, excluding those for which there were blank spaces. It was found that although there were minor disparities in spatial porosity plots from the two methods, the overall variance was negligible. This signified that the packing of the dynamic granular bed of material was accurately simulated by the contact model.

Table 5.4: Comparisons of mean and standard deviation obtained for PEPT and DEM porosity distributions

Test	Mean difference	Standard deviation
Mono-size 3mm 50 speed	0.0039	0.041
Mono-size 3mm 60 speed	0.0033	0.038
Mono-size 5mm 50 speed	0.0035	0.039
Mono-size 5mm 60 speed	0.0045	0.038
Mono-size 5mm 75 speed	0.0033	0.039

Power draw and dissipation

The Power draw for all DEM simulations was calculated according to two methodologies. The initial method was the force balance technique proposed by Cleary (Cleary, 2001), summarized in Section 2.1: Power Draw models. The second technique was the cumulated torque per bin approach developed in this thesis (See Section 4.2: Power draw). Calculated

values were compared to measured power as well as that of PEPT. The results were given in Figure 5.10 and Figure 5.11.

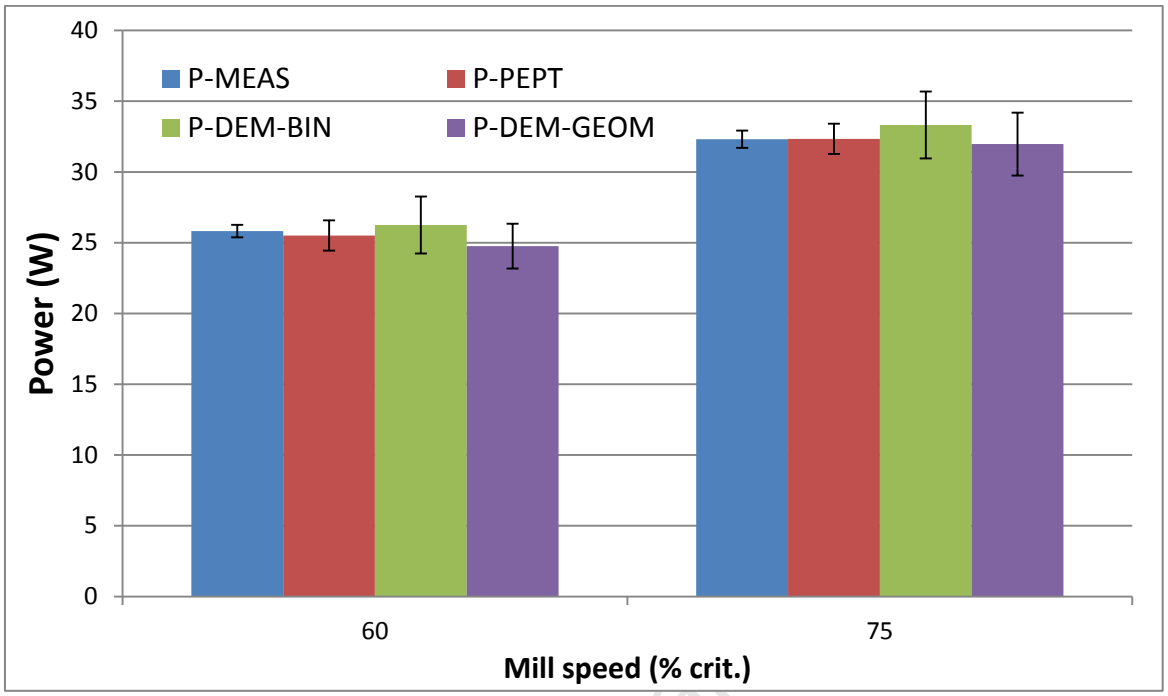

Figure 5.10: Plot of power draw values calculated from DEM (3mm mono-size)

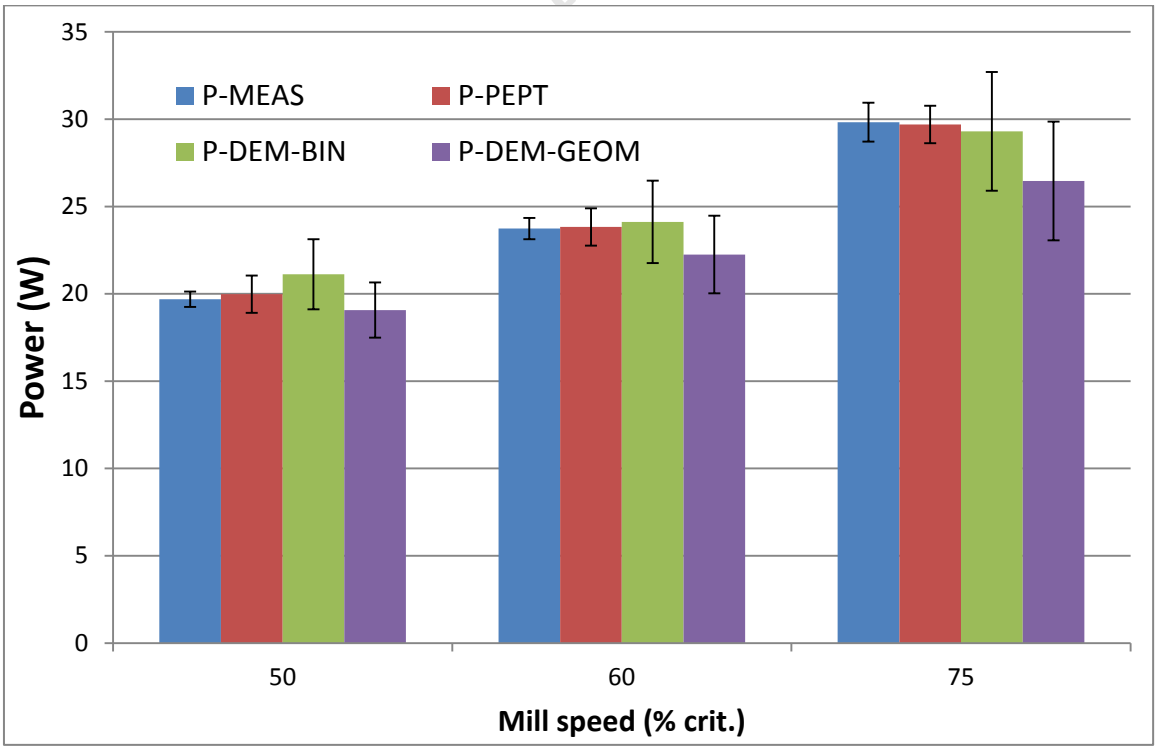

Figure 5.11: Plot of power draw values calculated from DEM (5mm mono-size)

In these figures, P_{MEAS} was the measured power draw, while P_{PEPT} was the PEPT power determined according to the cumulated torque per bin method. $P_{DEM\text{-}BIN}$ was the power draw calculated from DEM using the same methodology, while $P_{DEM\text{-}GEOM}$ was the power draw from DEM using the force balance approach. The values given for each method were the calculated mean, while the error bars were the statistical variance.

The power draw from the force balance method ($P_{DEM\text{-}GEOM}$) was within statistical agreement with measured values for all tests. However, its mean values consistently underestimated the measured power by marginal amounts. This was attributed to the force and velocity calculations on the mill shell from the simulation, which did not take account of frictional losses in the drive shaft. The actual mill motor applied a torque and rotational speed which overcame any additional resistance from bearings and other effects such as losses to friction and heat. The simulated mill did not model these forces and as a consequence this power calculation determined only the energy utilized by the mill in lifting the particles as the mill revolved at the selected speed. As shown in Figure 5.11 and Figure 5.12 however, these losses were sufficiently negligible that the calculated power maintained agreement with both measured and PEPT power. Similar observations were noted in the work on DEM simulations of granular charge motion in a tumbling mill by Cleary and Hoyer (Cleary and Hoyer, 2000).

The error associated with this technique increased with mill speed. This was because as speed increased, the impact behaviour of particles against the mill shell grew more aggressive and unpredictable. This led to fluctuations in the instantaneous power at each time step and in turn a higher variation in power.

The power per bin approach similarly yielded power values that were in statistical agreement with measured power for all conducted simulations. As highlighted in Figure 5.10 and Figure 5.11, the mean power from this method tended to slightly overestimate the mill power. This was attributed to the location probability distributions as determined from the average distribution of all particles for DEM. As shown in Figure 5.2, location probability distributions generated from DEM data determined that the mean particle position tended to be closer to the mill periphery. The torque contributions of voxels close to the edge of the mill were consequently higher than PEPT, although the velocity distributions from the two methods were identical. The accumulated total of all the power contributions led to a marginally higher power draw from DEM simulations. However, as the power draw was in agreement with

measurement, the use of the average charge position to represent the mass distribution was an adequate approximation.

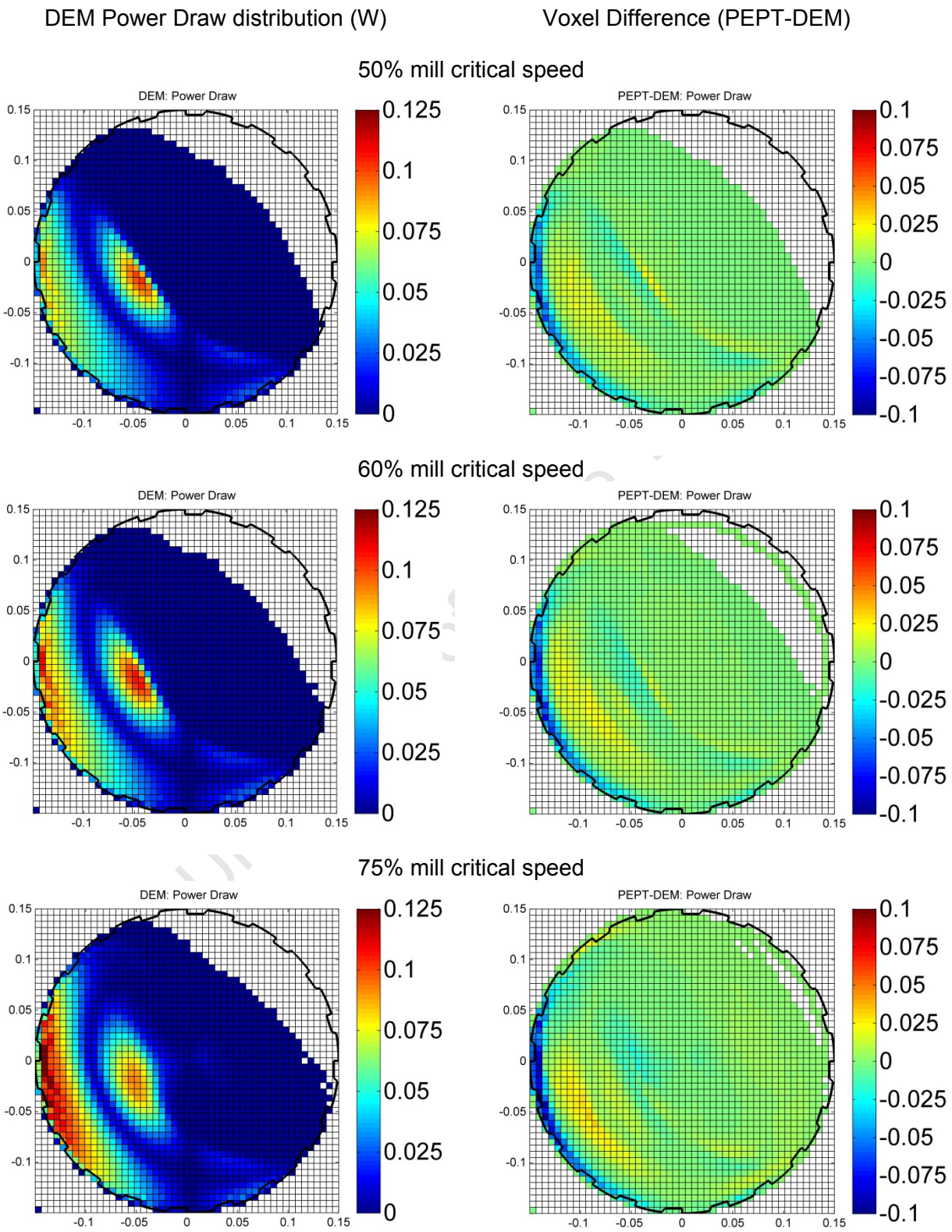

Figure 5.12: Power draw distributions for 5mm glass beads and difference from PEPT experiments

The spatial distributions from the cumulated torque per bin approach could be used to confirm these differences between PEPT and DEM power draw calculations. Plots of the DEM power draw of the mono-size simulations were provided alongside differences from PEPT power draw plots in Figure 5.12 and Figure 5.13. The plots indicated that the most significant difference between the two was the power determined along the outer mill shell, where DEM values were consistently higher than those of PEPT. As velocity distributions had been found to be similar, as were torque arm lengths, reasons for the difference were therefore owing to the location probability distributions as calculated from PEPT and DEM respectively. These distributions indicated that the granular charge body calculated from DEM had material packed closer to the mill shell than for PEPT. The higher mass present in these regions led to greater torque arm contributions and ultimately a higher power draw. Similarly in the body of the bulk charge, where PEPT power values were slightly higher than those of DEM, the higher mass present determined from PEPT distributions contributed to a slightly higher power contribution in these regions.

The PEPT power draw using the binning approach was consistently closer to the measured power. This suggested that the location probability distributions calculated from PEPT, which incorporated the residence time in each voxel, were a better approximation of the charge mass distribution than those from DEM, which were based on the instantaneous average particle positions.

The torque per bin approach was applied to calculate the power draw of each size from DEM simulations of the full size distribution experiments. In Table 5.5, the mean power draw of each size was compared against that obtained from PEPT.

Table 5.5: Measured, DEM and PEPT power draw values for full size distribution experiments

	60% mill crit.		75% mill crit.	
Size (mm)	P_{PEPT} (W)	$P_{DEM\text{-}BIN}$ (W)	P_{PEPT} (W)	$P_{DEM\text{-}BIN}$ (W)
2	3.62	3.84	4.65	4.84
3	4.75	5.05	6.55	6.79
4	5.13	5.61	6.8	6.91
5	4.8	5.06	6.1	6.06
6	4.18	4.64	6.42	5.52
8	2.56	3.22	3.42	3.75
Total power	25.04	27.43	33.94	33.88
Measured power	25.50		34.12	

The power draw of each size calculated from DEM was close to that of PEPT. This meant that the overall power draw predicted from DEM was similarly close to that of the measured power for these tests, and confirmed that the cumulative torque per bin methodology could be applied to determine the power draw of each size in a charge distribution.

While the mono-size tests showed that the smaller 3mm charge drew more power than the 5mm charge, the full size distribution tests did not indicate that the smallest particles drew the highest power. This was attributed to the mass fraction present in each size, which was set by the Weibull distribution used for the work (see Section 3.1) and not a consistent mass for each size.

To further investigate the effect of particle size on the mill power draw using a size distribution, two DEM simulations were conducted according to the methodology given in Section 3.1. These were performed with a modified size distribution for which the mass present in each size class was equal. The power draw of each size was calculated according to the torque per bin methodology, with the results given in Table 5.6. It was found that the mean power of each size decreased with increasing size. This was because, as indicated from the location probability distributions in Figure 5.3, the smaller particles tended to have mass distributions skewed closer to the mill periphery, which generated high torque about the mill centre.

Table 5.6: Mean power draw values calculated from DEM simulations with modified size distribution

		Power Draw	
Size	Mass	(W)	(W)
(mm)	(kg)	75% crit.	90% crit.
2	1.30	4.12	5.02
3	1.30	4.09	5.05
4	1.30	4.03	4.99
5	1.30	3.52	4.95
6	1.30	3.16	3.76
8	1.30	3.10	3.87

The force balance approach to determining power draw from DEM data showed agreement with measured power. Additionally, the power draw obtained from spatial distributions of location probability and velocity distributions yielded power draw values within agreement with PEPT and measurement. It was consequently found that the contact model as well as the material parameters used for the DEM simulations provided a good representation of the force environment, and by extension the energy utilization in the mill.

DEM Average Velocity field plots

DEM Power dissipation (W)

50% mill critical speed

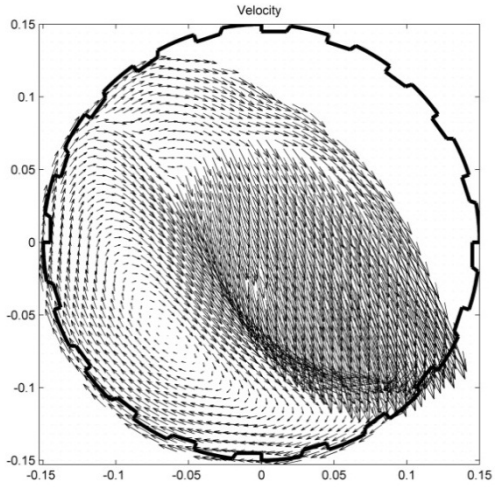

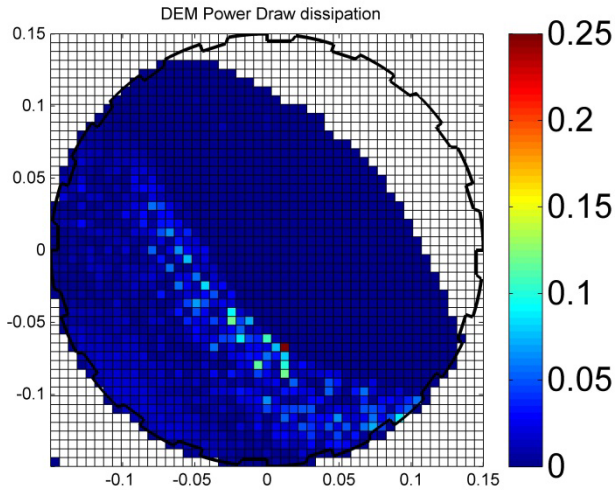

60% mill critical speed

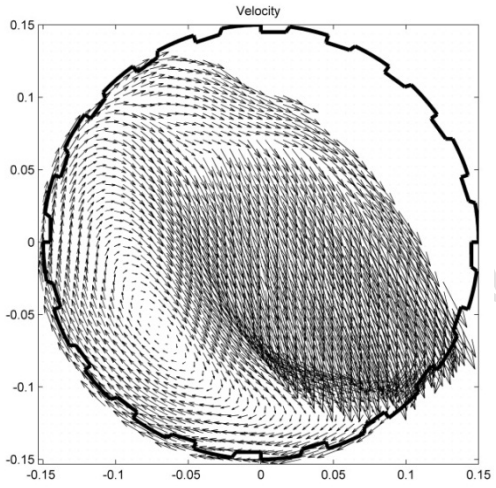

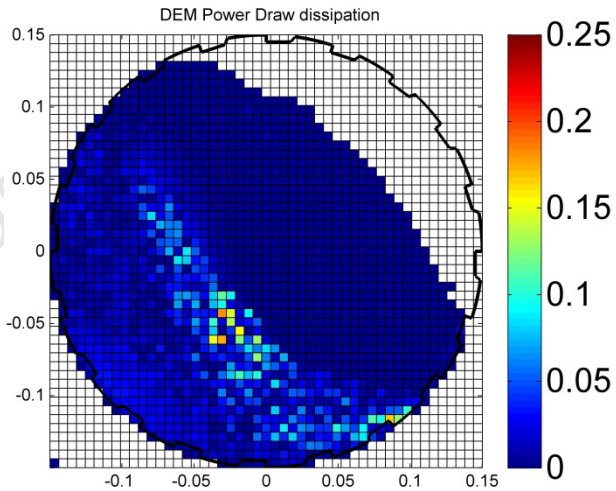

75% mill critical speed

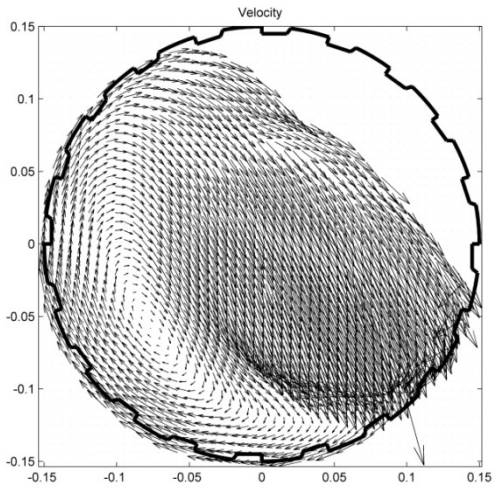

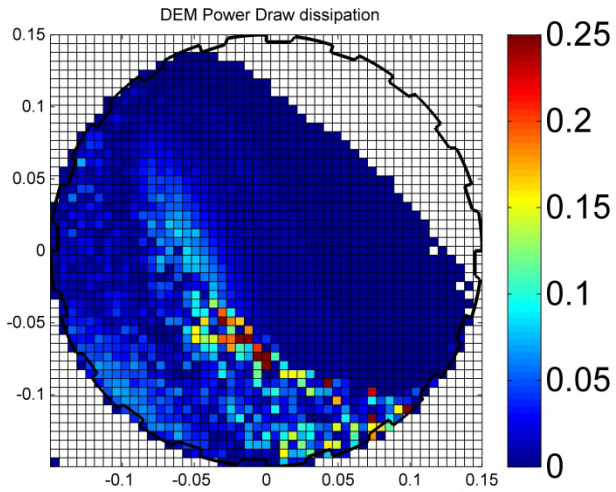

Figure 5.13: Plots of power dissipation from DEM simulations of 5mm mono-size experiments

As discussed in Section 2.2, collision energy losses during particle contacts were simulated by the viscous damping force. The force balance validated that the energy leaving the system through this means was a good approximation of the actual environment. Total accumulated energy losses over each revolution of the mill, divided by the total periodic time would therefore equate to the power dissipation per mill cycle. At steady state, as the energy dissipation rate would have to balance with the supplied power, this dissipated power would have to equal the power draw (Mishra et al., 1990).

The power dissipated to particle contacts was accumulated and plotted as spatial distributions, as shown in Figure 5.13. These plots highlighted the areas of greatest power dissipation in the mill due to contacts between colliding bodies. It was demonstrated that the highest area of dissipation was in the toe, due to impacts of cascading and cataracting particles at relatively high velocities in this region. This was in agreement with results of similar investigations on energy utilization in tumbling mills using DEM (Dragomir et al., 2009. Powell and McBride, 2004. Kulya, 2008. Nordell and Potapov, 2010). As speed increased, more charge began to cataract, which led to higher energy losses in this region. The average velocity field plots alongside the power draw plots further indicated that the position of the impact toe shifted closer towards the mill shell with increasing mill speed.

The power dissipated to particle collisions multiplied by the mill's periodic time represented the total energy loss per mill revolution at steady state (Mishra and Rajamani, 1992). The following section discusses how the total energy loss could be plotted as distributions known as the energy spectra.

5.3 DEM Energy spectra

All collision energy losses over the single steady state revolution of the mill were logged during each simulation. As discussed in Section 2.2 these values were determined from the Hertz-Mindlin contact model as a damping energy which was proportional to the relative velocity between colliding bodies.

Collision energy losses were binned in discrete energy levels of 1 μJ from minimum to maximum, with frequencies of collisions occurring between each increasing energy level accumulated. Plots of frequency versus collision energy as plotted in Figure 5.14, known as energy spectra curves, could then be plotted for a particular mill simulation. These curves,

traditionally presented with logarithmic scales on both axes, depicted an overall trend whereby the substantial majority of impacts occurred at relatively low energy losses, with frequencies decreasing by orders of magnitude as the collision energy losses increased. This result was in agreement with prior work on tumbling mill modelling using DEM (Rajamani et al., 2000. Cleary and Morrison, 2004. Powell et al., 2008).

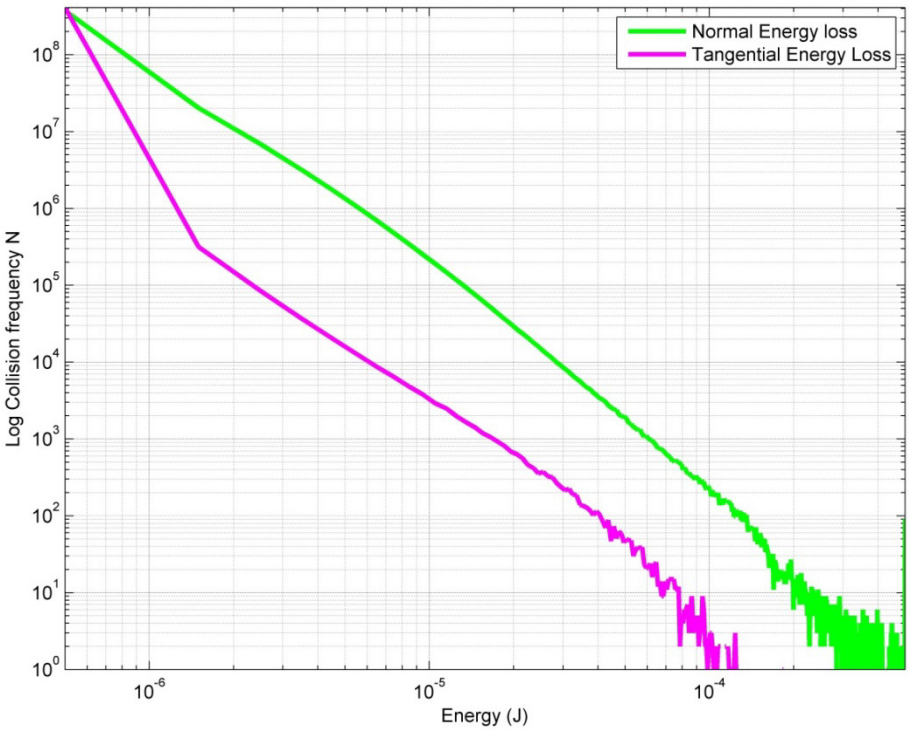

Figure 5.14: Energy spectra curves for 5mm mono size glass bead charge at 75% mill critical speed

Figure 5.14 depicts an energy spectra plot, which was obtained from a simulation of 5mm mono-size glass bead charge at 75% critical speed. Typically, energy spectra curves are presented in this form, with data points connected by lines and logarithmic scales applied to both axes. Here, the energy losses arising from collisions of 5mm beads against one another and the mill geometry were shown in terms of normal and tangential losses. For all simulations conducted, the normal energy loss was observed to be significantly higher than the tangential energy loss. This result was primarily due to the low friction coefficient of the glass beads which determined that under direct impact, low fractions of the normal energy loss would contribute to the tangential forces. Further, the geometry of spherical shapes was such that particles were more inclined to high normal forces under point loading than in the tangential orientation.

For this work, the scope of interest was describing the total power utilization to cause collisions. For this purpose, normal and tangential energy losses were combined to obtain a single energy spectra curve which quantified the distribution of the total energy loss. Such curves could be compared for different operating conditions to study their respective influence on the resulting distribution. By example, Figure 5.15 displays the effect of altering the mill speed on the energy spectra, using a comparison of 5mm mono-size simulations. This plot demonstrated that with an increase in mill speed, there was an increase in collision energy loss. This was explained by velocity distributions such as Figure 5.5 and spatial energy loss distributions such as Figure 5.13. These plots indicate that higher mill velocities gave particles higher kinetic energies, with more material being lifted by the higher centrifugal forces. This led to more cataracting and thus higher collision energy losses. This result was in agreement with that of Yang et al. (Yang et al., 2008), who found that at higher speeds in the cascading and cataracting regime, the energy spectra plots demonstrated a tendency toward higher energy losses.

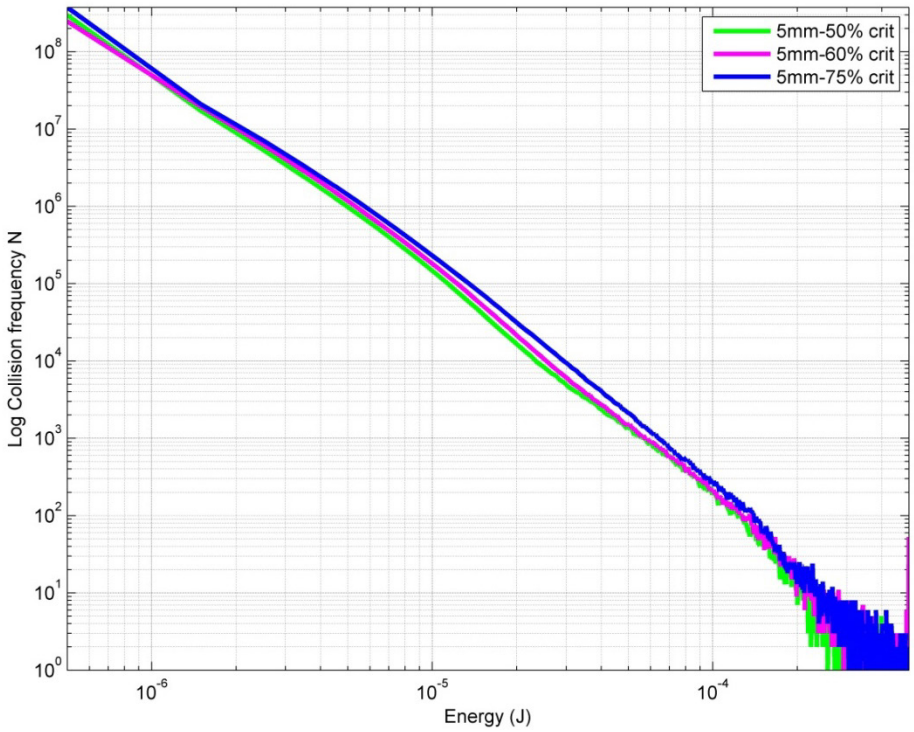

Figure 5.15: DEM Energy spectra curves for 5mm charge at 50%, 60% and 75% crit. speed

The area under the energy spectra curve represented the total energy expended during the mill revolution. Dividing this energy by the periodic time gave the total power dissipation per rotation cycle. As collision energies were extracted over a steady state revolution, this dissipated power would have to equal the power draw for the energy to balance.

The lower bound of the energy spectra curve had to be specified such that negligible energy losses below the value of E_0 (see Section 2.4) were not counted (Kulya, 2008). The value of E_0 had been found in prior research to vary with particle size (Whyte, 2005). Consequently, to determine E_0 for each particle size, the lower bound of the energy spectra was truncated such that the power dissipation matched the mean power draw of each size, as calculated from the cumulated torque per bin method. Values of E_0 determined for each particle size were listed in Table 5.7. It was found that these values were consistent with the typical energy ranges determined from prior work on DEM and single impact breakage tests (Bbosa, 2007. Kulya, 2008). E_0 was also found to decrease with increasing size as found in these experiments.

Table 5.7: Values of E_0 calculated for each particle size from DEM data

Size (mm)	E_0 (J)	E_0 (kWh/t)
2	0.00122	0.0323
3	0.00155	0.0122
4	0.00169	0.00561
5	0.00171	0.00291
6	0.00164	0.00161
8	0.00142	0.000591

5.4 Summary of results

The following is a summary of the key results from the analysis of DEM simulations and comparisons with PEPT data:

The overall shape of location probability distributions from mono-size DEM simulations was found to be similar to those from PEPT experiments. DEM distributions generated higher frequencies close to the rising mill periphery than PEPT, and depicted the bulk charge to have a fairly homogeneous density. This was because unlike location probability distributions obtained from PEPT, those of DEM represented a snapshot of instantaneous particle positions without an indication of time spent in the voxel. Consequently, these plots did not distinguish the particle location probability in as much detail and averaged the bulk charge to a continuum.

Spatial distributions of location probability for full size distribution experiments followed a similar trend to that observed from PEPT data. Smaller size particles were lifted more readily and thus cataracted more freely than larger sizes, which largely remained in the bulk charge. Segregation patterns were also observed in the transverse plane, where mid-size range particle sizes dominated the zone around the Centre of Circulation while larger particles circulated around the periphery of this region cascading along the free surface.

Spatial plots of time averaged velocities calculated in PEPT were compared to plots of average cell velocities determined from DEM. Negligible differences between the two methods were found in the voxels that encompassed the bulk charge. This signified that the charge motion simulated in DEM was a good representation of the environment. Values of the CoC for mono-size DEM experiments were found to be similar to those determined from PEPT. This further demonstrated that the circulating charge pattern from the two methods were similar.

Profiles of tangential velocities along diametrical lines through the CoC were determined for DEM simulations. The comparison between PEPT and DEM data yielded that the velocities along this profile were in good agreement in the region below the free surface. This reaffirmed that the granular flow simulated by DEM was representative of the actual charge motion.

DEM porosity distributions followed the trend of PEPT data, in that the charge was most densely packed in the rising bulk region, with higher porosity gradually developing at the free surface. Disparities between the two were marginal except along the outline of the mill periphery.

The Power draw calculated from the force balance approach was within statistical agreement with the measured power for all tests. Its mean values consistently underestimated the measured power by marginal amounts as it did not take account of additional mill losses in the drive shaft such as frication and heat. The error associated with this technique increased with mill speed, as the impact behaviour of particles against the shell grew more aggressive and unpredictable with increasing speed.

The cumulated power per bin approach similarly yielded power values that were in statistical agreement with measured power for all conducted simulations. Spatial plots of power draw from this technique were compared to those from PEPT experiments. It was found that the

power values determined along the outer mill shell in DEM were consistently higher than those of PEPT. This was due to the difference in charge distributions between the two methods.

As the power draw from DEM simulations was found to be consistently within agreement with measured power and PEPT data, the contact model used to simulate the charge environment was deemed to be a good representation of the mill environment.

It was demonstrated from spatial distributions of energy losses that the highest area of energy dissipation was in the toe, due to impacts of cascading and cataracting particles at relatively high velocities in this region. With increasing speed, as more charge began to cataract, higher energy losses were found in this region. The position of the impact toe moved from the bulk region closer to the mill shell with increasing mill speed.

Energy spectra plots of the collision environment showed that the vast majority of losses in the mill arose from relatively low level energy values. The area under the energy spectra curve represented the total energy expended during the steady state mill revolution. Dividing this energy by the periodic time provided the power dissipation.

The lower bound of the energy spectra curve, or E_0, was determined by truncating the collision energy spectra such that the total power dissipation matched the mean power draw per size calculated using the cumulated torque per bin method. Values of E_0 for each particle size were determined and found to be consistent with prior work and typical energy ranges from particle breakage experiments.

CHAPTER 6

DEVELOPMENT OF POWER DRAW MODEL

Overview
This chapter describes the methodology followed to develop a mathematical model for the power draw of each size class in the tumbling mill. A discussion of the key observations related to the mass and angular velocity distributions is initially made. Charge motion information derived from PEPT and DEM data is then described mathematically with the aid of assumptions based on known mechanisms influencing the mill power to form a basis for this model. The predictive capabilities of this model against power draw measurements from this study are investigated.

6.1 Model formulation

The methodology developed in this work to determine the power draw for each size class in a tumbling mill could be used to develop a mathematical model. As discussed in Section 4.2, the two primary contributing factors toward the power drawn by the mill were the granular charge mass and average angular velocity distributions. With these quantities determined in a spatial grid from DEM or PEPT data, the power draw of each size could subsequently be obtained by accumulating the torque arm contributions of every voxel in the grid as given by Equation 4.2. This technique for determining the power draw was a sum of the mechanical energy per unit time of the granular body in different regions of the mill.

Particle motion and velocity data extracted from PEPT and DEM data could be used as a basis to develop a model for the power draw which incorporated the mechanisms of charge motion observed in this work. Mathematical expressions for the behaviour of the charge body along the horizontal diameter of the mill were used to constitute the model. The approach taken to develop functions for these distributions is discussed in the following sections. The influence of different operating conditions on the power draw is discussed, following which the functions utilized to reproduce these effects are introduced.

6.2 Mass distribution

The granular charge distribution resulting from the motion of the mill dictated the torque about the mill centre. As the lever arm length could be simplified to the horizontal distance to the mill centre, the charge mass distribution that generated the mill torque could be obtained by determining the relative fractions of mass present in different regions along the horizontal mill diameter. In Figure 5.2 it was demonstrated that using PEPT and DEM data, the relative

frequencies of particle coordinates could be used as a proxy to determine such mass distributions along the mill diameter.

Figure 6.1 demonstrated charge distributions that were obtained from DEM and PEPT data for the full size distribution experiments. In these plots, the relative frequencies of the particle position data for each size were determined in discrete intervals along the horizontal mill diameter. The mass present in each interval could then be calculated by multiplying the relative frequency at each interval by the charge mass of the particular size class.

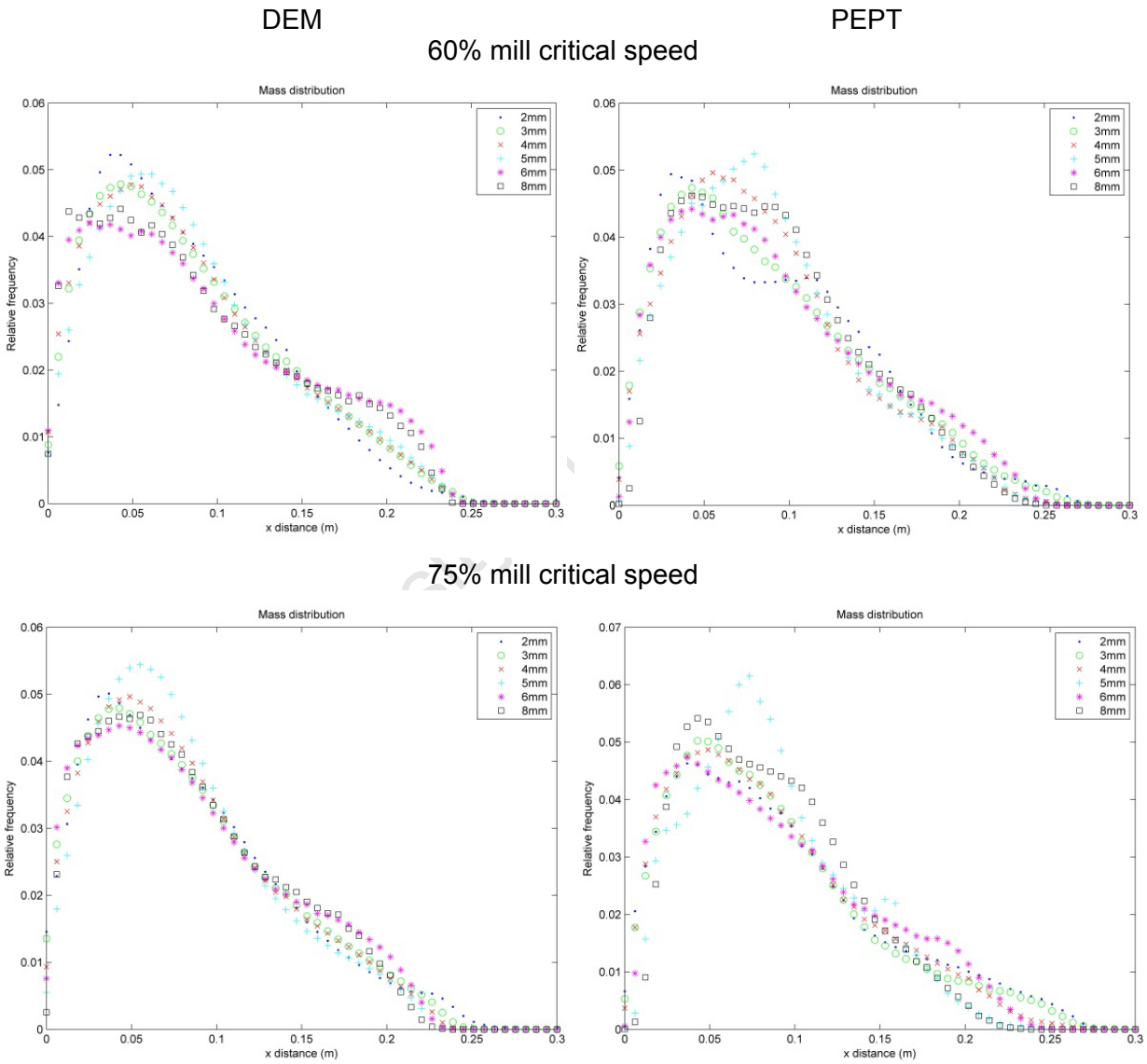

Figure 6.1: Mass distributions of charge particles along horizontal plane for DEM simulations and PEPT experiments using the full size distribution

For the above distributions, the zero reference position was set at the rising end of the internal mill diameter. The plots for each size followed a continuous distribution skewed toward the rising end of the rotating mill. Both PEPT experiments and DEM simulations were found to have similar distributions for each size, with minor variations between the two methods arising as a result of the methods used to determine the location probability (see Section 5.2).

While the distributions could be visualized to exhibit differences with particle size, this qualitative analysis could not be used to definitively compare trends. It was thus found that the function form in Equation 6.1 could be used to consistently describe the relative frequencies in each interval as a function of the position along the horizontal mill diameter.

$$y = T_1 \cdot x \cdot e^{(-T_2 \cdot x)} \qquad \textbf{Equation 6.1}$$

The equation expressed the dependent variable y, the relative frequency, as a function of the horizontal position *x* as a product of a first degree polynomial and an exponential function, using two parameters T_1 and T_2. Figure 6.2 illustrated an example of this function form fitted to data from a 5mm monosize DEM simulation. The fitted model was observed to closely follow the distribution behaviour of particles, only deviating marginally in the turbulent toe region of the mill. In this region, the relative occurrences were comparatively low, such that the differences were assumed to cause inconsequential changes to the mass contribution.

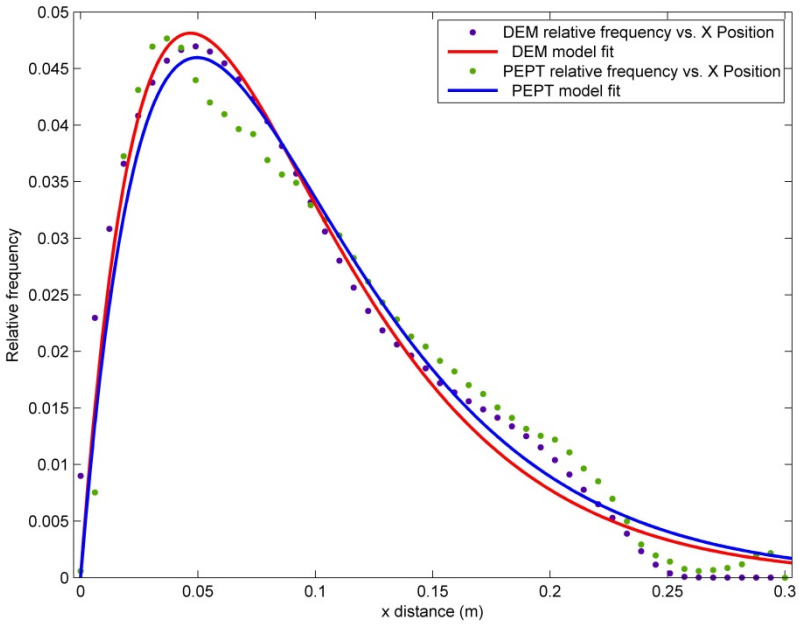

Figure 6.2: Mass distribution for 5mm monosize DEM simulation and PEPT experiment along with fitted function

A list of fitted parameters for PEPT experiments and DEM simulations were compiled in Table 6.1, along with coefficients of determination (R^2). The values of R^2 were found to be consistently close to unity, which demonstrated that the function form could be used to predict the behaviour of the charge distribution for the conditions investigated in this work.

Table 6.1: List of fitted parameters for mass distribution against Full size distribution data (DEM) at 75% crit. speed

Test type	Size (mm)	Speed (% crit.)	DEM			PEPT		
			T_1	T_2	R^2	T_1	T_2	R^2
Mono size	3	60	2.63	20.81	0.965	2.37	19.38	0.983
		75	2.80	21.41	0.975	2.52	20.16	0.971
	5	50	2.43	19.86	0.964	2.24	18.46	0.978
		60	2.60	20.53	0.974	2.42	19.22	0.977
		75	2.77	21.13	0.980	2.56	19.91	0.980
Full size dist.	2	60	3.11	21.82	0.984	2.60	20.48	0.936
	3		2.93	21.85	0.979	2.67	20.74	0.985
	4		2.95	21.93	0.974	2.70	20.43	0.974
	5		2.77	20.93	0.982	2.58	19.71	0.950
	6		2.58	21.01	0.869	2.51	19.98	0.980
	8		2.78	21.77	0.892	2.48	19.24	0.953
	2	75	3.05	22.41	0.972	2.68	20.98	0.983
	3		3.02	22.36	0.964	2.91	21.63	0.993
	4		3.10	22.38	0.982	2.90	21.48	0.993
	5		3.18	22.29	0.982	2.69	19.85	0.902
	6		2.90	21.96	0.939	2.72	20.92	0.964
	8		2.98	21.96	0.967	2.83	20.43	0.934

Values of the fitting parameters T_1 and T_2 for PEPT and DEM data from similar tests were found to be different. This was due to the different nature of the two methods which were used to determine spatial location probability distributions. It was observed however that the data from both methods highlighted similar patterns that could be used to evaluate the effects of altering operating variables on the parameters.

Parameter T_1 was a scaling factor which influenced the vertical position at the peak of the distribution. This peak, or mode, represented the most probable position where a particle of a given size would be found in the mill. Thus, the higher the value of parameter T_1, the higher the distribution would be about the mode. This parameter however did not alter the horizontal position of the peak.

Parameter T_2 defined the steepness or shallowness of the distribution about the mode. A higher value of T_2 gave a narrower distribution which approached and decayed from the mode at a lower horizontal position, while a lower value resulted in the opposite effect.

From full size distribution data, parameter T_1 was found to tend to decrease with increasing size while T_2 tended to increase. As depicted in Figure 6.4, this signified that smaller particles tended to have a higher peak position for the mode, which occurred at a lower horizontal distance and followed a narrower distribution. As particle sizes increased, the opposite effect was gradually observed, such that the vertical position of the mode decreased, the horizontal position of the mode increased and the distribution became wider. This effect demonstrated the segregation pattern that was observed from spatial distribution plots in this study (see Sections 4.2 and 5.2). In full size distribution tests, smaller particles were found to be lifted more readily and as a consequence cataracted more than larger particles, which largely remained in the body of the charge.

From considering the effects of charge motion discussed by Mellman (Mellmann, 2001), the effect of mill speed on the parameters of Equation 6.1 could be investigated. The schematic in Figure 6.3 illustrated the trend followed by the mass distribution at three different regimes of flow in increasing speeds from slipping to cataracting motion. At low speeds, majority of the charge was not lifted along with the rotating mill as the mill velocity could not overcome the slip effects between successive layers of charge. The resulting mass distribution would then be widely spread out, marginally skewed toward the rising end of the charge surface.

As the mill speed increased, the transition to cascading resulted in a shift in the motion of the charge as more material lifted along with the mill. The peak of the mass distribution would thus increase and shift further away from the mill centre. As the motion of the charge reached the cataracting regime, increasing amounts of the charge would be lifted along the mill interior, causing the mass distribution to become narrower about a higher mode closer to the mill shell.

Parameter values for T_1 and T_2 thus increased with mill speed as shown in Table 6.1. This was in agreement with the work of Mellmann (Mellmann, 2000) as it exhibited that, in the cascading and cataracting regime, as speed increased so did the likelihood that particles would be found closer to the shell, lifted along with the rotating mill. If the mill speed further increased to the critical speed and beyond, layers of charge would begin to centrifuge. As

more material would cling to the mill interior, the horizontal mass distribution would consequently shift closer to the mill centre once more.

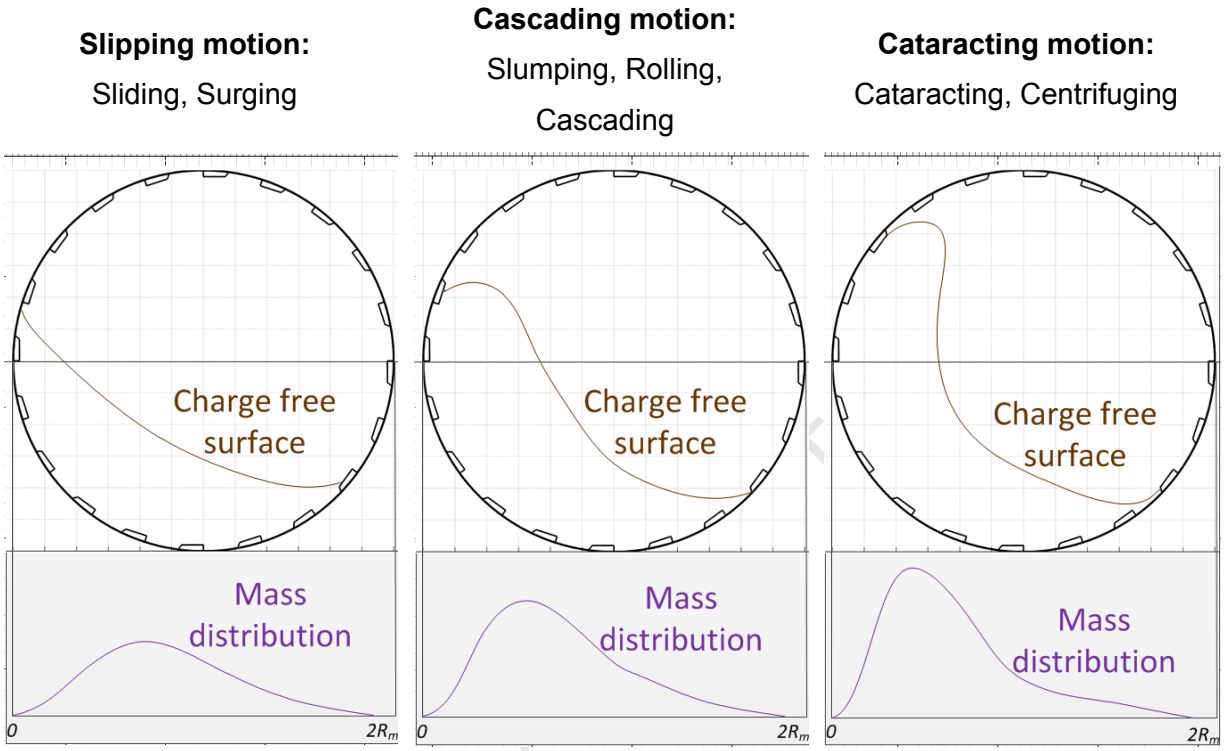

Figure 6.3: Schematic of charge shape at increasing mill speeds along with resulting shapes of mass distributions

The normalized form of Equation 6.1 was a probability distribution, Pr_p, which expressed the likelihood that a given particle size p would be found in a particular position along the mill diameter. This probability could be expressed between two positions x_1 and x_2 along the horizontal mill profile as given in Equation 6.2:

$$Pr_p[x_1 \leq x \leq x_2] = \frac{\int_{x_1}^{x_2} y\,dx}{\int_0^{2 \cdot Rm} y\,dx} \qquad \textbf{Equation 6.2}$$

Here, R_m is the internal mill radius. The mass present over this interval could then be determined by multiplying the probability by the total charge mass present in that particular size. Evaluating the integrals above yielded that the function to determine the probability distribution of each size over a specified horizontal interval was Equation 6.3.

$$Pr_p[x_1 \leq x \leq x_2] = \frac{e^{(-T_2 \cdot x_1)} \cdot (T_2 \cdot x_1 + 1) - e^{(-T_2 \cdot x_2)} \cdot (T_2 \cdot x_2 + 1)}{1 - e^{(-2 \cdot T_2 \cdot R_m)} \cdot (2 \cdot T_2 \cdot R_m + 1)} \qquad \textbf{Equation 6.3}$$

In this equation, the probability density function for particle position was found to be independent of parameter T_1. This meant that the probability that a particle would be found between two selected positions along the horizontal mill diameter could be expressed using the single parameter T_2.

The horizontal position of the mode could be determined by equating the differentiated form of Equation 6.1 to zero. This position was calculated to be given by Equation 6.4:

$$x_e = \frac{1}{T_2} \qquad \textbf{Equation 6.4}$$

The physical interpretation of the position of the mode x_e with regard to the charge motion is discussed in Section 6.3. Meanwhile, the mean of the probability distribution could be determined by evaluating the integrals in Equation 6.5:

$$Mean = \bar{x} = \frac{\int_0^\infty x \cdot y \, dx}{\int_0^\infty y \, dx} \qquad \textbf{Equation 6.5}$$

From the integrals above, the horizontal position for the distribution mean could be simplified to give Equation 6.6:

$$\bar{x} = \frac{2}{T_2} \qquad \textbf{Equation 6.6}$$

The mean horizontal position of charge particles of a given size corresponded to the x-ordinate of the centre of mass of particles in that size class. If the charge body were treated as a continuum, with the torque of each size described as acting at a single point with a lever arm to the mill centre, the lever arm length would be given by the distance between the mean and the centre. The x coordinate of the centre of mass could be calculated with respect to the mill centre using Equation 6.7:

$$x^* = R_m - \bar{x} \qquad \textbf{Equation 6.7}$$

Where x^* is the horizontal distance of the centre of mass from the mill centre. The behaviour of the mean distance with respect to particle size, mill speed and mill filling was then modelled in order to provide a method of predicting the value of T_2.

Many researchers have conducted work on evaluating the effects of mill speed on power draw (Datta et al., 1999, Liddel and Moys, 1988, Napier-Munn et al., 1999). It is known that as mill speed increases, power draw similarly increases non-linearly until approaching a

maximum at typically 85-90% of the mill critical speed. Thereafter, with increasing size, power draw begins to decrease.

Considering the simple lever arm equation for the power draw (Datta et al., 1999) describes the mechanism for this behaviour. As the charge mass and gravity remain constant, the only increasing operating variable is the mill speed. Over the interval from rest to the speed at which the maximum power draw occurs, the lever arm distance increases with increasing speed, as more charge overcomes slip effects and accumulates toward the mill shell, lifting along with the mill. As observed in this work, the mass distribution shifts closer to the mill periphery, resulting in a lever arm distance progressively further from the mill centre. Beyond the maximum power draw, the charge mass and gravity remain the same, while the mill speed continues to increase. However, as charge layers begin to centrifuge, the mass distribution begins to shift back toward the mill centre, which leads to the decrease in power draw. The lever arm distance continues to decrease until the mill is at full centrifuging motion. At this point the centre of mass is at the mill centre, which necessitates that the lever arm distance is zero.

Based on the above description, the behaviour of the horizontal distance to the mill centre with respect to mill speed was modelled in this work using a simple sine function of the form given in Equation 6.8:

$$x^*(\omega_m) = \frac{1}{2} \cdot (\sin(2 \cdot \omega_m - \omega_{max}) + 1) \qquad \textbf{Equation 6.8}$$

Here ω_m is the mill speed while ω_{max} is the velocity value at which the lever arm distance from the mill centre was its maximum. This value is typically 85-90% of the mill critical speed (Wills and Napier Munn, 2006). The lever arm distance in Equation 6.8 increases and decreases sinusoidally about this maximum.

A similar tendency was observed from prior research for the effect of volumetric filling on power draw (Datta et al., 1999, Liddel and Moys, 1988, Wills and Napier-Munn, 2006). While the mass increases with volumetric filling, the lever arm distance of the centre of mass increases until a maximum after which it decreases with further increase of mill filling. This effect was observed through power draw measurement, whereby mill power increased with mill filling until a maximum position stated to be between 40 - 50% filling, after which the power began to decrease (Wills and Napier Munn, 2006).

The effect of mill filling on the lever arm distance was modelled in this work to be a function of mill filling and particle size. Particle size was included in this model as it was observed from this study that along with filling the particle size present in the mill significantly affected the resulting mass distribution, and in turn the position of the centre of mass that that would arise from the granular motion. The mean horizontal distance of the charge to the mill centre as a function of mill filling and particle size was modelled using Equation 6.9:

$$x^*(J,p) = \frac{1}{L_1 \cdot L_2 \cdot \left(\frac{\bar{p}}{p}\right)} \cdot \left(\frac{1}{1 + \left(\frac{J - J_{max}}{L_2 \cdot \left(\frac{\bar{p}}{p}\right)} \right)^2} \right) \qquad \textbf{Equation 6.9}$$

In the above model, J is the mill volumetric filling while J_{max} was the filling for which the lever arm distance to the centre of mass was its maximum. L_1 is a fitted constant which influenced the maximum mean position, while L_2 is a similarly a fitting parameter for the influence of particle size. The particle size p was incorporated as a ratio to the mean particle size $\bar{p}$ of the charge distribution. If the particle size distribution in the mill was given by a function y, the mean size could be determined by Equation 6.10:

$$\bar{p} = \frac{\int_0^{p_{max}} p \cdot y \, dp}{\int_0^{p_{max}} y \, dp} \qquad \textbf{Equation 6.10}$$

Here, p_{max} is the highest particle size in the distribution. The full size distribution used in this work utilized a Weibull distribution given by Equation 3.2, for which the maximum particle size was 8mm. With this distribution used for the function y in Equation 6.10, the mean size of the full size distribution was 4mm.

The model exhibited the effect of particle size observed in this work, whereby as particle size increased the lever arm distance to the centre decreased, such that smaller particles would be calculated to have a mean position closer to the mill shell than large particles.

The horizontal lever arm distance to the mill centre as a function of particle size, mill speed and mill filling was therefore modelled as a product of Equation 6.9 and Equation 6.10 to give Equation 6.11:

$$x^* = \frac{1}{2 \cdot L_1 \cdot L_2 \cdot \left(\frac{\bar{p}}{p}\right)} \cdot \left(\frac{(\sin(2 \cdot \omega_m - \omega_{max}) + 1)}{1 + \left(\frac{J - J_{max}}{L_2 \cdot \left(\frac{\bar{p}}{p}\right)} \right)^2} \right) \qquad \textbf{Equation 6.11}$$

With this model, the maximum mean distance from the centre, which occurred when the mill speed and filling were set to ω_{max} and J_{max} respectively, was given by Equation 6.12:

$$x^*_{max} = \frac{1}{L_1 \cdot L_2 \cdot \left(\frac{\bar{p}}{p}\right)} \qquad \textbf{Equation 6.12}$$

The value of fitting parameter L_1 could be calculated based upon a specified value for the maximum mean distance. The horizontal mean position for each size could be calculated with respect to the rising end of the mill by Equation 6.13:

$$\bar{x} = R_m - x^* \qquad \textbf{Equation 6.13}$$

This mean was equated to Equation 6.6 as a means of determining parameter T_2 which in turn could be used to describe the overall charge distribution across the horizontal mill diameter. The charge distribution of each size could then be determined as a function of the mill speed and mill filling using a single fitting parameter L_2. This parameter was likely a consequence of other effects not considered in this work which are known to affect the power draw per size such as lifter geometry and particle density (Bond, 1961. Austin, 1990. Morell, 1992).

The two maxima, J_{max} and ω_{max} were both parameters which varied depending on the geometry of the mill, including the lifters, and the charge characteristics. For a specified mill and operating conditions, the volumetric filling and mill speed for which the power draw peaked could be determined by following methodologies similar to that given in the work by Powell (Powell et al., 2009). To utilize this approach, the power draw is obtained using techniques such as DEM or PEPT, or even by measurement. Several power readings are taken over a range of volumetric fillings and mill speeds such that the values lie either side of the peaks. The maximum mill power with respect to volumetric filling and mill speed is then obtained by fitting a polynomial to the data and calculating the position for which the peak occurs. The parameter L_1 can be determined using Equation 6.11 having evaluated the values of J_{max} and ω_{max}. For a given filling and speed, the lever arm distance to the mill centre is determined from the power draw and used to determine the fitting constant.

Developing a methodology to evaluate the specified parameters J_{max} and ω_{max} was outside the scope of this study. For this work, the specified variables were selected based on the power draw readings obtained and the ranges given in literature for the maxima with respect to volumetric filling and speed (Datta et al., 1999. Wills and Napier Munn, 2006). The parameters used to calibrate the model are given in Table 6.2 (p. 143).

In Figure 6.4, the model prediction for the charge distribution of all sizes in the full size distribution was plotted at 75% mill critical speed, with 31.25% volumetric loading. The plots followed the observed trend that smaller particles depleted from the centre and were more prone to be found in the rising end of the mill.

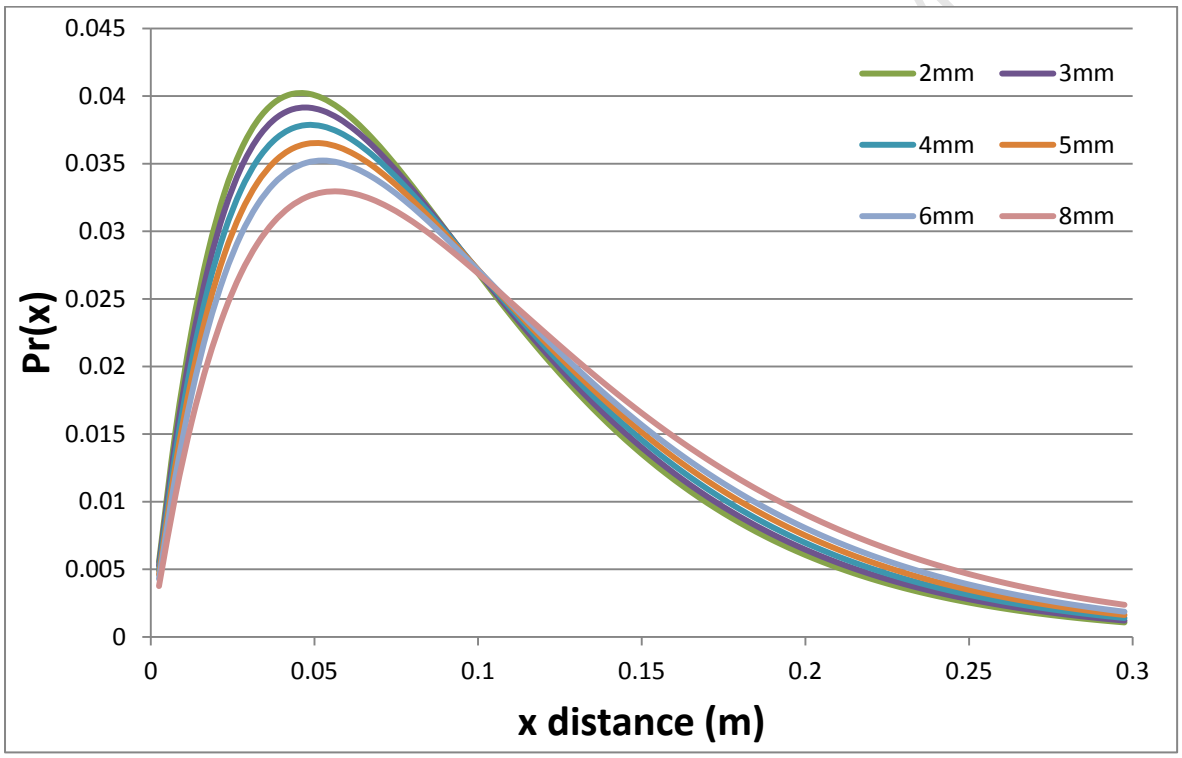

Figure 6.4: Model predictions for the charge distribution of 2-8mm particles

6.3 Angular velocity distribution

To develop the power draw model, a mathematical function for the average angular velocity along the horizontal mill diameter needed to be developed. From DEM and PEPT data, the mean angular velocity in discrete intervals along the horizontal profile was determined as illustrated in Figure 6.5. For these plots, the mean angular velocities were determined using only data from particles found below the charge free surface. This approach was followed

primarily because charge particles in the cataracting regime under free fall were found to have relatively high angular velocities which led to a misrepresentation of the typical velocities in the bed region. Also, as noted from prior research (Govender et al., 2012) and similarly observed in this study, the charge mass present in the cataracting region above the free surface was negligible compared to that of the dynamic bed and did not contribute significantly to the power draw (see Section 5.2).

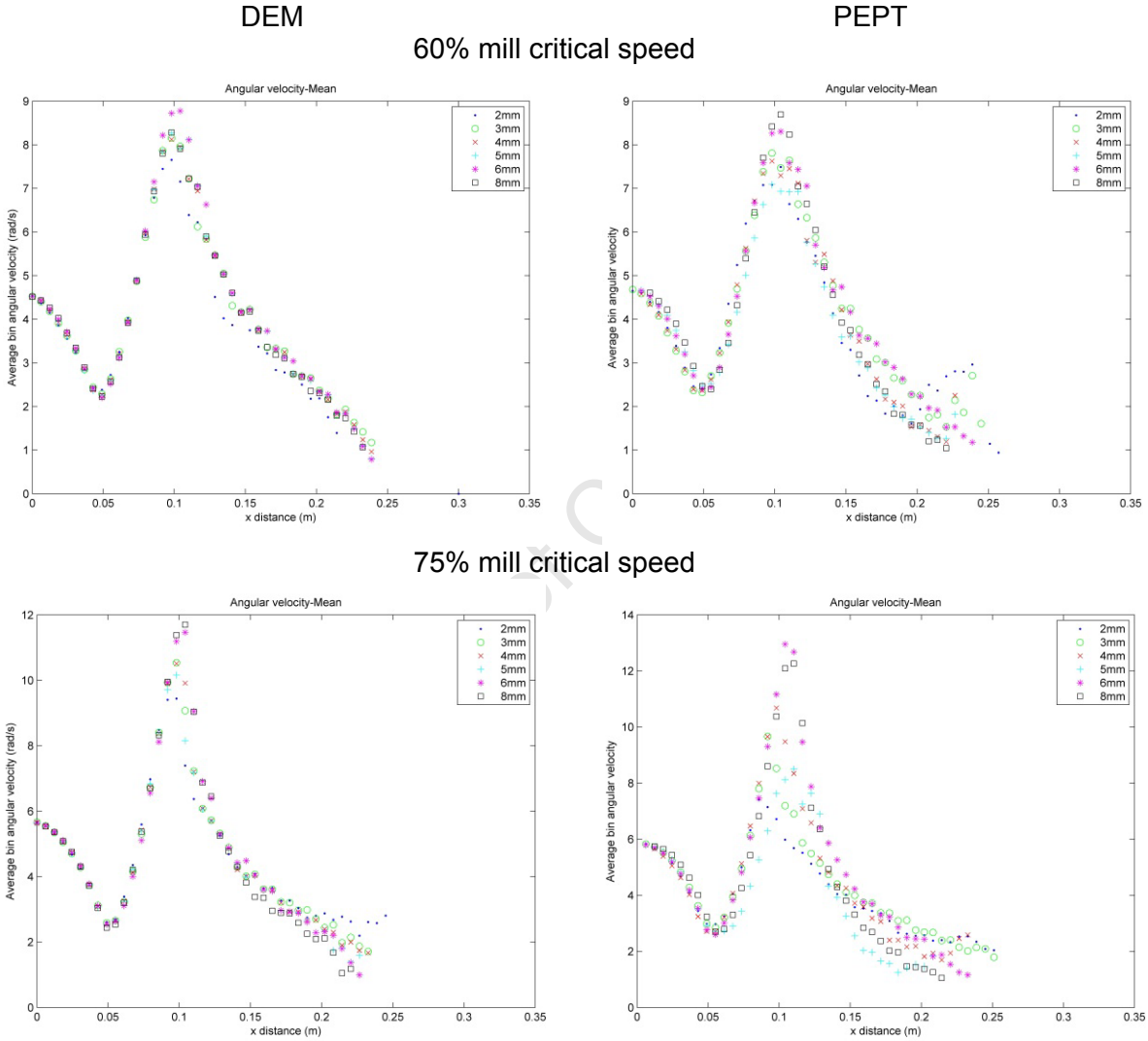

Figure 6.5: Plots of average angular velocity distributions along horizontal axis for full size distribution data

For all sizes, for both DEM and PEPT data, the velocity distributions followed identical trends at both mill speeds. Taking the zero position at the rising end of the internal mill radius, the average velocity at the initial position was approximately equal to the mill speed. The average velocity then decreased along an identical profile for all sizes until a minimum position. Over the interval until the local minimum point, although the packed granular body

consisted of different sizes, particles were lifted at identical speeds over each horizontal interval. Beyond this minimum, the average velocity at each interval then increased until reaching a peak in the cascading region, for which the looser packing of the descending body allowed for particles of different sizes to have distinctly different velocities. For both DEM and PEPT data, larger particles were observed to have higher angular velocities about this peak. This could be explained by the mass distributions which showed that the larger sized particles were more likely to be found closer to the centre of the mill. Larger sizes would tend to cascade with a shorter radial length leading to increased angular velocities while smaller particles, although descending with similar tangential velocities would follow a longer arc of greater radial distance, leading to lower angular velocities.

To mathematically describe the horizontal profiles of average angular velocities, the distributions were divided into two regions. The first covered the initial decrease of the velocities until the local minimum turning point. The second region began from this turning point to the end of the mill.

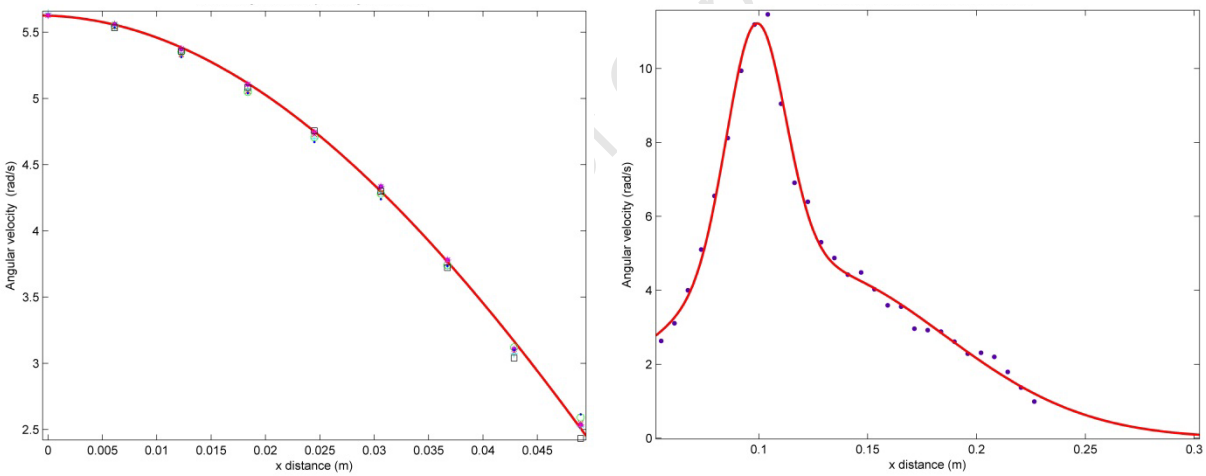

Figure 6.6: Two sections used to model the average angular velocity distribution along horizontal plane

For the first region a sine function of the form in Equation 6.14 could be used to model the decrease of angular velocities. This function was similar to the form of the sine function used to model the tangential velocity profile through the CoC (Equation 4.1). Three parameters were sufficient to describe this portion of the distribution. As the angular velocities of each size were closely similar in this region, a single set of parameters was fitted to data of sizes. Figure 6.6 (left) demonstrated a fit of the function to velocity data.

$$y = a_3 \cdot sin(b_3 \cdot x + c_3) \qquad \textbf{Equation 6.14}$$

In Equation 6.14 the independent variable *y*, the average angular velocity, was dependent on horizontal position *x* as a sine function of three fitted parameters a_3, b_3 and c_3. At the zero position the function was assumed to be equal to the angular mill speed. The rising velocity then decreased from this maximum value at a rate determined by the slip velocity between successive layers of charge. The value of a_3 was thus the mill speed, while c_3 was set to $\frac{\pi}{2}$ such that the maximum occurred at the zero value. The function then decayed depending on the value of the parameter b_3 until the local minimum position between the rising end of the mill and the centre.

Beyond this minimum, the average angular velocity could be modelled using a Gaussian distribution of two terms, as given in Equation 6.15.

$$y = a_4 \cdot e^{\left(-\left(\frac{x-b_4}{c_4}\right)^2\right)} - a_5 \cdot e^{\left(-\left(\frac{x-b_5}{c_5}\right)^2\right)} \qquad \textbf{Equation 6.15}$$

In this region, six parameters a_4, a_5, b_4, b_5, c_4 and c_5 were used to describe the velocity distribution of each size. The fitted parameters for all PEPT and DEM data were listed in Appendix A.

Several assumptions were employed to evaluate the parameter values for the two equations as a function of mill operating variables. For the first region described by Equation 6.14, the parameter b_3 was a multiplication factor which dictated the rate of decrease of average velocities inward from the mill periphery. This parameter would be influenced by the mill operating variables that affected the slip velocity of successive layers of charge, primarily the lifter geometry and mill speed. However, the parameter was not influenced by particle size, as it was found that the rising motion of the charge distribution followed an identical pattern for all sizes. It was assumed that the parameter b_3 could be determined using a fitting constant divided by the mill speed, as given in Equation 6.16:

$$b_3 = \frac{L_3}{\omega_m} \qquad \textbf{Equation 6.16}$$

According to the equation, the value of parameter b_3 decreased with increasing mill speed which signified that particle velocities decreased inward from the mill periphery at a lower rate. This was in accordance with the result (Section 4.2 and 5.2) that higher speeds would cause more particles to overcome slip effects and rise along with the mill. Angular velocities would thus decrease at a lower rate along the horizontal profile with an increase in speed.

The value of b_3 decreased with increasing speed until the maximum mill speed at which the highest lever arm distance from the mill centre x_{max}* occurred (see Section 6.2). Beyond this maximum speed, the charge began to centrifuge. To model this effect, beyond the speed at which the maximum power draw occurred, the average angular velocity of particles was equated to that of the mill speed to signify that the charge rotated with the mill.

Figure 6.7 provides a typical angular velocity profile for the second region, for which Equation 6.15 was used to describe the motion. The parameters which defined the shape of the profile are indicated in the diagram. Parameters b_4 and b_5 represent the horizontal positions of the respective peaks for each term, while a_4 and a_5 are the resulting angular velocities at these peaks. Parameters c_4 and c_5 are the widths of the distributions at half the vertical height of each peak.

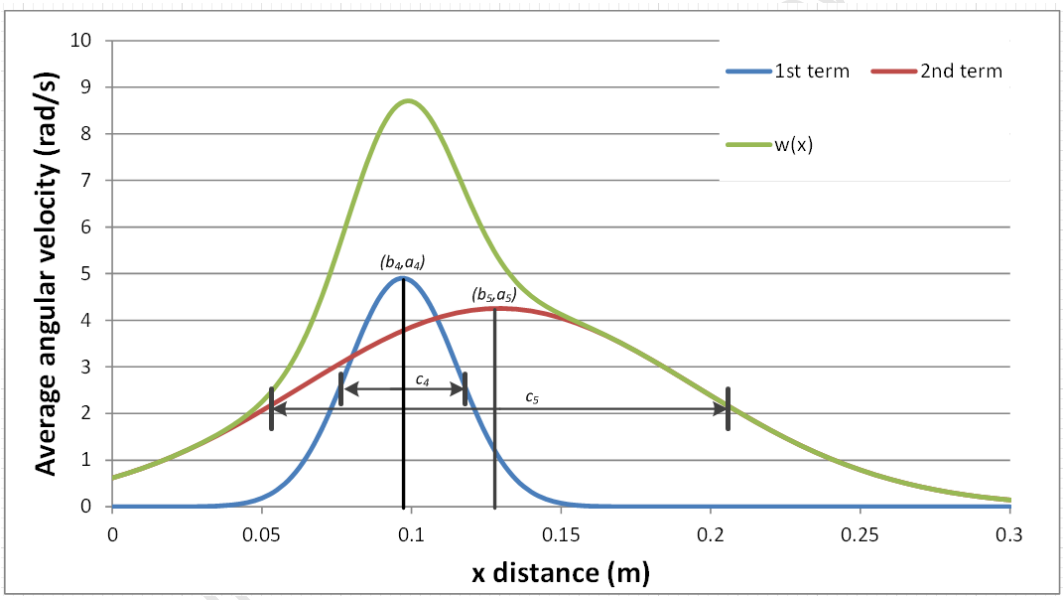

Figure 6.7: Typical average angular velocity profile in second region indicating parameters for each Gaussian function

Parameter b_4 was modelled to be the horizontal position of the mean. The width of the first term in the Gaussian distribution c_4 meanwhile was taken to equate to half the horizontal distance to the mode, as given by Equation 6.17:

$$c_4 = \frac{1}{2 \cdot T_2} \qquad \textbf{Equation 6.17}$$

In the impact toe region, the average angular velocity values were assumed to be equal independent of particle size and mill speed. This was consistent with spatial plots of velocity

from PEPT and DEM (see Sections 4.2 and 5.2). Parameter a_5 was therefore set as a fixed constant which represented the average angular velocity of charge particles in this region.

The value of b_5, the horizontal position of the second minor peak in the velocity function, was approximated to be three times the distance of the mode from the mill centre such that the position was equidistant to the length between the mean and mode, as given by Equation 6.18:

$$b_5 = \frac{3}{T_2} \qquad \textbf{Equation 6.18}$$

Meanwhile, the width c_5 was given by Equation 6.19 as equal to the distance to the mean:

$$c_5 = \frac{2}{T_2} \qquad \textbf{Equation 6.19}$$

The horizontal position of a_4 was where particles were found to have the highest average angular velocity. The maximum angular velocity was found to be a function of both mill speed and particle size, so that of a_4 could be calculated with the function given in Equation 6.20:

$$a_4 = L_4 \cdot p^{L_5} \cdot \omega_m^{L_6} - a_5 \cdot e^{\left(-\left(\frac{x-3\cdot T_2^{-1}}{2\cdot T_2^{-1}}\right)^2\right)} \qquad \textbf{Equation 6.20}$$

The physical interpretation of these parameters with regard to charge motion features is discussed in Section 6.3.

Based on the approach outlined above, the overall expression for the average angular velocity ω_p of each size p at a horizontal position x_v along the horizontal diameter the mill was given by the piecewise function Equation 6.21.

$$\omega_p(x_v) = \begin{cases} \omega_m \cdot sin\left(\frac{L_3}{\omega_m} \cdot x_v + \frac{\pi}{2}\right) & if\ x_v \le x_s \\ a_4 \cdot e^{\left(-\left(\frac{x_v - \bar{x}}{T_2^{-1}}\right)^2\right)} + a_5 \cdot e^{\left(-\left(\frac{x-3\cdot T_2^{-1}}{2\cdot T_2^{-1}}\right)^2\right)} & if\ x_v > x_s \end{cases} \qquad \textbf{Equation 6.21}$$

Here, x_s was the position of the local minimum in the rising region of the mill charge where the two functions intersected. The horizontal position of this intersection point could be found by solving for the value of x_v in the rising bulk region for which the difference between the

two functions was zero, as given by Equation 6.22. The physical significance of x_s and other parameters is summarized in Section 6.3.

$$\omega_m \cdot sin\left(\frac{L_3}{\omega_m} \cdot x_v + \frac{\pi}{2}\right) - a_4 \cdot e^{\left(-\left(\frac{x_v - \bar{x}}{T_2^{-1}}\right)^2\right)} + a_5 \cdot e^{\left(-\left(\frac{x - 3 \cdot T_2^{-1}}{2 \cdot T_2^{-1}}\right)^2\right)} = 0 \qquad \textbf{Equation 6.22}$$

6.3 Determination of charge motion features

While evaluating the values of the parameters used to describe the mass and velocity distributions was imperative, it was also of importance to consider their physical significance with respect to typical features used to describe charge motion.

Based on these distributions, several positions conventionally used to describe charge motion could be identified. Figure 6.8 demonstrated spatial distributions obtained from mono-size 5mm DEM data for average charge positions and average angular velocity. The schematic below these plots illustrated the mass and average velocity distributions arising from the spatial plots, for which parameters relating to charge motion x_s, x_e and x_t could be extracted.

The position of x_s, the intersection point of the piecewise angular velocity functions between the zero and the mill centre, was the horizontal position of the charge shoulder. As indicated in Figure 6.8, this was because the horizontal position where the minimum average angular velocity occurred was tangent to the equilibrium surface. This meant that a vertical line upward from x_s to the mill geometry provided the position of the charge shoulder for which charge particles of every size in the mill departed from the mill entering into either cascading or cataracting motion.

According to the angular velocity model in Equation 6.21, the horizontal position of the charge shoulder would be closer to the mill shell at low speeds, and the position would shift toward the centre with increasing speed as more charge would begin to cataract. This result was in agreement with existing power draw models such as Fuerstenau's (Fuerstenau et al., 1990) and Morell's (Morell, 1992) which indicated that the shoulder angle and angle of repose of the charge increased with mill speed to reflect that more charge was lifted, which would shift the horizontal position closer to the centre.

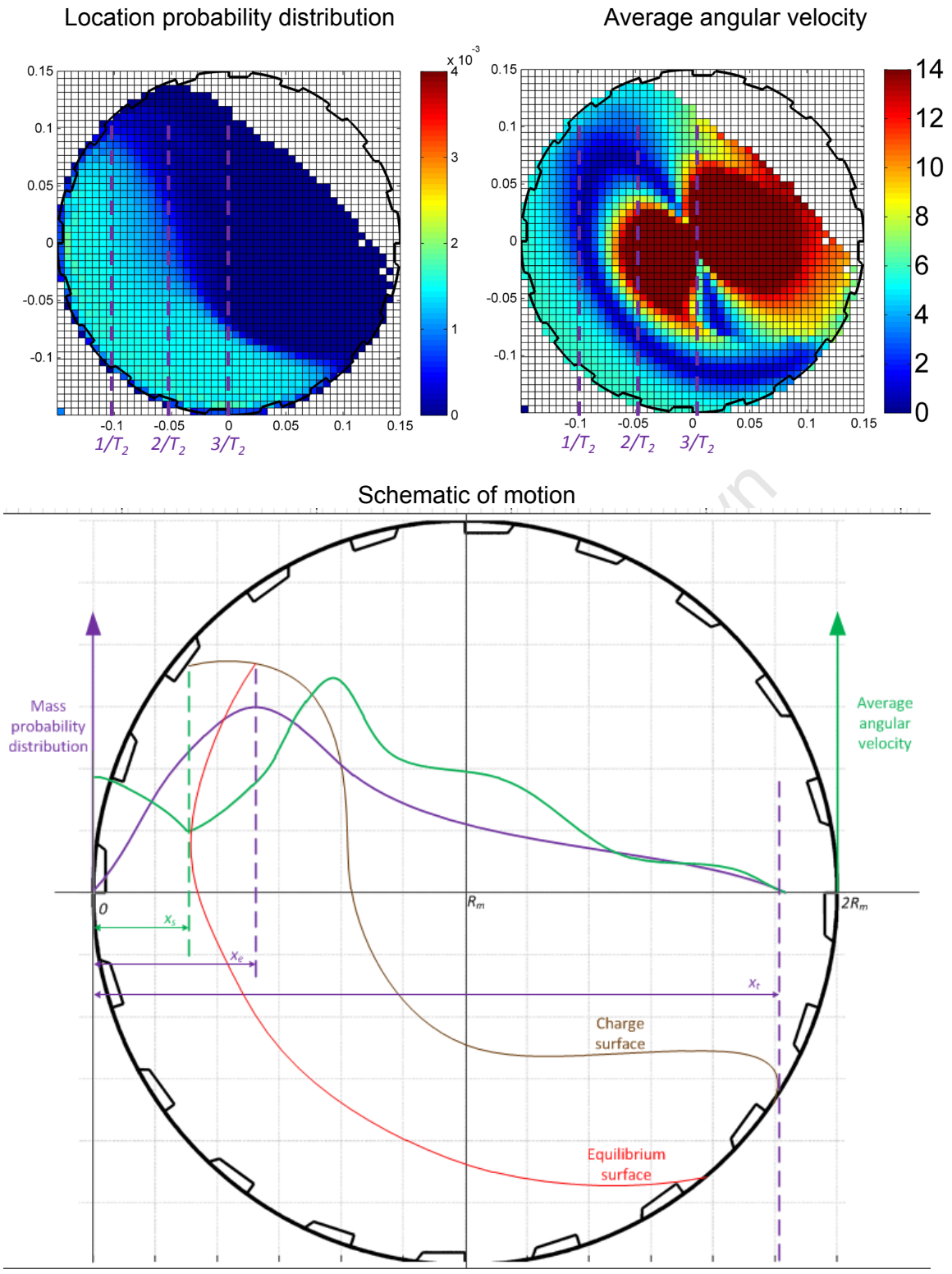

Figure 6.8: Schematic of horizontal positions that can be determined using mass and velocity distributions

The position of the shoulder continued to decrease with increasing speed until the point of centrifuging, at which point the shoulder position could no longer be used to describe the

charge motion. This was incorporated into the model by setting the average angular velocity as equal to the mill speed above the speed of the maximum power draw ω_{max}.

The mode was the position of the peak of the location probability distribution (see Sections 4.2 and 5.2). This position x_e was illustrated by the schematic to be the horizontal position at which there was the highest likelihood of finding particles of a given size. By comparing spatial plots of location probability and average angular velocity with the calculated positions of the mode, x_e was observed to be the intersection point of the equilibrium surface with the free surface. This was thus the likeliest position for which particles of a given size would transition across the equilibrium surface from rising into a cascading motion. The model calculated that the mode of smaller particles would be found closer to the mill shell than for larger particles. This was based on the calculation of the mass distributions for each size (see Section 6.2) which followed the trend that smaller particles were more likely to cataract at similar speeds than larger particles.

The mean particle position was twice the distance of the mode, x_e, from the mill shell. This position represented the centre of mass of charge particles in a given size class. It was noted from spatial distributions of the average angular velocity such as given in Figure 6.8, and the velocity model Equation 6.21 that at the mean horizontal position, angular velocities in the bulk region were at their maximum value.

The horizontal position of the impact toe of the cascading charge body was found to be approximately three times the distance of the mode from the mill shell. This meant that the distance between the mean and mode was equal to that between the mean and impact toe. On this basis, particles could thus be assumed to cascade between the mode and impact toe through a horizontal distance mirrored about the mean position.

Meanwhile, x_e was the horizontal position defined by the mode of the mass distribution. As illustrated, this was observed to indicate the horizontal position for which the charge particles of a given size would transition across the equilibrium surface from rising into a cascading or a cataracting motion. As the mode of smaller particles was found to be closer to the mill shell, this highlighted that smaller particles were more likely to transition across the equilibrium surface into cataracting motion than larger particles at similar speeds.

The bulk toe is the position of the intersection of the cascading charge with the mill (Powell and McBride, 2004). The bulk toe, x_t, could be visually identified using spatial location

probability distributions such as in Figure 6.8 to be the intersection point of the charge free surface with the mill. This information could be correlated with the model given in Equation 6.1 to calculate the threshold relative frequency for which the mass distribution decayed to the position of the bulk toe. From the average of threshold relative frequencies for all mass distributions calculated in this work, it was found that the position of the bulk toe was at approximately 0.35%. This meant that with the relative frequency set to 0.35%, or a value of 0.0035, the toe position x_t could be determined by calculating the solution of Equation 6.23 over discrete horizontal distances from the mill centre to the descending end of the mill. The toe position x_t could then be estimated as the midpoint of the interval.

$$0.0035 = \frac{e^{(-T_2 \cdot x_1)} \cdot (T_2 \cdot x_1 + 1) - e^{(-T_2 \cdot x_2)} \cdot (T_2 \cdot x_2 + 1)}{1 - e^{(-2 \cdot T_2 \cdot R_m)} \cdot (2 \cdot T_2 \cdot R_m + 1)} \qquad \textbf{Equation 6.23}$$

The distance of the bulk toe to the mill centre decreased with increasing speed. This was in agreement with existing power draw models such as Fuerstenau's (Fuerstenau et al., 1990) and Morell's (Morell, 1992), as it indicated that the bulk mass would increasingly be lifted along with the mill at higher speeds.

6.4 Power draw model

In Figure 6.9, a schematic of the overall approach taken to model the power draw was given. This method used the models given in Sections 6.2 and 6.3 to determine the mass and angular velocity distributions of the charge. With this information, a model for the power draw was developed with the mass distribution, angular velocity distribution and lever arm distance all expressed mathematically in terms of mill operating variables.

The internal mill diameter was discretized into *Q* intervals along the horizontal ordinate. The power draw of each size was then obtained using a summation of the products of mass and angular velocity contributions at each interval over the entire horizontal diameter as given by Equation 6.24.

$$P^*_{BIN(P)} = \sum_{n=0}^{n=Q} Pr_p\,(\Delta x_n) \cdot M_i \cdot g \cdot x_L \cdot \omega_p(x_v) \qquad \textbf{Equation 6.24}$$

Here, while *Q* is the number of terms used to compute the summation, x_n is the horizontal position along the mill given by Equation 6.26:

$$x_n = x_0 + n \cdot \frac{2 \cdot R_m}{Q}$$ **Equation 6.25**

The interval Δx_n used for the mass probability calculation is given by Equation 6.26:

$$\Delta x_n = x_n \leq x \leq x_{n+1}$$ **Equation 6.26**

Over this interval, the probability that particles of each size *p* can be found in the interval is calculated by Equation 6.27:

$$Pr_p(\Delta x_n) = \frac{e^{(-T_2 \cdot x_1)} \cdot (T_2 \cdot x_1 + 1) - e^{(-T_2 \cdot x_2)} \cdot (T_2 \cdot x_2 + 1)}{1 - e^{(-2 \cdot T_2 \cdot R_m)} \cdot (2 \cdot T_2 \cdot R_m + 1)}$$ **Equation 6.27**

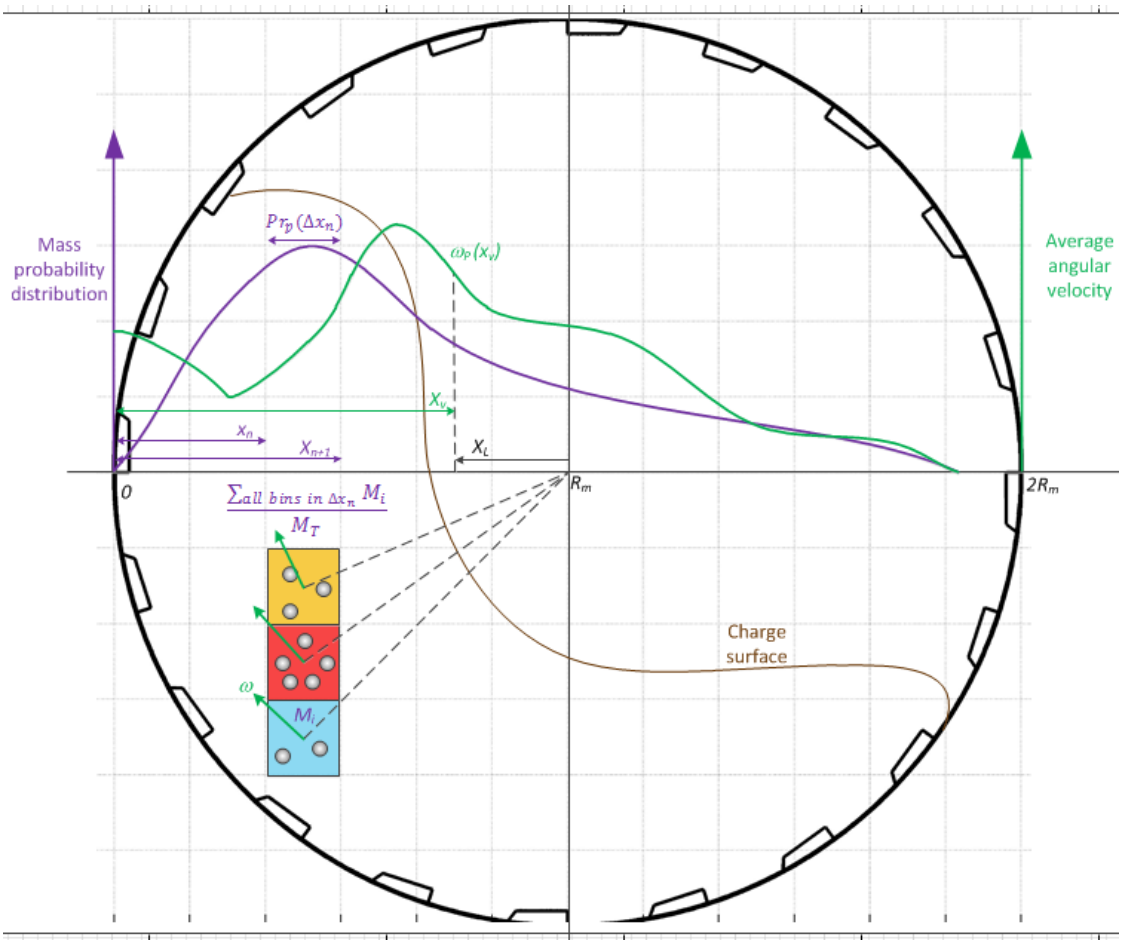

Figure 6.9: Schematic of overall approach taken to determine mass and velocity distribution

The parameter T_2 is calculated as a function of particle size, mill speed and mass fraction according to the methodology described in Section 6.2. To calculate the torque that the mass in each interval causes about the centre of the mill, the horizontal lever arm length x_L is expressed as the distance from the mill centre to the mid-point of each horizontal interval by Equation 6.28:

$$x_L = \left| \frac{x_n + x_{n+1}}{2} - R_m \right| \qquad \textbf{Equation 6.28}$$

Similarly, the horizontal position x_v for which the mean angular velocity for each interval is calculated is given by the mid-point of the horizontal position of the interval using Equation 6.29:

$$x_v = \frac{x_n + x_{n+1}}{2} \qquad \textbf{Equation 6.29}$$

Here, the angular velocity of each particle size is given by the piecewise function which describes the two velocity regions of the mill given in Equation 6.21.

Following this methodology, the power draw of each size class can be calculated and accumulated to obtain the overall power draw of the charge. To predict the power draw of the tests conducted in this study, several fitting parameters and mill properties had to be specified. These parameters were summarized in Table 6.2. As discussed in Section 6.2, the specified parameters were based on the range given in literature (Datta et al., 1999. Napier Munn et al., 1999. Wills and Napier Munn, 2006.) and were selected such that the model could be calibrated.

Table 6.2: Specified parameters and fitted constants for power draw model

Specified parameters	
Filling for maximum power draw (%)	50
Speed for maximum power draw (%)	90
Maximum lever distance from mill centre (m)	0.085
Fitted parameters	
L_2	48.00
L_3	8000 ($\omega_m < \omega_{max}$)
L_4	4
L_5	0.1
L_6	0.5

Table 6.3 listed the power draw predictions from the model compared to measured power draw values from mono size distribution experiments. The model predictions compared well with the measured power, and were able to describe the effect that, for the same mass fraction, smaller particles tended to draw a higher power draw than larger particles (see Section 5.2).

For full size distribution tests, power draw predictions for each size were also compared against calculations from both PEPT and DEM data, as well as the overall measured power. Table 6.4 listed the results of these comparisons which indicated that the model could be used to approximate the power draw of each size in the mill, which could then be accumulated to predict the overall mill power.

Table 6.3: Comparison of measured and predicted power draw from model for monosize tests

Size	*Speed*	P_{MEAS}	$P^*_{BIN(P)}$
(mm)	*(% crit)*	*(W)*	*(W)*
3	60	25.82	24.94
	75	32.31	32.81
5	50	19.69	19.11
	60	23.74	23.22
	75	29.83	30.1

Table 6.4: Comparison of DEM/PEPT power draw calculations with model predictions

	60% mill crit.			75% mill crit.		
Size (mm)	P_{PEPT} *(W)*	$P_{DEM\text{-}BIN}$ *(W)*	$P^*_{BIN(P)}$ *(W)*	P_{PEPT} *(W)*	$P_{DEM\text{-}BIN}$ *(W)*	$P^*_{BIN(P)}$ *(W)*
2	3.62	3.84	3.33	4.65	4.84	4.61
3	4.75	5.05	4.08	6.55	6.79	6.45
4	5.13	5.61	5.24	6.8	6.91	6.97
5	4.8	5.06	4.98	6.1	6.06	5.83
6	4.18	4.64	4.37	6.42	5.52	5.86
8	2.56	3.22	2.55	3.42	3.75	3.16
Total power	25.04	27.43	24.55	33.94	33.88	32.88
Measured power	25.5			34.12		

From the power draw model, distributions of the power draw for each size could be plotted to compare trends, as given in Figure 6.10. The model was a unique means of examining the power draw in the mill from the standpoint of the mechanisms that influenced the charge motion.

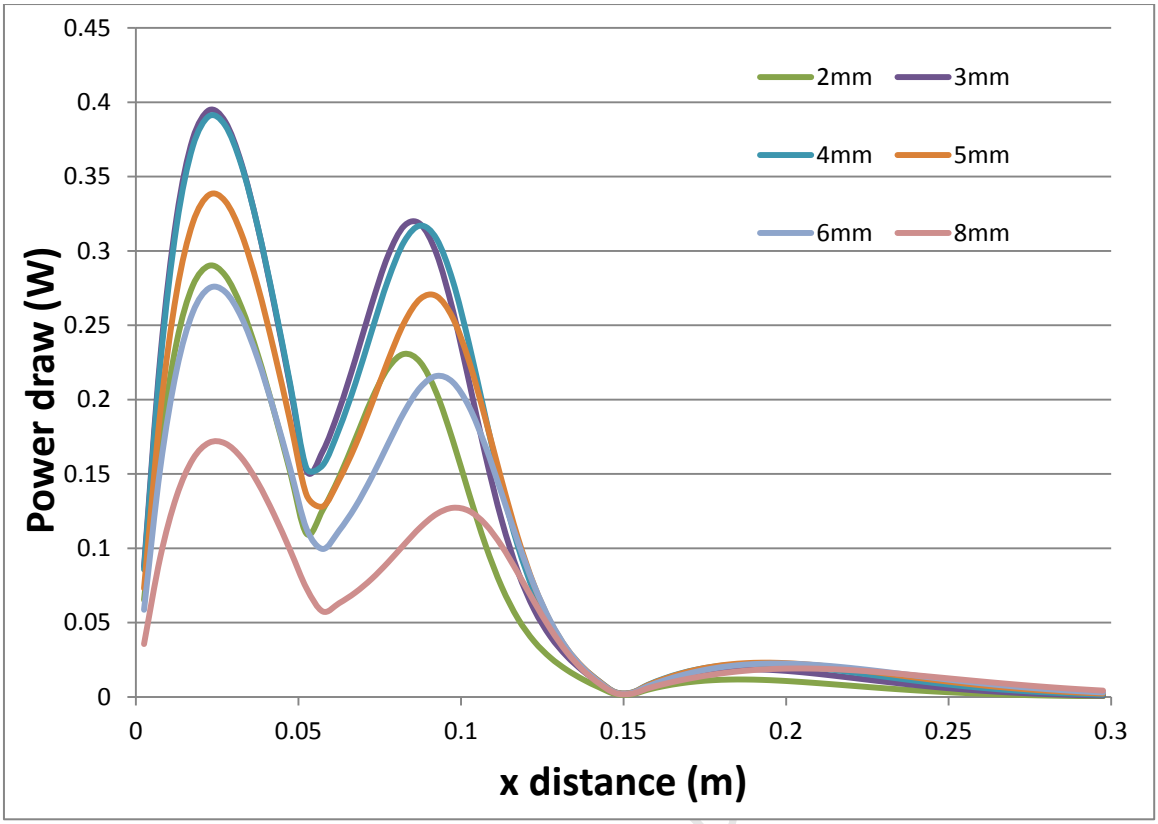

Figure 6.10: Power draw profiles obtained from power draw model for Full size distribution at 75% mill critical speed

CHAPTER 7

DEM ENERGY SPECTRA MODEL DEVELOPMENT

Overview
This chapter discusses collision and energy dissipation probability for a tumbling mill. The approach taken to develop the energy spectra model is then presented along with an investigation of its predictive capabilities.

7.1 Discussion of particle collision and energy dissipation probability

In Section 5.3, it was shown that energy spectra curves represented frequencies with which collisions occurred between discrete energy values during a single steady state revolution of the tumbling mill. The potential form of the model could be investigated by studying the particle collision probability with a view to using this information to predict the collision energy distribution in the mill.

From PEPT experiments, it was shown that the particle position oscillated along a path of varying amplitude along the axes *x* and *y* in the transverse plane (see Section 4.2). Its motion in both directions showed that the particle followed a path which visited virtually the entire area in this plane. Meanwhile, relative frequencies of particle locations along these axes indicated that the mean particle position was in the bulk region of the charge. In summary, although the particle followed a cyclical pattern which traveled over majority of the mill diameter, the most probable particle location, given by the mode of these distributions was in the rising bulk region of the charge.

With DEM, the energy dissipation in a collision between two bodies is a function of their respective properties and relative velocities (Zhu and Yu, 2002). According to frequency plots of particle velocities, it was shown in Section 5.2 that particles tended toward having low velocities. This could be explained by spatial plots of averaged absolute velocities, such as Figure 7.1(a) which indicated that the velocity in the bulk region, which was the most probable location of a particle, was relatively low. Spatial plots of power dissipation were plotted in Figure 5.13 which highlighted the areas of highest energy loss during the revolution of the mill. It was demonstrated that the region of highest energy losses was in the impact toe, where there was the highest velocity differential between falling particles in free flight and the relatively low velocity bulk body. From relative frequency distributions of the charge position, plotted in Figure 7.1(b and c), regions along the curve where high velocities

occurred could be isolated. These represented regions which had the potential to yield the highest energy losses.

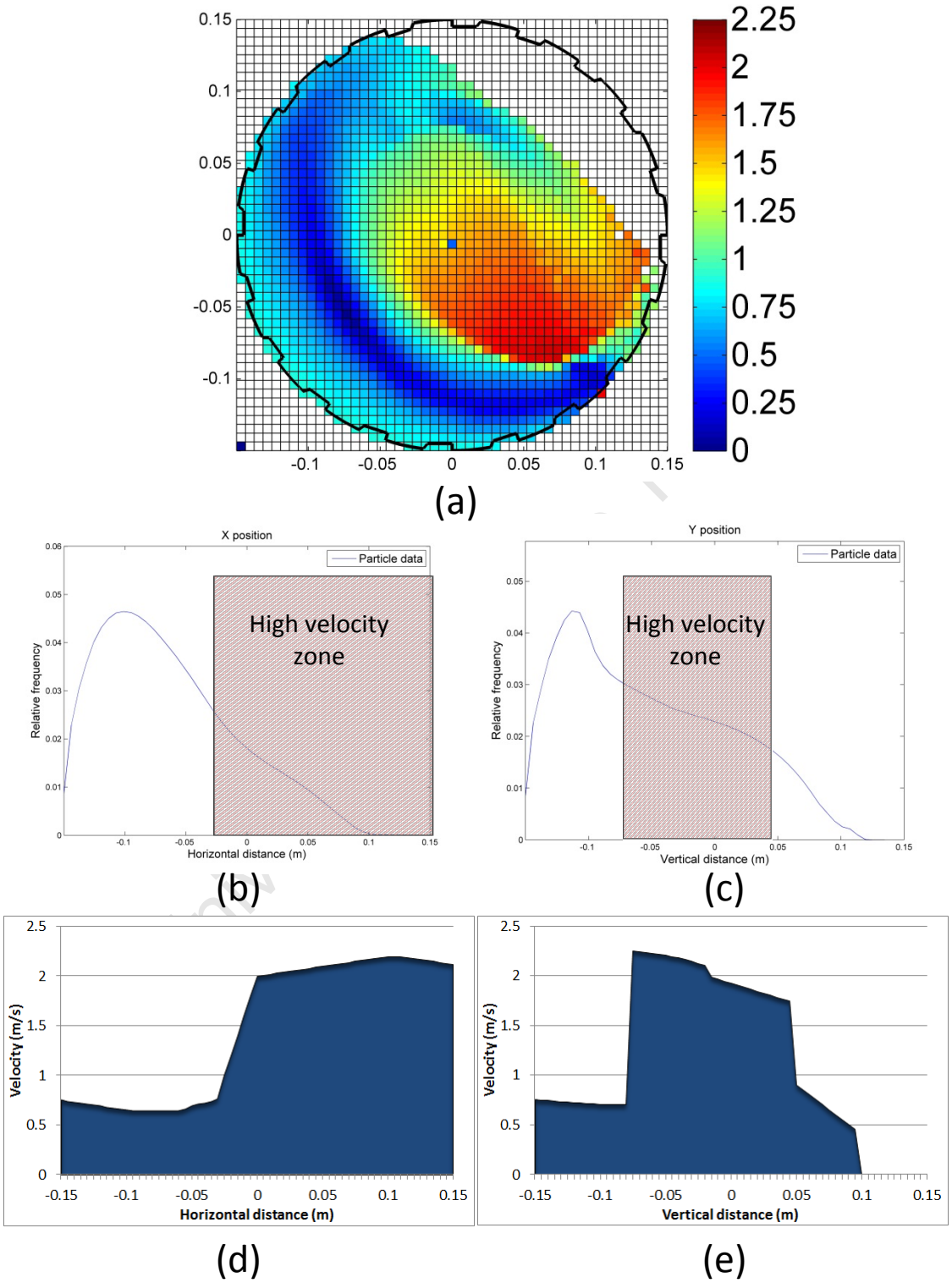

Figure 7.1: Plots of spatial velocity distribution (a), particle location probability (b, c) and velocity range (d, e)

The plots in Figure 7.1 (d and e) distributions demonstrated the velocity range (from zero to maximum) for particles at each position along the horizontal *x* and vertical *y* axes. It was observed that the region with the potential for the highest velocity differential between colliding particles occurred in the toe region, where the probability of finding particles was comparatively low. Furthermore, at each position along the axes although the velocity could vary between naught and the given maximum, frequency distributions such as Figure 5.5 demonstrated that the velocity would most likely be low.

From the foregoing, it can be concluded that for a given sized particle, the most probable location where it would collide with other particles would be in the bulk region, and in turn the most likely collision energy loss would be relatively low. The particle kinematic data can thus be used to infer the likely collision energy distribution for the entire charge.

The initial requirement to determine the probable collision energy was that two bodies were subject to a collision. The condition for a collision to occur between two spherical particles was that the particles were in single point contact, such that the distance between them was less than the sum of their respective radii. The probability that two particles were colliding at a given time, $Pr(C_{pp})$, can therefore be expressed as given in Equation 7.1:

$$Pr(C_{pp}) = Pr\left(\sqrt{(x_2 - x_1)^2 + (y_2 - y_1)^2 + (z_2 - z_1)^2} \leq R_2 + R_1\right) \quad \textbf{Equation 7.1}$$

Where:

(x_1, y_1,z_1) – Coordinates of centroid of first particle with reference to mill centre

(x_2, y_2,z_2) – Coordinates of centroid of second particle with reference to mill centre

R_1, R_2 – Radii of the two particles

A collision can also occur between a particle and the mill shell. This collision probability $Pr(C_{pm})$ can be expressed as given in Equation 7.2:

$$Pr(C_{pm}) = Pr\left(\sqrt{(x_1)^2 + (y_1)^2 + (z_1)^2} - R_1 \geq R_m\right) \quad \textbf{Equation 7.2}$$

In Equation 7.2, R_m is the inner radius of the mill. Both particle-particle and particle-mill interactions are regarded as collisions. The overall collision probability at a given time can be regarded as a discrete random variable of two elements, one in which collisions occurred and the other in which they did not, as given in Equation 7.3:

$$Pr(C_Y) + \Pr(C_N) = 1 \quad \textbf{Equation 7.3}$$

Here $Pr(C_Y)$ and $Pr(C_N)$ represent the probability that a collision occurred and did not occur respectively. The probability $Pr(C_Y)$ included both particle-particle $Pr(C_{pp})$ and particle-mill shell $Pr(C_{pm})$ collision probabilities.

Having met the requirement that a collision had occurred, the probability that this collision would take place between two arbitrary energy limits E_1 and E_2 can be expressed by the relative velocity between particles at the point of impact by Equation 7.4:

$$Pr(E_1 \leq E \leq E_2) = Pr[E_1 \leq \zeta \cdot (v_1 - v_2) \leq E_2] \qquad \textbf{Equation 7.4}$$

ζ is the damping coefficient, while v_1 and v_2 are the respective particle velocities at the point of impact. This probability is a continuous random variable as the energy can vary between the least value (at E_0 –see Section 5.3) and the maximum.

Thus, for a given time the overall collision energy dissipation probability of a given particle can be given according to conditional probability (discussed in Section 2.4) by Equation 7.5:

$$Pr(E_1 \leq E \leq E_2 | C_Y) = \frac{Pr[(E_1 \leq E \leq E_2) \cdot C_Y]}{Pr(C_Y)} \qquad \textbf{Equation 7.5}$$

With frequencies of particle collisions at different dissipation energies recorded for a mill over a single revolution at steady state, the relative frequencies between discrete energy intervals could be taken to represent the probability for that interval (see Section 2.4). In DEM, for a tumbling mill charge containing P particles the number of potential particle pairs at each discrete time-step was $\frac{P \cdot (P-1)}{2}$ (Mishra, 2003). This meant that for a simulation of 100,000 particles, there were almost 5 billion potential particle pairs present that could represent collisions.

Based on the location probability for a given particle, as the most probable location was in the bulk region of the charge, it was most likely that at a given time a particle would have at least several particle pairs with which it was in contact. Therefore, if one assumed that, at an instantaneous time-step, of the 5 billion possible pairs, $Pr(C_Y)$ was a conservative estimate of ~0.1 to 0.3, millions of collisions would have to be distributed over the energy interval from zero to the highest collision energy. This would further be multiplied by the total number of time-steps over the mill revolution.

For the tumbling mill used in this work, the maximum collision energy can be estimated from the highest kinetic energy generated by the moving particle. A calculation of this energy

using the mass of the largest particle (8mm) at 75% mill critical speed yielded a value of about 1.2 milli-Joules. For this example, several billion collisions would have to be divided over discrete energy intervals between E_0 and this value.

As shown by Equation 7.4, the probability that a collision would occur with a specific energy loss primarily relied upon the collision taking place between particles with a particular relative velocity v_1-v_2. For a selected random particle in a mono-size charge, its most probable position would be in the bulk charge, where the relative velocities between it and neighbouring particles would be low. For the entire charge body of that size it can be deduced that the likelihood of high energy dissipation between colliding particles would be very low. If assorted in discrete energy bands, frequencies of collisions then decreases with increasing energy.

For the example discussed above, millions of collisions would be apportioned over the relatively short energy interval from E_0 to 1.2 *mJ*. This requires that the intervals were sufficiently small to capture this decrease. Second, as frequencies decay from millions to zero, the decrease in frequency is of orders of magnitude with increasing energy. The probability distribution is thus an asymmetrical curve heavily skewed toward the lower end of the energy scale by the relatively high collision probabilities at these values.

As indicated by Equation 7.1, Equation 7.2 and Equation 7.4, the collision probability for particles in the charge body is a function of their radii and that of the mill. The particle collision probability distribution is influenced by factors such as mill velocity, internal geometry and the particle material properties and number present. The main factors that influence the collision probability are:

- Particle radius, mass, number of particles
- Particle velocity, trajectory
- Mill radius, geometry, velocity

The primary focus of this work was to model the influence of size on the energy spectra. The influence of particle size was investigated using the particle diameter, as size distributions typically quote particle diameters and not radii. The number of particles in the mill is expressed as a total volume. Dividing this volume by that of the mill gives the total volumetric filling. According to the work of Yang et al. (Yang et al., 2008) the velocity distribution of the charge can be expressed as a scalar multiple of the mill velocity through a probability

distribution. This distribution is influenced by factors such as the particle size, mill diameter and number and geometry of lifters. The velocity distribution of each size is related to the mill rotational speed and can be expressed as a function of the percentage mill critical speed. In this work the variables considered to have an influence on the energy spectra were:

- Particle size
- Mass fraction
- Mill speed
- Mill volumetric filling

As discussed in Section 2.2, many researchers have investigated the effect of these variables on the energy spectra. In this work, DEM simulations were conducted to quantify this influence with a view to using it to develop a model for the energy spectra. The next section describes the approach that was taken toward the formulation of this model.

7.2 Formulation of Energy Spectra model

In Section 5.3, it was demonstrated, using results extracted from DEM simulations, that collision frequencies between discrete energy bands could be displayed in a form known as an energy spectra plot. These distributions, such as Figure 5.14, indicated the total collision frequencies over a single steady state mill revolution, and represented the total power dissipation at steady state.

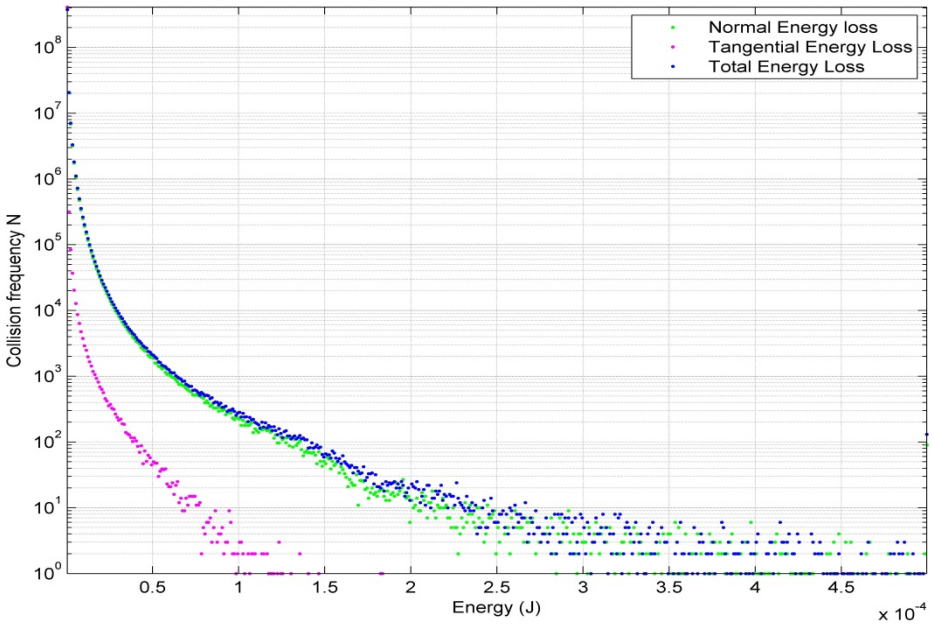

Figure 7.2: Energy spectra curves plotted with a logarithmic scale on the y axis alone

With the collision data in Figure 5.14 plotted as individual points, and a logarithmic scale applied to the collision frequency (y-axis) alone, the plot illustrated in Figure 7.2 is obtained. A similar trend was found for all energy spectra curves from DEM simulations performed in this study. This pattern suggested that the decrease in collision frequencies with respect to increasing collision energy followed an exponential decay.

The decay trend relating the logarithm of collision frequencies to energy can be expressed with an exponential function. Initially a two parameter exponential function in Equation 7.6 with fitting parameters K_1 and K_2 was used to relate collision frequency N to energy E.

$$Log(N) = K_1 \cdot e^{-K_2 \cdot E} \qquad \textbf{Equation 7.6}$$

Figure 7.3 showed an example of the least squares fit for the two parameter function to the total energy loss data given in Figure 7.2. Although the predictions from the equation followed the general trend of the simulation data correctly, it underestimated collision frequencies at the high energy scale, and overestimated values at the mid-range scale. Similar results were obtained when testing this function against other energy spectra data, indicating that the two parameter form was inadequate.

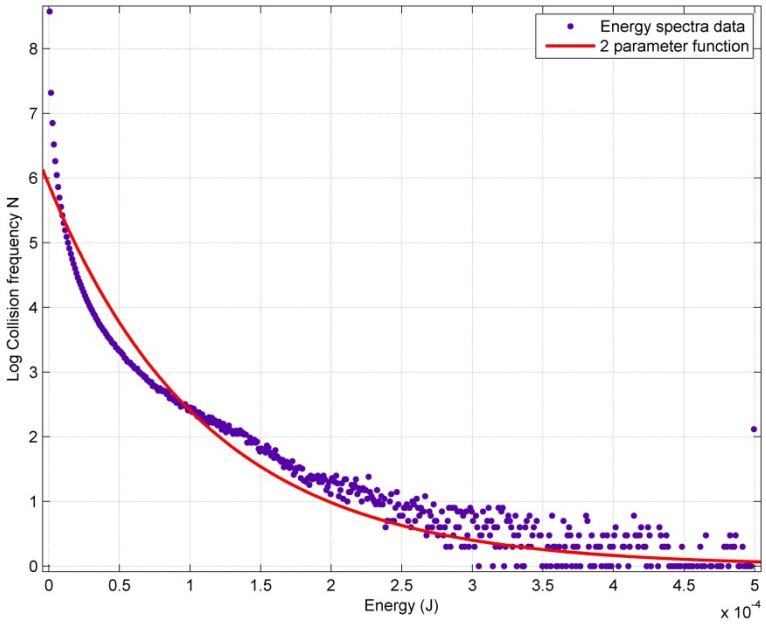

Figure 7.3: Two parameter exponential function fitted to total energy loss data

$$\log(N) = K_1 \cdot e^{-K_2 \cdot E} + K_3 \cdot e^{-K_4 \cdot E} \qquad \textbf{Equation 7.7}$$

A four parameter form of the model, given in Equation 7.7 was then attempted, with K_1 to K_4 as the fitted parameters. The least squares form of this function fitted to the same energy spectra data yielded the result shown in Figure 7.4. It was observed that the model captured the decay of collision frequencies with increasing energy well.

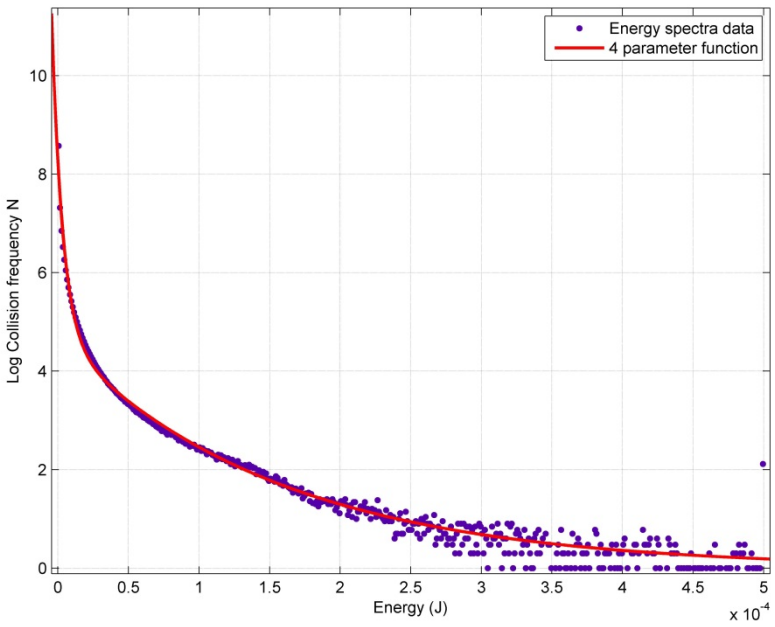

Figure 7.4: Four parameter exponential function fitted to energy spectra data

Quantitative examinations of the regression statistics for fits using Equation 7.6 and Equation 7.7 are given in Table 7.1. The coefficient of determination (R^2), sum of square error (*SSE*) and root mean square error (*RMSE*) show that the four parameter function had a better fit than the two parameter function. The R^2 value for the four parameter function was 0.99 and the SSE 7.84, compared to 0.84 and 96.86 for the two parameter function respectively.

Table 7.1: Comparison of regression statistics for two and four parameter functions fitted to the same energy spectra data

				95% conf. interval (% of value)			
Model	R^2	*SSE*	*RMSE*	K_1	K_2	K_3	K_4
2 parameter	0.813	96.86	0.583	1.94	3.94	-	-
4 parameter	0.993	7.84	0.166	1.42	2.32	3.31	6.78

Equation 7.7 was then fitted to all the energy spectra data from the simulations conducted in this study, and was found to give similarly good matches. The entire dataset of fitted parameters for all simulations along with error statistics are provided in Appendix B.

7.3 Interpretation of model parameters and simulation database

Prior to determining the effect of mill operating variables on the model parameters, it was important to understand the significance of each factor with regard to determining a given value of collision frequency. For this work, the model that was used to describe the energy spectra was given in Equation 7.7.

The key difference between the two exponential terms that composed the model was the decay rate, where the parameter K_4 gave a much greater decay rate than the other, K_2. At the artificial initial collision energy of zero, the frequency predicted by the model was the sum of the first and second initial value terms K_1 and K_3. The sum of these parameters represented the maximum number of collisions that could be obtained at any given energy. Parameters K_2 and K_4 meanwhile were the rate at which the respective initial value terms decreased with increasing energy.

Equation 7.7 was used to develop the probability distribution for collision energy per given particle size in the mill during a revolution. The energy spectra could be separated into various components, such as particle to particle losses, particle to mill shell losses, normal and tangential energy losses. However, as the focus of this study was the total power dissipation, which equated to the power draw at steady state, the scope was limited to modelling the total energy losses to each size for a single mill rotation.

A data base of DEM simulations was created for this thesis to investigate the energy spectra at different mill operating conditions, with a view to developing the model. These simulations were conducted using the methodology described in Section 3.3. Chapter 5 showed that this procedure produced a realistic representation of the mill environment which matched experimental results from PEPT data and power draw measurement. For these additional simulations, four mill speeds and fillings were investigated, and an identical size distribution of charge material was retained. Table 7.2 shows all the numerical simulations that were conducted in this work.

Table 7.2: DEM simulations conducted to develop energy spectra model

Mono-size					Full size distribution			
No.	Speed (%crit.)	Filling (%)	Size (mm)		No.	Speed (%crit.)	Filling (%)	Size (mm)
1	50	31.25	3		20	60	31.25	2
2	60	31.25	3		21	60	31.25	3
3	75	31.25	3		22	60	31.25	4
4	50	31.25	5		23	60	31.25	5
5	60	31.25	5		24	60	31.25	6
6	75	31.25	5		25	60	31.25	8
7	90	31.25	5		26	75	31.25	2
8	50	31.25	8		27	75	31.25	3
9	60	31.25	8		28	75	31.25	4
10	75	31.25	8		29	75	31.25	5
11	90	31.25	8		30	75	31.25	6
12	100	31.25	8		31	75	31.25	8
13	75	25	5		32	90	31.25	2
14	75	31.25	5		33	90	31.25	3
15	75	37.5	5		34	90	31.25	4
16	75	12.5	8		35	90	31.25	5
17	75	25	8		36	90	31.25	6
18	75	31.25	8		37	90	31.25	8
19	75	50	8					

7.4 Energy Spectra model

The exponential energy spectra model in Equation 7.7 had four parameters. Of these, the decay rates K_2 and K_4 were the two that most influenced the shape of the distribution, and in turn the number of collisions that would be predicted over a particular interval given an initial number of collisions at the minimum energy value. The decay rates K_2 and K_4 of Equation 7.7 were linearly regressed against the four mill operating variables discussed in Section 7.1. The methodology followed for this was based on the standard approach for the modelling of probability functions (Helstrom, 1984), which is summarized in Appendix B. The form of the energy spectra model that predicts collision frequency N in the tumbling mill as a function of energy E is proposed to be as follows:

$$log_{10}N = A \cdot e^{B\cdot\left(\frac{-1}{p\cdot\sqrt{\omega_m\cdot c}\cdot\sqrt[3]{J}}\right)\cdot E} + C \cdot e^{D\cdot\left(\frac{-\sqrt[3]{J}}{p\cdot\sqrt{\omega_m\cdot c}\cdot}\right)\cdot E} \quad \textbf{Equation 7.8}$$

In Equation 7.8 *p, ω_m, c* and *J* are the particle size, fractional mill critical speed, mass fraction and fractional volumetric filling respectively. The particle size is the diameter in metres, and *A, B, C* and *D* are fitted parameters.

The base 10 logarithm for *N* was chosen for convenience, such that the order of magnitude of collisions (10, 100, 1000 etc.) could be ascertained from the output of the model. The collision frequency *N* is a dimensionless quantity as it is a count of the total number of collisions that occur during a mill revolution. Consequently the right hand side of Equation 7.8 has to be dimensionless to maintain homogeneity. While mill speed and volumetric filling are expressed as dimensionless quantities in the model, particle size is given in metres and collision energy in Joules. Fitting parameters *B* and *D* have units of Newtons while *A* and *C* are dimensionless.

The best fit values for the parameters were obtained using multiple linear regression using the entire DEM simulation database in this work (see Appendix B). The fitted parameters *B* and *D* were found to be 14.34 and 800.01 respectively. For Equation 7.8 to maintain homogeneity, these parameters had units of Newtons. In order to subsequently test the overall predictions of the energy spectra curves against the simulation data, the model was initially converted to a probability density function such that points that characterized the distribution, (for example the mean) could be compared.

In Section 7.2, the parameterized form of the energy spectra model is given by Equation 7.7. Using the standard definition of logarithms (Stewart, 2010), the direct relationship for collision frequency *N* as a function of energy *E* is Equation 7.9:

$$N = 10^{K_1\cdot e^{-K_2\cdot E} + K_3\cdot e^{-K_4\cdot E}} \quad \textbf{Equation 7.9}$$

The total energy dissipated by the tumbling mill during the steady state revolution is then the integral of Equation 7.9 from the minimum energy E_0 to the maximum energy E_{max}, given by Equation 7.10:

$$E_{diss} = \int_{E_0}^{E_{max}} 10^{K_1\cdot e^{-K_2\cdot E} + K_3\cdot e^{-K_4\cdot E}} dE \quad \textbf{Equation 7.10}$$

Here, E_0 is the sub-minimum collision energy determined according to the procedure given in Section 5.3. E_{max} is the energy at which the frequency distribution decays to approximately 10^0 collisions. The dissipated energy divided by the mill periodic time is the total power lost to collisions during the rotation. At steady state, this is equivalent to the power draw of the mill (Mishra et al., 1990).

In Equation 7.9, as N provides frequencies at specific energy values E, the probability of having a collision between two energy limits E_1 and E_2 can be calculated by determining the integral of this function between the two limits divided by the total energy dissipated. Consequently the continuous probability density function to determine the probability that a collision will occur between energy values E_1 and E_2 (over the interval from E_0 to E_{max}) is Equation 7.11:

$$Pr[E_1 \leq E \leq E_2] = \frac{\int_{E_1}^{E_2} 10^{A \cdot e^{-B \cdot E} + C \cdot e^{-D \cdot E}} dE}{\int_{E_0}^{E_{max}} 10^{A \cdot e^{-B \cdot E} + C \cdot e^{-D \cdot E}} dE} \qquad \textbf{Equation 7.11}$$

Evaluating the integral of the energy spectra model is non-trivial as the integrand is a double exponential equation of N with respect to energy E. The solution of the numerator and denominator is consequently evaluated numerically in this thesis by Tanh-Sinh quadrature (see Section 2.4), a method prescribed for double exponential functions by Takahashi and Mori (Takahashi and Mori, 1974). The procedure followed to calculate this numerical approximation is presented in Appendix B.

The cumulative distribution function of the probability density up to any point less than E_{max} can be determined by integrating the numerator in Equation 7.11 using E_0 for E_1 and the specified point E_α as E_2 to give Equation 7.12:

$$F(E) = P(E_0 \leq E) = \frac{\int_{E_0}^{E_\alpha} 10^{A \cdot e^{-B \cdot E} + C \cdot e^{-D \cdot E}} dE}{\int_{E_0}^{E_{max}} 10^{A \cdot e^{-B \cdot E} + C \cdot e^{-D \cdot E}} dE} \qquad \textbf{Equation 7.12}$$

The number of collisions at the mode was determined using the energy spectra from the DEM data and energy spectra model using the energy value E_0. The mean and median of the distributions were also determined according to the standard procedure for probability density functions (Ross, 2009). These terms are customarily used to describe the trend of probability functions and were used as a basis to compare the DEM data and model predictions. Tanh-Sinh quadrature was used to evaluate the integrals required for the mean value (see Appendix B).

An energy termed the E_{90} was introduced in this work to represent the energy for which the cumulative distribution function was equal to 0.9. This value was the energy below which 90% of collisions occurred, or conversely the energy above which only 10% of collisions would be predicted to occur. This was calculated to provide an indication of the energy range at which relatively high energy collisions occurred for a particular mill operating condition.

In addition, as it would be of interest to quantify the number of collisions that occurred at relatively higher energies, a quantity named the N_{100} was defined. This value was the energy at which the distribution decayed to 100 collisions. The N_{100} provided another useful measure of the rate of decay of the energy spectra.

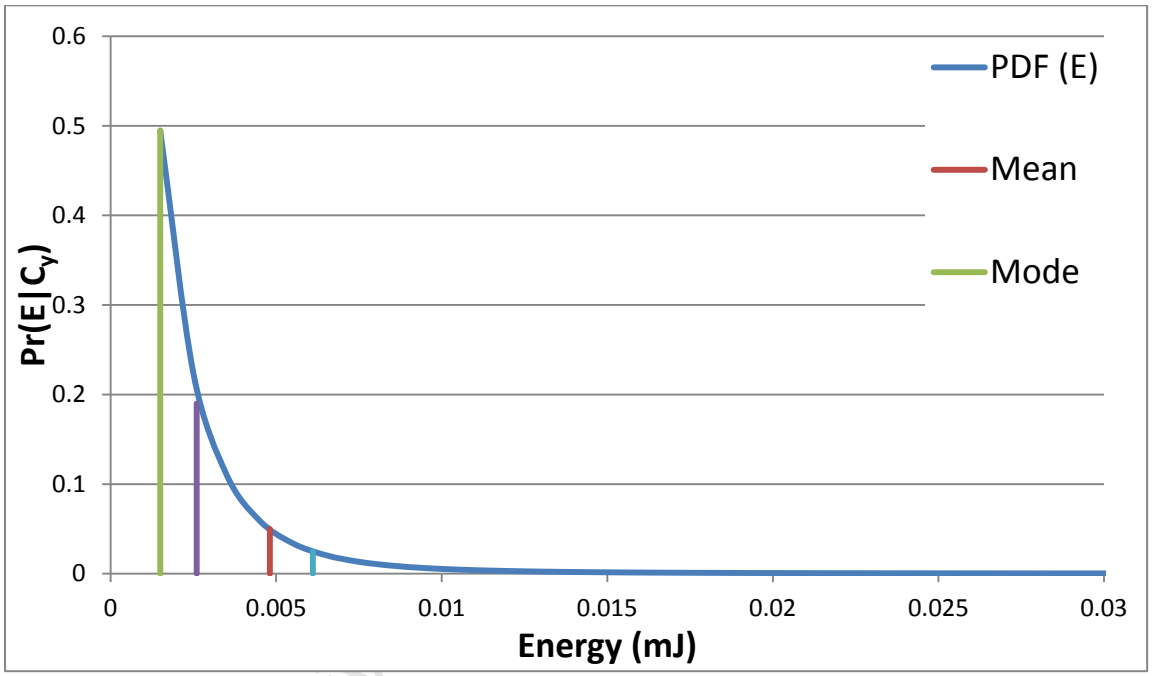

Figure 7.5: Example of a probability density function for the energy spectra

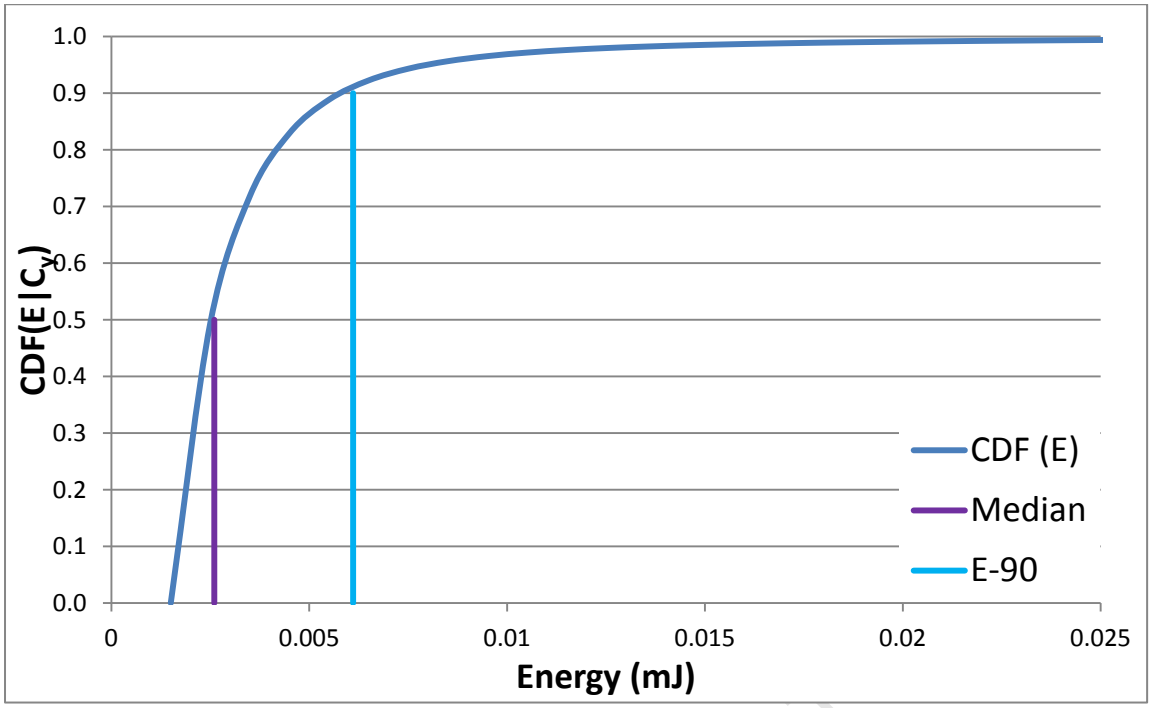

Figure 7.6: Example of a cumulative distribution function for the energy spectra

Figure 7.5 and Figure 7.6 demonstrate examples of the probability density and cumulative distribution functions obtained for 5mm mono-size glass beads at 75% mill critical speed and 31.25% volumetric filling. In Figure 7.5, the mean, mode, median and E_{90} positions of the distribution are identified. It was observed that, due to the dominance of the number of low energy collisions, the median and mean were very low over the energy range for which collisions occurred. Figure 7.7 illustrates the energy spectra plot for this distribution. This curve demonstrated that, while there were orders of magnitude more collisions at lower energies, there were a substantial number of collisions at the tail end of the distribution. This was indicated by the position of the N_{100} at approximately 0.17 *J*.

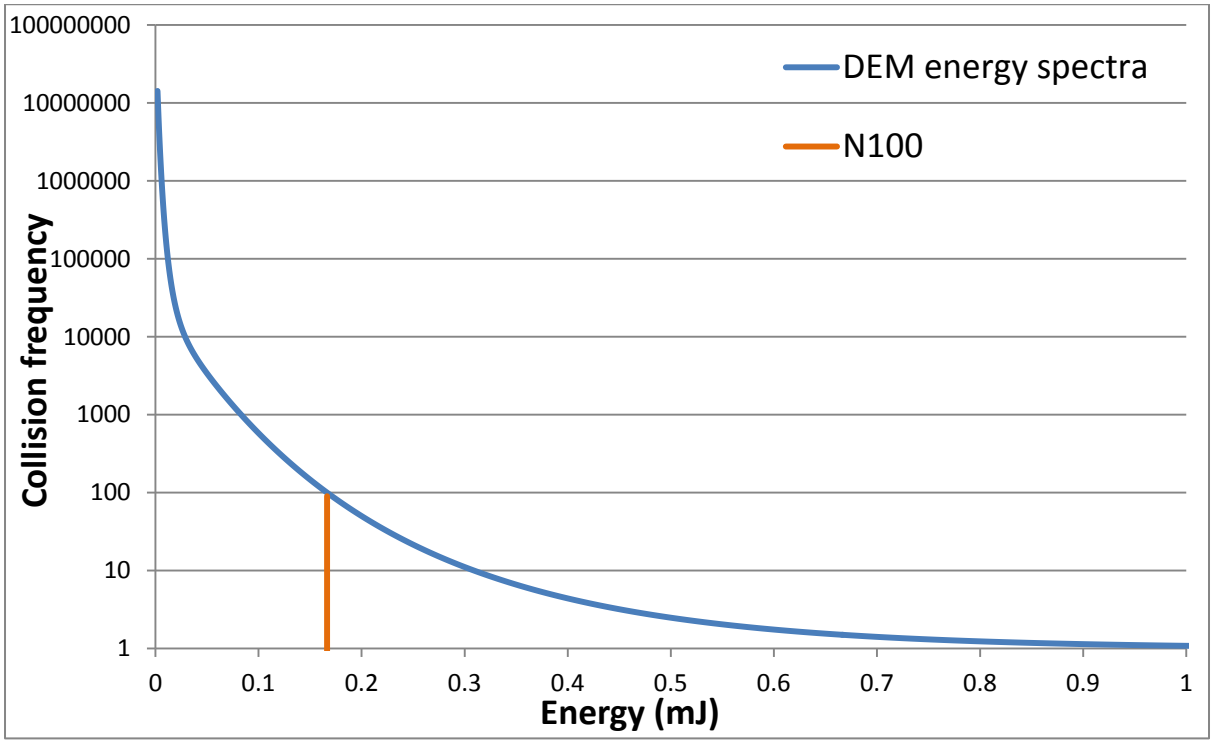

Figure 7.7: Energy spectra curve with the position of the N_{100} indicated

The energy spectra model was tested by comparing predictions of the five quantities described to data from DEM simulations. The accuracy of these predictions was evaluated by means of graphical plots as well as the coefficient of determination (R^2) and adjusted R-squared (R^2_{adj}) values. These were calculated following the methodology outlined in the work by Helstrom (Helstrom, 1984).

For graphical plots, the closer the data points are to the 45-degree parity line, the better the model predictions for a given value. Meanwhile the R^2 value provides a quantitative measure of how well the regression model fits to the DEM simulation and how close future predictions would likely be. An R^2 closer to 1 indicates that the model fits the data well while a value closer to zero indicates a poor prediction. The R^2_{adj} is a measure of the proportion of the data accounted for by the regression model, and gives an indication of the degree of mismatch in the predictions due to lack of fit, missing variables or basic error. If the R^2_{adj} is much lower than the R^2_{adj} value, it is an indication the regression equation may be overfitted to the sample, and of limited generalizability.

Mode

The mode is the energy for which the probability density function has its maximum value (Ross, 2009). As shown in Figure 7.5, the mode of the energy spectra model is consistently at the minimum energy value of E_0.

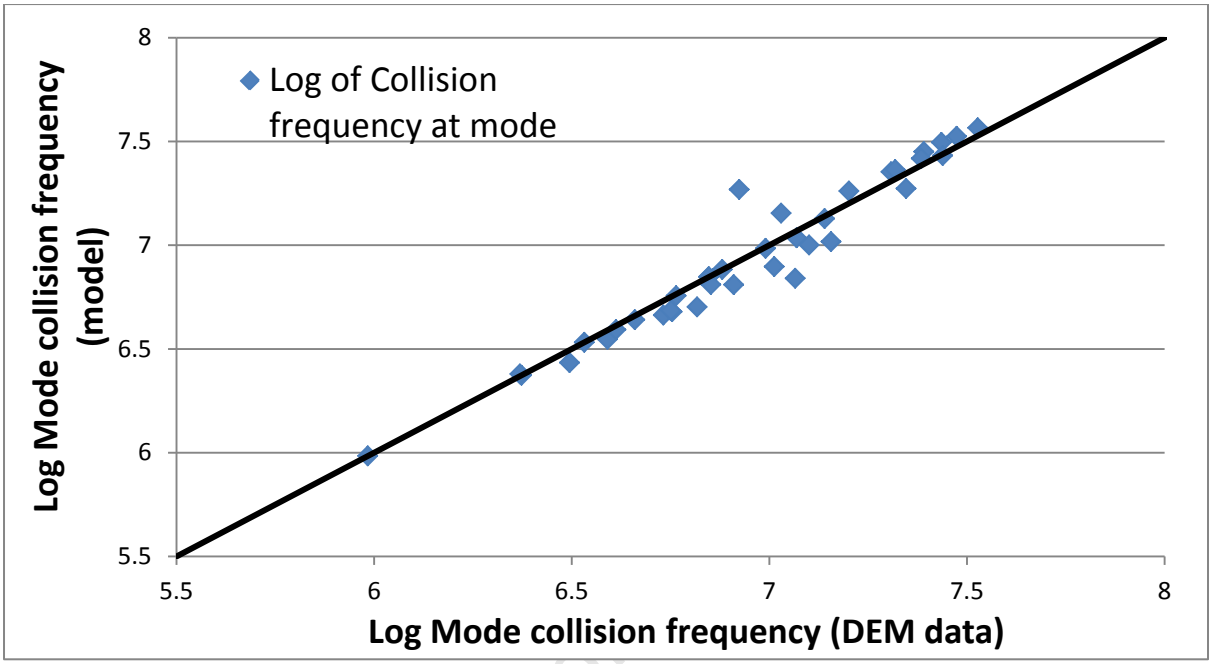

Figure 7.8: Comparison of the calculated and predicted mode for the energy spectra data from all conducted simulations

Figure 7.8 shows the comparison between the value of the collision frequency at the mode $\log_{10}(N)$ determined from DEM simulations against that predicted by the model. The model predicts the DEM data fairly well as majority of the values lie close to the 45-degree parity line. The R^2 value for this prediction is 0.92, while the R^2_{adj} is calculated to be 0.91.

Mean

The mean is calculated as the integral over the collision energy range weighted by the probability of each value. This value is useful as an estimate of the location of the distribution in terms of the energy range from the minimum to maximum collision energy.

The range of calculated values demonstrates that the mean energy in the mill is very low relative to higher collision energy values found from energy spectra plots. This reiterates the relative dominance of collisions at lower energies, and is in agreement with research which has found that the bulk of the work in tumbling mills is a result of cumulative damage leading to particle weakening and eventual failure (Tavares and de Carvalho, 2009).

Figure 7.9 shows differences between calculated and predicted values for the mean. The mean is predicted fairly well by the energy spectra model for majority of the conducted simulations. The R^2 of the fitting for the mean is 0.81 while the R^2_{adj} is 0.79.

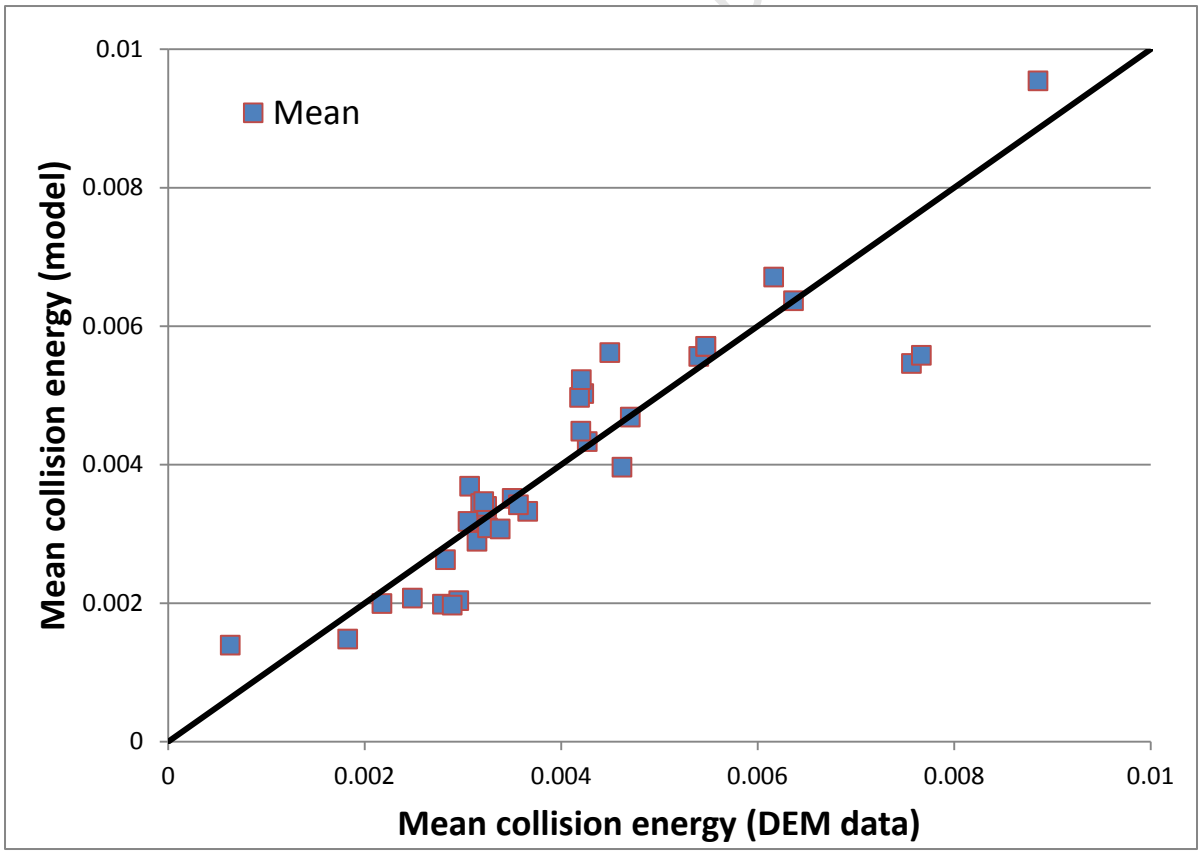

Figure 7.9: Comparison of the calculated and predicted mean for the energy spectra data from all conducted simulations

Median

Another method of describing the spread of the distribution is determining the median energy, or midway point in the cumulative distribution function, as shown in Figure 7.6. This is the numerical value separating the lower half of the total collision frequencies from the higher half.

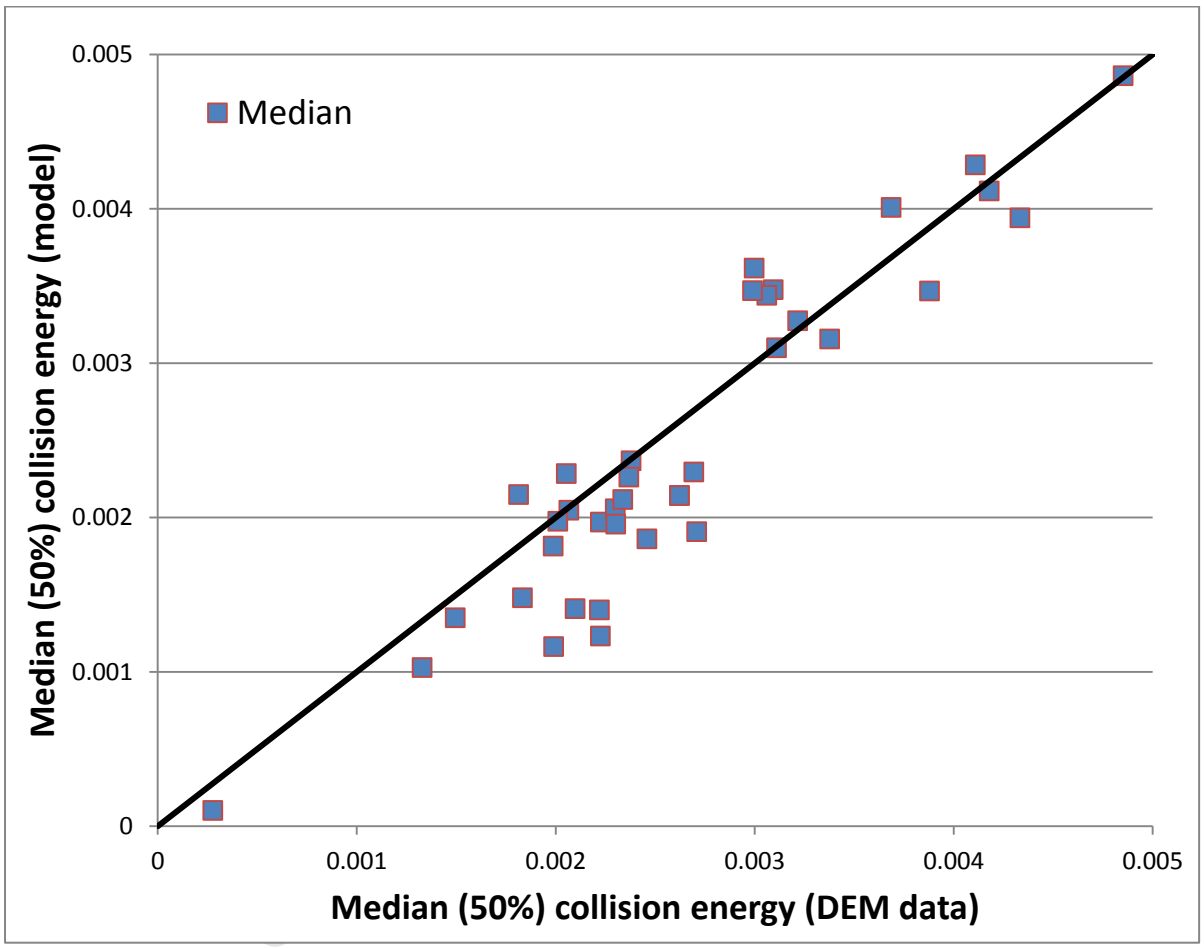

Figure 7.10: Comparison of the calculated and predicted median for the energy spectra data from all conducted simulations

Figure 7.10 displays the calculated and predicted median values for all simulations. The range of values indicates that the median energy is very low relative to the collision energy spectra range. The median is predicted well for majority of the simulations, although the points indicate that the model tends to slightly under predict the simulation value. The R^2 for the prediction of the median is 0.78 while the R^2_{adj} is 0.75.

E_{90}

The E_{90} is calculated as a quantity to locate the collision energy below which 90% of collisions occur. This value is calculated using Equation 7.12, with 0.9 specified as the value for the cumulative distribution. The results of the calculated and predicted values are plotted in Figure 7.11. The energy spectra model is found to predict the E90 well for almost all the simulations investigated. The R^2 is 0.95 while the R^2_{adj} is 0.94.

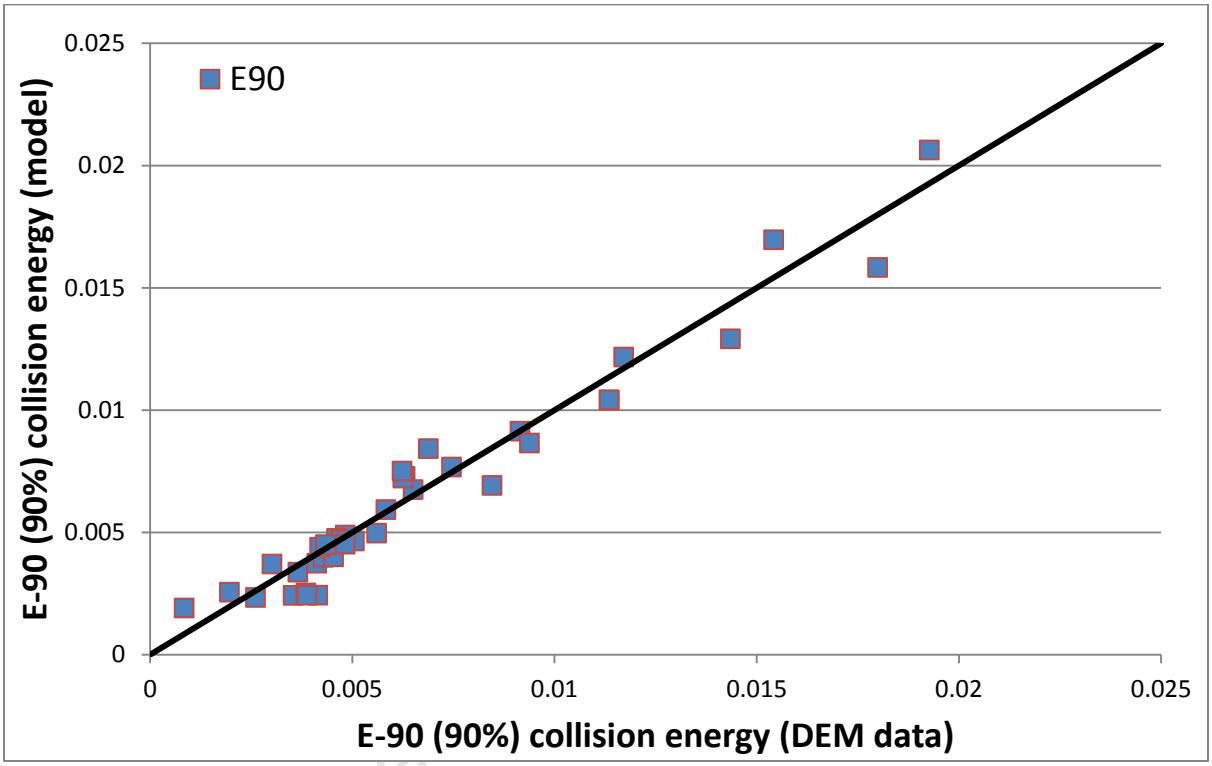

Figure 7.11: Comparison of the calculated and predicted E_{90} for the energy spectra data from all conducted simulations

N_{100}

As illustrated in Figure 7.7, the N_{100} is the energy at which collision energies decay to the 100 collision mark. This is proposed as a useful measure of the behaviour of the energy spectra at higher energies. A higher value signifies that the distribution tends to be more prone to high energy collisions, while a lower value indicates the opposite.

Figure 7.12 shows the differences between the calculated and predicted values for the N_{100}. This value is predicted fairly well for majority of the conducted simulations, particularly simulations for which it occurs at lower energies. The R^2 of the prediction is 0.86 while the R^2_{adj} is 0.84.

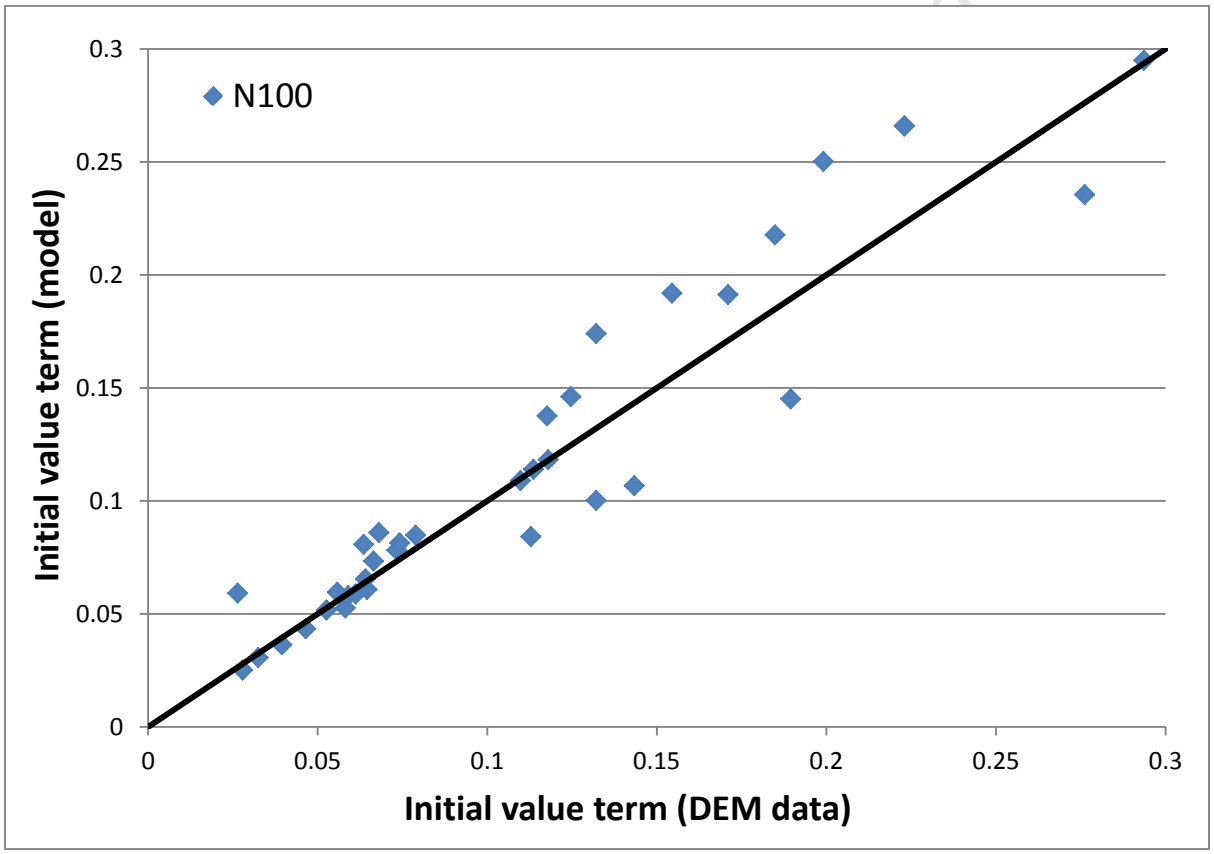

Figure 7.12: Comparison of the calculated and predicted N_{100} for the energy spectra data from all conducted simulations

CHAPTER 8

ANALYSIS OF ENERGY SPECTRA MODEL AND VALIDATION AGAINST DEM PILOT MILL DATA

Overview
This chapter discusses the interpretation of collision energy distributions from the developed model and examines the suitability of the model to predicting the energy spectra of a pilot scale SAG mill. A summary of the limitations of the model is also provided.

8.1 Discussion of energy spectra model

The energy spectra model developed in this work was a function which related the probable collision frequency to particle collision energy using a decaying double exponential relationship. This model described the distribution of the total energy losses to impacts by each particle size class over a single steady state mill revolution.

$$N = \left(10^{K_1 \cdot e^{-K_2 \cdot E}}\right) \cdot \left(10^{K_3 \cdot e^{-K_4 \cdot E}}\right) \qquad \textbf{Equation 8.1}$$

The parameterized form of the model could be presented as a multiple of two double exponents of bases 10 and *e*, as given in Equation 8.1. As shown, the equation was described by four parameters, where two were named initial value terms (K_1 and K_3) while the others were known as decay rates (K_2 and K_4). The product $10^{K_1} \cdot 10^{K_3}$ could be used as an estimate of the initial order of magnitude from which collision frequencies decreased at energy of E_0. The decay rates K_2 and K_4 meanwhile defined the respective rates at which their initial value terms decreased with increasing collision energy.

The key difference between the two double exponent terms was the value of the two decay rates, where one was significantly higher than the other. As K_4 was specified as the high decay rate this signified that the expression $10^{K_3 \cdot e^{-K_4 \cdot E}}$ would fall away much more rapidly with increasing energy. When this term decayed to a value of 1, the remainder of the frequency distribution would decay with increasing energy at orders of magnitude defined by the lower decay rate term K_2.

The parameters were found to be affected by the mill operating variables. As the decay rates most influenced the shape of the distribution, K_2 and K_4 were modelled as a function of the particle size, mass fraction, mill speed and volumetric filling investigated in this work.

Energy spectra plots were found to be influenced by mill operating variables such as speed, filling, particle size and mass fraction. Of these variables, the particle size and mass fraction were found to have the most pronounced influence on the resulting distribution, as depicted in Figure 8.1. Here, the predicted energy spectra curves for each particle size in the Full size distribution simulation of the 300mm tumbling mill at 75% critical speed and 31.25% volumetric filling is demonstrated.

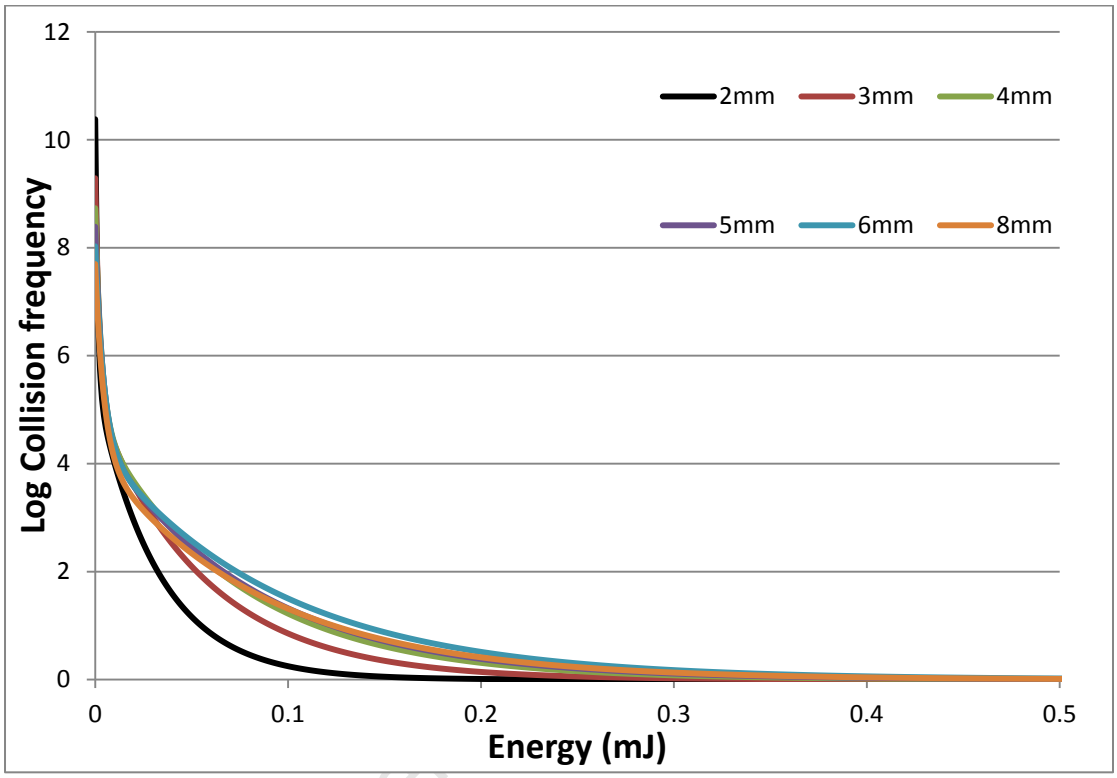

Figure 8.1: Comparison plot of the model prediction energy spectra curves obtained for different sizes in a simulation of a charge size distribution

The model predicts the noted trend from DEM simulations that smaller particles tended to collide with lower energies. This supports the notion that fine sizes in tumbling mills primarily fracture through cumulative damage at very low energy levels (Tavares and Carvalho, 2009). Although smaller particles tend to dominate the cataracting region, their lower momentum leads to low dissipation energies.

The model also follows the observation that larger particles tend to have lower collision frequencies at the mode E_0, while having higher frequencies at relatively high energies. This result indicates that larger sizes have a greater likelihood of losing energy to high level impacts. This is consistent with work that indicates that impact breakage behaviour dominates for coarser sizes in tumbling mills (Napier Munn et al., 1999). The plots of energy

spectra also follow the trends given in Section 2.2 in the work by Khanal and Morrison (Khanal and Morrison, 2009) which showed that larger particle sizes in the mill tended to collide at higher energies.

As shown in Figure 8.1, the highest particle size does not have the highest energy losses. This is due to the mass fraction, or amount of material present in its size class. A higher mass fraction in a particle size, or an increase in the number of particles, similarly increases the number of collisions that can potentially occur.

8.2 Validation of model against simulated pilot mill data

The energy spectra model in this work was developed from simulations of a laboratory scale tumbling mill. To investigate whether the derived relationship could be used at a larger scale, the model was tested against data from DEM simulations of a pilot tumbling mill by Kulya (Kulya, 2008).

In Kulya's work, simulations of a 1.695m diameter pilot SAG mill were conducted, using operating conditions based on actual tests carried out by Condori (Condori, 2006). A $\sqrt{2}$ series size distribution was used for the charge with a particle size of up to 180mm. Figure 8.2 depicted a picture and DEM schematic of the pilot mill used for the work, while Table 8.1 listed a summary of the operating conditions.

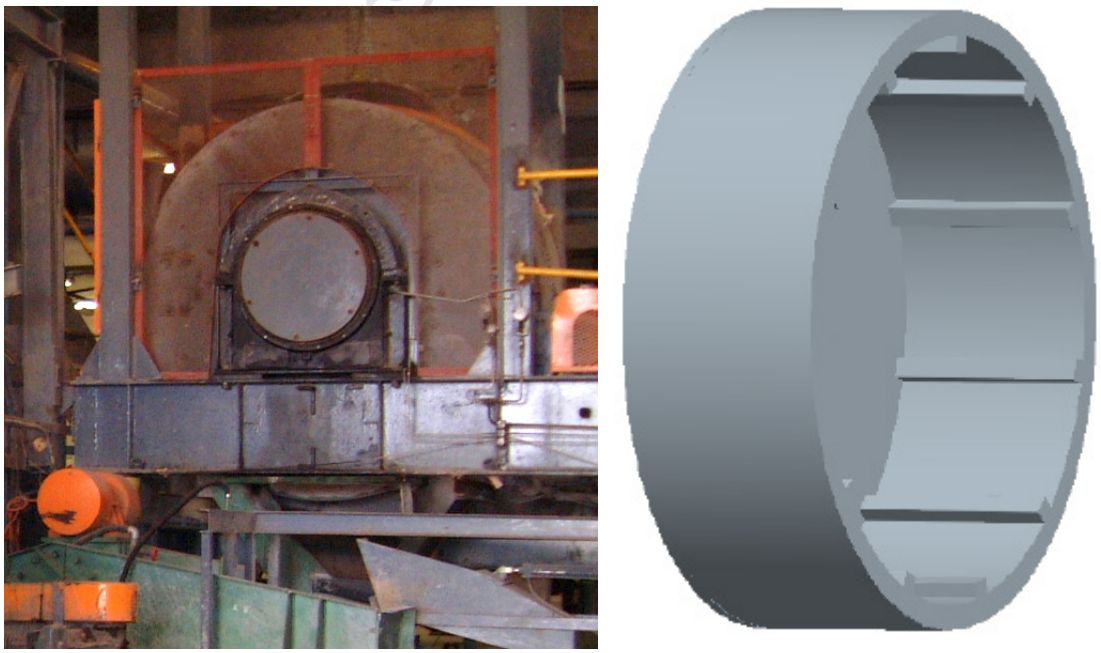

Figure 8.2: Picture of the MINTEK pilot plant mill and a schematic of the CAD geometry used for DEM simulations by Kulya (taken from Kulya, 2008)

Table 8.1: Mill operating conditions investigated in study by Kulya (Kulya, 2008)

Mill length (m)	0.575
Mill diameter (m)	1.695
Number of lifters	11
Lifter geometry	Square
Lifter width (mm)	45
Lifter height (mm)	55
Total volumetric filling (%)	35
Mill speed (% crit.)	75
Ball load (%)	5

A charge size distribution used by Kulya for DEM simulations was based on that of the pilot mill. Kulya truncated the distribution such that particles below 4.75mm were not considered, due to computational limitations. Figure 8.3 showed the particle size distribution of ore that was used, along with a list of the mass present in each size in Table 8.2. The mass fractions provided were determined for use in the energy spectra model. In addition to the charge, 5% of the load was composed of steel balls of 40, 60 80 and 100mm to assist with the grind.

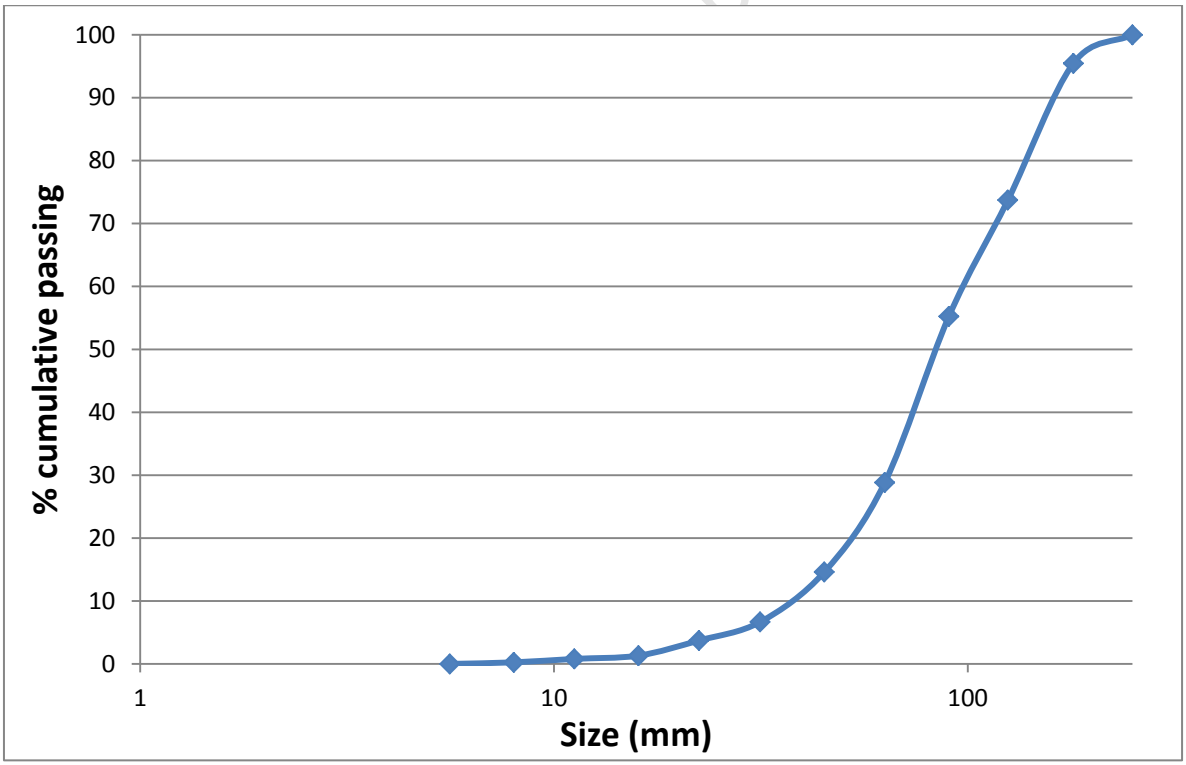

Figure 8.3: Particle size distribution used for DEM simulation by Kulya (redrawn after Kulya, 2008)

Table 8.2: Particle size distribution used for DEM simulation in study by Kulya along with calculated mass fractions (Kulya, 2008)

Size (mm)	Mass (kg)	% cumulative Passing	Mass fraction
250	-	100	0
180	24.55	95.47	0.045
125	117.85	73.73	0.217
90	100.25	55.24	0.185
63	143.16	28.83	0.264
45	77.11	14.61	0.142
31.5	43.03	6.67	0.079
22.4	16.01	3.72	0.030
16	13	1.32	0.024
11.2	2.82	0.8	0.005
8	2.97	0.25	0.005
5.6	1.36	0	0.003

Ore particles of every size in these simulations were simulated as spheres, while their material properties were selected based on work by Powell and McBride (Powell and McBride et al., 2004). The Hertz-Mindlin contact model was used for the investigation. The energy spectra of each particle size was extracted from the simulation and used for further analysis. These distributions were plotted according to logarithmic scales on both the frequency and energy axes in the manner shown in Figure 8.4.

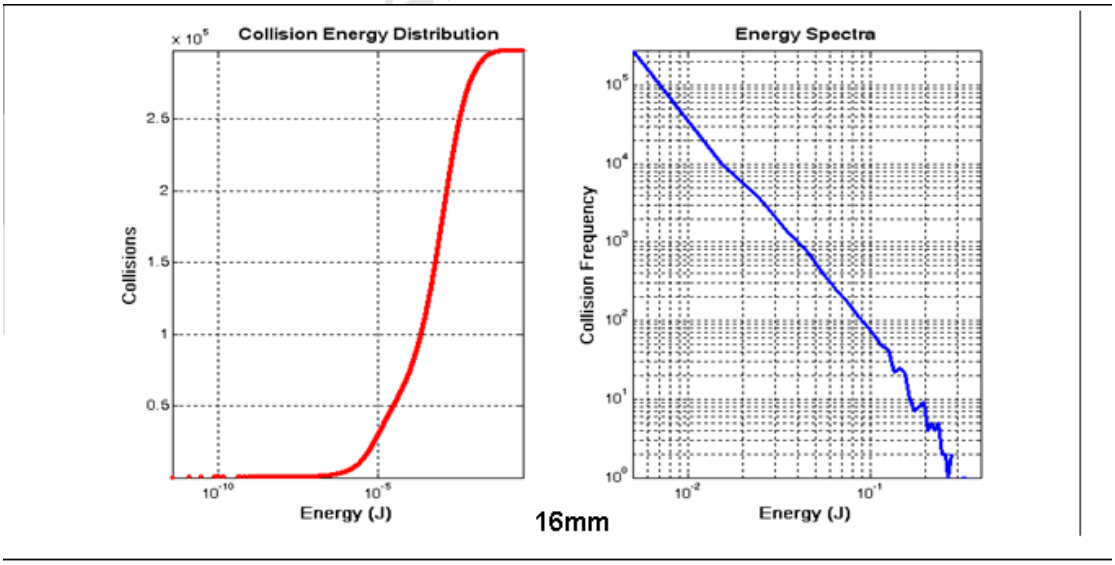

Figure 8.4: Example of the collision energy distribution and energy spectra curves obtained by Kulya (Kulya, 2008)

The energy spectra data provided conformed to the form of the energy spectra model developed in this work. Equation 8.1 could therefore be fitted to Kulya's data to obtain parameters that described the energy distribution of each curve.

The fitting parameters obtained for each particle size are listed in Table 8.3. The R^2 regression statistics indicated that the function was in good agreement with the data. The key difference between the parameters obtained for Kulya's work with those in this thesis is the value of the decay rates K_2 and K_4. The decay rates from the pilot scale mill are orders of magnitude lower than those obtained from the laboratory scale mill. This signifies that collisions decrease much less rapidly for the larger scale mill, meaning many more collisions occur than in the small scale mill.

Table 8.3: Parameters obtained for energy spectra model fitted to data from pilot mill simulation

Size (mm)	K_1	K_2	K_3	K_4	R^2
5.6	3.07	29.49	7.73	235.32	0.993
8	3.31	11.04	8.98	99.74	0.998
11.2	2.45	6.72	8.05	68.99	0.997
16	2.44	5.74	6.92	39.87	0.993
22.4	2.05	4.61	6.37	39.83	0.991
31.5	1.63	2.89	5.98	36.87	0.994
45	1.37	2.84	5.17	38.82	0.990
63	1.64	5.23	4.46	35.49	0.988
90	1.31	5.94	4.05	53.07	0.990
125	1.28	4.02	3.44	37.11	0.989
180	2.03	10.59	2.27	50.07	0.991

From this data, the energy spectra for each size could be plotted as given in Figure 8.5 and used to compare the distributions. It was found that the results followed the same trend as that found from DEM simulations in this thesis. The smaller particle sizes dominated the low level collision energies but had the lowest collision frequencies at higher energies. Further, while the energy spectra increased with particle size it was found that, due to the mass fraction of the charge, the highest particle size had a lowered energy spectra.

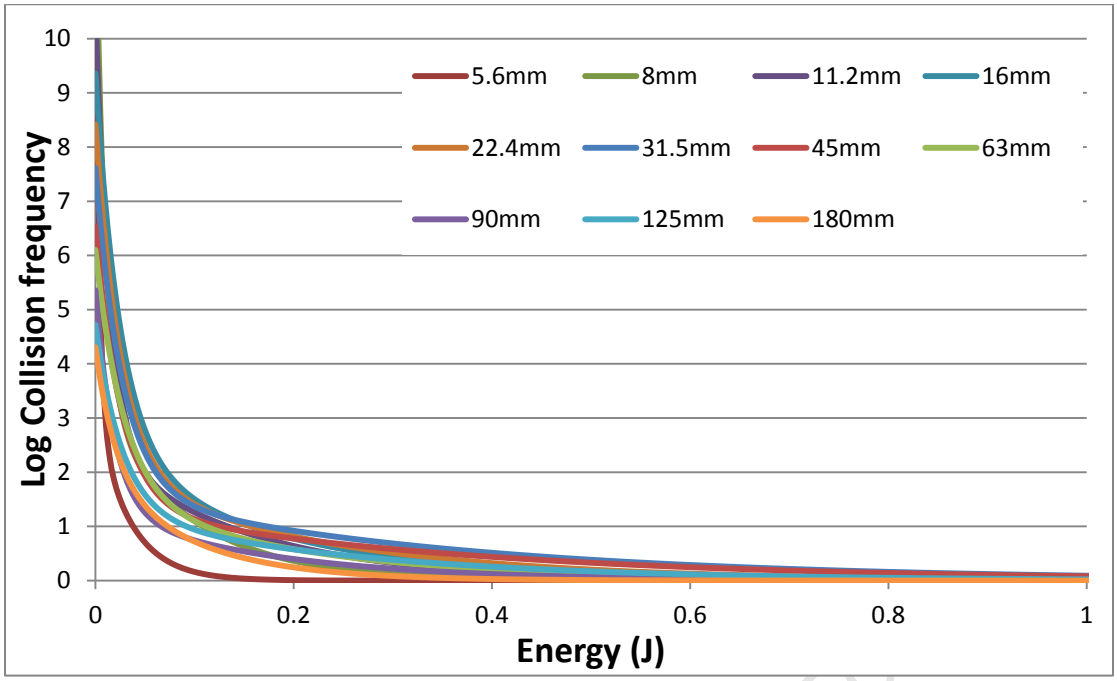

Figure 8.5: Energy spectra data obtained for all particle sizes in simulation of pilot mill

The energy spectra model (Equation 7.8) was fitted against the Kulya's data to investigate its validity using an independent dataset using a wider size distribution. A least squares regression of was conducted following the approach described in Section 7.4.

The fitting parameters for the decay rates B and D from Equation 7.8 were found to be 0.0223N and 0.365N respectively. Using a procedure similar to that in Section 7.4, key defining quantities derived from collision distributions could be used to examine how closely the model predicted the actual energy spectra data.

In Kulya's work, the value of E_0 was set to 0.01 kWh/t for all particle sizes. The methodology for the power draw per size developed in this thesis could not be applied to determine E_0 as there was insufficient data from Kulya's work. The value of E_0 for the energy spectra model was then set to 0.01kWh/t for all sizes.

The log of collision frequencies at the mode, which was the maximum point on the energy spectra curve, was determined at the energy E_0. Figure 8.6 was plotted to compare the values obtained for the orders of magnitude calculated from the model for each size to those of the simulation data. It was found that the model closely predicted the mode correctly except for the two highest sizes. This was attributed to the energy value of E_0 that was used for the calculation. The values of R^2 and R^2_{adj} for the fitting were 0.92 and 0.91 respectively.

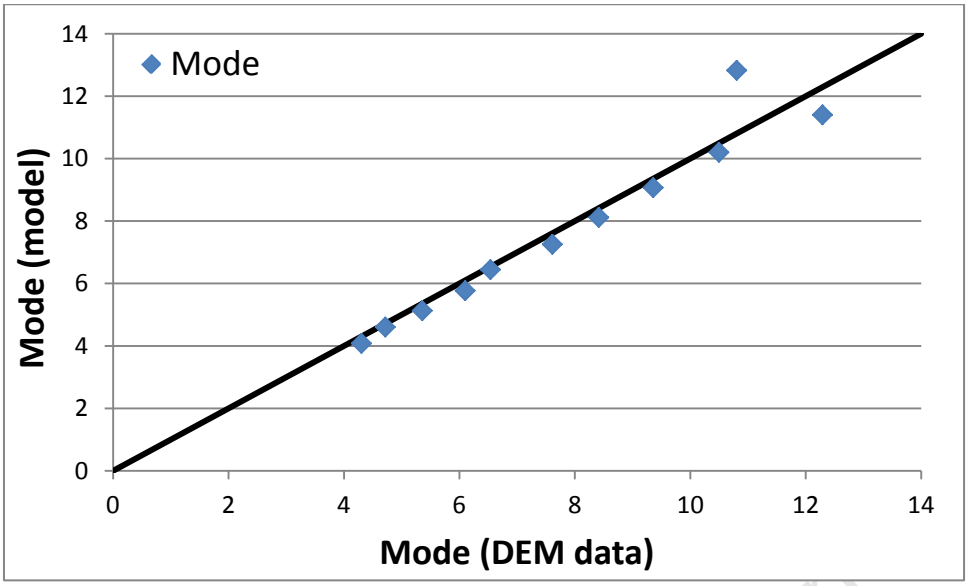

Figure 8.6: Comparison of the calculated and predicted mode for the energy spectra data obtained from pilot mill simulation

The mean predicted by the model was also compared to the pilot mill simulation. It was found that the mean was closely predicted except that there was a tendency for the model to over-predict the mean at higher sizes. This suggested that the value of E_0 needed to be lower for higher sizes to correctly predict the energy spectra. As shown in Section 5.3, E_0 decreased with increase in energy. The values of R_2 and R^2_{adj} for this fitting were 0.95 and 0.93 respectively.

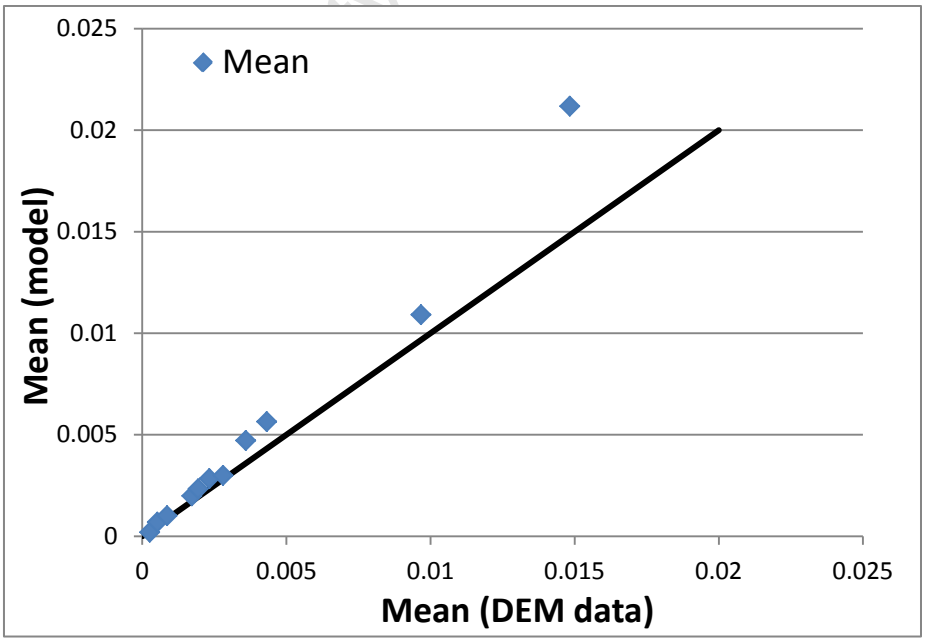

Figure 8.7: Comparison of the calculated and predicted mean for the energy spectra data obtained from pilot mill simulation

The N_{100} predicted by the model was similarly compared to that of the simulated data and found to give good agreement. The R^2 for this fitting was 0.91 while the R^2_{adj} was 0.89.

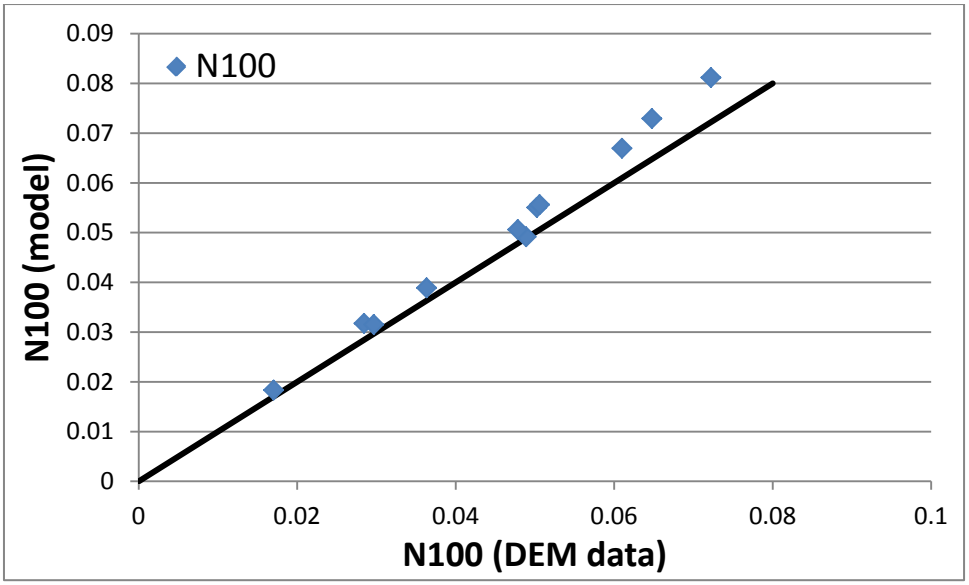

Figure 8.8: Comparison of the calculated and predicted N_{100} for the energy spectra data obtained from pilot mill simulation

In Kulya's work, the total power draw to the mill was determined as the total dissipated collision energy in each particle size divided by the mill periodic time. For the DEM simulation, Kulya predicted a power draw of 11.43 *kW*, which was stated to be close to the actual value of 11.93 *kW*. It was speculated that the discrepancy was due to the truncated size distribution used for the DEM simulation, which did not contain particles below 4.75mm due to computational constraints.

Kulya did not provide energy spectra data for the steel media. The steel accounted for more than half the charge mass in the mill, and would thus contribute significantly to the total power draw. Using the methodology outlined in Appendix B, the energy spectra model could be used to calculate the power dissipation from the ore body alone, for which the energy spectra data was available. This was equivalent to the net charge power draw at steady state. With this approach, the power was found to be 5.76 *kW*. It is speculated that the disparity between this power and that predicted by Kulya is due to the energy loss by the steel media.

8.3 Application and limitations of the energy spectra model

Testing the model prediction against pilot mill data revealed a number of areas of the model that would need to be addressed in future work. One notable limitation of the model was that it did not take account of the apportioning of energy between respective colliding bodies that were in contact. For instance, the energy spectra data of each size in the ore body represented the total energy losses to collisions, and therefore theoretically the energy available to cause breakage. However, the charge also consisted of four sizes of steel balls. As steel has a different density to that of ore, this material would be considered to have its own associated energy spectra. The bulk of the energy losses by this media would likely be expended in causing breakage of ore particles with which they were in contact, hence the steel media energy loss would have to be distributed to the ore body. The energy spectra model could therefore be extended in future work to take account of density.

CHAPTER 9

CONCLUSIONS AND RECOMMENDATIONS

Overview
This chapter presents the conclusions drawn from the results of this work, discusses the research novelty of this thesis and highlights the recommendations for future work.

9.1 Conclusions

The scope of work in this thesis was guided by two hypotheses. The first hypothesis postulated that the effect of particle size, mill speed and volumetric filling on the charge motion in a tumbling mill could be quantified using data from PEPT and DEM. The second hypothesis stated that the probability that collision energy losses would occur for particles of a given size in the mill could be predicted based on DEM data.

To interrogate these hypotheses, PEPT experiments were conducted using dry glass bead charge of 2-8mm in a laboratory scale tumbling mill. These tests composed of charge of a single size (mono-size tests) and charge in a Weibull distribution (full size distribution tests. DEM simulations of these experiments were carried out using an identical mill geometry and charge, whose material properties were selected to be similar to those of experiments. Data from these two approaches was used to determine the charge power draw and develop a mathematical model. The extracted collision frequency information from DEM was then used to develop a model for the energy spectra. The two hypotheses were confirmed based on the following conclusions from the objectives of this work:

Charge kinematic properties derived from PEPT

- Spatial distributions of location probability were determined by normalizing frequency distributions of particle coordinates in a discrete grid. This was performed for both mono-size charge and individual sizes in a distribution to compare their particle location probability densities. These distributions could be used to demonstrate key trends, such as the tendency for smaller particles to segregate toward the mill periphery more than larger particles.
- The Centre of Circulation (CoC) of mono-size charge could be determined as a unique point in the distribution about which the charge pivoted with the revolving mill. The higher and closer to the mill periphery the CoC was located, the greater was the tendency for the charge to cataract.

- Tangential velocity values along a diametrical line through the CoC could be determined and used as a representation of the granular flow profile. A mathematical model was fitted to these plots to provide a basis for comparison. This was a unique profile about which the charge motion behaviour at different conditions could be compared.
- Porosity distributions of mono-size experiments were obtained which indicated differences in charge packing density with size and mill speed. Smaller charge was found to have lower porosity values in the rising bulk region while porosity values in the bulk region were found to increase with mill speed.
- The charge power draw distribution was calculated from accumulating torque contributions of all regions in a transverse grid. These plots highlighted regions of the mill that drew the greatest power. The total power draw for all tests was found to be in statistical agreement with measured power.
- The accumulated power draw of all particle sizes in the grid was found to be in statistical agreement with the measured power. This confirmed that PEPT could be used to isolate the individual power draw of each size class within a distribution of charge.

Validation of DEM simulations using PEPT

- Distributions of the average particle position from DEM were compared to charge distributions from PEPT. Trends between the two methods were found to be similar although DEM data depicted distributions to be marginally closer to the mill shell. This was attributed to the difference in the approaches taken to determine location probability distributions from PEPT and DEM. PEPT distributions took account of the time spent in each voxel while those from DEM did not.
- Spatial plots of average velocities in DEM were directly compared to time average velocity distributions from PEPT. Negligible differences between the two methods were found in the voxels that encompassed the bulk charge.
- Values of the CoC for all mono-size DEM experiments were found to be closely similar to those determined from PEPT. This showed that DEM charge motion correctly determined the turning points of the charge.
- The comparison of tangential velocity profiles between DEM and PEPT yielded that the values were in good agreement in the region below the free surface. This was an indication that DEM simulations captured the granular flow motion of the packed bed.
- Porosity distributions from mono-size DEM simulations were closely similar to those from PEPT. Values of differences between the two methods were marginal except

along the outline of the mill periphery. This was due to the aliasing of PEPT data along the fringes of the mill in the spaces occupied by lifters.

- The power draw calculated from DEM data using a force balance approach against the mill geometry was found to be consistently in statistical agreement with measured power. This suggested that the forces calculated by the DEM contact model accurately approximated those of the tumbling mill environment
- Using an identical approach to the PEPT methodology the power draw of each size was determined to be in agreement with measured power. Spatial distributions of power draw between PEPT and DEM were compared and found to give good agreement. The power draw of each particle size was subsequently determined in an identical way to PEPT, and the total power draw was found to be in statistical agreement with measured power.
- Spatial plots of energy losses to particle collisions indicated that the highest energy dissipation was in the toe region due to the impact of falling material. The total energy dissipation was accumulated and divided by the mill periodic time to determine the total power dissipation, which was equivalent to the power draw as the system was at steady state.
- Plots of the collision frequency against discrete energy ranges, or energy spectra plots, indicated that the vast majority of collisions occurred at low energy ranges. The lower bound of the energy spectra curve, or E_0, was determined by truncating the collision energy spectra such that the total power dissipation matched the mean power draw. Values for E_0 for each particle size were found to be consistent with the typical energy range from particle breakage experiments.

Power draw modelling

- A model was developed to calculate the mass distribution along the horizontal mill profile as a function of particle size, mill speed and mill filling. The model was calibrated using PEPT and DEM data and found to closely follow the trends observed from both techniques.
- A fitted Gaussian function was found to closely approximate the behaviour of the average angular velocity of the charge along the horizontal mill profile. The function was fitted to both PEPT and DEM data, and its parameters were found to be influenced by mill speed and particle size.
- Features typically used to describe charge motion such as the shoulder and toe were determined from the mass distribution and average angular velocity functions. The shoulder was calculated as the intersection point of the piecewise angular velocity

function in the rising region, while the toe was obtained as the midpoint of the horizontal interval over which the mass distribution decreased to 0.35%.

- A model for the power draw was developed with the mass distribution, angular velocity distribution and lever arm distance all expressed mathematically in terms of mill operating variables. The model was found to closely predict all the measured power draw values as well as the PEPT and DEM power per size calculations in this work.

Development of energy spectra model

- A double exponential function was found to fit consistently to energy spectra data of each size in the charge distribution. The model consisted of four parameters, two of which were named initial value terms, while the others were known as decay rates. These parameters were found to be influenced by particle size, mass fraction, mill speed and volumetric filling.
- Initial value terms decreased with an increase in particle size. This signified that smaller sizes had higher numbers of collisions at very low energy levels.
- Decay rates decreased with increasing particle size and mass fraction. This indicated that as the particle size increased, it became more likely that a collision between particles would result in a higher energy loss.
- The decay rates were fitted to the particle size, mass fraction, mill speed and mill filling. Quantities such as the mean, median and number of collisions at the mode were determined from the modelled values and compared to the DEM data and found to give good agreement.
- The energy spectra model was tested against DEM simulation data from a pilot scale SAG mill. The double exponential function form was found to fit closely to the data from the pilot scale DEM simulation. The data was regressed against the operating variables using the model developed in this thesis. The mean, N_{100} and collision frequency at the mode were compared to the simulated data and found to give good agreement.

9.2 Research Novelty

The following are the original contributions made in this work toward modelling the charge power draw and collision energy dissipation.

Calculation of charge power draw per size

The methodology to determine charge power draw using accumulated lever arm contributions of voxels about the centre of the mill is demonstrated, using PEPT and DEM data, to be consistently accurate with measurement. Spatial distributions from this method are a unique means of examining and comparing regions of the granular body that draw the highest power from the rotating mill, and can be used to investigate the power utilization under different conditions. Using this approach, it is shown that the mechanical energy of the cascading charge needs to be included in determining the net mill power draw as it contributes significantly. Further, the approach is demonstrated to be a unique means of determining the power draw contribution of each size within a body of charge.

Mathematical model for mill power

The lever arm method developed in this work is used as a basis to develop a novel mathematical model for the power draw of a tumbling mill. The model uses a probability distribution for the granular charge mass which is found to be a function of the charge size, mill speed and volumetric filling. The probability distribution is used to determine the mill torque based on known charge behaviour from prior work. In addition, the average angular velocity of the charge is calculated as a function of the mill speed. Following the methodology given in this work, the power draw of each size class can subsequently be calculated and accumulated to predict the overall power draw of the charge.

Model for tumbling mill energy spectra

Based on frequency distributions of collision energies, a model for the energy spectra of each particle size per steady state mill revolution is developed in this thesis. The model is demonstrated to predict collision frequencies in close agreement with DEM simulation data and follows trends consistent with existing work on tumbling mill modelling. A methodology to determine the probability distribution function and cumulative distribution function of the energy spectra is also given in this work, and demonstrated to be a means of predicting the likelihood that collisions will occur within specific energy ranges. Both these distribution functions demonstrate trends consistent with existing research.

9.3 Recommendations for future work

Based on the outcomes of this thesis, the following recommendations are put forward for future work in this area:

- From discussion of the collision probability and energy dissipation, it is hypothesized that the energy spectra is influenced by particle properties such as density. The influence of density and other particle properties on the energy spectra should be further investigated.
- The geometry of the mill is also likely to influence the resulting collision probability, and in turn the energy spectra. DEM simulations of the tumbling mill using different numbers of lifters, and with different geometries, are recommended to observe the effect on the energy spectra.
- The simulations in this work are conducted in a dry environment. As a typical tumbling mill operation is in a wet environment, this will affect the charge motion and energy spectra. In future work, DEM simulations can be carried out in a multiphase system using Computational Fluid Dynamics (CFD) to observe the effects on the energy spectra. Such tests can be validated by comparison against PEPT data and measurement using the methodology developed in this thesis.
- The DEM simulations conducted in this study employed the use of spherical particles to simplify the charge environment. In future work, the effect of particle shape on the collision energy spectra can be investigated.

REFERENCES

Agrawala, S., Rajamani, R. K., Songfack, P., & Mishra, B. K. (1997). Mechanics of media motion in tumbling mills with 3d discrete element method. *Minerals Engineering, 10*(2), 215-227.

Anderson Jr., J. D. (1995). Computational Fluid Dynamics - The basics with applications. *McGraw-Hill*.

Arbiter, N., & Harris, C. C. (1982). Scale-up and Dynamics of Large Grinding Mills - a Case Study. *Design and Installation of Comminution Circuits, Mular A.L. and Jergensen II G.V. (eds), American Institute of Mining, Metallurgical, and Petroleum Engineers, New York, Ch 26*, 491-505.

Austin, L. G., Menacho, J. M., & Pearcy, F. A. (1987). A General Model for Semi-autogenous and Autogenous Milling. *Proceedings of the Twentieth International Symposium on the Application of Computers and Mathematics in the Mineral Industries, Volume 2: Metallurgy.*, 107-126.

Austin, L. G. (1990). A mill power equation for SAG mills. *Minerals and Metallurgical Processing*, 57-63.

Bailey, D. H., Li, X. S., & Jeyabalan, K. (2005). A Comparison of Three High-Precision Quadrature Schemes. *Experimental Mechanics, 14*(3), 317-329.

Barth, W. (1930). Power consumption in tube mills. *Forsclzung in Ingenieurwesen, 1*(9), 321-328.

Bbosa, L. S. (2007). Measurement of impact breakage properties of ore particles using a series of devices. *Centre for Minerals Research, Department of Chemical Engineering, University of Cape Town. Postgraduate thesis*.

Bbosa, L. S., Govender, I., Mainza, A. N., & Powell, M. (2011). Power draw estimations in experimental tumbling mills using PEPT. *Minerals Engineering, 24*, 319-324.

Bbosa, L. S., Powell, M., & Cloete, T. J. (2006). An investigation of impact breakage of rocks using the split Hopkinson pressure bar. *Journal of the South African Institute of Mining and Metallurgy, 106*(4), 291-296.

Boltzmann, L. (1884). Uber die Eigenschaften monozyklischer und amderer damit vervandter Systeme. *Creeles Journal, 98*, 68-94.

Bond, F. C. (1961). Crushing and grinding calculations. *Allis Chalmers Publication, No 07X9235B*.

Brodner, H. (2013). The tracking of particles in a tumbling mill using different lifter profiles using the PEPT system. *Centre for Minerals Research, Department of Chemical Engineering, University of Cape Town. Postgraduate thesis*.

Chandramohan, R., & Powell, M. (2005). Measurement of particle interaction properties for incorporation in the discrete element method simulation. *Minerals Engineering, 18*, 1142-1151.

Chandramohan, R. (2005). Measurement of particle interaction properties for the incorporation into discrete element methods. *Centre for Minerals Research, Department of Chemical Engineering, University of Cape Town. Postgraduate thesis*.

Cleary, P. W. (1998). Predicting charge motion, Power draw, Segregation and wear in ball mills using Discrete Element Methods. *Minerals Engineering, 11*(11), 1061-1080.

Cleary, P. W., & Hoyer, D. (2000). Centrifugal charge motion and power draw: comparison of DEM predictions with experiment. *International Journal of Mineral Processing, 59*, 131-148.

Cleary, P. W. (2001). Charge behaviour and power consumption in ball mills: sensitivity to mill operating conditions, liner geometry and charge composition. *International Journal of Mineral Processing, 63*, 79-114.

Cleary, P. W., & Morrison, R. D. (2004). Using DEM to model ore breakage within a pilot scale SAG mill. *Minerals Engineering, 17*, 1117-1124.

Cleary, P. W., & Morrison, R. D. (2011). Understanding fine ore breakage in a laboratory scale ball mill using DEM. *Minerals Engineering, 24*, 352-366.

Cleary, P. W., Morrison, R. D., & Morell, S. (2003). Comparison of DEM and experiment for a scale model SAG mill. *International Journal of Mineral Processing, 68*, 129-165.

Condori. (2006). Private Communication. *University of Cape Town, South Africa*.

Conway-Baker, J., Barley, R. W., Williams, R. A., Jia, X., Kostuch, J., McLoughlin, B., & Parker, D. J. (2002). Measurement of the motion of grinding media in a

vertically stirred mill using positron emission particle tracking (PEPT). *Minerals Engineering, 15*, 53-59.

Cundall, P. A., & Strack, O. D. L. (1979). A Discrete Numerical Model for Granular Assemblies. *Geotechnique, 29*, 47.

Datta, A., Mishra, B. K., & Rajamani, R. K. (1999). Analysis of Power Draw in ball mills by the Discrete Element Method. *Canadian Metallurgical Quarterly, 38*(2), 133-140.

Davis, E. W. (1919). Fine crushing in ball mills. *American Institute of Mining, Metallurgical, and Petroleum Engineers, 61*, 250-296.

de Oliviera, C. R., & Werlang, T. (2007). Ergodic hypothesis in classical statistical mechanics. *Revista Brasileira de Ensino de Fisica, 29*(2), 189-201.

DEM Solutions. (2006). EDEM 2.4 User Guide. *DEM Solutions, Copyright © 2005-2012*.

Djordjevic, N., Morrison, R. D., B., L., & Cleary, P. W. (2006). Modelling comminution patterns within a pilot scale AG/SAG mill. *Minerals Engineering, 19*, 1505-1516.

Djordjevic, N. (2003). Discrete Element Modelling of the influence of lifters on power draw of tumbling mills. *Minerals Engineering, 16*(4), 331-336.

Dong, H., & Moys, M. H. (2001). A technique to measure velocities of a ball moving in a tumbling mill and its applications. *Minerals Engineering, 14*(8), 841-850.

Dragomir, S., Sinnott, M., Semercigil, E., & Turan, O. (2009). Predicting energy dissipation characteristics of a tumbling granular-flow damper using DEM. *Seventh International Conference on CFD in the Minerals and Process Industries, CSIRO, Melbourne, Australia*, 9-11 December.

Dullen, F. A. L. (1992). Porous Media. Fluid Transport and Pore Structure. *Academic Press Inc., 2nd edition*.

Freund, J. E., & Walpole, R. E. (1987). Mathematical Statistics. *Prentice Hall*.

Fuerstenau, D. W., & Abouzeid, A.-Z. M. (2002). The energy efficiency of ball milling in comminution. *International Journal of Mineral Processing, 67*(1-4), 161-185.

Fuerstenau, D. W., Kapur, P. C., & Velamakanni, B. (1990). A multi-torque model for the effects of dispersants and slurry viscosity on ball milling. *International Journal of Mineral Processing, 28*, 81-89.

Gingold, R. A., & Monaghan, J. J. (1977). Smoothed particle hydrodynamics - Theory and application to non-spherical stars. *Monthly Notices of the Royal Astronomical Society, 181*, 375-389.

Govender, I., Powell, M., & Nurick, G. (2001a). 3D Particle Tracking: A rigorous technique for verifying DEM. *Minerals Engineering, 14*(10), 1329-1340.

Govender, I., Balden, V., Powell, M., & Nurick, G. (2001b). Validated DEM-potential major improvements to SAG mill modelling. *Proceedings International Autogenous and Semiautogenous Grinding Technology, IV*(30 September - 3 October), 101-114.

Govender, I., Mangesana, N., Mainza, A. N., & Franzidis, J.-P. (2011). Measurement of shear rates in a laboratory tumbling mill. *Minerals Engineering, 24*(3-4), 225-229.

Govender, I., McBride, A. T., & Powell, M. (2004). Improved Experimental Tracking Techniques for Validating Discrete Element Method Simulations of Tumbling Mills. *Journal of Experimental Mechanics, 44*(5), 593-607.

Govender, I., & Powell, M. (2006). An empirical power model derived from 3d particle tracking experiments. *Minerals Engineering, 19*, 1005-1012.

Govender, I., Tupper, G. B., & Mainza, A. N. (2011). Towards a mechanistic model for slurry transport in tumbling mills. *Minerals Engineering, 24*(3-4), 230-235.

Govender, I., Richter, M., Tupper, G. B., & Mainza, A. N. (2012). A granular flow model for tumbling mills. *Proceedings Comminution 2012, 17th-20th April 2012, Cape Town*.

Govender, I., Cleary, P. W., & Mainza, A. N. (2012). Comparisons of PEPT derived charge features in wet milling environments with a friction-adjusted DEM model. *In press*.

Harris, C. C., Scknock, E. M., & Arbiter, N. (1985). Grinding mill power consumption. *Minerals Processing and Technology Review, Revised Vol. 1*, 297-345.

HBM. (2012). T20WN Torque Transducer data sheet. *Hottinger Baldwin Messtechnik (HBM)*.

Heath, M. T. (1997). Scientific Computing, an introductory survey. *McGraw-Hill*.

Helstrom, C. W. (1984). Probability and Stochastic Processes for Engineers. *Macmillan Publishing Company*.

Hertz, H. (1882). Uber die Berhrung fester elastischer Korper (On the contact of elastic solids). *Journal fur die Reine und Angewandte Mathematik, 92*(156-171).

Hogg, R., & Fuerstenau, D. W. (1972). Power relationships for tumbling mills. *Society for Mining, Metallurgy and Exploration, Inc.- American Institute of Mining, Metallurgical, and Petroleum Engineers, Transactions of the AIME meeting*, 418-423.

JKTech Pty Ltd (2013) *JKSimMet v6.* www.jktech.au/jksimmet

Johnson, K. L. (1985). Contact Mechanics, second ed. *Cambridge University Press, New York*.

Juvinall, R. C., & Marshek, K. M. (2006). Fundamentals of machine component design. *John Wiley & Sons Inc., New York*.

Kahaner, D., Moler, C., & Nash, S. (1989). *Numerical Methods and Software*. Prentice Hall, Englewood Cliffs, NJ.

Kallon, D., Govender, I., & Mainza, A. N. (2011). Circulation rate modelling of mill charge using position emission particle tracking. *Minerals Engineering, 24*(3-4), 282-289.

Kasozi, A., & Madala, T. (2008). Contributions to the Mechanistic description of power draw in tumbling mills using data from a Positron Emission Particle Tracking system (PEPT). *University of Cape Town*. *Undergraduate thesis.*

Kawatra, S. K. (2006). Advances in Comminution. *Society for Mining, Metallurgy and Exploration, Inc.*

Khanal, M., & Morrison, R. D. (2009). Discrete Element Method Simulation of the Effect of Tumbling Time and Particle Size in a 300-mm Diameter Mill. *Chemical Engineering Technology, 32*(10), 1630-1634.

Kharaz, A. H., Gorham, D. A., & Salman, A. D. (2001). An experimental study of the elastic rebound of spheres. *Powder Technology, 120*(3), 281-291.

Kulya, C. (2008). Using Discrete Element Modelling (DEM) and Breakage Experiments To Model The Comminution Action in a Tumbling Mill. *Centre for*

Minerals Research, Department of Chemical Engineering, University of Cape Town. Postgraduate thesis.

Laurent, B. F. C., & Cleary, P. W. (2012). Comparative study by PEPT and DEM for flow and mixing in a ploughshare mixer. *Powder Technology, 228*, 171-186.

Liddell, K. S., & Moys, M. H. (1988). The effects of mill speed and load on the behaviour of the load in a rotary grinding mill. *Journal of the South African Institute of Mining and Metallurgy, 88*(February), 49-57.

Malone, K. F., & Xu, B. H. (2008). Determination of contact parameters for discrete element method simulations of granular systems *Particuology 6*, 521-528.

Mangesana, N. (2011). Developing a Methodology for Characterising In-situ Viscosity Profiles in Tumbling Mills. *Centre for Minerals Research, Department of Chemical Engineering, University of Cape Town. Postgraduate thesis*.

Martins, S., Li, Q. M., Radziszewski, P., Caron, S., Aguanno, M., Bakhos, M., & Petch, E. L. (2008). Validating the instrumented ball outputs with simple trajectories. *Minerals Engineering, 21*(11), 782-788.

Martins, S., Li, W., Radziszewski, P., Faucher, A., & Makni, S. (2012). Experimental and Simulated Instrumented Ball in a tumbling mill—a Comparison. *Proceedings Comminution 2012, 17th-20th April 2012, Cape Town*.

Mathworks. (2011). MATLAB. *The Mathworks, Inc. Copyright © 1984-2011*.

Mellmann, J. (2001). The transverse motion of solids in rotating cylinders—forms of motion and transition behavior. *Powder Technology, 118*, 251-270.

Mindlin, R. D., & Deresiewicz, H. (1953). Elastic spheres in contact under varying oblique forces. *Journal of Applied Mechanics 20*(327-344).

Mishra, B. K. (2003). A review of computer simulation of tumbling mills by the discrete element method: Part II- Practical applications. *International Journal of Mineral Processing, 71*(1-4), 95-112.

Mishra, B. K., & Murty, C. V. R. (2001). On the determination of contact parameters for realistic DEM simulations of ball mills. *Powder Technology, 115*, 290-297.

Mishra, B. K., & Rajamani, R. K. (1992). The discrete element method for the simulation of ball mills. *Applied Mathematical Modelling, 16*(11), 598-604.

Mishra, B. K., Rajamani, R. K., & Pariseau, W. G. (1990). Simulation of ball charge motion in ball mills. *Society for Mining, Metallurgy and Exploration, Inc., Transactions of the SME Annual meeting 1-5 March*, 90-137.

Misra, A., & Cheung, J. (1999). Particle motion and energy distribution in tumbling ball mills. *Powder Technology, 105*, 222-227.

Morell, S. (1992). Prediction of grinding-mill power. *Transactions of the Institution of Mining and Metallurgy Section C: Mineral Processing Extraction and Metallurgy, 101*(January-April), C25-C32.

Morell, S. (1993). The prediction of Power Draw in wet tumbling mills. *Julius Kruttschnitt Mineral Research Centre, Department of Mining, Metallurgical and Materials Engineering, University of Queensland, Postgraduate thesis*.

Mori, M., & Sugihara, M. (2001). The double-exponential transformation in numerical analysis. *Journal of Computational and Applied Mathematics, 127*, 287-296.

Moys, M. H. (1993). A model of mill power as affected by mill speed, load, volume, and liner design. *Journal of the South African Institute of Mining and Metallurgy, 93*(June), 135-141.

Napier-Munn, T. J., Morrison, R. D., & Kojovic, T. (1999). Minerals Comminution Circuits: Their operation and optimization. *Julius Kruttschnitt Mineral Research Centre, Department of Mining, Metallurgical and Materials Engineering, University of Queensland*.

National Instruments. (2010). LabVIEW SignalExpress 2010. *National Instruments, Copyright © 1999-2010, v9.3.0*.

Nordell, L., & Potapov, A. (2011). *Novel cominution machine may vastly improve crushing-grinding efficiency* Paper presented at the International autogenous grinding semiautogenous grinding and high pressure grinding roll technology 2011, Vancouver, Canada.

Parker, D. J., Dijkstra, A. E., W., M. I. T., & Seville, P. K. (1997). Positron emission particle tracking studies of spherical particle motion in rotating drums. *Chemical Engineering Science, 52*(13), 2011-2022.

Parker, D. J., & Fan, X. (2008). Positron emission particle tracking-Application and labelling techniques. *Particuology, 6*, 16-23.

Perez-Alonso, C., & Delgadillo, J. A. (2012). Experimental validation of 2D DEM code by digital image analysis in tumbling mills. *Minerals Engineering, 25*, 20-27.

Powell, M., Govender, I., & McBride, A. T. (2008). Applying DEM outputs to the unified comminution model. *Minerals Engineering, 21*, 744-750.

Powell, M., & Nurick, G. (1996a). A study of charge motion in Rotary Mills. Part 1-Extension of the theory. *Minerals Engineering, 9*(2), 259-268.

Powell, M., & Nurick, G. (1996b). A study of charge motion in Rotary Mills. Part 2-Experimental work. *Minerals Engineering, 9*(3), 343-350.

Powell, M., & Nurick, G. (1996c). A study of charge motion in Rotary Mills. Part 3-Analysis of Results. *Minerals Engineering, 9*(4), 399-418.

Powell, M. S., & McBride, A. T. (2004). A three-dimensional analysis of media motion and grinding regions in mills. *Minerals Engineering, 17*, 1099-1109.

Powell, M., van der Westhuizen, A. P., & Mainza, A. N. (2009). Applying grindcurves to mill operation and optimisation. *Minerals Engineering, 22*, 625-632.

Press, W. H., Teukolsky, S. A., Vetterling, W. T., & Flannery, B. P. (1986). Numerical Recipes 3rd Edition: The Art of Scientific Computing. *Cambridge University Press, New York*.

PTC. (2009). Pro/ Engineer Wildfire 5.0. *Parametric Technology Corporation (PTC), Copyright © 2009*.

Rajamani, R. K., Songfack, P., & Mishra, B. K. (2000). Impact energy spectra of tumbling mills. *Powder Technology, 108*, 116-121.

Rose, H. E., & Evans, D. E. (1956). The dynamics of the ball mill, part 11: the influence of the powder charge on power requirements. *Proceedings of the Institution of Mechanical Engineers, 784-792*.

Rose, H. E., & Evans, D. E. (1956). The dynamics of the ball mill, part I: power requirements based on the ball and shell system. *Proceedings of the Institution of Mechanical Engineers*, 773-783.

Ross, S. M. (2009). Introduction to Probability and Statistics for Engineers and Scientists. *Elsevier Academic Press*.

Sarracino, R. S., McBride, A. T., & Powell, M. (2004). Using particle flow code to investigate energy dissipation in a rotary grinding mill. *Proceedings Numerical Modeling in Micromechanics via Particle Methods, Itasca*, 111-118.

Shi, F., & Kojovic, T. (2007). Validation of a model for impact breakage incorporating particle size effect. *International Journal of Mineral Processing, 82*(3), 156-163.

Shi, F., Kojovic, T., Larbi-Bram, S., & Manlapig, E. (2009). Development of a rapid particle breakage characterisation device - The JKRBT. *Minerals Engineering, 22*(7-8), 602-612.

Sichalwe, K., Govender, I., & Mainza, A. N. (2011). Characterising porosity of multi-component mixtures in rotary mills *Minerals Engineering, 24*(3-4), 276-281.

Stewart, J. (2010). Calculus: Concepts and Contexts, Fourth Edition. *2005 Brooks/Cole, Cengage Learning*.

Taggart, A. F. (1945). Handbook of Mineral Dressing. *John Wiley & Sons Inc., New York*.

Takahashi, H., & Mori, M. (1974). Double exponential formulas for numerical integration, *Publication of the Research Institue of Maths and Science, Kyoto University, 9*, 721-741.

Tanaka, K., Nishida, M., Kunimochi, T., & Takagi, T. (2002). Discrete element simulation and experiment for dynamic response of two-dimensional granular matter to the impact of a spherical projectile. *Powder Technology, 124*(1-2), 160-173.

Tavares, L. M., & de Carvalho, R. M. (2009). Modeling breakage rates of coarse particles in ball mills. *Minerals Engineering, 22*, 650-659.
Tavares, L. M., & King, R. P. (2002). Modeling of particle fracture by repeated impacts using continuum damage mechanics. *Powder Technology, 123*, 138-146.

Tsuji, Y., Kawaguchi, T., & Tanaka, T. (1993). Discrete particle simulation of two-dimensional fluidized bed. *Powder Technology, 77*(1), 79-87.

van Nierop, M. A., Glover, G., Hinde, A. L., & Moys, M. H. (2001). A discrete element method investigation of the charge motion and power draw of an experimental two dimensional mill. *International Journal of Mineral Processing, 61*, 77-92.

Venugopal, R., & Rajamani, R. K. (2001). 3D simulation of charge motion in tumbling mills by the discrete element method. *Powder Technology, 115*(157-166).

Vogel, L., & Peukert, W. (2003). Breakage behaviour of different materials-construction of a mastercurve for the breakage probability. *Powder Technology, 129*, 101-110.

von Mises, R. (1981). Probability, Statistics, and Truth. *Dover Publications: Revised edition*.

Walton, O. R., & Braun, R. L. (1986). Viscosity, granular-temperature, and stress calculations for shearing assemblies of inelastic, frictional disks. *Journal of Rheology, 30*, 949-980.

Whyte, R. (2005). Measuring incremental damage in rock breakage by impact. *Julius Kruttschnitt Mineral Research Centre, Department of Mining, Metallurgical and Materials Engineering, University of Queensland, Undergraduate thesis*.

Wills, B. A., & Napier Munn, T. J. (2006). Mineral Processing Technology 7th Edition. *Elsevier Science and Technology Books*.

Yamane, K., Nakagawa, M., Altobelli, S. A., Tanaka, T., & Tsuji, Y. (1998). Steady particulate flows in a horizontal rotating cylinder. *Physics of Fluids, 10*(6), 1419-1427.

Yang, R. Y., Zou, R. P., & Yu, A. B. (2003). Microdynamic analysis of particle flow in a horizontal rotating drum. *Powder Technology, 130*, 138-146.

Yang, R. Y., Yu, A. B., McElroy, L., & Bao, J. (2008). Numerical simulation of particle dynamics in different flow regimes in a rotating drum. *Powder Technology, 188*, 170-177.

Zhu, H. P., & Yu, A. B. (2002). Averaging method of granular materials. *Physical Review, E66*(021302).

Zhu, H. P., Zhou, Z. Y., Yang, R. Y., & Yu, A. B. (2007). Discrete particle simulation of particulate systems: Theoretical developments. *Chemical Engineering Science, 62*, 3378-3396.

Zhu, H. P., Zhou, Z. Y., Yang, R. Y., & Yu, A. B. (2008). Discrete particle simulation of particulate systems: A review of major applications and findings. *Chemical Engineering Science, 63*(5278-5770).

APPENDIX A- MATLAB CODE

A I- PEPT code

Presented below is a list of the algorithms used in the MATLAB programming language to analyse data from PEPT experiments. The entire code for each routine follows.

AnalyseData- Extracts PEPT time and position data from text file and calculates average kinematic quantities in specified grid

Utilises the following subroutines:

DrawMillShellPEPT- Plots an outline of the mill periphery and lifter geometry

GetTrackData- Imports data from text file outputted from PEPT experiments into columns of time and particle position

InterpPEPT_mod- Interpolates PEPT data to provide coordinates with time intervals and determines first and second derivatives

BinInterpData_Mod- Populates data according to particle locations in the specified grid

Utilises the following subroutines:

Binary_search- Isolates particle location between specified values by means of a binary search

LinecentrecocPEPT- Obtains and plots tangential velocities along a diametrical line through the mill centre and centre of circulation

AnalyseData

```
clear all; close all; warning off; clc
%% Constants used in various calcs
% PEPT mill (300x270)mm = main chamber
M = 9.6; % mass of charge in kg
d = 8/1000; % diameter of tracer particle (size class of interest), in m
L = 270/1000; % length of mill main chamber, in m
D = 300/1000; % diameter of mill, in m
Bins = 50; % (Bins)^2 = # of bins
a = D/Bins; % azimuthal dimension of voxel with a square face
g = 9.81; % acceleration (magnitude) due to gravity
rho = 2500; % density of tracer particle (size class of interest), kg/m^3
Vol_tr = pi*(d^3)/6; % volume of tracer, in m^3
N = M/(rho*Vol_tr); % # of particles in tracer size class
h = 5/1000; % height of lifter, in m
Widt = 20/1000; % width of lifter, in m
Ang = 60; % Lifter angle, in degrees
NumLifts = 20; % # of lifters
Pcrit = 75;
OmegaMill = (Pcrit/100)*(42.3/sqrt(D))*(2*pi/60); % angular speed of mill


%% Setup mill
[MillShellX,MillShellY] = DrawMillShellPEPT(200,0,0,D, NumLifts,h,Widt,Ang,0,1);
millGeom = [MillShellX(:), MillShellY(:)];

% read in PEPT data
[t, x, y, z, e] = GetTrackData('path\data.a##');

%% Translation from PEPT coordinate system to mill center.

Shift = [294.1026  344.7284]; % Mill Centre using fopt 15, Events 250 for
%300mm mill with location runs a39-42
```

```
%%
%% smooth, interpolate, differentiate ... and double differentiate
sz = size(z,1);
z = smooth(z,3,'moving');
f = 30;
[z, tt, Vz, Az] = InterpPEPT_mod(z, t, f, sz);

y = smooth(y,3,'moving');
[y, tt, Vy, Ay] = InterpPEPT_mod(y, t, f, sz);

x = smooth(x,3,'moving');
[x, tt, Vx, Ax] = InterpPEPT_mod(x, t, f, sz);

T = tt;
Data = [x,z,y];

%% Translate to mill center
BallPositionArray(:,2) = Data(:,2) - Shift(1,1)/1000;
BallPositionArray(:,1) = Data(:,3) - Shift(1,2)/1000;
BallPositionArray(:,3) = Data(:,1);

%% choosing data such that XY corresponds to the azimuthal plane
Vx = Vy;
Vy = Vz;
Ax = Ay;
Ay = Az;

% tangential velocity
Vxy = [Vx'; Vy'];
V_Magsqrd = sqrt(sum(Vxy.^2))';

Rxy = [BallPositionArray(1:end,1)';BallPositionArray(1:end,2)'];
RxyMag = sqrt(sum(Rxy.^2));
dotVR = dot(Vxy,Rxy);
tp = (dotVR./(RxyMag.^2));
Vtang = Vxy - [tp.*Rxy(1,:);tp.*Rxy(2,:)];
```

```
VtangX = Vtang(1,:)';
VtangY = Vtang(2,:)';

VtangMag = sqrt(sum(Vtang.^2))';

% Acceleration magnitude
Axy = [Ax'; Ay'];
Amag = sqrt(sum(Axy.^2))';

%% remove coordinates that fall outside the mill radius
[th,r] = cart2pol(BallPositionArray(1:end,1),BallPositionArray(1:end,2));

[aa,bb] = find(r < 0.150);
tt = T(aa);
BallPositionArray = BallPositionArray(aa,:);
Vx = Vx(aa,:);
Vy = Vy(aa,:);

V_Magsqrd = V_Magsqrd(aa,:);
VtangX = VtangX(aa,:);
VtangY = VtangY(aa,:);
VtangMag = VtangMag(aa,:);
Vtang = [Vtang(1,aa);Vtang(2,aa)];
Ax = Ax(aa,:);
Ay = Ay(aa,:);
Amag = Amag(aa,:);

 BallPosTmp = BallPositionArray(1:end,:);
%% Binning and plotting
[gridXY, gridXYNotNorm, gridX, gridY, gridVx, gridVy, gridVtangX, gridVtangY, gridVtangMag, gridV_MagSqrd, gridAx,
gridAy, gridAmag] = ...
    BinInterpData_Mod(Bins, millGeom, BallPosTmp,Vx,Vy, VtangMag, VtangX, VtangY, V_Magsqrd, Ax, Ay, Amag);

%% Porosity (monosize only)
Porosity = 1 - pi/(6*L*a^2)*N*(d^3).*gridXY;
Porositymod=Porosity;
len = size(gridXY,1);
```

```
% Setting all PEPT porosities < 0.36 equal to 0.36 (limit of packing fraction is 0.64)
for i = 1:len;
    for j = 1:len;
        if Porositymod(i,j) < 0.36;
            Porositymod(i,j) = 0.36;
        end
    end
end

%% Bulk Density Distribution
DensDist = (M/(L*a^2).*gridXY);
%% Power draw
[H,V] = meshgrid(gridX,gridY);
GridXX = H;
GridYY = V;
gridRad = sqrt(GridXX.^2 + GridYY.^2);

% Torque per bin using the particles angular speed
P1_dist = abs((M*g).*gridXY.*GridXX.*((gridVtangMag./gridXYNotNorm)./gridRad));

len = size(P1_dist,1);
% setting zero count bins to white
for i = 1:len;
    for j = 1:len;
        if isnan(P1_dist(i,j));
            P1_dist(i,j) = 0;
        end
    end
end

P1 = sum(sum(P1_dist)); % Resultant Power using torque per bin approach

 GridV = sqrt(gridVx.^2 + gridVy.^2)./gridXYNotNorm;
 gridAmag = sqrt(gridAx.^2 + gridAy.^2)./gridXYNotNorm;

P3 = abs(M*g*(mean(BallPositionArray(:,1)))*OmegaMill); % CoM power calc. using angular speed of mill
%%
```

```
gridtmp = gridXY;
len = size(gridXY,1);
% setting zero count bins to white
for i = 1:len;
    for j = 1:len;
        if gridtmp(i,j) == 0;
            gridtmp(i,j) = 0/0;
        end
    end
end

figure(1)
pcolor(H,V,gridtmp)% percentage occupancy
hold on
plot(millGeom(:,1), millGeom(:,2),'k','LineWidth',2)
axis equal tight
set(gca,'CLim',[0, 4e-3])
colorbar('FontSize',20,'YTick',[0,1e-3,2e-3,3e-3,4e-3,5e-3])

%%
figure(2)
quiver(gridX,gridY,gridVx./gridXYNotNorm,gridVy./gridXYNotNorm,5,'k');
hold on
plot(millGeom(:,1), millGeom(:,2),'k','LineWidth',2)
axis equal tight
title('Velocity')

%%
gridtmp = GridV;
len = size(GridV,1);
% setting zero count bins to white
for i = 1:len;
    for j = 1:len;
        if gridtmp(i,j) == 0;
            gridtmp(i,j) = 0/0;
        end
    end
end
```

```
figure(3)
pcolor(H,V,gridtmp)% percentage occupancy
hold on
plot(millGeom(:,1), millGeom(:,2),'k','LineWidth',2)
axis equal tight
title('Velocity Map (m/s)')
set(gca,'CLim',[0, 2])
colorbar('FontSize',20,'YTick',[0,0.25,0.5,0.75,1,1.25,1.5,1.75,2])
%%
gridtmp = gridVtangMag;
for i = 1:len;
    for j = 1:len;
        if gridtmp(i,j) == 0;
            gridtmp(i,j) = 0/0;
        end
    end
end

figure(4)
pcolor(H,V,gridtmp)% percentage occupancy
hold on
plot(millGeom(:,1), millGeom(:,2),'k','LineWidth',2)
axis equal tight
title('Tangential Velocity Map')
colorbar

%%
figure(5)
quiver(gridX,gridY,gridVtangX./gridXYNotNorm,gridVtangY./gridXYNotNorm,20,'k');
hold on
plot(millGeom(:,1), millGeom(:,2),'k','LineWidth',2)
axis equal tight
title('Tangential Velocity')

%%
gridtmp = P1_dist;
% setting zero count bins to white
for i = 1:len;
```

```
    for j = 1:len;
        if gridtmp(i,j) == 0;
            gridtmp(i,j) = 0/0;
        end
    end
end
figure(6)
pcolor(H,V,gridtmp)% percentage occupancy
hold on
plot(millGeom(:,1), millGeom(:,2),'k','LineWidth',2)
axis equal tight
title('Power Draw (W)')
set(gca,'CLim',[0, 0.15])
colorbar('FontSize',20,'YTick',[0,0.025,0.05,0.075,0.1,0.125,0.15])
%%
gridtmp = Porosity;
% setting zero count bins to white
for i = 1:len;
    for j = 1:len;
        if gridtmp(i,j) > 0.999;
            gridtmp(i,j) = 0/0;
        end
    end
end
figure(8)
pcolor(H,V,gridtmp)% percentage occupancy
hold on
plot(millGeom(:,1), millGeom(:,2),'k','LineWidth',2)
axis equal tight
title('Porosity Distribution data')
set(gca,'CLim',[0, 1])
colorbar('FontSize',20,'YTick',[0,0.2,0.4,0.6,0.8,1])

%%
gridtmp = Porositymod;
% setting zero count bins to white
for i = 1:len;
    for j = 1:len;
```

```
        if gridtmp(i,j) > 0.999;
            gridtmp(i,j) = 0/0;
        end
    end
end
figure(9)
pcolor(H,V,gridtmp)% percentage occupancy
hold on
plot(millGeom(:,1), millGeom(:,2),'k','LineWidth',2)
axis equal tight
title('Porosity Distribution')
set(gca,'CLim',[0, 1])
colorbar('FontSize',20,'YTick',[0,0.2,0.4,0.6,0.8,1])

%%
gridtmp = gridAmag;
for i = 1:len;
    for j = 1:len;
        if gridtmp(i,j) == 0;
            gridtmp(i,j) = 0/0;
        end
    end
end
figure(10)
pcolor(H,V,gridtmp)% percentage occupancy
hold on
plot(millGeom(:,1), millGeom(:,2),'k','LineWidth',2)
axis equal tight
title('Acceleration')
colorbar

figure(11)
quiver(gridX,gridY,gridAx./gridXYNotNorm,gridAy./gridXYNotNorm,150,'k');
hold on
plot(millGeom(:,1), millGeom(:,2),'k','LineWidth',2)
axis equal tight
title('Acceleration')
```

DrawMillShellPEPT

```
function [MillShellX,MillShellY] = DrawMillShellPEPT(dens,Xshift,Yshift,ID,
num_lifters,hlifter,wlifter,theta_chamfer,rot,direction)

%-------------------------------------------------------------------------------------;
% xc = x - centre of circle
% yc = y - centre of circle
% ID = inner diameter of mill
%
% numlifters    >> number of lifters
% hlifter       >> height of lifter
% wlifter       >> width  of lifter
% thetalifter   >> chamfer angle
% rot           >> rotate mill in radians
% dens          >> number of points in lifter segment ... and then some for
%                  actual lifter
%-------------------------------------------------------------------------------------;
% division for first segment!
theta =  (2*pi) / (num_lifters);
%
% isosolese triangle (R, wlifter, theta_lifter)
theta_lifter = 2 * atan((wlifter / 2) / (sqrt((ID/2)^2 - (wlifter / 2)^2)));
%
theta_circular = theta - theta_lifter;
%
for i = 1: num_lifters
    %
    theta_i = (i) * theta;
    %
    x(1,i) = (ID/2) * cos(theta_i - theta);
    y(1,i) = (ID/2) * sin(theta_i - theta);

    for j = 1:dens;
    x(j+1,i) = (ID/2) * cos(theta_i - theta + theta_circular * j/dens);
    y(j+1,i) = (ID/2) * sin(theta_i - theta + theta_circular * j/dens);
    end
```

```
    x(dens+4,i) = (ID/2) * cos(theta_i);
    y(dens+4,i) = (ID/2) * sin(theta_i);

    x(dens+3,i) = ((ID/2) - hlifter) * cos(theta_i);
    y(dens+3,i) = ((ID/2) - hlifter) * sin(theta_i);

    x(dens+2,i) = x(dens+3,i) + (wlifter - hlifter/tan(theta_chamfer*pi/180)) * cos(theta_i - pi/2);
    y(dens+2,i) = y(dens+3,i) + (wlifter - hlifter/tan(theta_chamfer*pi/180)) * sin(theta_i - pi/2);
end

% fit straight lines along lifter faces

% face one
for i = 1: num_lifters
xx = [x(dens+1,i);x(dens+2,i)];
yy = [y(dens+1,i);y(dens+2,i)];

if xx(1,1) - xx(2,1) == 0;
    x1(:,i) = xx(1,1).*ones(dens,1);
    y1(:,i) = yy(1,1):(yy(2,1)-yy(1,1))/(dens-1):yy(2,1);
else
    [m,c,U,E] = strLineFit(xx,yy);
x1(:,i) = x(dens+1,i): (x(dens+2,i)-x(dens+1,i))/(dens-1) :x(dens+2,i);
y1(:,i) = m.*x1(:,i) + c;
end
end

% face two
for i = 1: num_lifters
xx = [x(dens+2,i);x(dens+3,i)];
yy = [y(dens+2,i);y(dens+3,i)];

if xx(1,1) - xx(2,1) == 0;
    x2(:,i) = xx(1,1).*ones(dens,1);
    y2(:,i) = yy(1,1):(yy(2,1)-yy(1,1))/(dens-1):yy(2,1);
else
    [m,c,U,E] = strLineFit(xx,yy);
```

```
x2(:,i) = x(dens+2,i): (x(dens+3,i)-x(dens+2,i))/(dens-1) :x(dens+3,i);
y2(:,i) = m.*x2(:,i) + c;
end
end

% face three
for i = 1: num_lifters
xx = [x(dens+3,i);x(dens+4,i)];
yy = [y(dens+3,i);y(dens+4,i)];

if xx(1,1) - xx(2,1) == 0;
    x3(:,i) = xx(1,1).*ones(dens,1);
    y3(:,i) = yy(1,1):(yy(2,1)-yy(1,1))/(dens-1):yy(2,1);
else
    [m,c,U,E] = strLineFit(xx,yy);
x3(:,i) = x(dens+3,i): (x(dens+4,i)-x(dens+3,i))/(dens-1) :x(dens+4,i);
y3(:,i) = m.*x3(:,i) + c;
end
end

x = [x(1:dens+1,:);x1;x2;x3];
y = [y(1:dens+1,:);y1;y2;y3];

[TH,R] = cart2pol(x,y);
TH = TH + rot;
[x,y] = pol2cart(TH,R);
 y = direction.*y;

Xshift = -Xshift;
Yshift = -Yshift;

x = x - Yshift;
y = y - Xshift;

MillShellX = x;
MillShellY = y;
```

GetTrackData

```
function [t, x, y, z, e] = GetTrackData(fileName)

%%%%%%%%%%%%%%%%%%%%%%%%%%%%%%%%%%%%%%%%%%%%%%%%%%%%%%%%%%%%%%%%%%%%%%%%%%%%%%%
%                              GET MILL DATA

% This function reads in and outputs the data for the specified data file

% ARGUMENTS:
% fileName -- Name of the file to be read

% RETURNS:
% t       -- List of times at which the particle coordinates were recorded
% x, y, z -- Lists of spatial coordinates of the particle at each time step
% e       -- List of errors associated with coords x,y,z (May be expanded
%            to output e_x, e_y, e_z instead)

global dataDirectory;

fullName = strcat(dataDirectory, fileName);

% Reads the particle data into cells (data)
fid = fopen(fullName);
Rdata = textscan(fid,'%n%n%n%n%n%n%n%n','headerlines',16);
fclose(fid);

t = Rdata{1};
x = Rdata{2};
y = Rdata{3};
z = Rdata{4};
e = Rdata{5};

%%%%%%%%%%%%%%%%%%%%%%%%%%%%%%%%%%%%%%%%%%%%%%%%%%%%%%%%%%%%%%%%%%%%%%%%%%%%%%%
%%%%%%%%%%%%%%%%%%%%%%%%%%%%%%%%%%%%%%%%%%%%%%%%%%%%%%%%%%%%%%%%%%%%%%%%%%%%%%%
```

InterpPEPT_mod

```
function [a, tt, Ve, Ac] = InterpPEPT_mod(X, t, f, N)
%
% Z  is the the input data to be interpolated
% t  is the time values corresponding to Z in milliseconds
% f  is the interpolation factor
% N  is the first N points from data in x
% Ve is Velocity
% Ac is Acceleration

T = t(1:N,1)./1000; % selects out the first N points of t and convert to seconds
X = X(1:N,1); % selects out the  first N points of Z


tt = T(1,1): (T(end,1)-T(1,1))/(length(T)*f) :T(end,1); % times to interpolated data
tt = tt';

X = X./1000; % convert to meters
a = interp1(T,X,tt,'cubic');
pp = interp1(tt,a,'cubic','pp');

Ve = fnval(fnder(pp),tt);
Ac = fnval(fnder(pp,2),tt);
```

BinInterpData_Mod

```
function [gridXY, gridXYNotNorm, gridX, gridY, gridVx, gridVy, gridVtangX, gridVtangY, gridVtangMag, gridV_MagSqrd,
gridAx, gridAy, gridAmag] = ...
    BinInterpData_Mod(Bins, millGeom, BallPos, Vx, Vy, VtangMag, VtangX, VtangY, V_Magsqrd, Ax, Ay, Amag)
%*************************************************************************************

%*************************************************************************************
% Divide the analysis domain into grid
global NoIntervals
lower_left = min(min(millGeom));     % co-ord lower left hand corner
upper_right = max(max(millGeom));    % co-ord upper right hand corner
NoIntervals = Bins-1;                % number of divisions in the x and y axes
grid_size = (upper_right(1,1)-lower_left(1,1))/NoIntervals; % grid size

gridX = lower_left(1) : grid_size : upper_right(1);
gridY = lower_left(1) : grid_size : upper_right(1);

gridXY=zeros(length(gridX));        % trajectory bin data
gridVx=zeros(length(gridX));
gridVy=zeros(length(gridX));
gridVtangMag=zeros(length(gridX));
gridVtangX=zeros(length(gridX));
gridVtangY=zeros(length(gridX));
gridV_MagSqrd=zeros(length(gridX));
gridAx = zeros(length(gridX));
gridAy = zeros(length(gridX));
gridAmag = zeros(length(gridX));
%*************************************************************************************
%bin trajectory data using the binary search routine
for j = 1 : length(BallPos)
    [tmp_1] = binary_search(gridX,0,length(gridX),BallPos(j,1));
    [tmp_2] = binary_search(gridY,0,length(gridY),BallPos(j,2));
    gridXY(tmp_2,tmp_1) = gridXY(tmp_2,tmp_1) + 1;
    gridVx(tmp_2,tmp_1) = gridVx(tmp_2,tmp_1) + Vx(j,1);
    gridVy(tmp_2,tmp_1) = gridVy(tmp_2,tmp_1) + Vy(j,1);
    gridV_MagSqrd(tmp_2,tmp_1) = gridV_MagSqrd(tmp_2,tmp_1) + V_Magsqrd(j,1);
```

```
    gridVtangX(tmp_2,tmp_1) = gridVtangX(tmp_2,tmp_1) + VtangX(j,1);
    gridVtangY(tmp_2,tmp_1) = gridVtangY(tmp_2,tmp_1) + VtangY(j,1);
    gridVtangMag(tmp_2,tmp_1) = gridVtangMag(tmp_2,tmp_1) + VtangMag(j,1);

    gridAx(tmp_2,tmp_1) = gridAx(tmp_2,tmp_1) + Ax(j,1);
    gridAy(tmp_2,tmp_1) = gridAy(tmp_2,tmp_1) + Ay(j,1);
    gridAmag(tmp_2,tmp_1) = gridAmag(tmp_2,tmp_1) + Amag(j,1);

end

%*************************************************************************************

gridXYNotNorm = gridXY;                 % un-normalised bin data
gridXY = gridXY ./ sum(sum(gridXY));
```

Binary_search

```
function [index] = binary_search(grid,start,finish,location);
%*************************************************************************************
%fname:     binary_search
%purpose:   perform a binary search to bin the data (2d histogram)
%           splits the domain into 2 and checks if the data point to be binned
%           is above or below the division. Continues dividing until start and
%           finish converge. Then returns the index position.
%           Vic Baldwin
%*************************************************************************************

if start == finish
    if grid(finish) > location  % check that last data point lies within the interval
        index=finish-1;
        return
    else
        index=finish;
        return
    end
end
%
split = start + round((finish-start)/2);    %splits the domain in half


if grid(split) < location   %if bin data value at mid point is greater than split value
%   split domain from the split to finish and recusively call binary_search
    [index] = binary_search(grid,split,finish,location);
elseif grid(split) > location  %if bin data value at mid point is less than split value
%   split domain from the start to split(-1) and recusively call binary_search
    [index] = binary_search(grid,start,split-1,location);
else
    [index] = binary_search(grid,split,finish,location);
end
```

LinecentrecocPEPT

```
%Written by Lawrence Bbosa Nov 11
%Plot tang velocities for line thru mill centre and COC
clc

%Formulation of line
Point1=[0 0]; % set first point at origin
Lifterht=5/1000;
Millspdconv=input('Enter mill speed in %crit ');
OmegaMill = (Millspdconv/100)*(42.3/sqrt(0.3))*(2*pi/60); % angular speed of mill

%Plot Figure to get second point
figure(1)
quiver(gridX,gridY,gridVx./gridXYNotNorm,gridVy./gridXYNotNorm,5,'k');
hold on
plot(millGeom(:,1), millGeom(:,2),'k','LineWidth',3)
axis equal tight
title('Velocity')

disp('Click on location of Centre of Circulation')
[Xcoc Ycoc]=ginput(1);
Point2=[Xcoc Ycoc];
print -djpeg -r600 Velocityfield


disp('your point is')
disp(Point2)

GradLine=(Point2(2)-Point1(2))/(Point2(1)-Point1(1));
Xpoints=gridX;
Ypoints=GradLine.*(Xpoints-Point1(1))+Point1(2);

%Identify bin location
gridLINE=zeros(length(gridX));
gridVTangVectorX=zeros(length(gridX));
```

```
gridVTangVectorY=zeros(length(gridX));
binsize=0.3/length(Xpoints);
VTangLine=0;
ybins=0;
for xbin=1:length(Xpoints)
    if Ypoints(xbin)<0
        ylocation=0.15-abs(Ypoints(xbin));
    else
        ylocation=Ypoints(xbin)+0.15;
    end
    ybin=ceil(ylocation/binsize);
    ybins(xbin)=ybin;
    gridLINE(ybin,xbin)=gridVtangMag(ybin,xbin)/gridXYNotNorm(ybin,xbin);
    gridVTangVectorX(ybin,xbin)=gridVtangX(ybin,xbin);
    gridVTangVectorY(ybin,xbin)=gridVtangY(ybin,xbin);
    VTangLine(xbin)=gridVtangMag(ybin,xbin)/gridXYNotNorm(ybin,xbin);
end


%Plots
gridtmp = gridLINE;
len = size(gridXY,1);
% setting zero count bins to white
for i = 1:len;
    for j = 1:len;
        if gridtmp(i,j) == 0;
            gridtmp(i,j) = 0/0;
        end
    end
end

figure(2)
pcolor(H,V,gridtmp)% percentage occupancy
hold on
quiver(gridX,gridY,gridVTangVectorX./gridXYNotNorm,gridVTangVectorY./gridXYNotNorm,10,'k');
plot(millGeom(:,1), millGeom(:,2),'k','LineWidth',3)
plot(Xpoints,Ypoints,'g','LineWidth',2)
axis equal tight
```

```
title('Line through CoC and Mill centre')
set(gca,'CLim',[0 1.8])
colorbar('FontSize',20,'YTick',[0.2 0.4 0.6 0.8 1 1.2 1.4 1.6 1.8])
colorbar
print -djpeg -r600 CoCLineplot

%Get radial distances, plot Graph of  vs Vtang
RadLine=0;
for gdf=1:length(Xpoints)
    if Xpoints(gdf)<0
        RadLine(gdf)=-1*sqrt(Xpoints(gdf).^2+Ypoints(gdf).^2);
    else
        RadLine(gdf)=sqrt(Xpoints(gdf).^2+Ypoints(gdf).^2);
    end
end

%CoC vertical line
RCoC=-1*sqrt(Xcoc.^2+Ycoc.^2);
YCoCline=0:0.01:max(VTangLine);
XCoCline(1:length(YCoCline))=RCoC;

%Mill shell end 1 vertical line
YMillEnd1=0:0.01:max(VTangLine);
XMillEnd1(1:length(YCoCline))=-0.15;

%Mill shell end 2 vertical line
YMillEnd2=0:0.01:max(VTangLine);
XMillEnd2(1:length(YCoCline))=0.15;

%Lifter line end 1
YLifterLine=0:0.01:max(VTangLine);
XLifterLine(1:length(YCoCline))=-0.15+Lifterht;

%Lifter line end 2
YLifterLine2=0:0.01:max(VTangLine);
XLifterLine2(1:length(YCoCline))=0.15-Lifterht;
```

```
%Mill speed line
XMillSpeedLine=-0.15:0.01:0.15;
YMillSpeedLine(1:length(XMillSpeedLine))=OmegaMill*0.15;

figure(3)
plot(RadLine,VTangLine,'bx','LineWidth',2)
hold on
plot(XCoCline,YCoCline,'k:','LineWidth',1);
plot(XMillEnd1,YMillEnd1,'k','LineWidth',5);
plot(XLifterLine,YLifterLine,'g:','LineWidth',1);
plot(XMillSpeedLine,YMillSpeedLine,'r:','LineWidth',1)

plot(XMillEnd2,YMillEnd2,'k','LineWidth',5);
plot(XLifterLine2,YLifterLine2,'g:','LineWidth',1);
legend('Tracer','CoC','Mill shell','Lifter ht','Mill speed','Location','SouthEast')
axis ([-0.16 0.16 0 max(YCoCline)+0.2]);

%Enable if plotting multiple sizes
RadLinePEPT1=RadLine;
VTangLinePEPT1=VTangLine;
save firstdata RadLinePEPT1 VTangLinePEPT1
```

A II- DEM code

Presented below is a list of the algorithms used in the MATLAB programming language to analyse data from DEM simulations. The entire code for each routine follows.

EDEMExtractPosVelJune12- Extracts particle position, velocity and force data from EDEM data to calculate average kinematic properties in transverse grid

Utilises the following subroutines:

BinParticledataJune12- Populates data according to particle locations in the specified grid

Utilises the following subroutines:

Binary_search*- Isolates particle location between specified values by means of a binary search

DrawMillShellPEPT*- Plots an outline of the mill periphery and lifter geometry

EDEMExtractCollisionDataJune12- Extracts normal, tangential and total energy loss from EDEM data

Utilises the following subroutines:

BinEnergydata- Accumulates collision energy data to obtain frequencies with which collisions occur between discrete intervals

EDEMExtractMillForcedata- Extracts the mill geometry forces and velocities at each node to determine power draw

LinecentrecocDEM- Obtains and plots tangential velocities along a diametrical line through the mill centre and centre of circulation

*- Algorithm provided under section A1-PEPT code

EDEMExtractPosVelJune12

```
% EDEM Analyst M file
% Written by Lawrence Bbosa Oct 19th 2009
% Purpose: To extract particle position, velocity and force data from .csv
% files and use it to calculate average kinematic properties in a 2d-grid
% about the transeverse mill face (X and Z ordinate)
%**********************************************************************
%Inputs: 2 CSV files output from EDEM
% Note: Assumes that data files are in the form
% File 1: Q1-X coord, Q2-Y coord Q3-Z coord
% with Q4-Q6 as velocities in directions X, Y and Z
% File 2: Q1, Q2 and Q3 are forces in respective
% directions
%**********************************************************************
warning off

clear all;
clc;

critspeed=input('Enter mill speed in %crit mill speed: ');
wmill= (critspeed/100)*(42.3/sqrt(0.3))*(2*pi/60); % angular speed of mill

tic
%**********************************************************************
%Input variables that have the be modified prior to running script
disp('Extracting Particle data...')
%Specify data file to be read
Analysisfile='\path\data.csv';

% Shift in X and Z direction required to orient the centre of the mill at
% the origin
XShift=-0.19;
ZShift=0.1901565;

ChargeMass=9.69; %Total mass of particles created in simulation
```

```
Milllength=0.27;

%Masses of particles based on properties given in DEM (in m)
%               2mm       3mm        4mm        5mm      6mm       8mm
%               1          2          3          4        5         6
Select=    [ 1.05e-5  3.53e-5    8.38e-5  1.636e-4 2.827e-4 6.702e-4];
ParticleMass=Select(4);  %Mass of each DEM particle

%Particle volume [3mm 5mm 8mm]
SelectVol=[1.41372e-8   6.54498e-8   2.68083e-7];
ParticleVol=SelectVol(2);

g=9.81;
NoIntervals=49;

%************************************************************************
%Initialize variables that will be used in code
ignoreline=true; % true=ignore current line in data file, false= read current line

ParticleDataX=[];  %Output variable of X coordinates
ParticleDataY=[];  %Output variable of Y coordinates
ParticleDataZ=[];  %Output variable of Z coordinates
ParticleDataVelX=[];  %Output variable of Velocity magnitudes
ParticleDataVelY=[];
ParticleDataVelZ=[];

Time=[];          %Output variable of corresponding time for Particle Data outputs
n=1;   %initialize count which will create columns in output data file for each timestep
rowmultq1=1; %initialize multiplier count variables which will be used to append data to outputs
rowmultq2=1;
rowmultq3=1;
rowmultq4=1;
rowmultq5=1;
rowmultq6=1;

linebreak=254; %Default no of columns at which line data continues to next line
%Angular velocity of bin
```

```
wbin=zeros(NoIntervals+1,NoIntervals+1);

%************************************************************************

% Read in data file
fid=fopen(Analysisfile,'r');
while 1
    line = fgetl(fid);   %Read every line in the data file
    if ~ischar(line), break, end % Halt and end if a non string is encountered
    %loop to make sure lines before TIME are skipped
    if (size(line,2)>=4 &line(1:4)== 'TIME')
        ignoreline=false;
    end
    LineSize=size(line,2);
    if (ignoreline==false & LineSize>=1)
        if ((LineSize>=5) & line(1:5)=='TIME:')
            Time2=str2double(line(7:end)); %Check whether current line is TIME heading, if so obtains time
            Time(1,n)=Time2;              %Get output row vector whose columns list time at each timestep
            continue;
            %Loops to search where the next data output query begins for X,
            %Y, Z and Velocity
        elseif ((LineSize>=17) & line(1:26)== 'Q01 : Particle Position X:')
            linedata=line(27:end);    %Get data from after the query name
            ParticleDataX(1:size(str2num(linedata),2),n)=[str2num(linedata)']; %Add to Particle DataX output on
column n
            Q=1;
            continue;
        elseif ((LineSize>=17) & line(1:26)== 'Q02 : Particle Position Y:')
            linedata=line(27:end);    %Get data from after the query name
            ParticleDataY(1:size(str2num(linedata),2),n)=[str2num(linedata)']; %Add to Particle DataY output on
column n
            Q=2;
            continue;
        elseif ((LineSize>=17) & line(1:26)== 'Q03 : Particle Position Z:')
            linedata=line(27:end);    %Get data from after the query name
            ParticleDataZ(1:size(str2num(linedata),2),n)=[str2num(linedata)']; %Add to Particle DataZ output on
column n
            Q=3;
```

```
            continue;
        elseif ((LineSize>=17) & line(1:26)== 'Q04 : Particle Velocity X:')
            linedata=line(27:end);    %Get data from after the query name
            ParticleDataVelX(1:size(str2num(linedata),2),n)=[str2num(linedata)']; %Add to Particle DataV output on
column n
            Q=4;
            continue;
        elseif ((LineSize>=17) & line(1:26)== 'Q05 : Particle Velocity Y:')
            linedata=line(27:end);    %Get data from after the query name
            ParticleDataVelY(1:size(str2num(linedata),2),n)=[str2num(linedata)']; %Add to Particle DataV output on
column n
            Q=5;
            continue;
        elseif ((LineSize>=17) & line(1:26)== 'Q06 : Particle Velocity Z:')
            linedata=line(27:end);    %Get data from after the query name
            ParticleDataVelZ(1:size(str2num(linedata),2),n)=[str2num(linedata)']; %Add to Particle DataV output on
column n
            Q=6;
            continue;
        elseif ((LineSize>=17) & Q==1) %for cases where data continues to next line
            linedata=line(1:end);    %takes entire line of data
            Rowend=(rowmultq1*linebreak)+1; % Row number to append data to
            ParticleDataX(Rowend:(Rowend+size(str2num(linedata),2)-1),n)=[str2num(linedata)']; %Add this data to
Particle DataX output
            rowmultq1=rowmultq1+1;       % adds one to the multiplier, each appending is a multiple of 254
            continue;
        elseif ((LineSize>=17) & Q==2) %for cases where data continues to next line
            linedata=line(1:end);    %takes entire line of data
            Rowend=(rowmultq2*linebreak)+1; % Row number to append data to
            ParticleDataY(Rowend:(Rowend+size(str2num(linedata),2)-1),n)=[str2num(linedata)']; %Add this data to
Particle DataY output
            rowmultq2=rowmultq2+1;
            continue;
        elseif ((LineSize>=17) & Q==3) %for cases where data continues to next line
            linedata=line(1:end);    %takes entire line of data
            Rowend=(rowmultq3*linebreak)+1; % Row number to append data to
            ParticleDataZ(Rowend:(Rowend+size(str2num(linedata),2)-1),n)=[str2num(linedata)']; %Add this data to
Particle DataZ output
```

```
            rowmultq3=rowmultq3+1;
            continue;
        elseif ((LineSize>=17) & Q==4) %for cases where data continues to next line
            linedata=line(1:end);    %takes entire line of data
            Rowend=(rowmultq4*linebreak)+1; % Row number to append data to
            ParticleDataVelX(Rowend:(Rowend+size(str2num(linedata),2)-1),n)=[str2num(linedata)']; %Add this data to
Particle DataV output
            rowmultq4=rowmultq4+1;
            continue;
        elseif ((LineSize>=17) & Q==5) %for cases where data continues to next line
            linedata=line(1:end);    %takes entire line of data
            Rowend=(rowmultq5*linebreak)+1; % Row number to append data to
            ParticleDataVelY(Rowend:(Rowend+size(str2num(linedata),2)-1),n)=[str2num(linedata)']; %Add this data to
Particle DataV output
            rowmultq5=rowmultq5+1;
            continue;
        elseif ((LineSize>=17) & Q==6) %for cases where data continues to next line
            linedata=line(1:end);    %takes entire line of data
            Rowend=(rowmultq6*linebreak)+1; % Row number to append data to
            ParticleDataVelZ(Rowend:(Rowend+size(str2num(linedata),2)-1),n)=[str2num(linedata)']; %Add this data to
Particle DataV output
            rowmultq6=rowmultq6+1;
            continue;
        end
    end
    if (LineSize==0 & ignoreline==false) %Loop to identify when next time step is reached
        n=n+1; %Adds one to timestep count
        rowmultq1=1;    %Resets multiplier for row appending
        rowmultq2=1;
        rowmultq3=1;
        rowmultq4=1;
        rowmultq5=1;
        rowmultq6=1;
    end
end

%**************************************************************************
fclose all;
```

```
disp('Extracting Force data...')
%Pull out force data
Analysisfile2='\path\data2.csv';

%************************************************************************
%Initialize variables that will be used in code
ignoreline=true; % true=ignore current line in data file, false= read current line

ParticleForceX=[];  %Output variable of Velocity magnitudes
ParticleForceY=[];
ParticleForceZ=[];

Time=[];          %Output variable of corresponding time for Particle Data outputs
n=1;   %initialize count which will create columns in output data file for each timestep
rowmultq1=1; %initialize multiplier count variables which will be used to append data to outputs
rowmultq2=1;
rowmultq3=1;

%************************************************************************

% Read in data file
fid=fopen(Analysisfile2,'r');
while 1
    line = fgetl(fid);   %Read every line in the data file
    if ~ischar(line), break, end % Halt and end if a non string is encountered
    %loop to make sure lines before TIME are skipped
    if (size(line,2)>=4 &line(1:4)== 'TIME')
        ignoreline=false;
    end
    LineSize=size(line,2);
    if (ignoreline==false & LineSize>=1)
        if ((LineSize>=5) & line(1:5)=='TIME:')
            Time2=str2double(line(7:end)); %Check whether current line is TIME heading, if so obtains time
            Time(1,n)=Time2;              %Get output row vector whose columns list time at each timestep
            continue;
            %Loops to search where the next data output query begins for X,
            %Y, Z and Velocity
```

```
        elseif ((LineSize>=29) & line(1:29)== 'Q01 : Particle Total Force X:')
            linedata=line(30:end);    %Get data from after the query name
            ParticleForceX(1:size(str2num(linedata),2),n)=[str2num(linedata)']; %Add to Particle DataX output on
column n
            Q=1;
            continue;
        elseif ((LineSize>=29) & line(1:29)== 'Q02 : Particle Total Force Y:')
            linedata=line(30:end);    %Get data from after the query name
            ParticleForceY(1:size(str2num(linedata),2),n)=[str2num(linedata)']; %Add to Particle DataY output on
column n
            Q=2;
            continue;
        elseif ((LineSize>=29) & line(1:29)== 'Q03 : Particle Total Force Z:')
            linedata=line(30:end);    %Get data from after the query name
            ParticleForceZ(1:size(str2num(linedata),2),n)=[str2num(linedata)']; %Add to Particle DataZ output on
column n
            Q=3;
            continue;
        elseif ((LineSize>=17) & Q==1) %for cases where data continues to next line
            linedata=line(1:end);    %takes entire line of data
            Rowend=(rowmultq1*linebreak)+1; % Row number to append data to
            ParticleForceX(Rowend:(Rowend+size(str2num(linedata),2)-1),n)=[str2num(linedata)']; %Add this data to
Particle DataX output
            rowmultq1=rowmultq1+1;       % adds one to the multiplier, each appending is a multiple of 254
            continue;
        elseif ((LineSize>=17) & Q==2) %for cases where data continues to next line
            linedata=line(1:end);    %takes entire line of data
            Rowend=(rowmultq2*linebreak)+1; % Row number to append data to
            ParticleForceY(Rowend:(Rowend+size(str2num(linedata),2)-1),n)=[str2num(linedata)']; %Add this data to
Particle DataY output
            rowmultq2=rowmultq2+1;
            continue;
        elseif ((LineSize>=17) & Q==3) %for cases where data continues to next line
            linedata=line(1:end);    %takes entire line of data
            Rowend=(rowmultq3*linebreak)+1; % Row number to append data to
            ParticleForceZ(Rowend:(Rowend+size(str2num(linedata),2)-1),n)=[str2num(linedata)']; %Add this data to
Particle DataZ output
            rowmultq3=rowmultq3+1;
```

```
            continue;
        end
    end
    if (LineSize==0 & ignoreline==false) %Loop to identify when next time step is reached
        n=n+1; %Adds one to timestep count
        rowmultq1=1;    %Resets multiplier for row appending
        rowmultq2=1;
        rowmultq3=1;
    end
end

%**************************************************************************
fclose all;

toc

disp('Calculating kinematic properties...')
tic

%Shift Particle position data so that mill centre is at 0,0
ParticleDataX=ParticleDataX+XShift;
ParticleDataZ=ParticleDataZ+ZShift;

%Eliminate particles stuck in mill inlet from binned averages
for i = 1:size(ParticleDataX,1);
    for j = 1:size(ParticleDataX,2);
        if ParticleDataY(i,j) > 0.315;
            ParticleDataX(i,j)=-0.15;
            ParticleDataZ(i,j)=-0.15;
        end
    end
end

% Calculate tangential velocities
for db=1:1:size(ParticleDataX,2);

    Vxz{db}= [ParticleDataVelX(:,db)' ; ParticleDataVelZ(:,db)'];
```

```
    ParticleDataAbsVel{db}=sqrt(sum(Vxz{db}.^2))';

    Rxz{db}=[ParticleDataX(:,db)'; ParticleDataZ(:,db)'];

    RxzMag{db}=sqrt(sum(Rxz{db}.^2));

    dot_VR=dot(Vxz{db},Rxz{db});

    tr=(dot_VR./(RxzMag{db}.^2));

    ParticleDataTangentialVel{db}=Vxz{db}-[tr.*Rxz{db}(1,:) ; tr.*Rxz{db}(2,:)];

    ParticleDataTangentialVelX{db}=ParticleDataTangentialVel{db}(1,:)';
    ParticleDataTangentialVelZ{db}=ParticleDataTangentialVel{db}(2,:)';

    ParticleDataTangentialVelMag{db}=sqrt(sum(ParticleDataTangentialVel{db}.^2))';

end

%Particle Power dissipation
ParticlePowerX=ParticleForceX.*abs(ParticleDataVelX);
ParticlePowerY=ParticleForceY.*abs(ParticleDataVelY);
ParticlePowerZ=ParticleForceZ.*abs(ParticleDataVelZ);

ParticlePowerTotalX=(sum(ParticlePowerX));
ParticlePowerTotalY=(sum(ParticlePowerY));
ParticlePowerTotalZ=(sum(ParticlePowerZ));
ParticlePowerTotal=abs(ParticlePowerTotalX+ParticlePowerTotalY+ParticlePowerTotalZ);

toc

%Binning properties
disp('Binning grid data and determining cell averages...')
%Initialize Grid in XZ plane
lower_left = [-0.15 -0.15];     % co-ord lower left hand corner for grid x
upper_right = [0.15 0.15];    % co-ord upper right hand corner for grid x
```

```
grid_size = (upper_right(1,1)-lower_left(1,1))/NoIntervals; % grid size

grid = lower_left(1) : grid_size : upper_right(1);
tic

gridXZTotal=zeros(length(grid));
gridXZNotNormTotal=zeros(length(grid));
gridVelXTotal=zeros(length(grid));
gridVelYTotal=zeros(length(grid));
gridVelZTotal=zeros(length(grid));
gridVelTangentialMagTotal=zeros(length(grid));
gridVelTangentialXTotal=zeros(length(grid));
gridVelTangentialZTotal=zeros(length(grid));
gridForceXTotal=zeros(length(grid));
gridForceYTotal=zeros(length(grid));
gridForceZTotal=zeros(length(grid));
gridPowerXTotal=zeros(length(grid));
gridPowerYTotal=zeros(length(grid));
gridPowerZTotal=zeros(length(grid));
gridPackingFractionTotal=zeros(length(grid));
gridPorosityTotal=zeros(length(grid));

for db=1:1:size(ParticleDataX,2);

    [gridX{db},gridZ{db},gridXZ{db},gridXZNotNorm{db},gridVelX{db},gridVelY{db},gridVelZ{db},...
    gridVelTangentialMag{db},gridVelTangentialX{db},gridVelTangentialZ{db},gridForceX{db},...

gridForceY{db},gridForceZ{db},gridPowerX{db},gridPowerY{db},gridPowerZ{db},gridPackingFraction{db},gridPorosity{db}]
=...
         BinParticledataJune12(ParticleDataX(:,db),ParticleDataZ(:,db),...
         ParticleDataVelX(:,db),ParticleDataVelY(:,db),ParticleDataVelZ(:,db),...
         ParticleDataTangentialVelMag{db},ParticleDataTangentialVelX{db},ParticleDataTangentialVelZ{db},...
         ParticleForceX(:,db),ParticleForceY(:,db),ParticleForceZ(:,db),...
         ParticlePowerX(:,db),ParticlePowerY(:,db),ParticlePowerZ(:,db),...
         ParticleVol,Milllength);
```

```
    gridXZTotal=gridXZTotal+gridXZ{db};
    gridXZNotNormTotal=gridXZNotNormTotal+gridXZNotNorm{db};
    gridVelXTotal=gridVelXTotal+gridVelX{db};
    gridVelYTotal=gridVelYTotal+gridVelY{db};
    gridVelZTotal=gridVelZTotal+gridVelZ{db};
    gridVelTangentialMagTotal=gridVelTangentialMagTotal+gridVelTangentialMag{db};
    gridVelTangentialXTotal=gridVelTangentialXTotal+gridVelTangentialX{db};
    gridVelTangentialZTotal=gridVelTangentialZTotal+gridVelTangentialZ{db};
    gridForceXTotal=gridForceXTotal+gridForceX{db};
    gridForceYTotal=gridForceYTotal+gridForceY{db};
    gridForceZTotal=gridForceZTotal+gridForceZ{db};
    gridPowerXTotal=gridPowerXTotal+gridPowerX{db};
    gridPowerYTotal=gridPowerYTotal+gridPowerY{db};
    gridPowerZTotal=gridPowerZTotal+gridPowerZ{db};
    gridPackingFractionTotal=gridPackingFractionTotal+gridPackingFraction{db};
    gridPorosityTotal=gridPorosityTotal+gridPorosity{db};

end


gridXZAverage= gridXZTotal./db;
gridXZNotNormAverage= gridXZNotNormTotal./db;
gridVelXAverage=gridVelXTotal./db;
gridVelYAverage=gridVelYTotal./db;
gridVelZAverage=gridVelZTotal./db;
gridVelTangentialMagAverage=gridVelTangentialMagTotal./db;
gridVelTangentialXAverage=gridVelTangentialXTotal./db;
gridVelTangentialZAverage=gridVelTangentialZTotal./db;
gridForceXAverage=gridForceXTotal./db;
gridForceYAverage=gridForceYTotal./db;
gridForceZAverage=gridForceZTotal./db;
gridPowerXAverage= gridPowerXTotal./db;
gridPowerYAverage=gridPowerYTotal./db;
gridPowerZAverage=gridPowerZTotal./db;
gridPackingFractionAverage=gridPackingFractionTotal./db;
gridPorosityAverage=gridPorosityTotal./db;
```

```
%determing absolute and angular velocities
gridX2=gridX{db};
gridZ2=gridZ{db};
gridXZ2=gridXZ{db};

gridVelAbsAverage=sqrt( gridVelXAverage.^2 + gridVelZAverage.^2 );

[H,V] = meshgrid(gridX2,gridZ2);
GridXX2 = H;
GridZZ2 = V;
gridRad2 = sqrt(GridXX2.^2 + GridZZ2.^2);

gridVelAngular=gridVelTangentialMagAverage./gridRad2;

toc


disp('Determining Power Draw and plotting data')
tic

% Calculate Power Draw using 2 methods
gridPowerTorquebinTotal=zeros(length(grid));

for dc=1:1:size(ParticleDataX,2);

    %Method 1- PCOM
    PowerDrawCOM(1,dc)=ChargeMass*g*abs(mean(ParticleDataX(:,dc)))*wmill;

    %Method 2-PBIN

gridPowerTorquebin{dc}=abs(ChargeMass*g.*gridXZ{dc}.*GridXX2.*(gridVelTangentialMag{dc}./gridXZNotNorm{dc}./gridRad2
));
    len = size(gridPowerTorquebin{dc},1);
% setting zero count bins to white
for i = 1:len;
    for j = 1:len;
```

```
        if isnan(gridPowerTorquebin{dc}(i,j))==1;
            gridPowerTorquebin{dc}(i,j) = 0;
        end
    end
end
    PowerDrawBinDEM(1,dc)=sum(sum(gridPowerTorquebin{dc}));

    gridPowerTorquebinTotal=gridPowerTorquebinTotal+gridPowerTorquebin{dc};

end

gridPowerTorquebinAverage=gridPowerTorquebinTotal./dc;
len=size(gridPowerTorquebinAverage,1);
for i = 1:len;
    for j = 1:len;
        if isnan(gridPowerTorquebinAverage(i,j))==1;
            gridPowerTorquebinAverage(i,j) = 0;
        end
    end
end

%Plots

CentXY=[0,0];
[MillShellX,MillShellY] = DrawMillShellPEPT(200,CentXY(1,2)/1000,CentXY(1,1)/1000,300/1000,
20,5/1000,20/1000,60,0,1);
%DrawMillShellPEPT(dens,Xshift,Yshift,ID, num_lifters,hlifter,wlifter,theta_chamfer,rot,direction)
%millGeom = [MillShellX(:)-CentXY(1,1)/1000 MillShellY(:)-CentXY(1,2)/1000];
millGeom = [MillShellX(:) MillShellY(:)];

%%
gridtmp = gridXZAverage;
len = size(gridXZ2,1);
% setting zero count bins to white
for i = 1:len;
    for j = 1:len;
        if gridtmp(i,j) == 0;
```

```
            gridtmp(i,j) = 0/0;
        end
    end
end

figure(1)
pcolor(H,V,gridtmp)% percentage occupancy
hold on
plot(millGeom(:,1), millGeom(:,2),'k','LineWidth',2)
axis equal tight
title('Average position')
colorbar

%%
gridtmp = gridVelXAverage./gridXZNotNormAverage;
len = size(gridXZ2,1);
% setting zero count bins to white
for i = 1:len;
    for j = 1:len;
        if gridtmp(i,j) == 1/0;
            gridtmp(i,j) = 0/0;
        end
    end
end
gridtmp2 = gridVelZAverage./gridXZNotNormAverage;
len = size(gridXZ2,1);
% setting zero count bins to white
for i = 1:len;
    for j = 1:len;
        if gridtmp(i,j) == 1/0;
            gridtmp(i,j) = 0/0;
        end
    end
end

figure(2)
```

```
hold on
quiver(gridX2,gridZ2,gridtmp,gridtmp2,5,'k');
plot(millGeom(:,1), millGeom(:,2),'k','LineWidth',2)
axis equal tight
title('Velocity')

% %%
gridtmp = gridVelAbsAverage./gridXZNotNormAverage;
len = size(gridXZ2,1);
% setting zero count bins to white
for i = 1:len;
    for j = 1:len;
        if gridtmp(i,j) == 0;
            gridtmp(i,j) = 0/0;
        end
    end
end

figure(3)
pcolor(H,V,gridtmp)% percentage occupancy
hold on
plot(millGeom(:,1), millGeom(:,2),'k','LineWidth',2)
axis equal tight
title('Velocity Map (m/s)')
colorbar
%

gridtmp = gridPorosityAverage;
% setting zero count bins to white
len = size(gridXZ2,1);
for i = 1:len;
    for j = 1:len;
        if gridtmp(i,j) > 0.99;
            gridtmp(i,j) = 0/0;
        end
    end
end
figure(4)
```

```
pcolor(H,V,gridtmp)% percentage occupancy
hold on
plot(millGeom(:,1), millGeom(:,2),'k','LineWidth',2)
axis equal tight
title('Porosity Distribution')
colorbar

gridtmp = gridVelTangentialMagAverage./gridXZNotNormAverage;
% setting zero count bins to white
len = size(gridXZ2,1);
for i = 1:len;
    for j = 1:len;
        if gridtmp(i,j) == 0;
            gridtmp(i,j) = 0/0;
        end
    end
end
figure(5)
pcolor(H,V,gridtmp)% percentage occupancy
hold on
plot(millGeom(:,1), millGeom(:,2),'k','LineWidth',2)
axis equal tight
title('Tangential Velocity')
colorbar

figure(6)
quiver(gridX2,gridZ2,gridVelTangentialXAverage./gridXZNotNormAverage,gridVelTangentialZAverage./gridXZNotNormAverage
,20,'k');
hold on
plot(millGeom(:,1), millGeom(:,2),'k','LineWidth',2)
axis equal tight
title('Tangential Velocity')

gridtmp = gridPowerTorquebinAverage;
% setting zero count bins to white
len = size(gridXZ2,1);
for i = 1:len;
    for j = 1:len;
```

```
        if gridtmp(i,j) == 0;
            gridtmp(i,j) = 0/0;
        end
    end
end
figure(7)
pcolor(H,V,gridtmp)% percentage occupancy
hold on
plot(millGeom(:,1), millGeom(:,2),'k','LineWidth',2)
axis equal tight
title('Power Distribution Torque per bin')
colorbar

toc
```

BinParticledataJune12

```
% EDEM Analyst M file
% Written by Lawrence Bbosa Oct 23rd 2009
% Purpose: To populate particle data into discrete bins
%**************************************************************************
%Inputs
% Grid position, velocity, force, power and porosity data from main EDEM
% analyst algorithm

%**************************************************************************

function [gridX,gridZ,gridXZ,gridXZNotNorm,gridVelX,gridVelY,gridVelZ,...
    gridVelTangentialMag,gridVelTangentialX,gridVelTangentialZ,gridForceX,...
    gridForceY,gridForceZ,gridPowerX,gridPowerY,gridPowerZ,gridPackingFraction,gridPorosity]=...
         BinParticledataJune12(ParticleDataX,ParticleDataZ,...
         ParticleDataVelX,ParticleDataVelY,ParticleDataVelZ,...
         ParticleDataTangentialVelMag,ParticleDataTangentialVelX,ParticleDataTangentialVelZ,...
         ParticleForceX,ParticleForceY,ParticleForceZ,...
         ParticlePowerX,ParticlePowerY,ParticlePowerZ,...
         ParticleVol,Milllength);


%Initialize Grid in XZ plane
lower_left = [-0.15 -0.15];     % co-ord lower left hand corner for grid x
upper_right = [0.15 0.15];      % co-ord upper right hand corner for grid x
NoIntervals = 49;                % number of divisions in the x and y axes
grid_size = (upper_right(1,1)-lower_left(1,1))/NoIntervals; % grid size

gridX = lower_left(1) : grid_size : upper_right(1);

gridZ = lower_left(1) : grid_size : upper_right(1);

Mill_ID=300;

%Lifter data
```

```
Mult=1.3;
hlifter=5/1000;
wlifter=20/1000;
theta_chamfer=(60*pi/180);
Area_lifter=0.5*(wlifter+(wlifter-hlifter/tan(theta_chamfer)))*hlifter;
num_lifters=20;
TotalArealifters=num_lifters*Area_lifter;

%Initialise grids
gridXZ=zeros(length(gridX));
gridXZNotNorm=zeros(length(gridX));
gridVelX=zeros(length(gridX));
gridVelY=zeros(length(gridX));
gridVelZ=zeros(length(gridX));
gridVelTangentialMag=zeros(length(gridX));
gridVelTangentialX=zeros(length(gridX));
gridVelTangentialZ=zeros(length(gridX));
gridForceX=zeros(length(gridX));
gridForceY=zeros(length(gridX));
gridForceZ=zeros(length(gridX));
gridPowerX=zeros(length(gridX));
gridPowerY=zeros(length(gridX));
gridPowerZ=zeros(length(gridX));
gridPackingFraction=zeros(length(gridX));

%Bin data using a binary search algorithm
for j=1:length(ParticleDataX)
    [tmp_1] = binary_search(gridX,0,length(gridX),ParticleDataX(j,1));
    [tmp_2] = binary_search(gridZ,0,length(gridZ),ParticleDataZ(j,1));

    gridXZ(tmp_2,tmp_1) = gridXZ(tmp_2,tmp_1) + 1;

    gridVelX(tmp_2,tmp_1)=gridVelX(tmp_2,tmp_1) + ParticleDataVelX(j,1);
    gridVelY(tmp_2,tmp_1)=gridVelY(tmp_2,tmp_1) + ParticleDataVelY(j,1);
    gridVelZ(tmp_2,tmp_1)=gridVelZ(tmp_2,tmp_1) + ParticleDataVelZ(j,1);

    gridVelTangentialMag(tmp_2,tmp_1)=gridVelTangentialMag(tmp_2,tmp_1)+ ParticleDataTangentialVelMag(j,1);
```

```
    gridVelTangentialX(tmp_2,tmp_1)=gridVelTangentialX(tmp_2,tmp_1)+ ParticleDataTangentialVelX(j,1);
    gridVelTangentialZ(tmp_2,tmp_1)=gridVelTangentialZ(tmp_2,tmp_1)+ ParticleDataTangentialVelZ(j,1);

    gridForceX(tmp_2,tmp_1)=gridForceX(tmp_2,tmp_1) + ParticleForceX(j,1);
    gridForceY(tmp_2,tmp_1)=gridForceY(tmp_2,tmp_1) + ParticleForceY(j,1);
    gridForceZ(tmp_2,tmp_1)=gridForceZ(tmp_2,tmp_1) + ParticleForceZ(j,1);

    gridPowerX(tmp_2,tmp_1)=gridPowerX(tmp_2,tmp_1) + ParticlePowerX(j,1);
    gridPowerY(tmp_2,tmp_1)=gridPowerY(tmp_2,tmp_1) + ParticlePowerY(j,1);
    gridPowerZ(tmp_2,tmp_1)=gridPowerZ(tmp_2,tmp_1) + ParticlePowerZ(j,1);
end

gridXZNotNorm = gridXZ;                 % un normalised bin data
gridXZ = gridXZ ./ sum(sum(gridXZ));    % normalise the bin data

%determine porosity
gridPackingFraction=zeros(length(gridXZNotNorm));        % Particle position bin data
gridPorosity=zeros(length(gridXZNotNorm));

%Calculate total area in mill shell periphery - lifter area
Rad_diff=(Mill_ID-(hlifter*Mult));
MillPeriph_Area=pi*(Mill_ID^2-(Mill_ID-(hlifter*Mult))^2);

%count number of cells in lifter area
numcells=0;
for i=1:size(gridXZNotNorm,2) %for every timestep
    for j = 1 : size(gridXZNotNorm,2) %for every data point

        Rxz=(gridX(i)^2+gridZ(i)^2);
        if Rxz >= (0.5*Mill_ID)-(hlifter*1.3);
            numcells=numcells+1;
        end
    end
end
Lifter_Area=(MillPeriph_Area-TotalArealifters)/numcells;

BinVolume=zeros(length(gridXZNotNorm));
```

```
for i=1:size(gridXZNotNorm,2) %for every timestep
    for j = 1 : size(gridXZNotNorm,2) %for every data point

        Rxz=(gridX(i)^2+gridZ(i)^2);
        if Rxz >= (0.5*Mill_ID)-(hlifter*1.3);
            BinVolume(i,j)=Lifter_Area*Milllength;
        else
            BinVolume(i,j)=(grid_size^2*Milllength);
        end
    end
end

for i=1:size(gridXZNotNorm,2) %for every timestep
    for j = 1 : size(gridXZNotNorm,2) %for every data point

        ParticleBinVol=gridXZNotNorm(i,j)*ParticleVol;
        gridPackingFraction(i,j)=ParticleBinVol/BinVolume(i,j);
        gridPorosity(i,j)=1-gridPackingFraction(i,j);
    end
end
```

EDEMExtractCollisionDataJune12

```
% EDEM Analyst M file
% Written by Lawrence Bbosa Oct 22nd 2009
% Purpose: To extract normal, tangential and Total Energy losses from
% collisions in EDEM
%**************************************************************************
%Inputs: CSV file output from EDEM
% Note: Assumes that data file is in the form Q1-Normal Energy
% losses,Q2-Tangential Energy losses Q3-Total Energy losses

%**************************************************************************

clear all;
clc;
tic

%Specify data file to be read
Analysisfile='\path\data.csv';

%Initialize variables that will be used in code
ignoreline=true; % true=ignore current line in data file, false= read current line

CollisionDataNorm=[];  %Output variable of X coordinates
CollisionDataTang=[];  %Output variable of Y coordinates
CollisionDataTotal=[];  %Output variable of Z coordinates
Time=[];          %Output variable of corresponding time for Particle Data outputs
n=1;   %initialize count which will create columns in output data file for each timestep
rowmultq1=1; %initialize multiplier count variables which will be used to append data to outputs
rowmultq2=1;
rowmultq3=1;

%Store variables on hard disk rather than memory
cwd = pwd;
cd(tempdir);
pack
```

```
cd(cwd)

linebreak=254; %Default no of columns at which line data continues to next line

% Read in data file
fid=fopen(Analysisfile,'r');
while 1
    line = fgetl(fid);   %Read every line in the data file
    if ~ischar(line), break, end % Halt and end if a non string is encountered
    %loop to make sure lines before TIME are skipped
    if (size(line,2)>=4 &line(1:4)== 'TIME')
        ignoreline=false;
    end
    LineSize=size(line,2);
    if (ignoreline==false & LineSize>=1)
        if ((LineSize>=5) & line(1:5)=='TIME:')
            Time2=str2double(line(7:end)); %Check whether current line is TIME heading, if so obtains time
            Time(1,n)=Time2;              %Get output row vector whose columns list time at each timestep
            continue;
            %Loops to search where the next data output query begins for X,
            %Y, Z and Velocity
        elseif ((LineSize>=39) & line(1:35)== 'Q01 : Collision Normal Energy Loss:')
            linedata=line(36:end);    %Get data from after the query name
            CollisionDataNorm(1:size(str2num(linedata),2),n)=[str2num(linedata)']; %Add to Particle DataX output on
column n
            Q=1;
            continue;
        elseif ((LineSize>=39) & line(1:39)== 'Q02 : Collision Tangential Energy Loss:')
            linedata=line(40:end);    %Get data from after the query name
            CollisionDataTang(1:size(str2num(linedata),2),n)=[str2num(linedata)']; %Add to Particle DataY output on
column n
            Q=2;
            continue;
        elseif ((LineSize>=39) & line(1:34)== 'Q03 : Collision Total Energy Loss:')
            linedata=line(35:end);    %Get data from after the query name
            CollisionDataTotal(1:size(str2num(linedata),2),n)=[str2num(linedata)']; %Add to Particle DataZ output on
column n
            Q=3;
```

```
            continue;
        elseif ((LineSize>=39) & line(1:35)== 'Q04 : Collision Normal Energy Loss:')
            Q=0;  %Eliminates irrelevant data if more queries are called
            continue;
        elseif ((LineSize>=39) & Q==1) %for cases where data continues to next line
            linedata=line(1:end);    %takes entire line of data
            Rowend=(rowmultq1*linebreak)+1; % Row number to append data to
            CollisionDataNorm(Rowend:(Rowend+size(str2num(linedata),2)-1),n)=[str2num(linedata)']; %Add this data to
Particle DataX output
            rowmultq1=rowmultq1+1;       % adds one to the multiplier, each appending is a multiple of 254
            continue;
        elseif ((LineSize>=39) & Q==2) %for cases where data continues to next line
            linedata=line(1:end);    %takes entire line of data
            Rowend=(rowmultq2*linebreak)+1; % Row number to append data to
            CollisionDataTang(Rowend:(Rowend+size(str2num(linedata),2)-1),n)=[str2num(linedata)']; %Add this data to
Particle DataY output
            rowmultq2=rowmultq2+1;
            continue;
        elseif ((LineSize>=39) & Q==3) %for cases where data continues to next line
            linedata=line(1:end);    %takes entire line of data
            Rowend=(rowmultq3*linebreak)+1; % Row number to append data to
            CollisionDataTotal(Rowend:(Rowend+size(str2num(linedata),2)-1),n)=[str2num(linedata)']; %Add this data
to Particle DataZ output
            rowmultq3=rowmultq3+1;
            continue;
        end
    end
    if (LineSize==0 & ignoreline==false) %Loop to identify when next time step is reached
        n=n+1; %Adds one to timestep count
        rowmultq1=1;    %Resets multiplier for row appending
        rowmultq2=1;
        rowmultq3=1;
    end
end
fclose all;

%Populate collision frequency data bins
```

```
PowerD=sum(CollisionDataTotal);
%
% %Combine Collision data matrices into column vectors
CollisionDataNormCombine=[CollisionDataNorm(:,1)];   %Initialize combined column vectors
CollisionDataTangCombine=[CollisionDataTang(:,1)];
CollisionDataTotalCombine=[CollisionDataTotal(:,1)];
for a=2:1:size(CollisionDataNorm,2)
    CollisionDataNormCombine=[CollisionDataNormCombine;CollisionDataNorm(:,a)]; %Append each column to end of the
combined vectors row
    CollisionDataTangCombine=[CollisionDataTangCombine;CollisionDataTang(:,a)];
    CollisionDataTotalCombine=[CollisionDataTotalCombine;CollisionDataTotal(:,a)];
end

%calculated as sum of total energy losses/(2*Periodic Time)
[freqNormSummed,freqTangSummed,freqTotalSummed,Energybins]=BinEnergydata(CollisionDataNormCombine,CollisionDataTangC
ombine,CollisionDataTotalCombine);

toc
```

BinEnergydata

```
% EDEM Analyst M file
% Written by Lawrence Bbosa Oct 22nd 2009
% Purpose: To count frequencies with which energy values occur and populate data into discrete bins
%**************************************************************************
%Inputs: Collision data for normal, tangential and total energy loss
%**************************************************************************

function
[freqNormSummed,freqTangSummed,freqTotalSummed,Energybins]=BinEnergydata(CollisionDataNormCombine,CollisionDataTangC
ombine,CollisionDataTotalCombine);

%Initialize variables that will be used
Energybins= 5e-7:1e-6:5e-4;     %Set the bin ranges


%Calculate collision frequencies for the set bin ranges
freqNorm=hist(CollisionDataNormCombine,Energybins);    %Matrix that contains collision frequencies for each timestep
freqTang=hist(CollisionDataTangCombine,Energybins);
freqTotal=hist(CollisionDataTotalCombine,Energybins);

%Sum matrices up to obtain collision frequencies for entire revolution
freqNormSummed=freqNorm;
freqTangSummed=freqTang;
freqTotalSummed=freqTotal;

logFreqTotalSummed=log10(freqTotalSummed);
logFreqNormSummed=log10(freqNormSummed);
logFreqTangSummed=log10(freqTangSummed);
```

EDEMExtractMillForcedata

```
 %EDEM Analyst M file
% Written by Lawrence Bbosa September 2010
% Purpose: To extract force data from EDEM and use it to determine power
% draw

%************************************************************************
%Inputs: CSV file output from EDEM in the form
%Q1-Q3- Geometry forces X, Y and Z
%Q4-Q6- Geometry velocities X, Y and Z

%************************************************************************

warning off

clear all;
clc;
tic
%************************************************************************
%Input variables that have the be modified prior to running script
disp('Extracting Geometry data...')
%Specify data file to be read
Analysisfile='\path\data.csv';

%************************************************************************
%Initialize variables that will be used in code
ignoreline=true; % true=ignore current line in data file, false= read current line

ForceX=[];   % Set up variables that will be used
ForceY=[];
ForceZ=[];
VelX=[];
VelY=[];
VelZ=[];
```

```
Time=[];          %Output variable of corresponding time for Particle Data outputs
n=1;   %initialize count which will create columns in output data file for each timestep
rowmultq1=1; %initialize multiplier count variables which will be used to append data to outputs
rowmultq2=1;
rowmultq3=1;
rowmultq4=1;
rowmultq5=1;
rowmultq6=1;

linebreak=254; %Default no of columns at which line data continues to next line

%**************************************************************************

% Read in data file
fid=fopen(Analysisfile,'r');
while 1
    line = fgetl(fid);   %Read every line in the data file
    if ~ischar(line), break, end % Halt and end if a non string is encountered
    %loop to make sure lines before TIME are skipped
    if (size(line,2)>=4 &line(1:4)== 'TIME')
        ignoreline=false;
    end
    LineSize=size(line,2);
    if (ignoreline==false & LineSize>=1)
        if ((LineSize>=5) & line(1:5)=='TIME:')
            Time2=str2double(line(7:end)); %Check whether current line is TIME heading, if so obtains time
            Time(1,n)=Time2;               %Get output row vector whose columns list time at each timestep
            continue;
            %Loops to search where the next data output query begins for X,
            %Y, Z and Velocity
        elseif ((LineSize>=17) & line(1:29)== 'Q01 : Geometry Total Force X:')
            linedata=line(30:end);    %Get data from after the query name
            ForceX(1:size(str2num(linedata),2),n)=[str2num(linedata)']; %Add to Particle DataX output on column n
            Q=1;
            continue;
        elseif ((LineSize>=17) & line(1:29)== 'Q02 : Geometry Total Force Y:')
```

```
            linedata=line(30:end);    %Get data from after the query name
            ForceY(1:size(str2num(linedata),2),n)=[str2num(linedata)']; %Add to Particle DataY output on column n
            Q=2;
            continue;
        elseif ((LineSize>=17) & line(1:29)== 'Q03 : Geometry Total Force Z:')
            linedata=line(30:end);    %Get data from after the query name
            ForceZ(1:size(str2num(linedata),2),n)=[str2num(linedata)']; %Add to Particle DataZ output on column n
            Q=3;
            continue;
        elseif ((LineSize>=17) & line(1:26)== 'Q04 : Geometry Velocity X:')
            linedata=line(27:end);    %Get data from after the query name
            VelX(1:size(str2num(linedata),2),n)=[str2num(linedata)']; %Add to Particle DataV output on column n
            Q=4;
            continue;
        elseif ((LineSize>=17) & line(1:26)== 'Q05 : Geometry Velocity Y:')
            linedata=line(27:end);    %Get data from after the query name
            VelY(1:size(str2num(linedata),2),n)=[str2num(linedata)']; %Add to Particle DataV output on column n
            Q=5;
            continue;
        elseif ((LineSize>=17) & line(1:26)== 'Q06 : Geometry Velocity Z:')
            linedata=line(27:end);    %Get data from after the query name
            VelZ(1:size(str2num(linedata),2),n)=[str2num(linedata)']; %Add to Particle DataV output on column n
            Q=6;
            continue;
        elseif ((LineSize>=17) & Q==1) %for cases where data continues to next line
            linedata=line(1:end);    %takes entire line of data
            Rowend=(rowmultq1*linebreak)+1; % Row number to append data to
            ForceX(Rowend:(Rowend+size(str2num(linedata),2)-1),n)=[str2num(linedata)']; %Add this data to Particle
DataX output
            rowmultq1=rowmultq1+1;     % adds one to the multiplier, each appending is a multiple of 254
            continue;
        elseif ((LineSize>=17) & Q==2) %for cases where data continues to next line
            linedata=line(1:end);    %takes entire line of data
            Rowend=(rowmultq2*linebreak)+1; % Row number to append data to
            ForceY(Rowend:(Rowend+size(str2num(linedata),2)-1),n)=[str2num(linedata)']; %Add this data to Particle
DataY output
            rowmultq2=rowmultq2+1;
            continue;
```

```
        elseif ((LineSize>=17) & Q==3) %for cases where data continues to next line
            linedata=line(1:end);    %takes entire line of data
            Rowend=(rowmultq3*linebreak)+1; % Row number to append data to
            ForceZ(Rowend:(Rowend+size(str2num(linedata),2)-1),n)=[str2num(linedata)']; %Add this data to Particle
DataZ output
            rowmultq3=rowmultq3+1;
            continue;
        elseif ((LineSize>=17) & Q==4) %for cases where data continues to next line
            linedata=line(1:end);    %takes entire line of data
            Rowend=(rowmultq4*linebreak)+1; % Row number to append data to
            VelX(Rowend:(Rowend+size(str2num(linedata),2)-1),n)=[str2num(linedata)']; %Add this data to Particle
DataV output
            rowmultq4=rowmultq4+1;
            continue;
        elseif ((LineSize>=17) & Q==5) %for cases where data continues to next line
            linedata=line(1:end);    %takes entire line of data
            Rowend=(rowmultq5*linebreak)+1; % Row number to append data to
            VelY(Rowend:(Rowend+size(str2num(linedata),2)-1),n)=[str2num(linedata)']; %Add this data to Particle
DataV output
            rowmultq5=rowmultq5+1;
            continue;
        elseif ((LineSize>=17) & Q==6) %for cases where data continues to next line
            linedata=line(1:end);    %takes entire line of data
            Rowend=(rowmultq6*linebreak)+1; % Row number to append data to
            VelZ(Rowend:(Rowend+size(str2num(linedata),2)-1),n)=[str2num(linedata)']; %Add this data to Particle
DataV output
            rowmultq6=rowmultq6+1;
            continue;
        end
    end
    if (LineSize==0 & ignoreline==false) %Loop to identify when next time step is reached
        n=n+1; %Adds one to timestep count
        rowmultq1=1;    %Resets multiplier for row appending
        rowmultq2=1;
        rowmultq3=1;
        rowmultq4=1;
        rowmultq5=1;
        rowmultq6=1;
```

```
    end
end

%**************************************************************************
fclose all;
disp('Calculating Power Draw...')
%Calculate Power Draw by summing up unbalanced Force*Velocity on Geometry
GeometryPowerX=ForceX.*abs(VelX);
GeometryPowerY=ForceY.*abs(VelY);
GeometryPowerZ=ForceZ.*abs(VelZ);

PowerDrawX=sum(GeometryPowerX);
PowerDrawY=sum(GeometryPowerY);
PowerDrawZ=sum(GeometryPowerZ);

PowerGeom=abs(PowerDrawX+PowerDrawY+PowerDrawZ);

toc
```

LinecentrecocDEM

```
%Written by Lawrence Bbosa Nov 11
%Plot tang velocities for a line thru mill centre and COC
clc

%Formulation of line
Point1=[0 0]; % set first point at origin
Lifterht=5/1000;
Millspdconv=input('Enter mill speed in %crit ');
OmegaMill = (Millspdconv/100)*(42.3/sqrt(0.3))*(2*pi/60); % angular speed of mill

%Plot Figure to get second point
figure(1)
quiver(gridX2,gridZ2,gridVelXAverage./gridXZNotNormAverage,gridVelZAverage./gridXZNotNormAverage,5,'k');
hold on
plot(millGeom(:,1), millGeom(:,2),'k','LineWidth',3)
axis equal tight
title('Velocity')
print -djpeg -r600 Velocityfield

disp('Click on location of Centre of Circulation')
[Xcoc Ycoc]=ginput(1);
Point2=[Xcoc Ycoc];

disp('your point is')
disp(Point2)

GradLine=(Point2(2)-Point1(2))/(Point2(1)-Point1(1));
Xpoints=gridX2;
Ypoints=GradLine.*(Xpoints-Point1(1))+Point1(2);

%Identify bin location
gridLINE=zeros(length(gridX2));
gridVTangVectorX=zeros(length(gridX2));
gridVTangVectorY=zeros(length(gridX2));
```

```
binsize=0.3/length(Xpoints);
VTangLine=0;
ybins=0;
for xbin=1:length(Xpoints)
    if Ypoints(xbin)<0
        ylocation=0.15-abs(Ypoints(xbin));
    else
        ylocation=Ypoints(xbin)+0.15;
    end
    ybin=ceil(ylocation/binsize);
    ybins(xbin)=ybin;
    gridLINE(ybin,xbin)=gridVelTangentialMagAverage(ybin,xbin)/gridXZNotNormAverage(ybin,xbin);
    gridVTangVectorX(ybin,xbin)=gridVelTangentialXAverage(ybin,xbin);
    gridVTangVectorY(ybin,xbin)=gridVelTangentialZAverage(ybin,xbin);
    VTangLine(xbin)=abs(gridVelTangentialMagAverage(ybin,xbin))/gridXZNotNormAverage(ybin,xbin);
end


%Plots
gridtmp = gridLINE;
len = size(gridXZ2,1);
% setting zero count bins to white
for i = 1:len;
    for j = 1:len;
        if gridtmp(i,j) == 0;
            gridtmp(i,j) = 0/0;
        end
    end
end

figure(2)
pcolor(H,V,gridtmp)% percentage occupancy
hold on
quiver(gridX2,gridZ2,gridVTangVectorX./gridXZNotNormAverage,gridVTangVectorY./gridXZNotNormAverage,10,'k');
plot(millGeom(:,1), millGeom(:,2),'k','LineWidth',3)
plot(Xpoints,Ypoints,'g','LineWidth',2)
axis equal tight
title('Line through CoC and Mill centre')
```

```
colorbar

%Get radial distances, plot Graph of  vs Vtang
RadLine=0;
for gdf=1:length(Xpoints)
    if Xpoints(gdf)<0
        RadLine(gdf)=-1*sqrt(Xpoints(gdf).^2+Ypoints(gdf).^2);
    else
        RadLine(gdf)=sqrt(Xpoints(gdf).^2+Ypoints(gdf).^2);
    end
end

%CoC vertical line
RCoC=-1*sqrt(Xcoc.^2+Ycoc.^2);
YCoCline=0:0.01:max(VTangLine);
XCoCline(1:length(YCoCline))=RCoC;

%Mill shell end 1 vertical line
YMillEnd1=0:0.01:max(VTangLine);
XMillEnd1(1:length(YCoCline))=-0.15;

%Mill shell end 2 vertical line
YMillEnd2=0:0.01:max(VTangLine);
XMillEnd2(1:length(YCoCline))=0.15;

%Lifter line end 1
YLifterLine=0:0.01:max(VTangLine);
XLifterLine(1:length(YCoCline))=-0.15+Lifterht;

%Lifter line end 2
YLifterLine2=0:0.01:max(VTangLine);
XLifterLine2(1:length(YCoCline))=0.15-Lifterht;

%Mill speed line
XMillSpeedLine=-0.15:0.01:0.15;
YMillSpeedLine(1:length(XMillSpeedLine))=OmegaMill*0.15;
```

```
figure(3)
plot(RadLine,VTangLine,'bx','LineWidth',2)
hold on
plot(XCoCline,YCoCline,'k:','LineWidth',1);
plot(XMillEnd1,YMillEnd1,'k','LineWidth',5);
plot(XLifterLine,YLifterLine,'g:','LineWidth',1);
plot(XMillSpeedLine,YMillSpeedLine,'r:','LineWidth',1)

plot(XMillEnd2,YMillEnd2,'k','LineWidth',5);
plot(XLifterLine2,YLifterLine2,'g:','LineWidth',1);
legend('Tracer','CoC','Mill shell','Lifter ht','Mill speed','Location','SouthEast')
axis ([-0.16 0.16 0 max(YCoCline)+0.2]);


%Enable if plotting multiple sizes
RadLinePEPT1=RadLine;
VTangLinePEPT1=VTangLine;
save firstdata RadLinePEPT1 VTangLinePEPT1
```

A III – Code for PEPT/DEM comparison

Presented below is a list of the algorithms used in the MATLAB programming language to compare the data analysis of PEPT and DEM data. The entire code for each routine follows.

plotfreqdistDEMPEPT- Plots relative frequency distributions along each of the transverse mill axes for PEPT and DEM data

PEPTDEMCompareplots- Plots and compares spatial distribution plots obtained for PEPT and DEM

Porositycompare- Calculates the spatial porosity distributions for PEPT and DEM data while recalculating porosity values at the mill periphery to account for the presence of lifters

plottfreqdistDEMPEPT

```
% Written by Lawrence Bbosa April 12th 2012
% Purpose: To plot frequency distributions of particle positions along each
% of the transverse mill axes for DEM and PEPT data
%**********************************************************************

clc
clear all
% Load DEM data file
load('path\data.mat')

gridXsum=sum(gridXZNotNormAverage);
gridXsumNorm1=gridXsum./sum(gridXsum);

gridYsum=sum(gridXZNotNormAverage');
gridYsumNorm1=gridYsum./sum(gridYsum);

%Load PEPT data file
load('path\data.mat')

gridXsum=sum(gridXYNotNorm);
gridXsumNorm2=gridXsum./sum(gridXsum);

gridYsum=sum(gridXYNotNorm');
gridYsumNorm2=gridYsum./sum(gridYsum);

figure(1)
plot(gridX,gridXsumNorm1)

hold on
title('X position')
ylabel('Relative frequency')
xlabel('x distance (m)')
plot(gridX,gridXsumNorm2,'g')
%set(gcf, 'PaperPositionMode', 'auto');
```

```
legend('DEM','PEPT','Location','NorthEast')
axis ([-0.15 0.15 0 max(gridXsumNorm2)+0.01]);
print -djpeg -r600 xrelativefreq

figure(2)
plot(gridY,gridYsumNorm1)

hold on
title('Y position')
ylabel('Relative frequency')
xlabel('y distance (m)')
plot(gridY,gridYsumNorm2,'g')
%set(gcf, 'PaperPositionMode', 'auto');
legend('DEM','PEPT','Location','NorthEast')
axis ([-0.15 0.15 0 max(gridYsumNorm2)+0.01]);
print -djpeg -r600 yrelativefreq
```

PEPTDEMCompareplots

```
%Compare plots of DEM and PEPT data
clc
%
%Set variables to compare
%DEM
gridtmp1 = gridXZAverage;

%PEPT
gridtmp2 = gridXY;

%%
gridtmp = gridtmp2;
len = size(gridXY,1);
% setting zero count bins to white
for i = 1:len;
    for j = 1:len;
        if gridtmp(i,j) == 0;
            gridtmp(i,j) = 0/0;
        end
    end
end

figure(1)
pcolor(H,V,gridtmp)% percentage occupancy
hold on
plot(millGeom(:,1), millGeom(:,2),'k','LineWidth',2)
axis equal tight
set(gca,'CLim',[0, 4e-3])
colorbar('FontSize',10,'YTick',[0,1e-3,2e-3,3e-3,4e-3])
t = title('PEPT');
set(t, 'FontSize', 12);
set(gcf, 'PaperPositionMode', 'auto');
print -djpeg -r600 PositionPEPT
```

```
gridtmp = gridtmp1;
len = size(gridXY,1);
% setting zero count bins to white
for i = 1:len;
    for j = 1:len;
        if gridtmp(i,j) == 0;
            gridtmp(i,j) = 0/0;
        end
    end
end

figure(2)
pcolor(H,V,gridtmp)% percentage occupancy
hold on
plot(millGeom(:,1), millGeom(:,2),'k','LineWidth',2)
axis equal tight
set(gca,'CLim',[0, 4e-3])
colorbar('FontSize',10,'YTick',[0,1e-3,2e-3,3e-3,4e-3])
t = title('DEM');
set(t, 'FontSize', 12);
set(gcf, 'PaperPositionMode', 'auto');
print -djpeg -r600 PositionDEM

gridtmp = gridtmp2-gridtmp1;
gridtmpsum=sum(sum(gridtmp));
gridtmp=gridtmp./gridtmpsum;
len = size(gridXZ2,1);
% setting zero count bins to white
for i = 1:len;
    for j = 1:len;
        if gridtmp(i,j) == 0;
            gridtmp(i,j) = 0/0;
        end
    end
end

figure(3)
pcolor(H,V,gridtmp)% percentage occupancy
```

```
hold on
plot(millGeom(:,1), millGeom(:,2),'k','LineWidth',2)
axis equal tight
colorbar %('FontSize',20,'YTick',[0,1e-3,2e-3,3e-3,4e-3])
t = title('PEPT-DEM');
set(t, 'FontSize', 12);
set(gcf, 'PaperPositionMode', 'auto');
print -djpeg -r600 PositionCompare

%%
Porositymod=Porosity;
len = size(gridXY,1);
% Setting all PEPT porosities < 0.4 equal to 0.4
for i = 1:len;
    for j = 1:len;
        if Porositymod(i,j) < 0.33;
            Porositymod(i,j) = 0.33;
        end
    end
end

gridtmp = Porositymod;
len = size(gridXY,1);
% setting zero count bins to white
for i = 1:len;
    for j = 1:len;
        if gridtmp(i,j) > 0.99;
            gridtmp(i,j) = 0/0;
        end
    end
end

figure(4)
pcolor(H,V,gridtmp)% percentage occupancy
hold on
plot(millGeom(:,1), millGeom(:,2),'k','LineWidth',2)
axis equal tight
set(gca,'CLim',[0, 1])
```

```
colorbar('FontSize',20,'YTick',[0,0.1,0.2,0.3,0.4,0.5,0.6,0.7,0.8,0.9,1])
title('PEPT: Porosity')
set(gcf, 'PaperPositionMode', 'auto');
print -djpeg -r600 PorosityPEPT

gridtmp = gridPorosityAverage;
len = size(gridXZ2,1);
% setting zero count bins to white
for i = 1:len;
    for j = 1:len;
        if gridtmp(i,j) > 0.99;
            gridtmp(i,j) = 0/0;
        end
    end
end

figure(5)
pcolor(H,V,gridtmp)% percentage occupancy
hold on
plot(millGeom(:,1), millGeom(:,2),'k','LineWidth',2)
axis equal tight
set(gca,'CLim',[0, 1])
colorbar('FontSize',20,'YTick',[0,0.1,0.2,0.3,0.4,0.5,0.6,0.7,0.8,0.9,1])
title('DEM: Porosity')
set(gcf, 'PaperPositionMode', 'auto');
print -djpeg -r600 PorosityDEM

gridtmp = Porositymod-gridPorosityAverage;
len = size(gridXY,1);
% setting zero count bins to white
for i = 1:len;
    for j = 1:len;
        if gridtmp(i,j) == 0;
            gridtmp(i,j) = 0/0;
        end
    end
end
```

```
figure(6)
pcolor(H,V,gridtmp)% percentage occupancy
hold on
plot(millGeom(:,1), millGeom(:,2),'k','LineWidth',2)
axis equal tight
set(gca,'CLim',[-1 1])
colorbar('FontSize',20,'YTick',[-1,-0.75,-0.5,-0.25,0,0.25,0.5,0.75,1])
title('PEPT-DEM: Porosity')
set(gcf, 'PaperPositionMode', 'auto');
print -djpeg -r600 PorosityCompare

%%

gridtmp = GridV;
len = size(gridXY,1);
% setting zero count bins to white
for i = 1:len;
    for j = 1:len;
        if gridtmp(i,j) == 0;
            gridtmp(i,j) = 0/0;
        end
    end
end

figure(7)
pcolor(H,V,gridtmp)% percentage occupancy
hold on
plot(millGeom(:,1), millGeom(:,2),'k','LineWidth',2)
axis equal tight
set(gca,'CLim',[0, 2.25])
colorbar('FontSize',20,'YTick',[0,0.25,0.5,0.75,1,1.25,1.5,1.75,2,2.25])
title('PEPT: Velocity')
set(gcf, 'PaperPositionMode', 'auto');
print -djpeg -r600 VelocityPEPT
```

```
gridtmp = gridVelAbsAverage./gridXZNotNormAverage;
len = size(gridXZ2,1);
% setting zero count bins to white
for i = 1:len;
    for j = 1:len;
        if gridtmp(i,j) ==0;
            gridtmp(i,j) = 0/0;
        end
    end
end

figure(8)
pcolor(H,V,gridtmp)% percentage occupancy
hold on
plot(millGeom(:,1), millGeom(:,2),'k','LineWidth',2)
axis equal tight
set(gca,'CLim',[0, 2.25])
colorbar('FontSize',20,'YTick',[0,0.25,0.5,0.75,1,1.25,1.5,1.75,2,2.25])
title('DEM: Velocity')
set(gcf, 'PaperPositionMode', 'auto');
print -djpeg -r600 VelocityDEM

gridtmp = GridV-(gridVelAbsAverage./gridXZNotNormAverage);
len = size(gridXY,1);
% setting zero count bins to white
for i = 1:len;
    for j = 1:len;
        if gridtmp(i,j) == 0;
            gridtmp(i,j) = 0/0;
        end
    end
end

figure(9)
pcolor(H,V,gridtmp)% percentage occupancy
hold on
plot(millGeom(:,1), millGeom(:,2),'k','LineWidth',2)
set(gca,'CLim',[-1 1])
```

```
colorbar('FontSize',20,'YTick',[-1,-0.75,-0.5,-0.25,0,0.25,0.5,0.75,1])
title('PEPT-DEM: Velocity')
set(gcf, 'PaperPositionMode', 'auto');
print -djpeg -r600 VelocityCompare

%%

gridtmp = P1_dist;
len = size(gridXY,1);
% setting zero count bins to white
for i = 1:len;
    for j = 1:len;
        if gridtmp(i,j) == 0;
            gridtmp(i,j) = 0/0;
        end
    end
end

figure(10)
pcolor(H,V,gridtmp)% percentage occupancy
hold on
plot(millGeom(:,1), millGeom(:,2),'k','LineWidth',2)
axis equal tight
set(gca,'CLim',[0, 0.125])
colorbar('FontSize',20,'YTick',[0,0.025,0.05,0.075,0.1,0.125])
title('PEPT: Power Draw')
set(gcf, 'PaperPositionMode', 'auto');
print -djpeg -r600 PowerDrawPEPT

gridtmp = gridPowerTorquebinAverage;
len = size(gridXZ2,1);
% setting zero count bins to white
for i = 1:len;
    for j = 1:len;
        if gridtmp(i,j) ==0;
            gridtmp(i,j) = 0/0;
        end
```

```
    end
end

figure(11)
pcolor(H,V,gridtmp)% percentage occupancy
hold on
plot(millGeom(:,1), millGeom(:,2),'k','LineWidth',2)
axis equal tight
set(gca,'CLim',[0, 0.125])
colorbar('FontSize',20,'YTick',[0,0.025,0.05,0.075,0.1,0.125])
title('DEM: Power Draw')
set(gcf, 'PaperPositionMode', 'auto');
print -djpeg -r600 PowerDrawDEM

gridtmp = P1_dist-gridPowerTorquebinAverage;
% gridtmpsum=sum(sum(gridtmp));
% gridtmp=gridtmp./gridtmpsum;
len = size(gridXY,1);
% setting zero count bins to white
for i = 1:len;
    for j = 1:len;
        if gridtmp(i,j) == 0;
            gridtmp(i,j) = 0/0;
        end
    end
end

figure(12)
pcolor(H,V,gridtmp)% percentage occupancy
hold on
plot(millGeom(:,1), millGeom(:,2),'k','LineWidth',2)
axis equal tight
set(gca,'CLim',[-0.1 0.1])

colorbar('FontSize',20,'YTick',[-0.1 -0.075 -0.05 -0.025 0 0.025 0.05 0.075 0.1])
title('PEPT-DEM: Power Draw')
set(gcf, 'PaperPositionMode', 'auto');
```

```
print -djpeg -r600 PowerDrawCompare


diffVel=GridV-(gridVelAbsAverage./gridXZNotNormAverage);
len = size(gridXY,1);
% setting zero count bins to white
for i = 1:len;
    for j = 1:len;
        if isnan(diffVel(i,j)) ==1;
            diffVel(i,j) = 0;
        end
    end
end

diffPower=P1_dist-gridPowerTorquebinAverage;
len = size(gridXY,1);
% setting zero count bins to white
for i = 1:len;
    for j = 1:len;
        if isnan(diffPower(i,j)) ==1;
            diffPower(i,j) = 0;
        end
    end
end
```

Porositycompare

```
% Written by Lawrence Bbosa June 5th 2012
% Purpose: To recalculate the porosity distribution of the mill to correct
% for velues at the mill periphery where the voxel volumes are reduced due to
% the presence of lifters
%**********************************************************************

clc

%Lifter data
Mult=1;
hlifter=5/1000;
wlifter=20/1000;
theta_chamfer=(60*pi/180);
Area_lifter=0.5*(wlifter+(wlifter-hlifter/tan(theta_chamfer)))*hlifter;
num_lifters=20;
TotalArealifters=num_lifters*Area_lifter;

%Particle volume [3mm 5mm 8mm]
SelectVol=[1.41372e-8   6.54498e-8   2.68083e-7];
ParticleVol=SelectVol(1);
dens=2500;
ChargeMass=9.662;
NumpartPEPT=ChargeMass/(dens*ParticleVol);

Mill_ID=0.3;

%Calculate total area in mill shell periphery - lifter area
R2=Mill_ID;
R1=Mill_ID-(hlifter*Mult);
MillPeriph_Area=pi*(R2^2-R1^2);

%count number of cells in lifter area
numcells=0;
for i=1:size(gridXZNotNormAverage,2) %for every timestep
```

```
    for j = 1 : size(gridXZNotNormAverage,2) %for every data point
        Rxz=sqrt(gridX2(i)^2+gridZ2(j)^2);
        if Rxz >= (0.5*Mill_ID)-(hlifter*Mult);
            if Rxz < (0.51*Mill_ID)
                numcells=numcells+1;
            end
        end
    end
end
Lifter_Area=(MillPeriph_Area-TotalArealifters)/numcells;

BinVolume=zeros(length(gridXZNotNormAverage));
for i=1:size(gridXZNotNormAverage,2) %for every timestep
    for j = 1 : size(gridXZNotNormAverage,2) %for every data point
        Rxz=sqrt(gridX2(i)^2+gridZ2(j)^2);
        if Rxz >= (0.5*Mill_ID)-(hlifter*Mult);
            if Rxz > 0.51*Mill_ID
                BinVolume(i,j)=0/0;
            else
                BinVolume(i,j)=Lifter_Area*Milllength;
            end
        else
            BinVolume(i,j)=(grid_size^2*Milllength);
        end
    end
end


%%
%%%%%%%%%%%%%%%%%%%%%%%%%%%%%%%%%%%%%%%%%%%%%%%%
% DEM Porosity calculation
gridPfmod=zeros(length(gridXZNotNormAverage));
gridPmod=zeros(length(gridXZNotNormAverage));
for i=1:size(gridXZNotNormAverage,2) %for every timestep
    for j = 1 : size(gridXZNotNormAverage,2) %for every data point
        ParticleBinVol=gridXZNotNormAverage(i,j)*ParticleVol;
        gridPfmod(i,j)=ParticleBinVol/BinVolume(i,j);
        gridPmod(i,j)=1-gridPfmod(i,j);
```

```
%         if gridPmod(i,j) < 0.3
%             gridPmod(i,j)=0.3;
%         end
    end
end

gridtmp = gridPorosityAverage;
% setting zero count bins to white
len = size(gridXZ2,1);
for i = 1:len;
    for j = 1:len;
        if gridtmp(i,j) > 0.99;
            gridtmp(i,j) = 0/0;
        end
    end
end
figure(1)
pcolor(H,V,gridtmp)% percentage occupancy
hold on
plot(millGeom(:,1), millGeom(:,2),'k','LineWidth',2)
axis equal tight
title('Porosity Distribution')
axis equal tight
set(gca,'CLim',[0, 1])
colorbar('FontSize',20,'YTick',[0,0.1,0.2,0.3,0.4,0.5,0.6,0.7,0.8,0.9,1])
title('DEM: Porosity unmodified')


gridtmp = gridPmod;
% setting zero count bins to white
len = size(gridXZ2,1);
for i = 1:len;
    for j = 1:len;
        if gridtmp(i,j) > 0.99;
            gridtmp(i,j) = 0/0;
        end
    end
end
```

```
figure(2)
pcolor(H,V,gridtmp)% percentage occupancy
hold on
plot(millGeom(:,1), millGeom(:,2),'k','LineWidth',2)
axis equal tight
title('Porosity Distribution')
axis equal tight
set(gca,'CLim',[0, 1])
colorbar('FontSize',20,'YTick',[0,0.1,0.2,0.3,0.4,0.5,0.6,0.7,0.8,0.9,1])
title('DEM:Porosity')
print -djpeg -r600 PorosityDEM
%%
%PEPT porosity
%Mult=Mult*2;

%Calculate total area in mill shell periphery - lifter area
R2=Mill_ID;
R1=Mill_ID-(hlifter*Mult);
MillPeriph_Area=pi*(R2^2-R1^2);

%count number of cells in lifter area
numcells2=0;
for i=1:size(gridXZNotNormAverage,2) %for every timestep
    for j = 1 : size(gridXZNotNormAverage,2) %for every data point
        Rxz=sqrt(gridX2(i)^2+gridZ2(j)^2);
        if Rxz >= (0.5*Mill_ID)-(hlifter*Mult);
            if Rxz < (0.7*Mill_ID)
                numcells2=numcells2+1;
            end
        end
    end
end
Lifter_Area=(MillPeriph_Area-TotalArealifters)/numcells2;

BinVolume=zeros(length(gridXZNotNormAverage));
for i=1:size(gridXZNotNormAverage,2) %for every timestep
    for j = 1 : size(gridXZNotNormAverage,2) %for every data point
        Rxz=sqrt(gridX2(i)^2+gridZ2(j)^2);
```

```
        if Rxz >= (0.5*Mill_ID)-(hlifter*Mult);
            if Rxz > 0.7*Mill_ID
                BinVolume(i,j)=0/0;
            else
                BinVolume(i,j)=Lifter_Area*Milllength;
            end
        else
            BinVolume(i,j)=(grid_size^2*Milllength);
        end
    end
end

gridPfmod2=zeros(length(gridXZNotNormAverage));
gridPmod2=zeros(length(gridXZNotNormAverage));
for i=1:size(gridXZNotNormAverage,2) %for every timestep
    for j = 1 : size(gridXZNotNormAverage,2) %for every data point
        Rxz=sqrt(gridX2(i)^2+gridZ2(j)^2);
        ParticleBinVol=NumpartPEPT*ParticleVol*gridXY(i,j);
        gridPfmod2(i,j)=ParticleBinVol/BinVolume(i,j);
        gridPmod2(i,j)=1-gridPfmod2(i,j);
        if gridPmod2(i,j) < 0.33
            gridPmod2(i,j)=0.33;
        end
        if Rxz>=0.5*Mill_ID;
            gridPmod2(i,j)=0/0;
        end
    end
end

gridtmp = Porositymod;
% setting zero count bins to white
len = size(gridXZ2,1);
for i = 1:len;
    for j = 1:len;
        if gridtmp(i,j) > 0.99;
            gridtmp(i,j) = 0/0;
        end
    end
```

```
end
figure(3)
pcolor(H,V,gridtmp)% percentage occupancy
hold on
plot(millGeom(:,1), millGeom(:,2),'k','LineWidth',2)
axis equal tight
title('Porosity Distribution')
axis equal tight
set(gca,'CLim',[0, 1])
colorbar('FontSize',20,'YTick',[0,0.1,0.2,0.3,0.4,0.5,0.6,0.7,0.8,0.9,1])
title('PEPT: Porosity unmodified')


gridtmp = gridPmod2;
% setting zero count bins to white
len = size(gridXZ2,1);
for i = 1:len;
    for j = 1:len;
        if gridtmp(i,j) > 0.99;
            gridtmp(i,j) = 0/0;
        end
    end
end
figure(4)
pcolor(H,V,gridtmp)% percentage occupancy
hold on
plot(millGeom(:,1), millGeom(:,2),'k','LineWidth',2)
axis equal tight
axis equal tight
set(gca,'CLim',[0, 1])
colorbar('FontSize',20,'YTick',[0,0.1,0.2,0.3,0.4,0.5,0.6,0.7,0.8,0.9,1])
title('PEPT:Porosity')
print -djpeg -r600 PorosityPEPT
%%
%PEPT-DEM
gridPEPTDEM=gridPmod2-gridPmod;

gridtmp = gridPEPTDEM;
```

```
% setting zero count bins to white
len = size(gridXZ2,1);
for i = 1:len;
    for j = 1:len;
        if gridPmod(i,j) > 0.9
            gridtmp(i,j) = 0/0;
        end
    end
end
figure(5)
pcolor(H,V,gridtmp)% percentage occupancy
hold on
plot(millGeom(:,1), millGeom(:,2),'k','LineWidth',2)
axis equal tight
axis equal tight
set(gca,'CLim',[-1 1])
colorbar('FontSize',20,'YTick',[-1,-0.75,-0.5,-0.25,0,0.25,0.5,0.75,1])
title('PEPT-DEM:Porosity')
print -djpeg -r600 PorosityPEPTvDEM
```

APPENDIX B- ENERGY SPECTRA DATA AND MODELLING APPROACH

The collision frequency data for the total energy losses extracted from DEM simulations is regressed using Equation (B1):

$$\log(N) = K_1 \cdot e^{-K_2 \cdot E} + K_3 \cdot e^{-K_4 \cdot E} \quad \textbf{(B1)}$$

The parameter *N* represents the number of collisions and *E* is the collision energy loss

Values of parameters K_1, K_2, K_3 and K_4 are presented in this Appendix along with the R^2, Square Sum of Errors (SSE) and Root Mean Square Error (RMSE)

B I- DEM SIMULATION DATA

Mono-size simulations

Table B1: Parameters obtained for Equation (B1) fitted to mono-size simulations

Speed	Filling	Size		K_1	K_2	K_3	K_4		R^2	*SSE*	*RMSE*
(%crit.)	(%)	(mm)			(x 10^3)		(x 10^3)				
50	31.25	3		6.47	11.05	4.85	256.05		0.994	10.72	0.163
60	31.25	3		5.97	10.32	4.46	221.28		0.993	14.26	0.181
75	31.25	3		5.41	9.32	4.30	204.49		0.990	20	0.210
50	31.25	5		4.49	5.95	3.97	154.15		0.992	15.75	0.186
60	31.25	5		4.49	5.43	3.74	140.72		0.984	37.49	0.275
75	31.25	5		4.49	4.86	3.48	125.86		0.988	28.31	0.239
90	31.25	5		4.49	4.44	3.27	114.89		0.990	22.73	0.214
50	31.25	8		3.85	3.72	3.40	96.34		0.987	25.56	0.227
60	31.25	8		3.85	3.40	3.21	87.95		0.988	23.23	0.216
75	31.25	8		3.85	3.04	2.98	78.66		0.993	12.33	0.168
90	31.25	8		3.85	2.77	2.80	71.81		0.990	20	0.210
100	31.25	8		3.85	2.63	2.71	68.12		0.992	17.79	17.790
75	25	5		4.49	5.23	3.74	116.92		0.989	18.25	0.193
75	31.25	5		4.49	4.86	3.48	125.86		0.989	25.33	0.226
75	37.5	5		4.49	4.58	3.27	133.66		0.990	22.73	0.214
75	12.5	8		3.85	4.11	4.03	58.14		0.986	31	0.250
75	25	8		3.85	3.27	3.21	73.08		0.993	12.292	0.172
75	31.25	8		3.85	3.04	2.98	78.66		0.993	14.135	0.179
75	50	8		3.85	2.60	2.55	91.86		0.995	7.598	0.173

Full size distribution simulations

Table B2: Parameters obtained for Equation (B1) fitted to full size distribution simulations

Speed	Filling	Size		K_1	K_2	K_3	K_4		R^2	*SSE*	*RMSE*
(%crit.)	(%)	(mm)			(x 10^3)		(x 10^3)				
60	31.25	2		6.08	36.54	5.06	946.09		0.999	0.8053	0.104
60	31.25	3		5.32	20.44	4.43	529.31		0.999	0.5259	0.100
60	31.25	4		4.84	15.02	4.03	388.88		0.998	1.41287	0.121
60	31.25	5		4.49	12.55	3.74	324.88		0.997	0.1383	2.928
60	31.25	6		4.23	11.26	3.52	291.47		0.998	0.7185	0.108
60	31.25	8		3.85	10.18	3.21	263.51		0.997	3.1725	0.134
75	31.25	2		6.08	32.68	4.70	846.21		0.996	4.041	0.144
75	31.25	3		5.32	18.29	4.12	473.43		0.998	0.8386	0.111
75	31.25	4		4.84	13.43	3.74	347.83		0.995	4.9889	0.150
75	31.25	5		4.49	11.22	3.48	290.58		0.995	5.043	0.153
75	31.25	6		4.23	10.07	3.27	260.70		0.997	1.079	0.123
75	31.25	8		3.85	9.10	2.98	235.69		0.994	5.8312	0.154
90	31.25	2		6.08	29.84	4.43	772.48		0.994	5.858	0.144
90	31.25	3		5.32	16.69	3.88	432.18		0.996	1.5753	0.138
90	31.25	4		4.84	12.26	3.52	317.52		0.994	6.4972	0.143
90	31.25	5		4.49	10.25	3.27	265.26		0.994	5.699	0.147
90	31.25	6		4.23	9.19	3.08	237.99		0.996	1.49	0.133
90	31.25	8		3.85	8.31	2.80	215.15		0.993	6.837	0.152

B II- ENERGY SPECTRA MODEL

The energy spectra model (B1) is a sum of two exponential decay functions as illustrated in Figure B1, a plot of the 5mm mono-size DEM simulation data used as an example in Section 6.1.

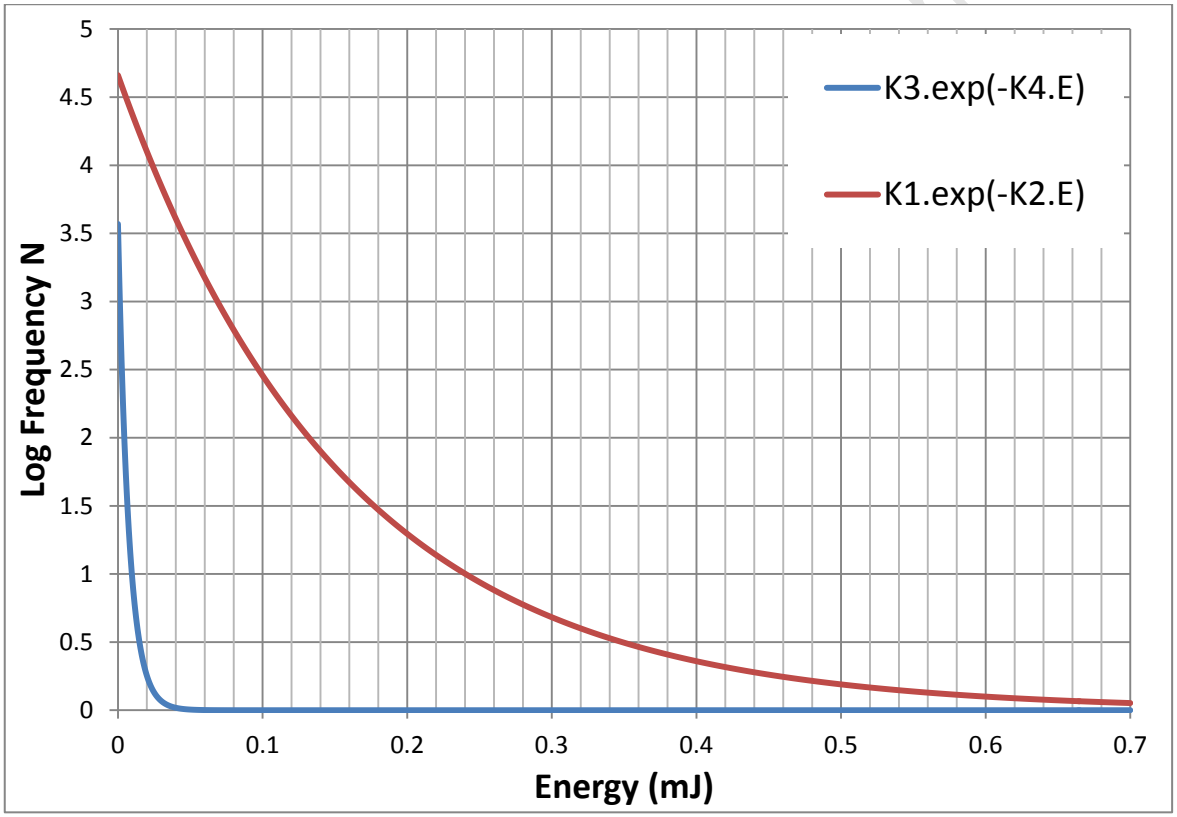

Figure B1: Plot of exponential distributions that compose the energy spectra model

These four parameters are named as follows:

K_1- First Initial Value Term

K_2- Low decay rate

K_3- Second Initial Value Term

K_4- High decay rate

Determination of parameter relationship with mill variables

The sum of the initial value terms K_1 and K_3 is the collision frequency at the minimum energy value of E_0. This is the theoretical maximum number of collisions that can occur at any given energy value and is influenced by the mill operating conditions.

The decay rates K_2 and K_4 define the rate at which the collision frequencies decay from their respective initial values. As shown in Figure B1, K_4 is much higher than K_2. The two decay rates are the parameters which most dictate the shape of the overall collision energy distribution, and are thus modelled in this thesis to be a function of mill operating variables.

K_2 and K_4 are modelled as a function of the investigated mill operating variables using multiple linear regression. Particle size, mass fraction, mill speed and volumetric filling are fitted separately against the model parameters using Equation (B2). For each endeavor, simulation data is selected such that a single operating variable is altered while the others remain the same.

$$y = K_5 \cdot x^{K_6} \quad \textbf{(B2)}$$

In the above equation, *y* represents each particular model parameter (K_2 *or* K_4), while *x* is the mill operating variable in question. While K_5 is simply an arbitrary constant used to establish the relationship, the second fitting constant K_6 is used to identify the order of magnitude for which the model

parameter is affected by the mill variable. With orders of magnitude established for each mill variable, Equation (B3) is then used to predict the overall relationship between the model parameter (*y)* and the mill variable.

$$y = K_7 \cdot p^{K_8} \cdot c^{K_9} \cdot {\omega_m}^{K_{10}} \cdot J^{K_{11}} \quad \textbf{(B3)}$$

Here, *p, c,* ω_m and *J* are the particle size, mass fraction, mill speed and mill filling respectively. K_8, K_9, K_{10} and K_{11} are the orders of magnitude determined from the least squares fitting with Equation (B2). K_7 meanwhile is the fitting constant that scales the mill variables to each parameter. To determine K_7 and the orders of magnitude of K_8, K_9, K_{10} and K_{11}, multiple linear regression is performed using a modified version of (B3) to give (B4):

$$\log(y) = \log(K_7) + (K_8 \cdot \log(p)) + (K_9 \cdot \log(c)) + (K_{10} \cdot \log(\omega_m)) + (K_{11} \cdot \log(J)) \quad \textbf{(B4)}$$

The regression statistics from Equation (B4) are used to calculate values for K_2 and K_4 which yield the lowest residuals when fitted against the entire DEM simulation dataset. The effect of each operating condition on the model parameters follows, with a summary of the values obtained given in Table B3.

Table B3: Orders of magnitude for four mill varaibles fitted against decay rate parameters

	K_2	K_4
Particle size (K_8)	-1	-1
Mass fraction (K_9)	-0.5	-0.5
Mill speed (K_{10})	-0.5	-0.5
Mill volumetric filling (K_{11})	-0.33	0.33

Particle size and mass fraction

The sum of initial value terms K_1 and K_3 for full size distribution simulations at 60, 75 and 90% mill critical speed is depicted in Figure B2. This plot shows that the initial collsion energy for the energy spectra decreases with increasing particle size. The significance of this is that smaller sizes have higher numbers of collisions at the lower energy scale than coarser sizes. This is in accord with existing work on tumbling mill modelling which finds that finer particles in the mill are mainly subjected to numerous low energy contacts as opposed to impacts at high forces (Govender et al., 2012). The plots also suggest that mill speed has little influence on the initial value terms as the values obtained at the three mill speeds are fairly close.

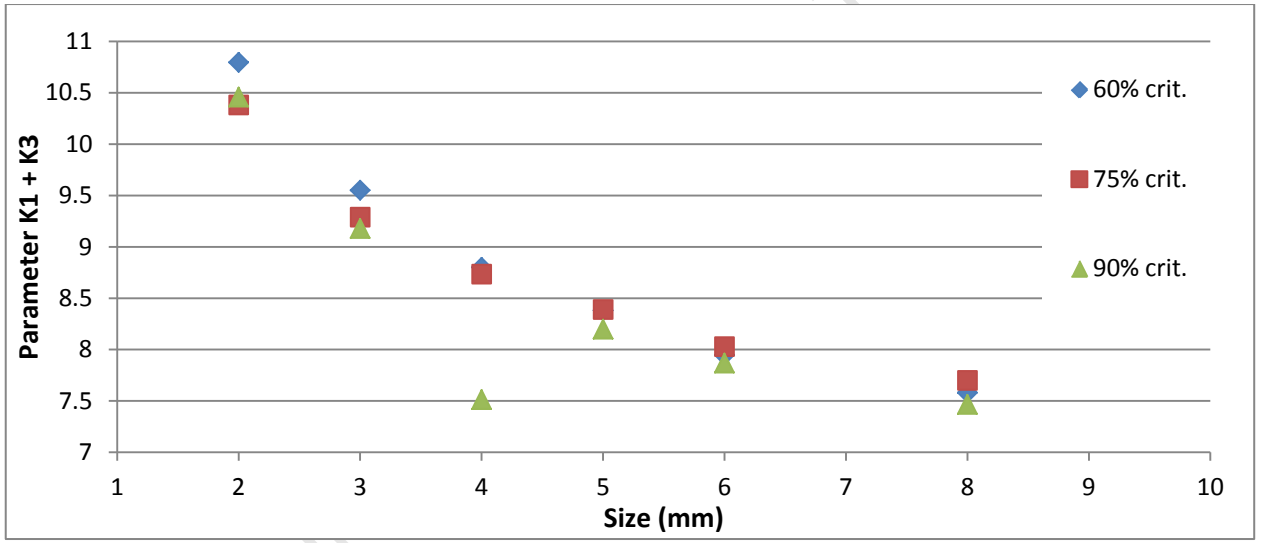

Figure B2: Relationship between parameter *A+C* with Particle size

The relationship between the decay rates K_2 and K_4 with particle size are plotted in Figure B3 and Figure B4. Similar to the initial value terms, both decay rates decrease with increasing particle size. This result follows on from the observations for the initial value terms, in that it highlights that as particle size

increases, it becomes more likely that a collision between particles results in a higher energy loss. This is because lower decay rates mean that collision frequencies decrease over a wider energy range. This is in line with existing research work as discussed in Section 2.2, which indicates that the presence of coarser sizes in the tumbling mill encourages higher breakage energies.

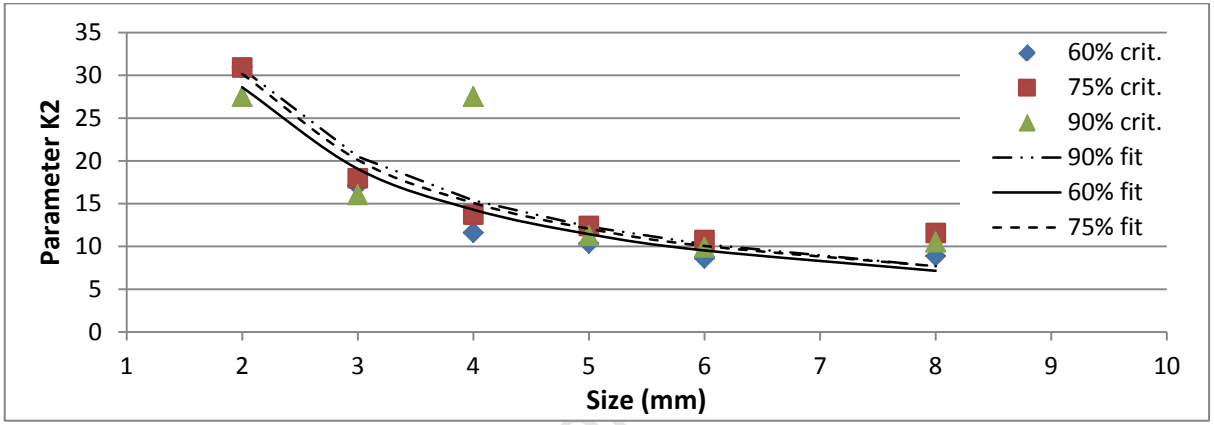

Figure B3: Relationship between parameter K_2 with Particle size

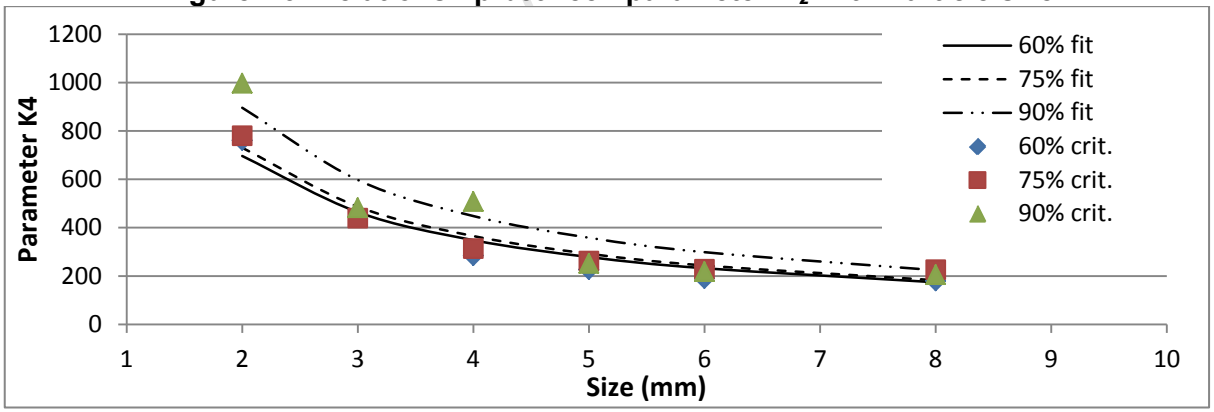

Figure B4: Relationship between parameter K_4 with Particle size

In addition to the general trend of the two decay rates, the plots show the least squares fits found by fitting Equation (B5) to this data. The mass fraction *c*, is included in the regression as it is not consistent for each size class present in the distribution. Based on the Weibull particle size distribution employed for this thesis (see Section 3.1), the mass fraction present in each size is given in Table B4.

$$y = K_{12} \cdot p^{K_8} \cdot c^{K_9} \quad \textbf{(B5)}$$

K_{12} is an arbitrary fitting constant, while K_8 and K_9 are the orders of magnitude required to reduce the fitted variable to a linear form against parameters K_2 and K_4. The order of magnitude for particle size is initially investigated with DEM mono-size data, for which the mass fraction is consistently 1, using Equation (B2). The parameters K_8 and K_9 are then calculated using Equation (B5) with full size distribution data, for which the particle size and mass fraction are altered. This least squares regression results in the fits illustrated in Figure B3 and Figure B4. A value of -1 is calculated for the order of magnitude for particle size K_8 and -0.5 for that of mass fraction K_9. These orders of magnidtude apply to both decay rates K_2 and K_4. This means that the two decay rates give a linear relationship with the inverse of particle size and the inverse square root of the mass fraction present in the respective size class.

Table B4: Mass fractions of each particle size used in DEM simulations

Size (mm)	Mass fraction
2	0.14
3	0.20
4	0.20
5	0.19
6	0.16
8	0.11

Mill speed

As shown from Figure B2, the mill speed does not significantly alter the sum of intial value terms in Equation (B1). The relationship between decay rates K_2 and K_4 with mill speed is demonstrated in Figure B5 and Figure B6. Both decay rates are found to decrease with increasing mill speed. This signifies that as mill speed increases, it becomes more likely that a collision between particles would result in a higher energy loss. This is in accord with the work of Yang et al. who made a similar observation (Yang et al., 2008).

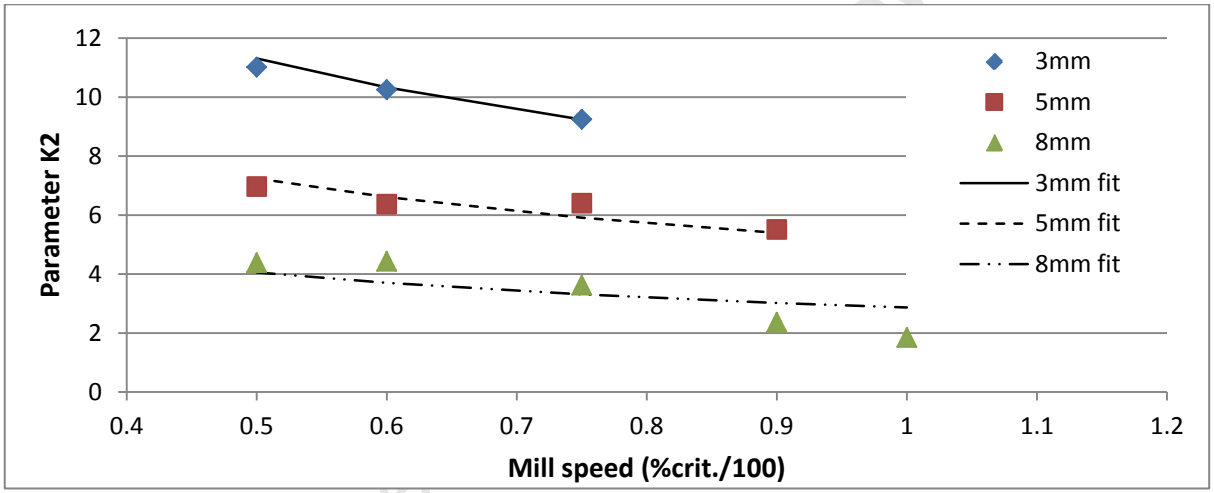

Figure B5: Relationship between parameter K_2 with Mill speed

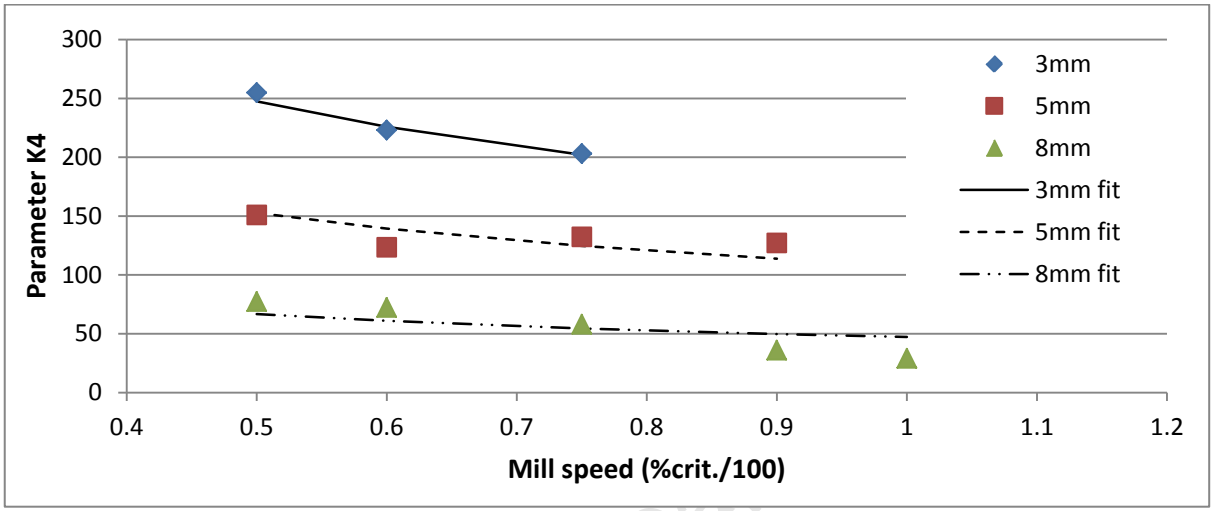

Figure B6: Relationship between parameter K_4 with Mill speed

The least squares fits found by fitting the decay rates to the mill speed using Equation (B2) are shown in the plots. It is found that the order of magnitude for mill speed K_6 is -0.5 for both decay rates K_2 and K_4. This means that both decay rate parameters decrease in linear proportion to the inverse square root of the mill speed.

Volumetric filling

The influence of mill filling on decay rates K_2 and K_4 is investigated. Figure B7 and Figure B8 illustrate the trend obtained for each respective parameter. The low decay rate K_2 is found to decrease marginally with increasing mill filling for the filling range investigated. This decrease occurs with a consistent value for the initial value term K_1. This suggests that mill filling increases, it becomes more likely that a collision between particles results in a higher energy loss. This is likely due to the higher number of particles with an increase in filling which increases the probability of collisions at higher energy losses (see Section 7.1).

The decay rate K_4 however increases for 5mm data while remaining fairly consistent for 8mm data with increasing filling. This increase occurs with a consistent value for the initial value term K_3. The increase in the high decay rate term implies that at the very low energy range over which the second term of the energy spectra model (B1) is active (see Figure B1), the collision frequencies decrease more rapidly with increasing filling. The overall effect of mill filling on the energy spectra for the range investigated is that as filling increases the number of collisions at very low energies decrease while those at higher energies increase.

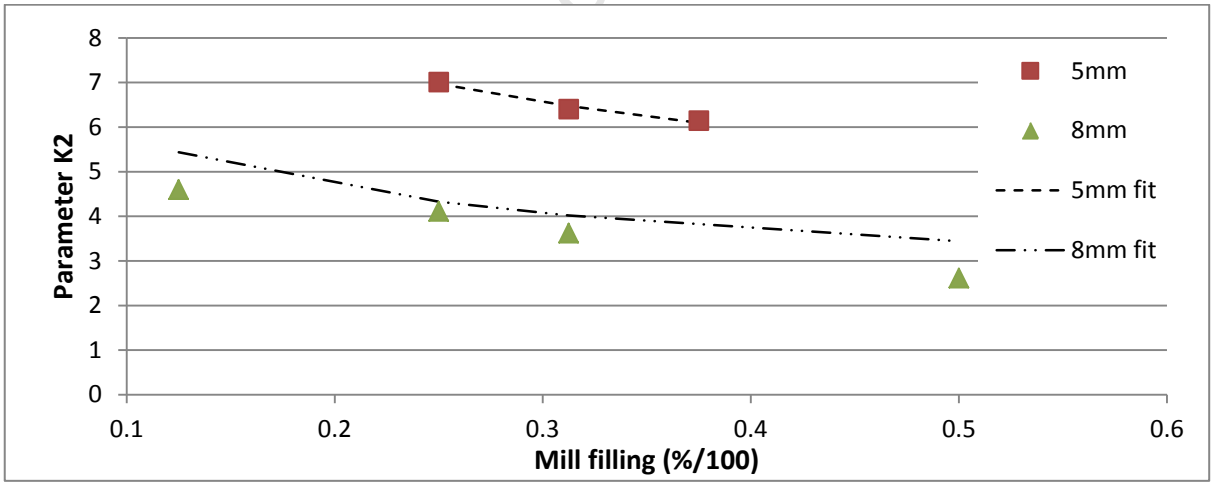

Figure B7: Relationship between parameter K_2 with Mill filling

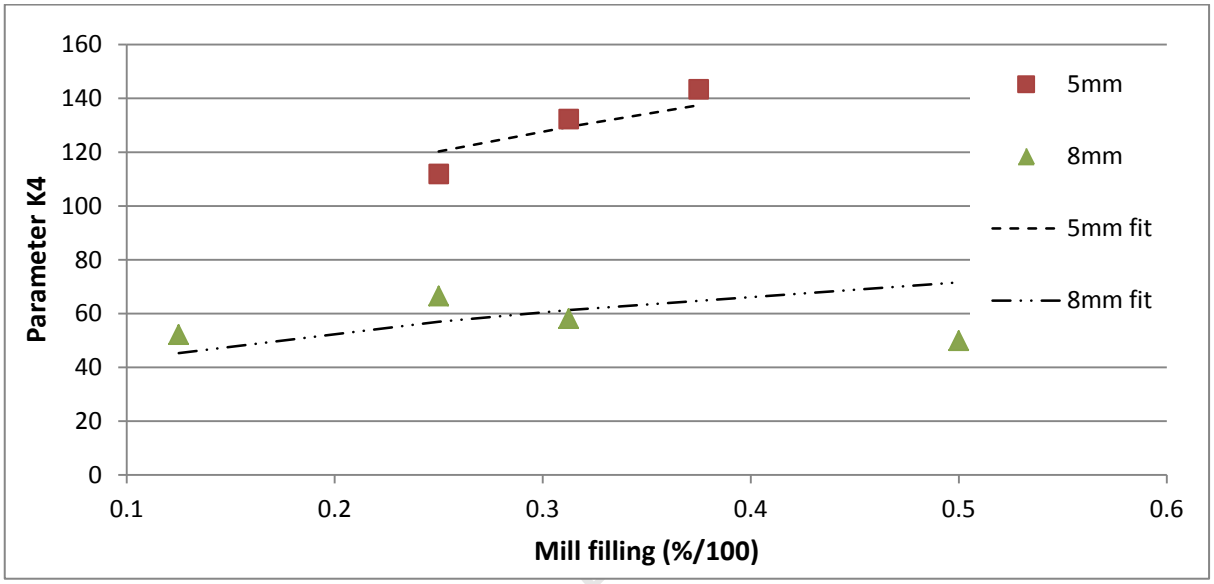

Figure B8: Relationship between parameter K_4 with Mill filling

A K_6 value of -0.33 is found for the low decay rate K_2 while 0.33 is found for the high decay rate K_4. This means that the two decay rates have a linear relationship with the cube root of mill filling, although for the lower decay rate it is the inverse while for the higher decay rate it is directly proportional.

Tanh-Sinh Quadrature of Energy Spectra model

From taking Equation (B1) and applying the standard laws of logarithms, the direct relationship for collision frequency *N* as a function of energy *E* is given by (B6):

$$N = 10^{K_1 \cdot e^{-K_2 \cdot E} + K_3 \cdot e^{-K_4 \cdot E}} \quad \textbf{(B6)}$$

The total energy dissipated by the tumbling mill during the steady state revolution is then the integral of (B6) from the minimum energy E_0 to the maximum energy E_{max}, given by (B7):

$$E_{diss} = \int_{E_0}^{E_{max}} 10^{K_1 \cdot e^{-K_2 \cdot E} + K_3 \cdot e^{-K_4 \cdot E}} dE \quad \textbf{(B7)}$$

Tanh-Sinh Quadrature (see Section 2.4) is utilized in this thesis to approximate the solution of the integrals associated with the energy spectra model. The integral is initially transformed from a function of energy $f(E)$, using a change of variable to a new function $g(t)$. The trapezoidal formula is then applied with an equal mesh size *h* given by (B8):

$$h = \frac{2 \cdot t_a}{M - 1} \quad \textbf{(B8)}$$

Where *M* is the number of terms used for the summation. 25 terms are used for evaluations in this work, which is found to be adequate for the degree of accuracy required. The value of t_a, for which the summation is truncated is 2. At each point *i* from 1 to 25 the value of the variable t_i is found using (B9):

$$t_i = t_a + h \cdot (i - 1) \quad \textbf{(B9)}$$

while the Tanh-Sinh function in (B10) is used for the transformation:

$$g(t_i) = Tanh\left(\frac{\pi}{2} \cdot \sinh(t_i)\right) \quad \textbf{(B10)}$$

The numerical solution for the integral of the energy spectra model over specified limits *a* and *b* is therefore approximated using (B11):

$$\int_a^b f(E)dE = \sum_{i=1}^{M} f(E_j) \cdot w_j \quad \textbf{(B11)}$$

where the abscissas E_j and the weights w_j are determined by (B12) and (B13) respectively.

$$E_j = \left(\left(\frac{b-a}{2}\right) \cdot g(t_i)\right) + \left(\frac{b+a}{2}\right) \quad \textbf{(B12)}$$

$$w_j = \left(\frac{\frac{\pi}{2} \cdot \cosh(t_i) \cdot \left(\frac{b-a}{2}\right) \cdot h}{cosh^2\left(\frac{\pi}{2} \cdot \sinh(t_i)\right)}\right) \quad \textbf{(B13)}$$

The integrals for the probability density function derived from the energy spectra model (Equation 7.11) are also evaluated using (B11), specifying limits *a* and *b* to reflect those in each integral. As the selected values of E_1 and E_2 are defined to be only over the interval from E_0 to E_{max}, the collision energy probability is always a fraction of the total dissipated energy. In accordance with probability theory, with limits E_1 and E_2 specified as E_0 and E_{max} the probability is 1.

With Tanh-Sinh quadrature, the mill power dissipation (equivalent to the power draw at steady state) of each size can be evaluated from the energy spectra model using (B14):

$$P_{DISS(P)} = \frac{\sum_{i=1}^{i=M}\left(10^{A\cdot e^{-B\cdot\left[\left(\frac{E_{max}-E_0}{2}\right)\cdot g(t_i)+\left(\frac{E_{max}+E_0}{2}\right)\right]}}\right)\cdot\left(10^{C\cdot e^{-D\cdot\left[\left(\frac{E_{max}-E_0}{2}\right)\cdot g(t_i)+\left(\frac{E_{max}+E_0}{2}\right)\right]}}\right)\cdot\left(\frac{\frac{\pi}{2}\cdot\cosh(t_i)\cdot\left(\frac{b-a}{2}\right)\cdot\left(\frac{2\cdot t_a}{M-1}\right)}{cosh^2\left(\frac{\pi}{2}\cdot\sinh(t_i)\right)}\right)}{T} \quad \textbf{(B14)}$$

In (B14), *T* is the periodic time for the mill rotation. The mean of the probability density function for the energy spectra is calculated by (B15):

$$\bar{E} = \frac{\int_{E_0}^{E_{max}} E\cdot 10^{K_1\cdot e^{-K_2\cdot E}+K_3\cdot e^{-K_4\cdot E}}dE}{\int_{E_0}^{E_{max}} 10^{K_1\cdot e^{-K_2\cdot E}+K_3\cdot e^{-K_4\cdot E}}dE} \quad \textbf{(B15)}$$

Here, the Tanh-Sinh method can similarly be applied to approximate the solution to the integral in the numerator using (B16):

$$\int_a^b E\cdot f(E) = \sum_{t_M=1}^{25} E_j\cdot f(E_j)\cdot w_j \quad \textbf{(B16)}$$